INSTITUTE OF SPACE AND ASTRONAUTICAL SCIENCE
YOSHINODAI, CHUO, SAGAMIHARA, KANAGAWA 252-5210

ISAS RESEARCH NOTE

ISAS RN 863

An X-ray Study of Classical Novae

Dai Takei

September 2011

1 : Rikkyo University

An X-ray Study of Classical Novae

Dai Takei

Department of Physics, Graduate School of Science, Rikkyo University
3-34-1, Nishi-Ikebukuro, Toshima, Tokyo, 171-8501, Japan
takei@ast.rikkyo.ac.jp

Thesis submitted to the Department of Physics,
Graduate School of Science, Rikkyo University
on November 26, 2010
in partial fulfillment of the requirements
for the degree of Doctor of Philosophy in Physics

Abstract

A classical nova explosion occurs in a binary system consisting of a white dwarf. The understanding of the mechanism of the explosions is quite important to reveal the nature not only of white dwarfs but also of several physics such as binary evolutions and space plasma. X-ray spectroscopy is a powerful tool for revealing these high energy phenomena. However, observing classical novae in X-rays has been quite difficult because of their faintness and transient behaviors. By collaborating with amateur astronomers worldwide and the *Swift* satellite for X-ray monitoring classical novae, we present the result of X-ray spectroscopic observations using the *Suzaku* and the *XMM-Newton* satellites in this thesis.

We established the effective observing system of classical novae using X-ray satellites despite the observational difficulties, and we successfully detected X-ray emission from a total of four classical novae (Suzaku J0105−72, V458 Vulpeculae, V2491 Cygni, and V2672 Ophiuchi). Various aspects of X-ray emission have been studied, including their typical behaviors and the diagnostics that they bring. The highlights of the results are (1) the first discovery of the non-thermal emission in the initial phase of classical novae, (2) the confirmation of the reestablished accretion in the post-outburst evolution, (3) the characterization of the chemical composition for the ejected material, (4) the diagnosis of the atmosphere on the white dwarf surface, and (5) a proposed classification for the X-ray emission from classical novae. We further discuss the mechanism of these high energy phenomena, based on our results and those in the literature. Finally, we show a general picture of classical novae, as well as a schematic view of the X-ray emission and their diagnostic utility to reveal physical quantities in classical novae.

Contents

List of Figures

List of Tables

Chapter 1

Introduction

Many stars twinkle in the night sky. Some of them show variability in brightness, which is easily noticeable with naked eyes. People started to recognize variable stars well before the days of Christ. Among these variable stars, those causing a sudden increase in brightness are called "nova stellarum" (Brahe, 1969) meaning "new star" in Latin; they usually change brightness so drastically that invisible stars with naked eyes become suddenly visible. Early astronomers likened them to the birth of a star. In recent studies, the sudden increase in brightness is considered to be caused by an explosion in the stellar evolution, and it is classified according to three different mechanisms; classical novae, dwarf novae, and supernovae.

Classical novae are in the middle of the three different novae both in energy scale and rate of appearance. Dwarf novae are smaller in scale but happen more often. Supernovae are larger in scale but happen less often. Classical novae are characterized by a sudden increase in the optical brightness by $\sim$10 mag within a few days. It occurs in a binary system composed of a white dwarf and a companion, which is either a dwarf or a giant star. When hydrogen-rich material from the companion is accumulated on the white dwarf surface to reach a critical mass, a nuclear burning is ignited to cause a nuclear runaway, which leads to a massive explosion in the system. The study of classical novae have a wide range of astrophysical importance, including the understanding of the white dwarf, the evolution of binary systems, population synthesis, cosmic-ray acceleration, space plasma physics, etc. However, in spite of the scientific importance, systematic studies of classical novae are difficult due to their transient behaviors.

A classical nova explosion produces several radiative sources, which become bright in broad wavelengths from radio to γ-rays in different time scales. In particular, some essential characteristics of an explosion can be observed in X-rays; e.g., the nuclear process on the white dwarf surface, shock-heated plasma within the expanding ejected material, and the release of gravitational energy through accretion. To make a major progress in the study of classical novae, systematic X-ray observations are necessary for these phenomena.

In order to conduct a systematic study of the X-ray emission from classical novae, we employ two strategies. One is the survey of archived observational data in X-rays. A systematic search for unexpected classical novae is possible in this method. The other is target-of-opportunity X-ray observations in collaboration with amateur astronomers and

a monitoring X-ray program. Almost all classical novae are discovered in ground-based observations by amateur astronomers. The combination of these efforts and the current X-ray observatories can provide opportunities unavailable before. Based on the two strategies, we conduct deep X-ray spectroscopy of recent classical novae using the *Suzaku*, *XMM-Newton* X-ray observatories and retrieve archived data taken by the *Swift* observatory.

The plan of this thesis is as follows. We review the basic characteristics of white dwarfs, binary systems, classical novae, and previous studies with high energy astrophysical missions in Chapter 2. Chapter 3 describes five objectives for this thesis and the strategy to take to address these objectives. The basic features of the astronomical satellite and instruments used in this thesis are summarized in Chapter 4. The results of our X-ray observations for each classical nova are explained in Chapter 5. In Chapter 6, we address the five objectives raised for this thesis, in which we discuss the mechanisms of X-ray phenomena, and propose a picture of the evolution of X-ray emission in classical novae. Finally, we summarize the thesis in Chapter 7.

Chapter 2

Review

In this chapter, we briefly review the basic characteristics of white dwarfs (section 2.1), binary systems (section 2.2), classical novae (section 2.3), and the result of previous observations with high energy astrophysical missions (section 2.4).

Contents

2.1 White Dwarfs

2.1.1 Introduction

A white dwarf is an electron degenerate object, which is one of the final evolutionary states of typical stars. When stars consume nuclear fuels, most of them except for particularly massive ones above ∼8 solar mass ($M_\odot$) collapse into white dwarfs (figure 2.1). While the mass of a white dwarf is comparable to that of the Sun, the radius is similar to that of the Earth (∼5000 km), indicating that a white dwarf is a compact object with a high density of $\sim 10^6$ g cm^{-3}. As the nuclear reaction does not occur in white dwarfs, an object cools by radiation spending a long time.

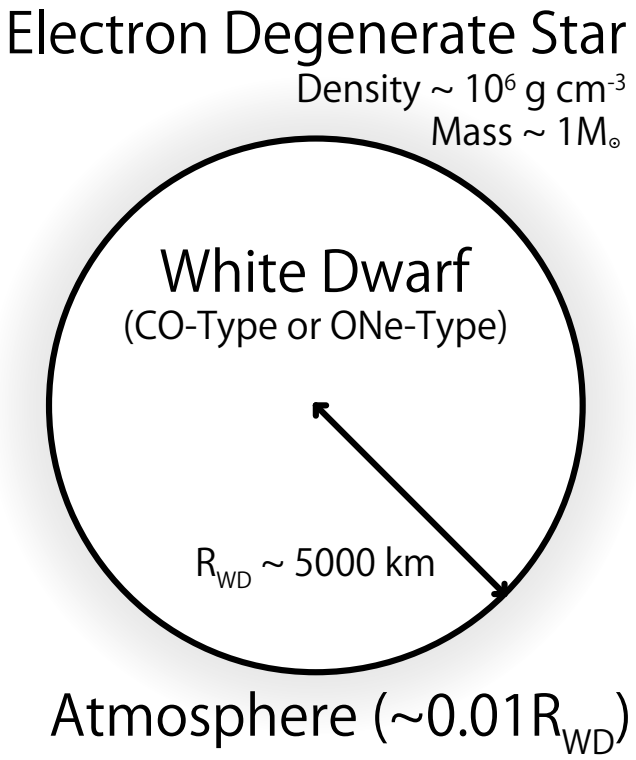

Figure 2.1: Schematic view of a white dwarf.

While a main-sequence star supports its own gravity by thermal pressure with nuclear fusion at the center, a white dwarf supports its gravity with degenerate electron. In the Pauli exclusion principle, two Fermions are not allowed to occupy the same quantum state simultaneously. As an electron can take two different spin orientations, only two particles can occupy the same quantum state, which is filled at a high density. This is the origin of the degeneracy pressure supporting the gravity of a white dwarf with no energy sources by a nuclear fusion. Reviews of white dwarfs can be found in e.g.,Shapiro & Teukolsky (1986).

2.1.2 Common Features

2.1.2.1 Mass-Radius Relationship

The relationship between the mass ($M_{\rm WD}$) and the radius ($R_{\rm WD}$) of a white dwarf was proposed by Nauenberg (1972). The radius of a white dwarf depends on the total kinetic energy of the electron motions and its own gravitational energy. An analytic approximation for the mass-radius relation is described as

$$R_{\rm WD} \;=\; 0.78 \times 10^9 \left((\frac{M_{\rm Ch}}{M_{\rm WD}})^{2/3} - (\frac{M_{\rm WD}}{M_{\rm Ch}})^{2/3} \right)^{1/2} \;\; [\rm cm], \tag{2.1}$$

where more massive white dwarfs are smaller (figure 2.2). Due to the relativistic correction term, the radius becomes zero for a finite value of the white dwarf mass. Therefore, the upper bound for the white dwarf mass ($M_{\rm Ch}$) is present at about 1.4 $M_{\odot}$, which is called the Chandrasekhar limit (e.g., Chandrasekhar 1931b,a).

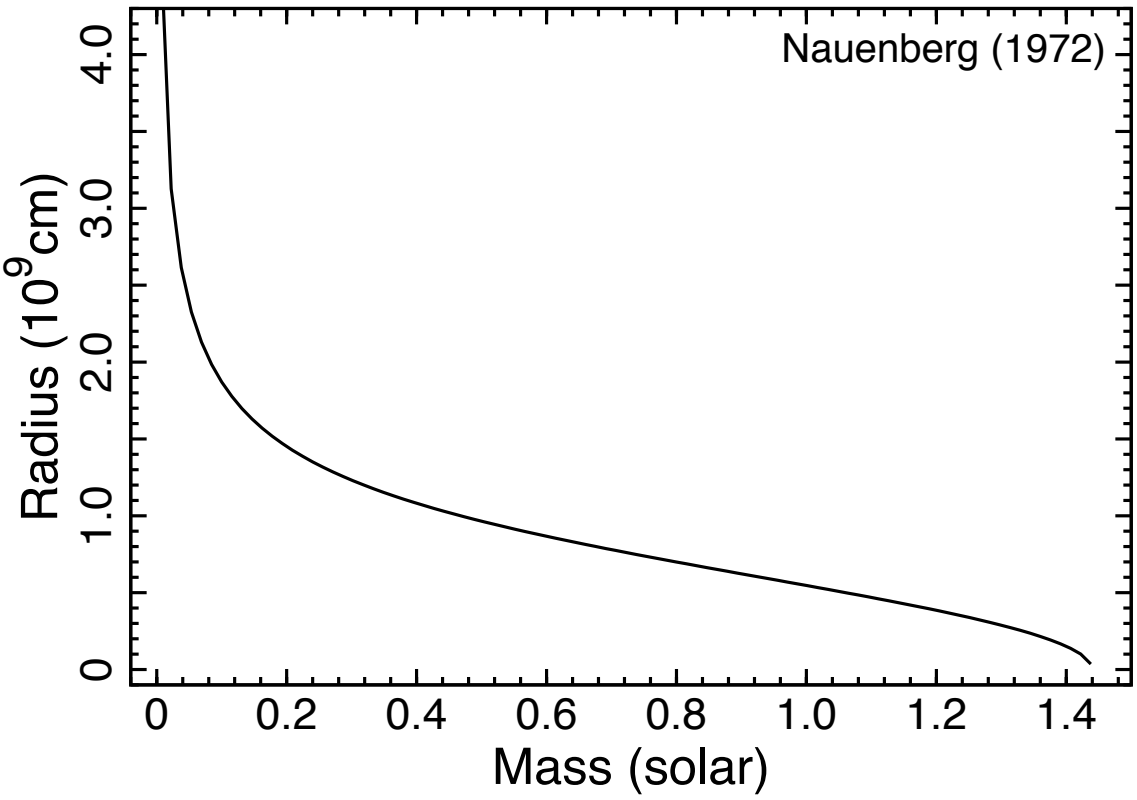

Figure 2.2: Mass-radius relationship of a white dwarf (Nauenberg, 1972).

2.1.2.2 Chemical Composition

At the end of the stellar evolution, a core and an outer layer are formed. The core is mainly composed of nuclear products and becomes a white dwarf, while the outer layer is composed of remaining light elements (H and He) and forms a planetary nebula. The nuclear reaction depends on the temperature of stars. The major nuclear reaction in less massive stars does not go beyond elements heavier than O, while that in massive stars reaches up to Ne and Mg. Therefore, less massive stars typically collapse into a carbon-oxygen (CO) type core, and massive stars collapse into an oxygen-neon (ONe) type core (figure 2.1). Therefore, the initial mass of a white dwarf core also depends on the chemical composition: the CO-type core is less than $\sim$1.2 $M_\odot$, and the ONe-type core is more than $\sim$1.1–1.2 $M_\odot$ (Iben & Tutukov, 1989).

2.1.2.3 Atmosphere

Quite a thin layer ($\sim$0.01 $R_{\rm WD}$) of hydrogen and helium-rich material exists on the surface of a white dwarf as atmosphere (figure 2.1), which consists of material and the residual envelope of the progenitor star. As heavier elements sink to the bottom of the white dwarf by the gravity, the atmosphere consists of lighter elements.

2.1.2.4 Chandrasekhar Limit

If the white dwarf mass reaches the Chandrasekhar limit, the system cannot be supported by the electron degeneracy pressure against gravitational collapse. Further evolution of the system is expected in the high density medium. For a CO-type core, the carbon-oxygen nuclear burning is ignited by dense material. This heats up the core, and the increase in the temperature leads to further reaction in the nuclear fusion. Eventually, a Type Ia supernova explosion occurs at the end of the nuclear reaction, which is called the Carbon detonation. In contrast, an ONe-type core collapses into a neutron degenerate star, because C, the dominant energy source, is deficient in its core, and an implosion occurs instead of a supernova explosion.

2.2 Binary Systems

2.2.1 Introduction

A single white dwarf just fades out depending only on the cooling time in the evolution. However, if a white dwarf comprises a binary system with a star, the evolution becomes quite complex. Intense activities can be seen in the system because nuclear fuels are provided from the companion star. The binary system composed of a white dwarf and a dwarf or a giant companion is called the cataclysmic variable (CV) as it shows rapid changes in brightness. We next briefly review the mechanisms of the binary system composed of a white dwarf.

2.2.2 Mass-Transfer Systems

2.2.2.1 Roche Lobe

Each component in a binary system has its individual gravitational field. The equipotential surface by the primary and the secondary forms a calabash-like shape, which is called the Roche lobe (figure 2.3). If material of a companion star leaks through the Lagrangian point (L1), it falls on to the white dwarf, transferring mass from the secondary to the primary.

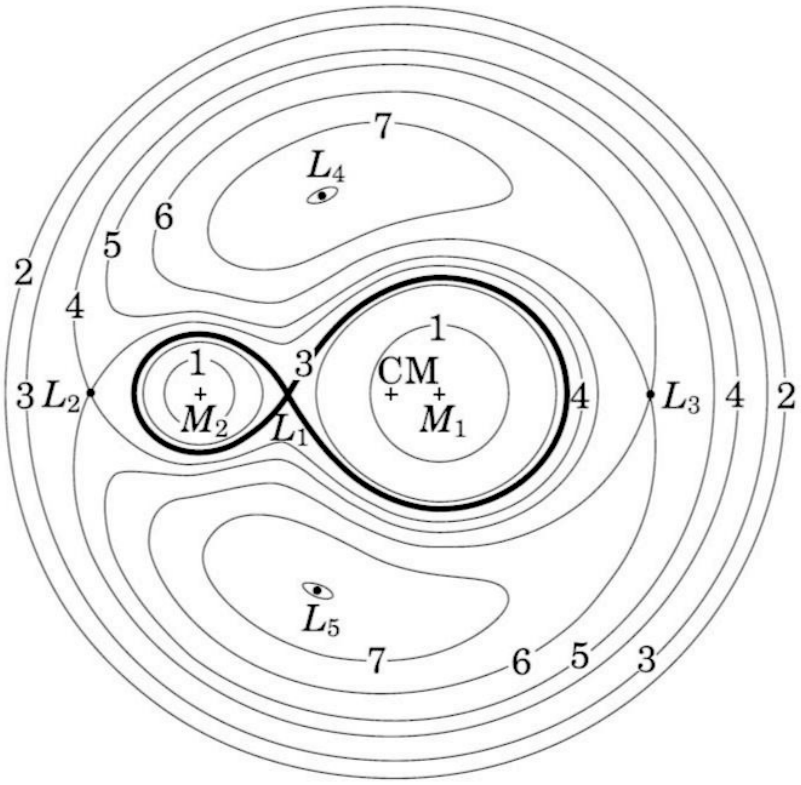

Figure 2.3: Roche lobe and an equipotential surface (Frank et al., 2002). The ratio between the mass of primary and secondary objects is $M_1 : M_2 = 4 : 1$.

2.2.2.2 Mass-Transfer Models

Two major ideas have been considered to explain the mass transfer. One is a Roche lobe overflow, in which material fills and overflows its gravitational field, then it falls on to the white dwarf. The Roche lobe overflow is caused by an expansion of a star as well as by a shrinkage of a Roche lobe with angular momentum loss due to e.g., a magnetic braking (Verbunt & Zwaan, 1981) and a gravitational radiation (Faulkner, 1971). This model is typically applied for close binary systems. The other is a wind-fed model, in which the strong stellar wind from a red giant companion star can exceed its gravitational field, then material falls on to the white dwarf. In this case, the companion star does not fill its Roche lobe for transferring material.

2.2.3 Accretion Mechanisms

When mass transfer occurs in a binary system, hydrogen-rich material from the companion star is accumulated on the white dwarf surface. The form of mass accretion mainly depends on a magnetic field strength on the white dwarf surface (e.g., Warner 2003). We next review three types of accretion mechanisms depending on the strength of its magnetic field.

2.2.3.1 Non-magnetic or Weakly Magnetized Systems

Most of cataclysmic variables contain a non-magnetic or weakly magnetized ($\lesssim 10^5$ gauss) white dwarf (e.g., Warner 2003). In this system, infalling material from the companion star forms an accretion disk around the white dwarf (figure 2.4). Weak X-ray emission is a common signature in this system.

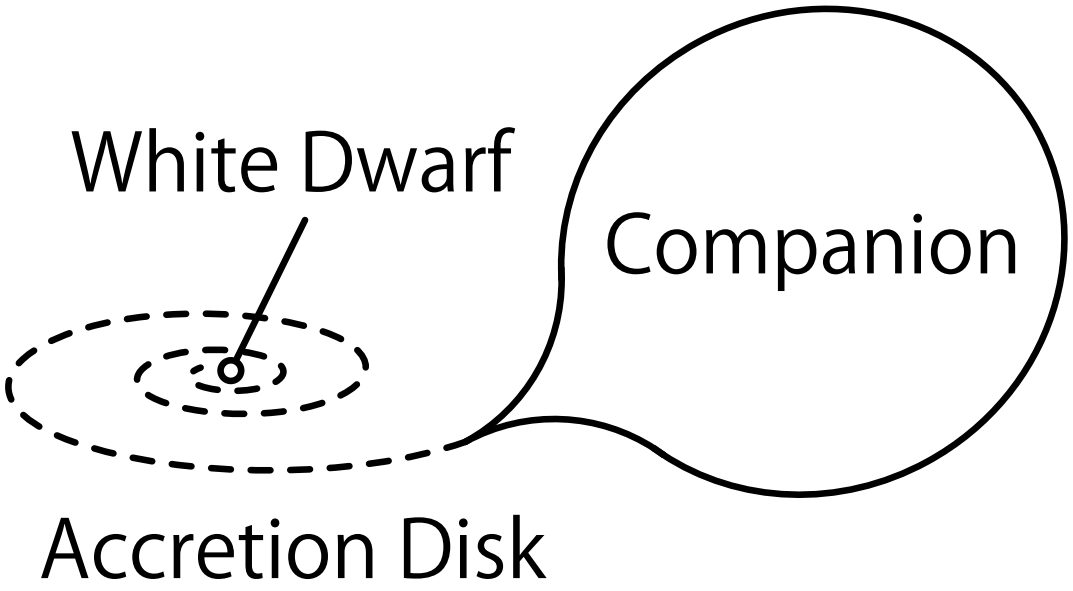

Figure 2.4: Schematic view of a non-magnetic or weakly magnetized system.

2.2.3.2 Polar Systems

The polar is a subclass of cataclysmic variables, which is a binary system composed of a strongly magnetized ($\gtrsim 10^7$ gauss) white dwarf and a companion (e.g., Cropper 1990). In this system, the motion of infalling material is governed by their strong magnetic field, thus instead of a disk an accretion funnel is formed along the magnetic field lines (figure 2.5). The modulation due to the white dwarf spin and the orbital motion is typically confirmed in both optical and X-ray observations. Bright soft as well as weak hard X-ray emission are common signatures in this system.

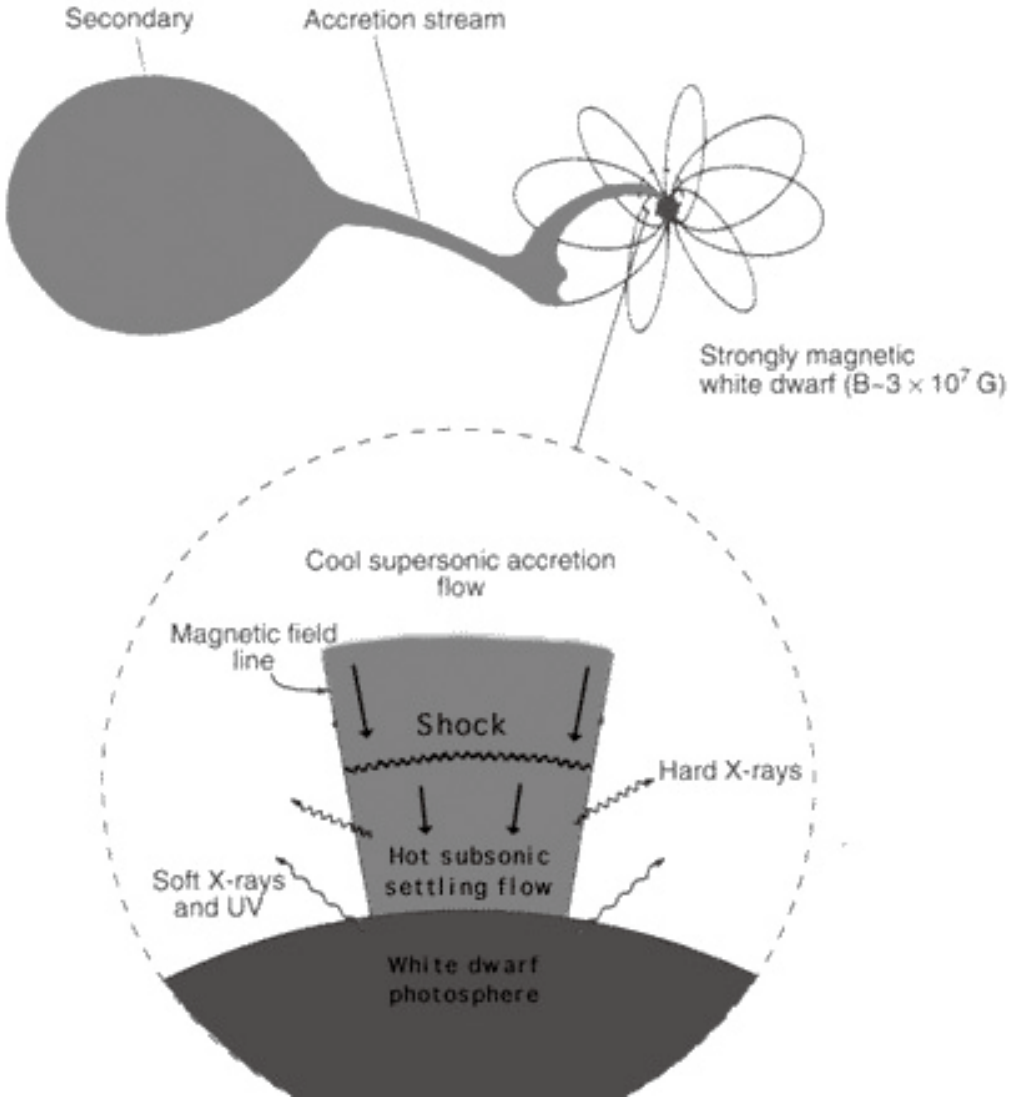

Figure 2.5: Schematic view of a polar system (http://heasarc.gsfc.nasa.gov/docs/objects/cvs/cvstext.html).

2.2.3.3 Intermediate Polar Systems

The intermediate polar (IP) is another subclass of cataclysmic variables, which is a binary system containing a moderately magnetized ($\sim 10^5$–10^7 gauss) white dwarf (e.g., Patterson 1994). In this system, infalling material from the companion star forms an accretion disk around the white dwarf, which is truncated at the Alfvén radius where the magnetic pressure and the ram pressures are equal to each other, from which matter accretes along the field lines (figure 2.6). The modulation due to the white dwarf spin and the orbital motion is confirmed in both optical and X-ray observations. Bright hard X-ray emission with the Fe Kα lines in different ionization stages is a common signature, which is considered to be caused by shocks of the accretion funnel.

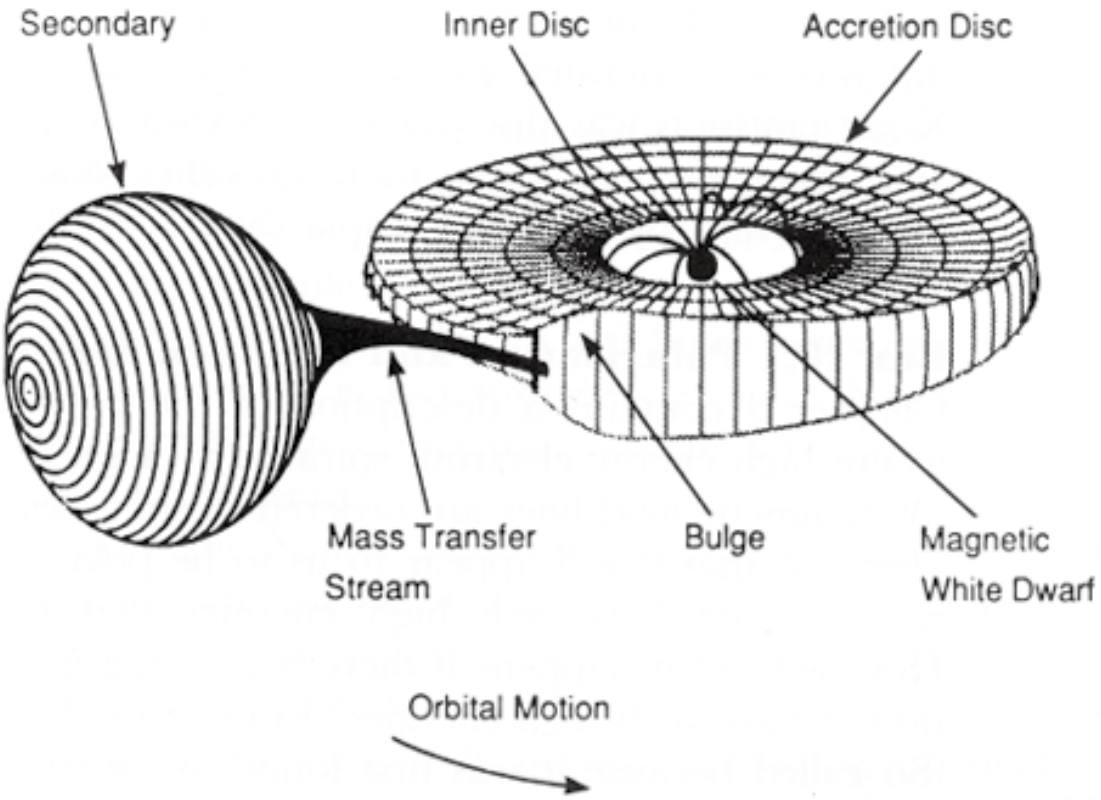

Figure 2.6: Schematic view of an IP system (http://heasarc.gsfc.nasa.gov/docs/objects/cvs/cvstext.html).

2.3 Classical Novae

2.3.1 Introduction

A classical nova occurs in an accreting binary system composed of a white dwarf and a main-sequence or a giant star. Hydrogen-rich material filling the Roche lobe around the companion accretes to the white dwarf. When the amount of accreted material reaches a critical mass, hydrogen fusion is ignited explosively to cause a thermonuclear runaway on the white dwarf surface. A schematic view of the classical nova explosion is show in figure 2.7. We here briefly review the observational properties and the theoretical studies of classical novae. Readers can refer to e.g., Warner (2003) and Bode & Evans (2008) for extensive reviews of classical novae, including basic properties (Warner, 2008), nucleosynthesis (Starrfield et al., 2008), and X-ray observations (Krautter, 2008).

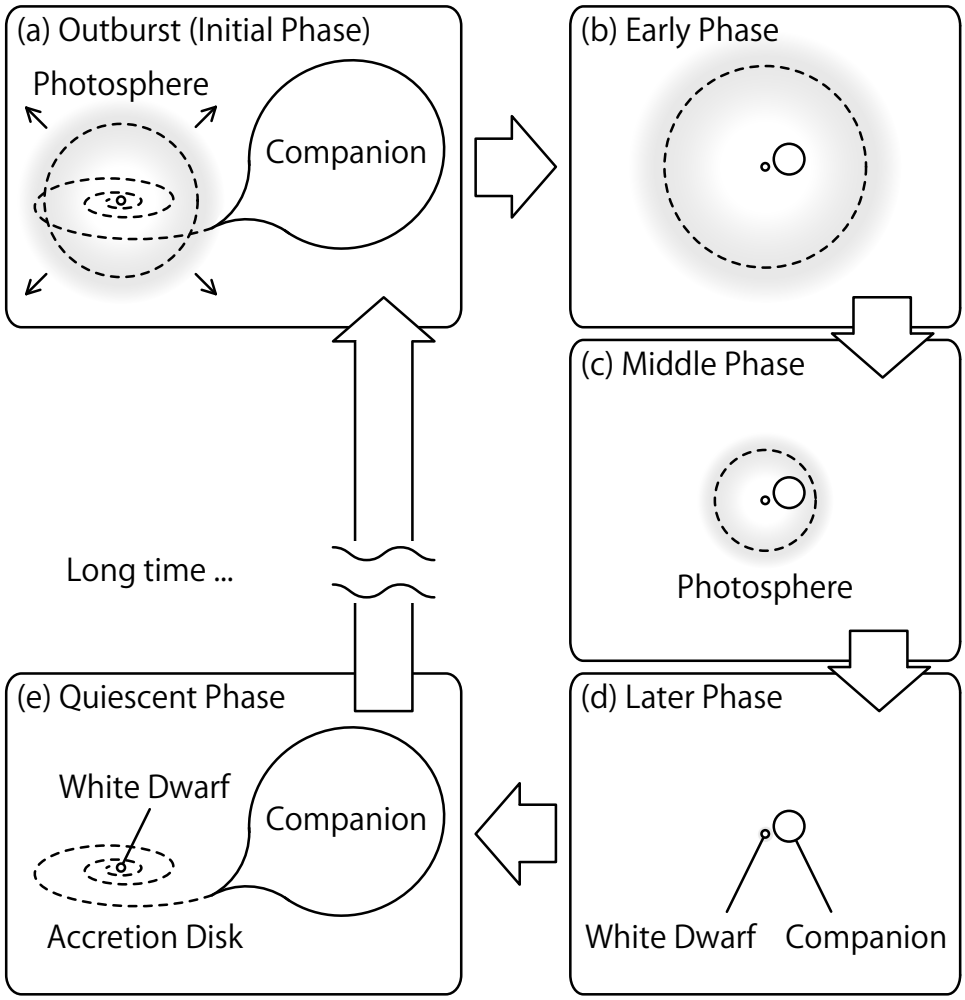

Figure 2.7: Schematic view of a classical nova evolution.

2.3.2 Observational Properties

2.3.2.1 Time Development during the Outburst

Figure 2.8 shows a schematic view of the time development in the optical brightness during a nova outburst. The eruption of a classical nova outburst is characterized by a sudden increase in the optical brightness by ∼10 mag within a few days. The brightness reaches the maximum, and then rapidly declines in the early phase. In the subsequent transition phase, some distinctive characteristics have been reported; (1) a large dip in the brightness, (2) oscillations with a period of ∼10 days and an amplitude of up to ∼1.5 mag, (3) a plateau in the brightness, (4) rebrightening with a clear secondary peak and a following rapid decay, and (5) a continuous decline with no feature. After the transition phase, the brightness follows an extrapolated decline from the early phase, and it settles back to the quiescent level.

A sequence of the nova events from the rise to the decay occurs in the time scale of several dozen days to years. Therefore, classical novae can be typically classified according to the speed of the development (section 2.3.2.3). The time development of classical novae has also been studied in theoretical works (e.g., Hachisu & Kato 2006).

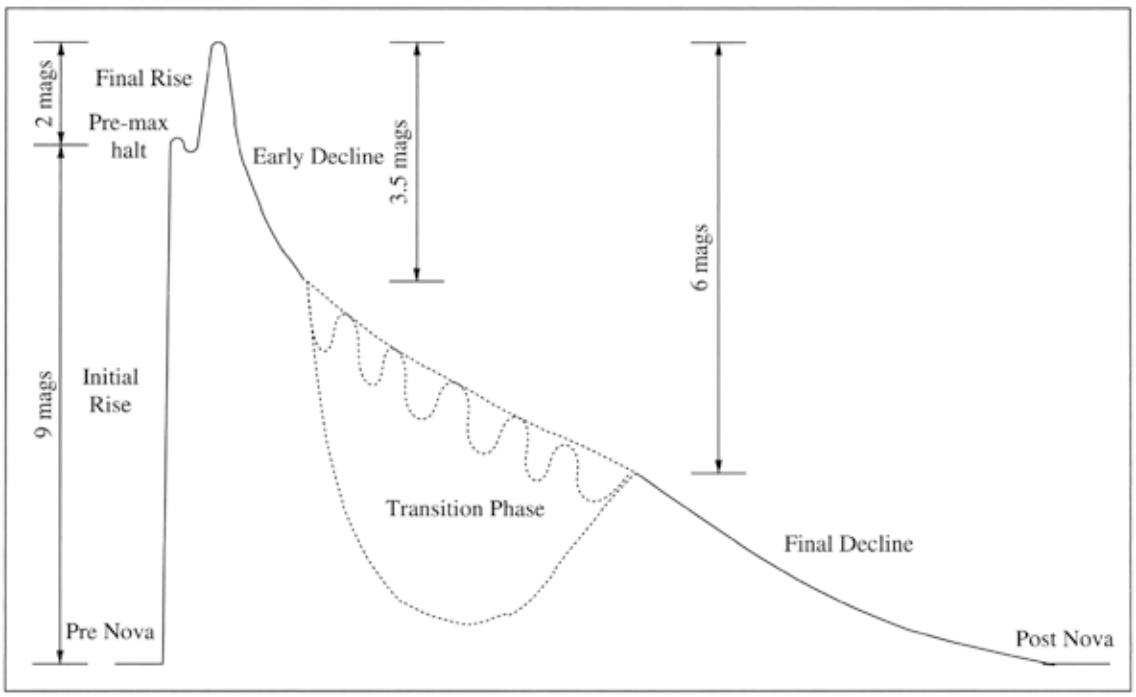

Figure 2.8: Schematic view of an optical time-development during a nova outburst (Warner, 2008).

2.3.2.2 Frequency and Distribution

The discovery rate of classical novae has continuously increased in recent years with significant improvements in the observing system and technique of amateur astronomers. While classical novae were discovered at the rate of $\sim$3 yr^{-1} in the 20th century, the value has grown to $\sim$10 yr^{-1} in the 21st century[1]. The distribution of Galactic classical novae are shown in figure 2.9. Based on the observational bias and the interstellar extinction, the rate of classical nova eruptions in the Galaxy is estimated to be 73$\pm$24 yr^{-1} (Liller & Mayer, 1987), 29$\pm$18 yr^{-1} (Ciardullo et al., 1990), 30$\pm$10 yr^{-1} (M. Hernanz & J. José, 2002), and 34^{+15}_{-12} yr^{-1} (Darnley et al., 2006).

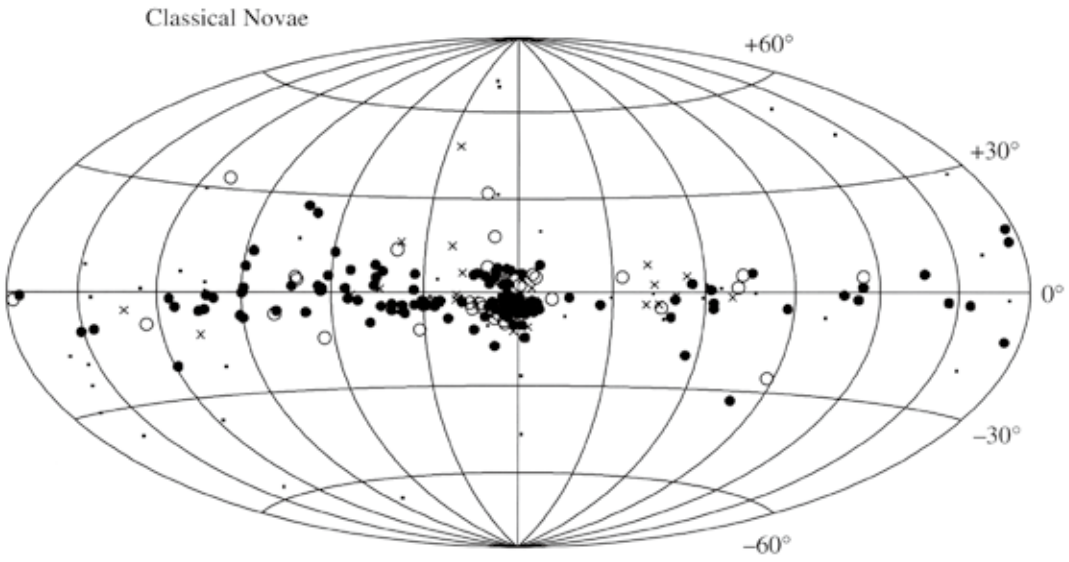

Figure 2.9: Galactic distribution of classical novae (Warner, 2008; Bode & Evans, 2008). All data are from the catalog of cataclysmic variables by Downes et al. (2005).

[1]See http://www.cfa.harvard.edu/iau/nova_list.html for the number.

2.3.2.3 Classification

As classical novae have several time scales, a classification was proposed based on the decline speed in the optical magnitude (e.g., Payne-Gaposchkin 1957). Classical novae are typically classified by t_2 and t_3 values, which are respectively the number of days to fade by 2 and 3 mag from the optical maximum. We summarize the classification by the decline speed of classical novae in table 2.1.

Table 2.1: Speed class of classical novae (Payne-Gaposchkin, 1957).

Speed class	t_2 (days)
Very fast	<10
Fast	11–25
Moderately fast	26–80
Slow	81–150
Very slow	151–250

Other classifications were proposed based on other characteristics. If the binary system causes classical nova explosions more than once in historical records, it is referred to as a "recurrent" nova. The explosions from systems containing a red giant companion are called as "symbiotic" novae. A classification based on optical spectroscopic features was proposed by e.g., Williams et al. (1991).

2.3.2.4 MMRD Relationship

An empirical relation is confirmed between the maximum absolute magnitude and the rate of decline (MMRD) among classical novae; the intrinsically brighter ones fade faster. The MMRD relationship was found in nearby galaxies such as M31 and the Magellanic Clouds for the first time. The distances to the galaxies, which includes several classical novae, are already given by other methods so that the absolute magnitudes and the rates of decline for classical novae can be estimated. Then, Capaccioli et al. (1989) concluded that the MMRD relationship can be applied for the Galaxy. Figure 2.10 shows the MMRD relationship for the Galactic classical novae, and it is usually expressed through the form

$$M = a_n + b_n \log(t_n), \tag{2.2}$$

where M is absolute magnitude, t_n is the number of days to fade by n mag from the optical maximum, a_n and b_n are estimated by observations.

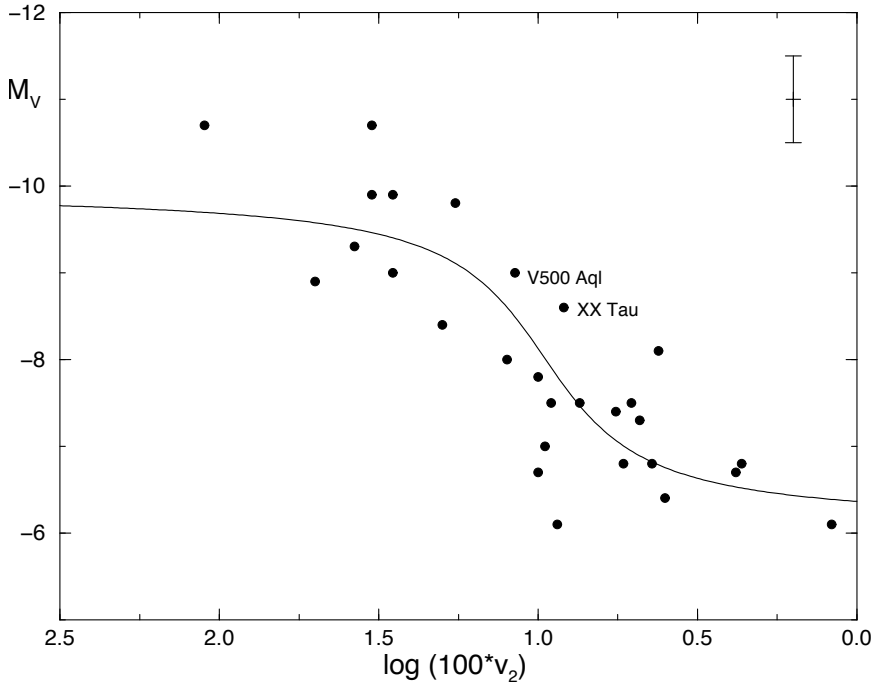

Figure 2.10: MMRD relationship in the Galaxy (Downes & Duerbeck, 2000). M_v is the absolute magnitudes, and v_2 is the decline rate to fade by 2 mag from the optical maximum in the unit of mag day^{-1}. The average error of a data point is indicated in the upper right-hand corner.

The MMRD relationship is a good distance indicator for classical novae. The combination of the apparent magnitude (m) and the estimated absolute magnitude (M) provides the luminosity distance (D_L) to the object using

$$M = m - 5(\log_{10}(D_L) - 1), \tag{2.3}$$

where D_L is in the unit of parsecs. The distance estimation is essential to evaluate the luminosity, and this method is applied for most of classical novae in recent studies.

2.3.2.5 Multi-Wavelength Behavior

Classical novae are observed over an extremely wide energy (wavelength) range from radio to γ-ray in the outburst (figure 2.11). Therefore, several radiating components have been considered; e.g., the photosphere, the dust, the nebula, etc. We concentrate on X-ray emission in this research, which will be separately reviewed in section 2.4.

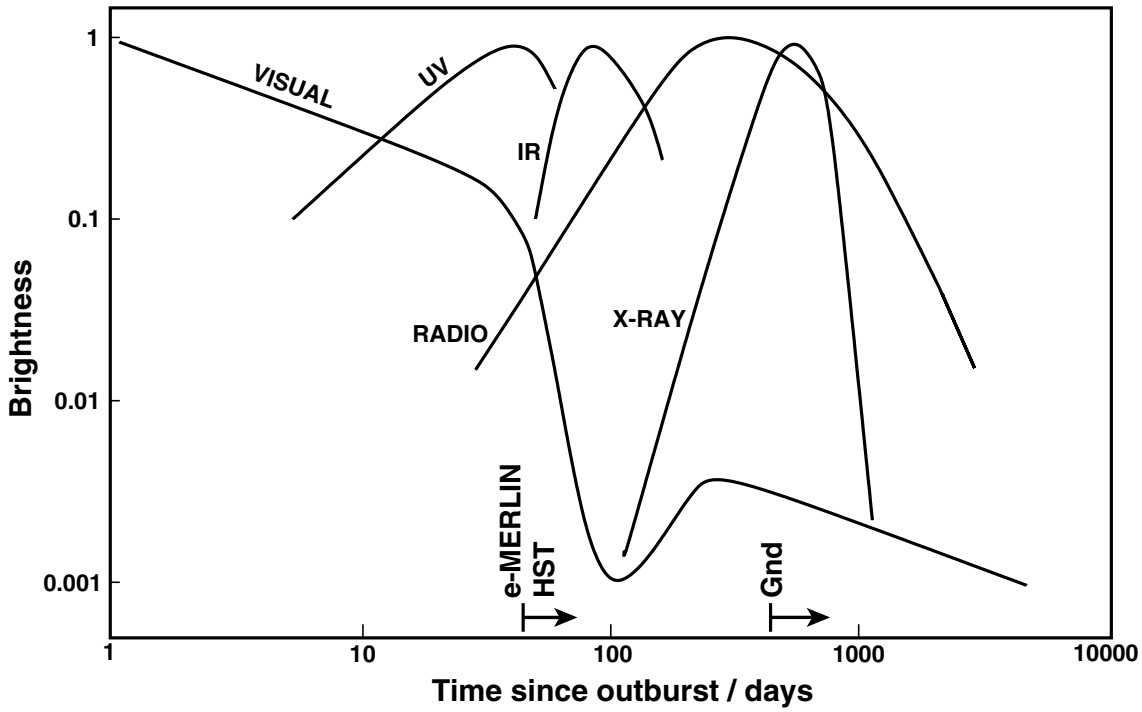

Figure 2.11: Multi-frequency development of a classical nova outburst (Bode, 2010).

2.3.3 Theoretical Studies

2.3.3.1 Nuclear Reaction

The dominant energy source of a classical nova explosion is a nuclear fusion of accreted hydrogen-rich material. The nuclear reactions of hydrogen burning have two mechanisms; the proton-proton chain (p-p chain) and the carbon-nitrogen-oxygen cycle (CNO cycle). An essential difference between these two reactions can be seen in the dependence of the temperature (figure 2.12).

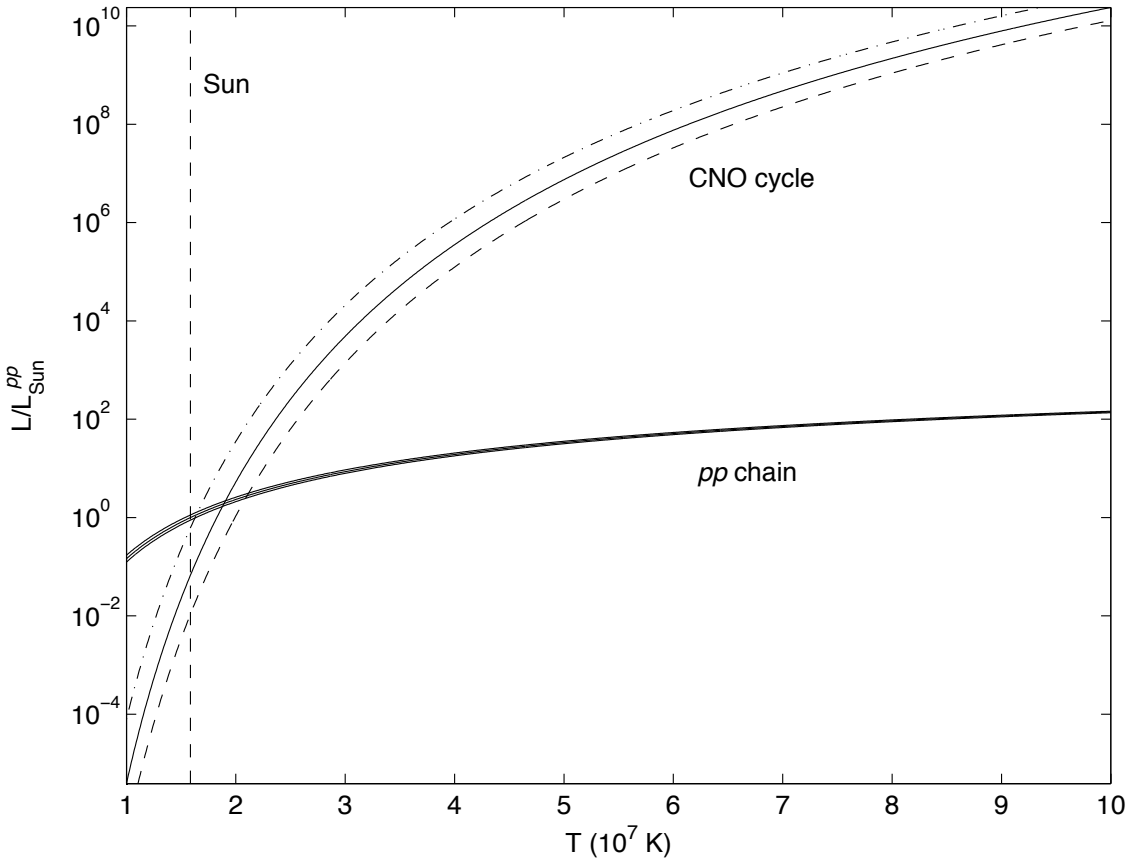

Figure 2.12: Log-linear plot of dimensionless luminosity over temperature, for the p-p chain and the CNO cycle. The vertical line shows the luminosity in the unit of solar luminosity. All curves are normalized with respect to the p-p luminosity inside the Sun (Ferro et al., 2004).

Proton-Proton Chain

The *p*-*p* chain is one of the nuclear reactions to convert hydrogen to helium. This reaction starts at a temperature of $\sim 10^6$ K. The energy output rate of the *p*-*p* chain has a temperature dependence of $\epsilon_{\rm PP} \propto T^4$. The *p*-*p* chain consists of three branches (pp-I, pp-II, and pp-III). The *p*-*p* chain is dominant at temperatures of $\lesssim 1.4\times10^7$, ~ 1.4–2.3×10^7, and $\gtrsim 2.3\times10^7$ K, respectively. The three reactions are described as follows,

$$ {}^1_1\mathrm{H} + {}^1_1\mathrm{H} \rightarrow {}^2_1\mathrm{H} + \mathrm{e}^+ + \nu_\mathrm{e}, \tag{2.4} $$
$$ {}^2_1\mathrm{H} + {}^1_1\mathrm{H} \rightarrow {}^3_2\mathrm{He} + \gamma, \tag{2.5} $$

pp-I branch

$$ {}^3_2\mathrm{He} + {}^3_2\mathrm{He} \rightarrow {}^4_2\mathrm{He} + {}^1_1\mathrm{H} + {}^1_1\mathrm{H}, \tag{2.6} $$

pp-II branch

$$ {}^3_2\mathrm{He} + {}^4_2\mathrm{He} \rightarrow {}^7_4\mathrm{Be} + \gamma, \tag{2.7} $$
$$ {}^7_4\mathrm{Be} + \mathrm{e}^- \rightarrow {}^7_3\mathrm{Li} + \nu_\mathrm{e}, \tag{2.8} $$
$$ {}^7_3\mathrm{Li} + {}^1_1\mathrm{H} \rightarrow {}^4_2\mathrm{He} + {}^4_2\mathrm{He}, \tag{2.9} $$

pp-III branch

$$ {}^3_2\mathrm{He} + {}^4_2\mathrm{He} \rightarrow {}^7_4\mathrm{Be} + \gamma, \tag{2.10} $$
$$ {}^7_4\mathrm{Be} + {}^1_1\mathrm{H} \rightarrow {}^8_5\mathrm{Li} + \gamma, \tag{2.11} $$
$$ {}^8_5\mathrm{B} \rightarrow {}^8_4\mathrm{Be} + \mathrm{e}^+ + \nu_\mathrm{e} + \gamma, \tag{2.12} $$
$$ {}^8_4\mathrm{Be} \rightarrow {}^4_2\mathrm{He} + {}^4_2\mathrm{He}. \tag{2.13} $$

The total energy via these chains is $\sim$20–30 MeV per one cycle. The time scale of the reaction takes an average of $\sim 10^9$ years at the temperature at the center of the Sun, which is longer than that of the CNO cycle.

CNO Cycle

The CNO cycle is the other nuclear reaction to convert hydrogen to helium, in which the cycle produces one ${}^{4}_{2}\mathrm{He}$ from four ${}^{1}_{1}\mathrm{H}$ using carbon, nitrogen, and oxygen isotopes. This cycle starts at the temperature of $\sim 10^7$ K, and it becomes the dominant energy source at $\sim 2\times 10^7$ K instead of the *p-p* chain reaction (figure 2.12). The energy output rate of the CNO cycle has a strong dependency on the temperature ($\epsilon_{\mathrm{CNO}} \propto T^{18}$). While the cycle has several branch, the main fusion reaction is described as follows,

$$
\begin{aligned}
{}^{12}_{6}\mathrm{C} + {}^{1}_{1}\mathrm{H} &\rightarrow {}^{13}_{7}\mathrm{N} + \gamma, && (2.14)\\
{}^{13}_{7}\mathrm{N} &\rightarrow {}^{13}_{6}\mathrm{C} + \mathrm{e}^{+} + \nu_{\mathrm{e}}, && (2.15)\\
{}^{13}_{6}\mathrm{C} + {}^{1}_{1}\mathrm{H} &\rightarrow {}^{14}_{7}\mathrm{N} + \gamma, && (2.16)\\
{}^{14}_{7}\mathrm{N} + {}^{1}_{1}\mathrm{H} &\rightarrow {}^{15}_{8}\mathrm{O} + \gamma, && (2.17)\\
{}^{15}_{8}\mathrm{O} &\rightarrow {}^{15}_{7}\mathrm{N} + \mathrm{e}^{+} + \nu_{\mathrm{e}}, && (2.18)\\
{}^{15}_{7}\mathrm{N} + {}^{1}_{1}\mathrm{H} &\rightarrow {}^{12}_{6}\mathrm{C} + {}^{4}_{2}\mathrm{He}. && (2.19)
\end{aligned}
$$

The total product energy via the cycle is $\sim$30 MeV per one cycle. The time scale of the reaction takes an average of $\sim 10^8$ yr at the temperature of the Sun, which is shorter than that of the *p-p* chain. The nuclear process of the equation 2.17 is the bottleneck of the entire cycle as the slowest reaction, indicating that ${}^{14}_{7}\mathrm{N}$ becomes abundant in the cycle.

2.3.3.2 Cause of the Classical Nova Explosion

The gravitational force compresses the accreted material on the white dwarf surface, where the temperature is determined by the mass accretion rate, the total mass of the accumulated material, and the white dwarf mass. The evolutionary behaviors of binary systems depends on the mass accretion rate (figure 2.13). When the accretion rate is larger than $\sim 10^{-7}\ M_\odot\ \mathrm{yr}^{-1}$, the temperature of the accreted material becomes sufficiently high to ignite nuclear fusion of the CNO cycle, thus a steady nuclear burning occurs on the white dwarf surface. When the accretion rate is lower than $\sim 10^{-7}\ M_\odot\ \mathrm{yr}^{-1}$, the temperature does not increase sufficiently high to ignite nuclear fusion, thus hydrogen-rich material only accumulates on the white dwarf surface. Classical novae are caused by the accumulated material, and the explosion occurs only from the binary systems that the accretion rate is sufficiently small.

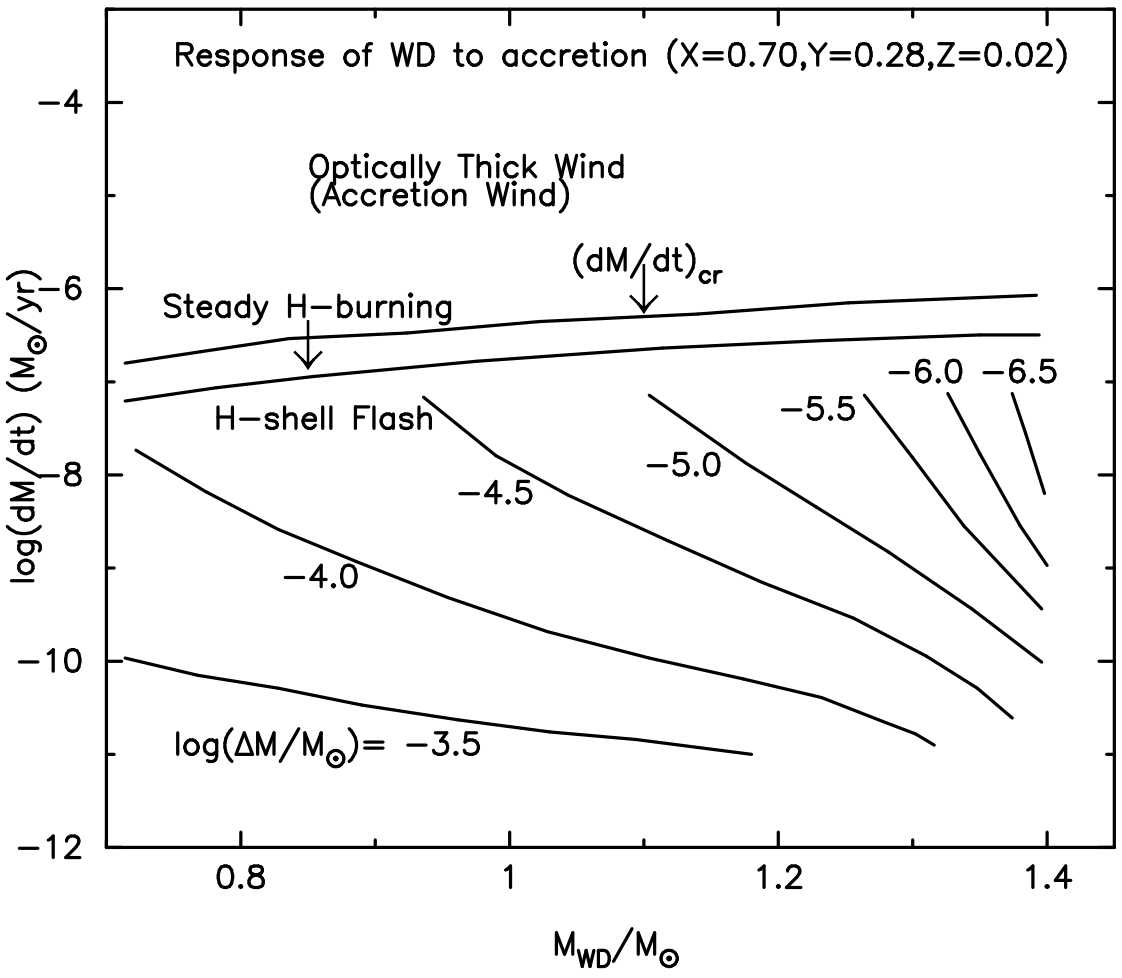

Figure 2.13: Response of white dwarf binaries in the mass and the accretion rate (Hachisu & Kato, 2001).

Under a high pressure at the white dwarf surface, the temperature of the accumulated material increases without their volume expansion. Therefore, the heat dissipation of accumulated material is only caused by a diffusion process on the white dwarf surface. The produced energy of nuclear fusion can be released by the material diffusion while the amount of accumulated material is small and its temperature is low. However, the energy production eventually exceeds the heat dissipation with the continuing mass accretion process. Then, an increase in the temperature leads to further activities of nuclear fusion, and its reaction continues by itself. The classical nova explosion occurs in such sudden and continuous nuclear reaction, which is called a thermonuclear runaway.

2.4 High Energy Phenomena in Classical Novae

2.4.1 Introduction

High energy phenomena in classical novae have been studied in many different ways despite the faint and transient nature of classical novae. We first summarize the previous X-ray and γ-ray observations over decades including several missions with rockets and satellites. All published results are listed in table 2.2 at the end of the next subsection.

2.4.2 Knowledge of High-Energy Phenomena

2.4.2.1 Initial Attempts in X-ray Observations

***SAS-3* Observatory**

The Third Small Astronomy Satellite (*SAS-3*)[2] is an X-ray astrophysics mission in the United States from 1975 to 1979. The *SAS-3* conducted a continuous search for X-ray novae and transient sources, which is equipped with four scientific instruments in the 0.1–55 keV energy range. More details of *SAS-3* can be found in e.g., Mayer (1975).

- **Observation of V1500 Cyg :** An X-ray observation of the classical nova V1500 Cyg was performed with the *SAS-3*, but no flux was detected over the 0.1–50 keV energy range both in pre- and post-outburst phases (Hoffman et al., 1976). An attempt to observe X-rays from classical novae was made for the first time.

***Ariel V* Observatory**

The *Ariel V* satellite[2] is a high energy astrophysics mission as a collaboration between the United Kingdom and the United States. *Ariel V* provided monitoring X-ray observations with a payload in the 0.3–40 keV energy range during a period from 1974 to 1980. More details of *Ariel V* can be found in e.g., Smith & Courtier (1976).

- **Observation of NQ Vul :** The classical nova NQ Vul was observed with the Rotation Modulation Collimator sensitive in 0.3–30 keV onboard the satellite, but no significant X-ray was detected (Cruise, 1977).

[2]See http://heasarc.gsfc.nasa.gov/docs/heasarc/missions/past.html for details.

2.4.2.2 X-ray Survey of Quiescent Emission

***HEAO-1* Observatory**

The *HEAO-1* satellite[2] is a series of scientific missions called the high energy astronomy observatories by NASA. *HEAO-1* conducted a soft X-ray survey during a period from 1977 to 1979 with collimated gas proportional counters on the A2 experiment. One of the detectors (LED1), which was used for researches of classical novae, is sensitive in the 0.2–2.8 keV energy range with an effective area of $\sim$174 cm^2 (see e.g., Rothschild et al. 1979 for details). More details of *HEAO-1* can be found in e.g., Bradt et al. (1992).

- **Quiescent Emission of Classical Novae :** The X-ray survey was performed at positions including 102 classical novae and seven recurrent novae (Cordova et al., 1981a). X-ray sources were detected at the positions of 10 classical novae and one recurrent nova. We listed the *HEAO-1* observations for the detected sources in table 2.2. Almost all the observations were conducted long after the nova eruption with the exception of the classical nova LW Ser, in which X-rays were detected in time averaged data of both pre- and post-outburst scanning period. Based on the result, the upper limit for the average X-ray luminosities of classical novae in quiescence was estimated to be $\sim 10^{33}$ erg s^{-1} in the LED1 bandpass.

***Einstein* Observatory**

The *Einstein* satellite[2] is the second mission of the high energy astronomy observatories by NASA. *Einstein* provided few arcsecond angular resolution and a great sensitivity with onboard imaging X-ray telescope during a period from 1978 to 1981. The satellite has several X-ray instruments in operation: Imaging Proportional Counter (IPC), High Resolution Imager (HRI), Solid State Spectrometer (SSS), Focal Plane Crystal Spectrometer (FPCS), Monitor Proportional Counter (MPC), and Objective Grating Spectrometer (OGS). More details of *Einstein* can be found in e.g., Giacconi et al. (1979).

- **Quiescent Emission of Classical Novae :** X-ray observations were performed at positions including 19 classical and recurrent novae with the *Einstein* satellite. As a result, nine novae were detected (V603 Aql, V841 Oph, GK Per, RR Pic, CP Pup, V1059 Sgr, T CrB, V1017 Sgr, and PU Vul), while ten novae were not detected (DQ Her, V553 Her, RS Oph, T Pyx, U Sco, CP Lac, V1500 Cyg, V446 Her, T Aur, and CK Vul) in the 0.1–4.0 keV energy band (e.g., Becker & Marshall 1981a; Cordova et al. 1981b; Cordova & Mason 1984; Patterson & Raymond 1985b,a; Eracleous et al. 1991). The X-ray spectra in the same energy band were relatively hard (Cordova & Mason, 1984), and the average X-ray luminosity of the novae is estimated to be $\sim 5 \times 10^{31}$ erg s^{-1} (Becker, 1981). A significant difference is found in the X-ray luminosity between fast and slow novae (Cordova & Mason, 1984), and the luminous X-ray novae were all fast novae (figure 2.15). The distribution of the X-ray luminosity from these novae are shown in figure 2.14. The spectra from luminous four novae (V603 Aql, GK Per, CP Pup, and PU Vul) were fitted by a thermal bremsstrahlung model with a temperature of

$\gtrsim$0.5 keV and a luminosity of $\sim 10^{32}$ erg s^{-1} in the 0.1–3.5 keV energy band (Eracleous et al., 1991).

- **Time Variabilities of V603 Aql :** The short time variabilities were confirmed in the classical nova V603 Aql on 64 years after the outburst. A short flux amplification and large amplitude flickerings in a time scale of $\sim$200–300 s were found in the X-ray light curve (Drechsel et al., 1983; Cordova & Mason, 1984). The X-ray spectra were characterized by a thermal model with a temperature of $\gtrsim$20–30 keV, and the maximum luminosity of $3 \sim 10^{33}$ erg s^{-1}. Based on the results, the accretion rate is estimated to be $\sim 10^{16}$ g s^{-1} (Drechsel et al., 1983).

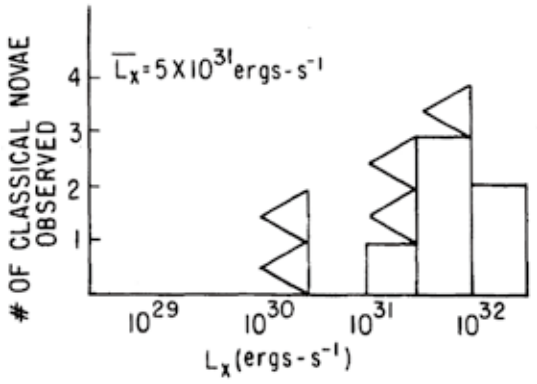

Figure 2.14: Distribution of X-ray luminosity for classical novae (Becker, 1981).

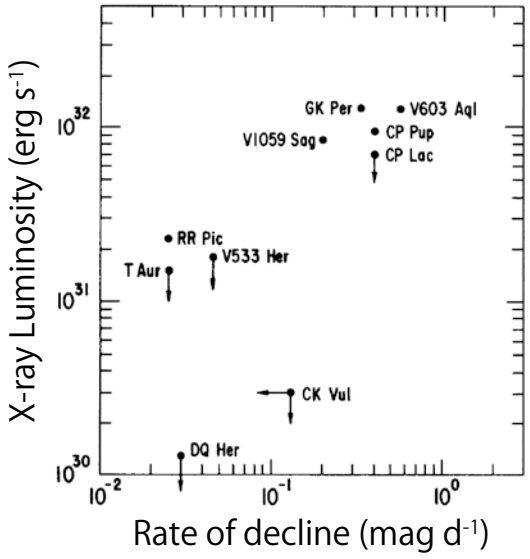

Figure 2.15: Luminosity in the 0.15–4.5 keV band versus rate of decline (Becker & Marshall, 1981a).

2.4.2.3 Beginning of X-ray Studies in the Post-Outburst Developments

***EXOSAT* Observatory**

The *EXOSAT* observatory[2] is a high energy astrophysics mission by the European Space Agency (ESA) from 1983 to 1986. The satellite provided pointing X-ray observations with three instruments in operation: low energy imaging telescopes, medium energy proportional counters, and gas scintillation proportional counters. Studies of classical novae were performed with the low energy detectors sensitive in the 0.04–2 keV energy range and the medium energy proportional counters in the 1–50 keV energy range. More details of the *EXOSAT* can be found in e.g., Taylor et al. (1981).

- **Super-Soft Emission from GK Muscae :** The *EXOSAT* observed the classical nova GQ Mus (Nova Muscae 1983) around 462 days after the eruption, and clearly detected soft X-ray emission in the post-outburst phase for the first time (Oegelman et al., 1984). The X-ray energy flux with the low-energy detectors was $\sim 10^{-13}$–10^{-14} erg cm^{-2} s^{-1}, which was explained by either a shocked shell of circumstellar material emitting a $\sim 10^{7}$ K thermal bremsstrahlung radiation at a $\sim 10^{35}$ erg s^{-1} luminosity, or a white dwarf remnant emitting a $\sim 10^{5}$ K blackbody radiation at a $\sim 10^{37}$ erg s^{-1} luminosity. A total of four X-ray observations were conducted for GQ Mus, in which a significant flux decline was found 914 days after the outburst (Oegelman et al., 1987). Similar soft X-ray emission was also confirmed from two other classical novae (PW Vul and QU Vul) with subsequent observations of the *EXOSAT* (Oegelman et al., 1987). X-ray light curves of the three samples show a clear development with a rise and a fall in a time scale of several years.

- **Hard Thermal Emission from RS Ophiuchi :** The recurrent nova RS Oph was also observed with the *EXOSAT* during the outburst in 1985 (Mason et al., 1987). X-rays were detected in six observations starting 54 days after the outburst. The observed flux in the $\sim$1–6 keV energy band is 1.5×10^{-10} erg cm^{-2} s^{-1} on day 54. The X-ray spectra up to $\sim$6 keV was interpreted by the blast wave model, in which X-ray emission is produced by the collisions of the nova ejecta and the pre-existing circumstellar wind by a red giant companion.

- **Quiescent Emission from V603 Aquilae :** In another case, spectroscopy of quiescent emission was conduced for the old classical nova V603 Aql $\sim$66 years after the outburst (Haefner et al., 1988). The X-ray spectra were fitted with both power-law and optically-thin thermal plasma models convolved with a photoelectric absorption. The temperature of the thermal component is $>$6 keV, and the absorption column density was estimated to be $<2 \times 10^{21}$ cm^{-2}.

2.4.2.4 Early Progress in the X-ray Phenomena

***ROSAT* Observatory**

The Roentgen Satellite ($ROSAT$)[2] is an astronomical mission for X-ray and ultraviolet emission under a collaboration between Germany, the United States, and the United Kingdom during a period from 1993 to 2001. The $ROSAT$ conducted an all-sky survey with unprecedented sensitivity in the soft X-ray band during the first six months of the mission, and later performed pointing observations. The mission has two X-ray instruments in operation: Position Sensitive Proportional Counter (PSPC) and High Resolution Imager (HRI) sensitive in ∼0.1–2.5 keV. More details of the $ROSAT$ can be found in e.g., Trümper (1984).

- **Hard-Thermal Emission from V838 Herculis :** One of the progresses that $ROSAT$ made is the first discovery of hard X-ray emission from classical novae in the post-outburst development (Lloyd et al., 1992). X-ray emission dominant above ∼1 keV was detected from the classical nova V838 Herculis five days after the outburst (figure 2.16). The X-ray spectrum was explained by optically-thin thermal plasma emission with a temperature of $\sim 10^8$ K, suggesting that the origin of X-rays is shock-heated material. The interaction of the nova ejecta with pre-existing circumstellar material was argued to explain the results.

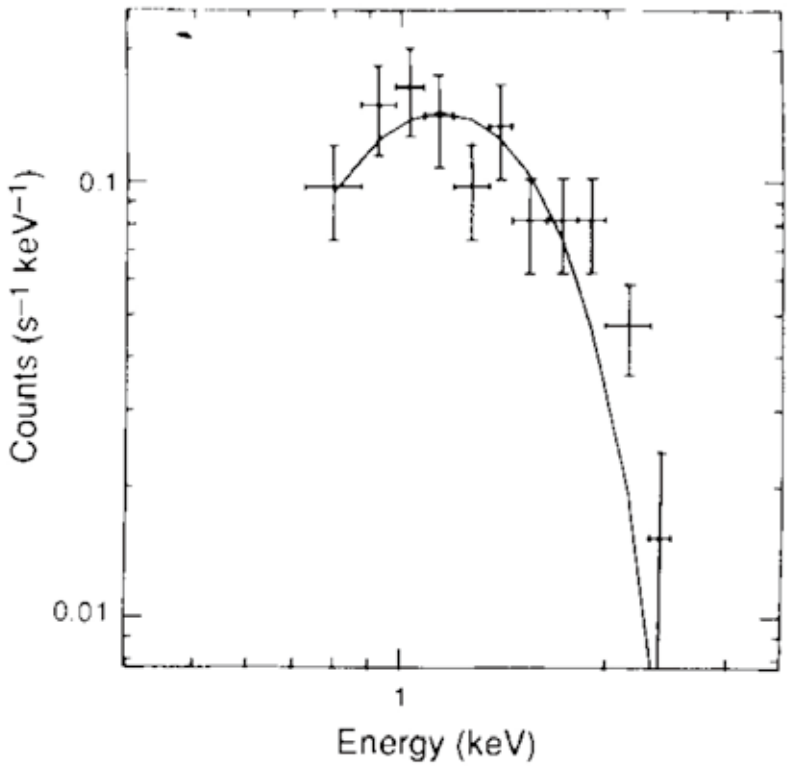

Figure 2.16: X-ray spectrum of V838 Herculis with the $ROSAT$ (Lloyd et al., 1992).

- **Establishment of Super-Soft X-ray Emission :** The super-soft X-ray emission was also confirmed in several classical novae with the *ROSAT*, which provides spectroscopy with high sensitivity. The super-soft X-ray emission from the classical nova GQ Muscae was observed about nine years after the outburst (Oegelman et al., 1993) with the *ROSAT*. The spectra were explained by a soft blackbody model with a temperature of $\sim 3.5 \times 10^5$ K convolved with a photoelectric absorption, in which the hydrogen column density ($N_{\rm H}$) is estimated to be $\sim 3.4 \times 10^{21}$ cm^{-2}. The luminosity is similar to the Eddington limit of a white dwarf with a mass of 1 $M_{\odot}$. Based on the results, Oegelman et al. (1993) concluded that a nuclear fusion of accreted hydrogen-rich material occurs on the white dwarf surface. The subsequent observations were performed $\sim$10 and $\sim$10.6 years after the outburst (Shanley et al., 1995). The X-ray flux significantly decreased, and the temperature of the soft X-ray emission also dropped in the observations. Shanley et al. (1995) concluded that the cooling time-scale of the plasma temperature ($\tau_{\rm c}$) was $\sim$3–4 yr, which is caused by the turn-off of the nuclear process. The spectra were also re-analyzed with a metal enhanced white dwarf atmosphere model, and the results were compared with the spectra from other classical novae V838 Her, V351 Pup, and QU Vul (Balman & Krautter, 2001).

- **Monitoring Observations for V1974 Cygni :** A total of eighteen observations were conducted for the classical novae V1974 Cyg in the post-outburst development (Krautter et al., 1996). Such monitoring observations at a high cadence was done for the first time in classical novae. The X-ray light curve was obtained over $\sim$2 years for the X-ray emission from the beginning to the end. The X-ray flux increased from the discovery until day 147, then it plateaued in days 255–511, and finally declined thereafter (figure 2.17).

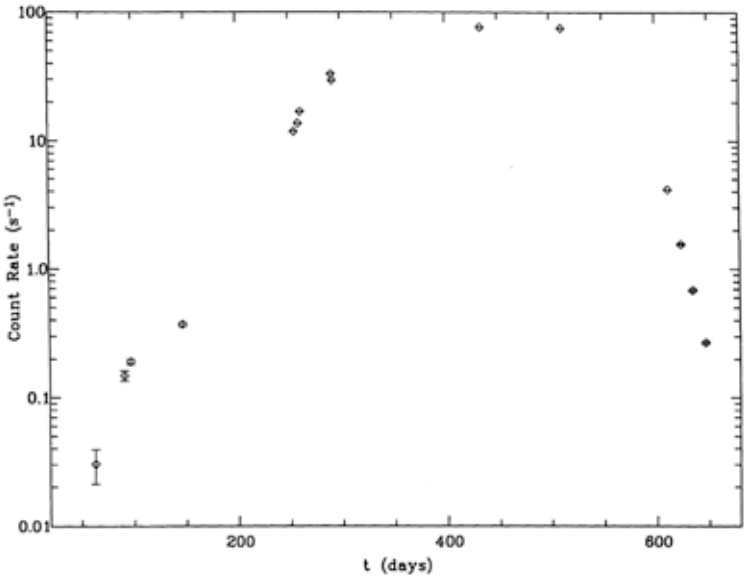

Figure 2.17: X-ray light curve of V1974 Cyg with the *ROSAT* (Krautter et al., 1996).

The X-ray spectral development is different for the soft ($\lesssim$1 keV) and the hard ($\gtrsim$1 keV) parts (figure 2.18). The hard component is relatively stable in the early phase, and the peak flux was observed on day $\sim$150. The hard component is considered to be caused by interactions in the shell with an inhomogeneous density. In contrast, the soft component is highly variable in the later phase. The stable hard component and the variable soft component suggest a variably decreasing column density. A column density declines on a time scale of t^{-2}. In further progress, the white dwarf atmosphere model below 0.1–1.0 keV and optically-thin thermal plasma model above $\sim$1 keV were also applied to explain the X-ray spectra and its evolution (Balman et al., 1998).

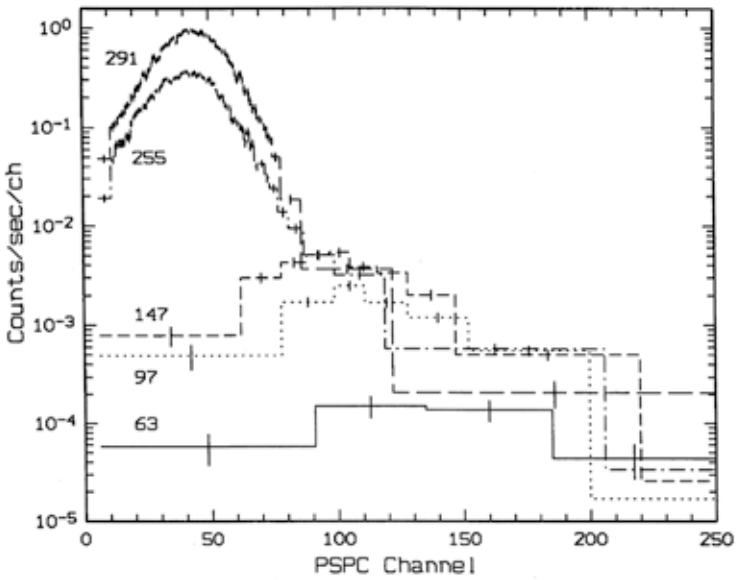

Figure 2.18: X-ray spectra of V1974 Cyg with the *ROSAT* (Krautter et al., 1996).

- **Nova-Remnant Emission from GK Persei :** The *ROSAT* was able to resolve the shell of classical novae in X-rays for the first time. The image of the X-ray nebula composed of knots and clumps was obtained in the classical nova GK Persei (Balman & Ögelman, 1999). The nebula is extended by $\sim$50″ at a distance of $\sim$470 pc (figure 2.19) 95 years after the outburst. The ejecta velocity and mass are $\sim$1200 km s^{-1} and 7×10^{-5} $M_{\odot}$, respectively. The X-ray spectra of the nebula were explained by a two-temperature optically-thin thermal plasma model convolved with a photoelectric absorption. The X-ray luminosity is $\sim8\times10^{31}$ erg s^{-1} in the 0.1–2.4 keV energy range. The temperatures of the cool and the hot plasma components are respectively 2×10^{6} and 1×10^{7} K. Also, the absorption column densities of the cool and the hot plasma components are 1.3×10^{21} and 2×10^{22} cm^{-2}, respectively. The volume emission measure is 2×10^{55} cm^{-3} for both plasma components. The power-law model was also applied for the presence of non-thermal emission, but it was inconsistent with the data. Based on the results, the interaction of the circumstellar matter with the ejecta was discussed to explain the spectra.

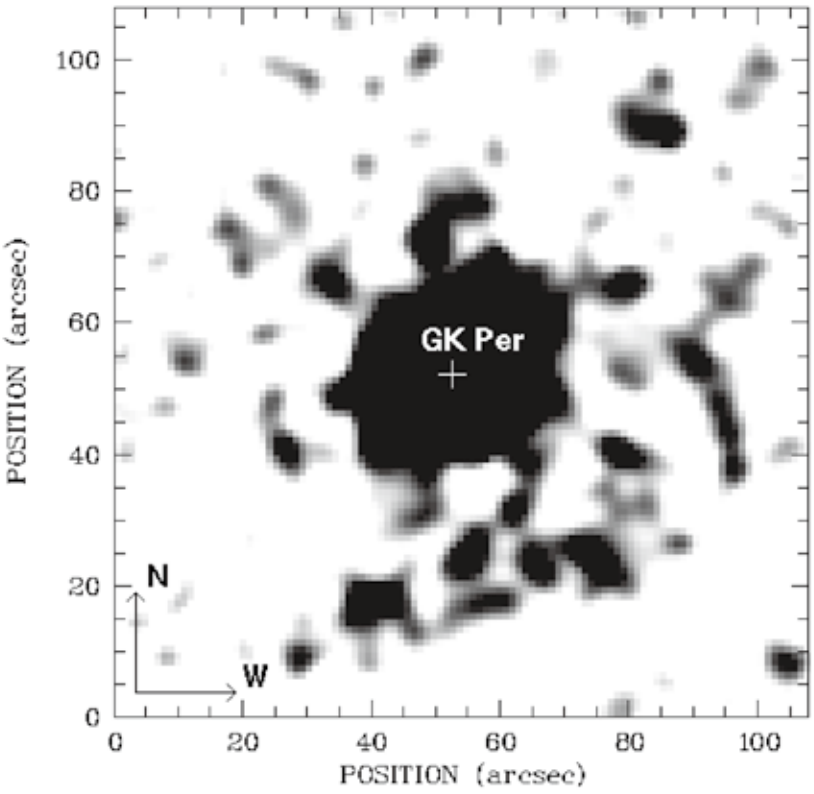

Figure 2.19: X-ray image of the classical nova GK Per with the *ROSAT* (Balman & Ögelman, 1999).

- **Quiescent Emission from CP Puppis :** A spectroscopy of quiescent emission was conducted for the old classical nova CP Pup (Balman et al., 1995). The X-ray spectra were explained by an optically-thin thermal plasma model convolved with a photoelectric absorption. The plasma temperature and luminosity are $\sim$3 keV and $\sim 10^{32}$ ergs s^{-1}, respectively. The absorption column density is estimated to be $\sim 10^{21}$ cm^{-2}. A significant modulation of $\sim$88 min was detected in the emission, indicating that the origin of X-rays is the accretion process in the white dwarf.

- **Emission from V351 Puppis and RS Ophiuchi :** Puzzling X-ray emission was detected from V351 Pup and RS Oph. In the case of V351 Pup, the observation was performed about 16 months after the outburst with the *ROSAT* (Orio et al., 1996; Balman & Krautter, 2001). The X-ray spectra were explained by an optically-thin thermal plasma component with a temperature of $\sim$1 keV. The luminosity was $\sim 8 \times 10^{33}$ erg s^{-1} in the 0.2–2.4 keV energy band. Such a thermal component is typically confirmed from classical novae. However, it is difficult to constrain the origin whether it is either by the shock-heated ejecta or by the reestablished accretion process, because the emission was detected after a certain period of time after the outburst (Orio et al., 1996). In RS Ophiuchi, the X-ray emission was detected with the *ROSAT* about 7

years after the outburst (Orio, 1993). The spectra were explained by an optically-thin thermal plasma model with a temperature of $\sim$1 keV. The X-ray luminosity is estimated to be 3×10^{31}–2×10^{32} erg s^{-1}. If the origin of the X-ray emission is the accretion process, the mass accretion rate is estimated to be $\lesssim10^{-9}$ $M_\odot$ y^{-1}. The value is not sufficient to cause an outburst every 10–20 yr in the recurrent novae RS Oph.

- **Summary of the *ROSAT* Observations :** Finally, the *ROSAT* observations at positions including 108 classical and recurrent novae were summarized in Orio et al. (2001a). The super-soft X-ray emission was found in two classical novae (1974Cyg and GQ Mus), and hard-thermal X-ray emission was confirmed from three classical novae (V1974 Cyg, V351 Pup, V838 Her) in our Galaxy. The positions of 81 classical novae in our Galaxy were observed long after their outburst, and X-rays were detected from eleven of them (QU Vul, V446 Her, CP Pup, CP Lac, DQ Her, RR Pic, V603 Aql, T Sco, V841 Oph, RS Oph, and GK Per). The origin of the X-ray emission in GK Per is considered to be a combination of the expanding ejecta and the accretion process. Based on the result, typical X-ray luminosity of classical novae in quiescence was estimated to be $\sim10^{30}$–10^{33} erg s^{-1}. Orio et al. (2001a) noticed that luminous X-ray emission at quiescence was found from all fast novae in the outburst.

2.4.2.5 Deep Spectroscopy for the X-ray Emission

***ASCA* Observatory**

The Advanced Satellite for Cosmology and Astrophysics (*ASCA*)[2] is the Japanese fourth X-ray astronomical mission. The *ASCA* had a moderate imaging capability in a broad energy band (∼0.4–10 keV), and a large effective area, which was operated during a period from 1993 to 2001. Two scientific instruments were installed in the satellite: Gas Imaging Spectrometer (GIS) and Solid-state Imaging Spectrometer (SIS). The SIS is the first X-ray CCD cameras used in the X-ray astronomy. More details of *ASCA* can be found in e.g., Tanaka et al. (1994).

- **Hard-Thermal Emission from V382 Velorum :** The *ASCA* observed the classical nova V382 Vel around 20.5 days after the beginning of visual brightening in the eruption. X-ray emission was clearly detected in the post-outburst development in the 1–10 keV energy band (Mukai & Ishida, 2001). The observed X-ray flux was 2×10^{-11} erg s^{-1} cm^{-2}, which was explained by a thermal bremsstrahlung continuum ($k_{\rm B}T \sim 10$ keV) with a weak Fe Kα emission line at ∼6.7 keV convolved with a partial-covering photoelectric absorption model ($N_{\rm H} \sim 1\times10^{23}$ cm^{-2}). The X-ray luminosity was estimated to be $\sim5\times10^{34}$ erg s^{-1}, and the volume emission measure is 2×10^{57} cm^{-3}. Mukai & Ishida (2001) discussed the nature of V382 Vel using the *ASCA* the *RXTE* observatories described in below.

***RXTE* Observatory**

The Rossi X-ray Timing Explorer (*RXTE*)[2] is a high energy mission by NASA to explore high timing behaviors of astronomical objects in the X-ray energy band. The *RXTE* provides unprecedented time resolution with a moderate spectral resolution in a broad energy band (∼2–250 keV) since 1995. The mission has three instruments in operation: Proportional Counter Array (PCA), High Energy X-ray Timing Experiment (HEXTE), and All-Sky Monitor (ASM). More details of *RXTE* can be found in e.g., Bradt et al. (1993).

- **Hard-Thermal Emission from V382 Velorum :** The *RXTE* observed the classical nova V382 Vel around 5.7, 31, 35, 50, and 59 days after the beginning of visual brightening in the eruption (Mukai & Ishida, 2001). The combination of *RXTE* and *ASCA* revealed the X-ray spectral evolution with a total of five observations. The plasma temperature, X-ray luminosity, and column density of the photoelectric absorption are respectively estimated to be ∼2.5 keV, 8×10^{34} erg s^{-1}, and 2×10^{22} cm^{-2} on day 50. The results of the *ASCA* and the *RXTE* revealed that the X-ray spectra become softer with a decreasing temperature and a diminishing column density. To explain the spectral evolution, Mukai & Ishida (2001) applied the internal shock model, in which shocks occur with the collision of a fast material with pre-existing slow material from the white dwarf remnant. The plasma with non-equilibrium ionization is also considered to explain the weakness of Fe Kα emission line at 6.7 keV.

- **Hard-Thermal Emission from RS Ophiuchi :** The recurrent nova RS Oph was observed with the *RXTE* around 3, 6, 10, 14, 17, and 21 days after the outburst in 2006 (Sokoloski et al., 2006). On day 3, the X-ray spectra up to ∼20 keV (figure 2.20) were explained by a thermal bremsstrahlung component with a temperature of $\sim 10^7$ K convolved with a photoelectric absorption ($N_{\rm H} \sim 6\times10^{22}$ cm^{-2}). The temperature decreases as a function of a time ($t^{-2/3}$) from day 3. The observed X-ray flux is 3×10^{-9} erg s^{-1} cm^{-2} in the 0.5–20 keV energy range, which also decreases as a function of a time ($t^{-5/3}$) from the beginning of the outburst. Based on the results, an X-ray emitting blast wave through the wind from a red giant companion is discussed to explain the evolution.

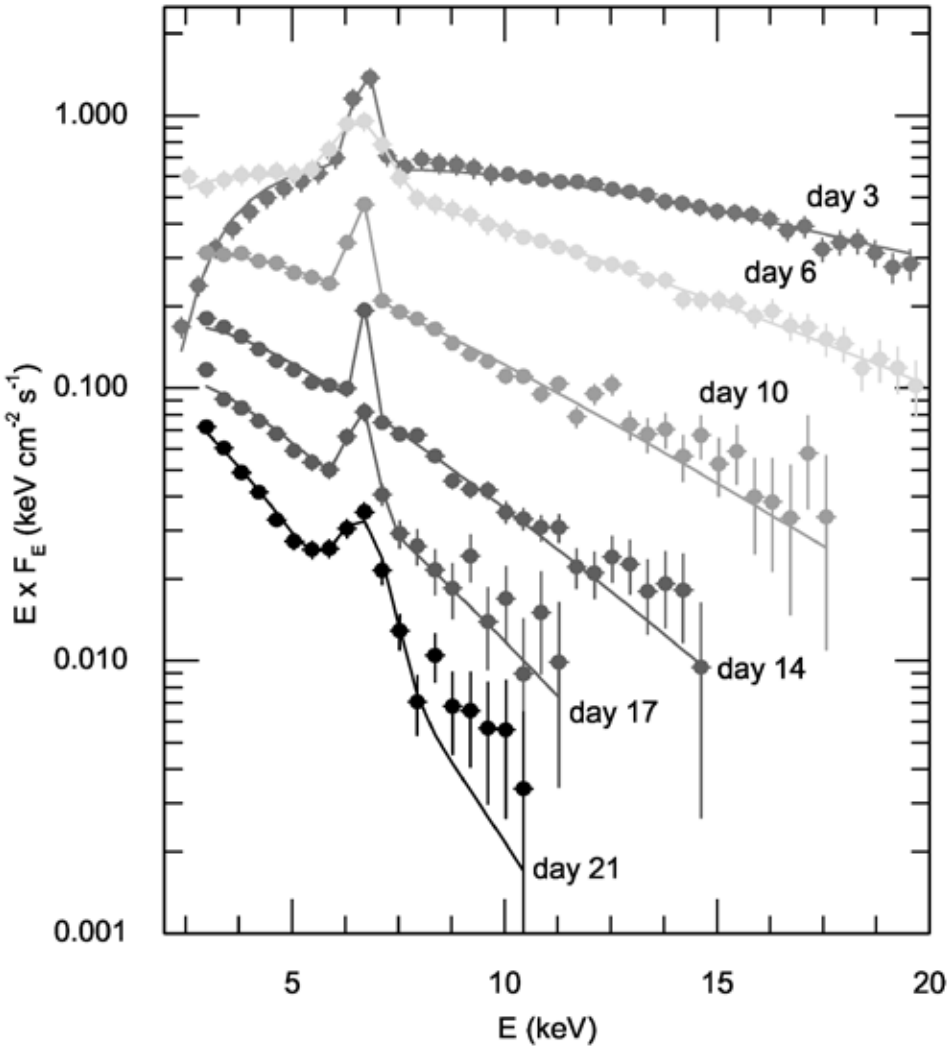

Figure 2.20: X-ray spectra of RS Oph with the *RXTE* satellite (Sokoloski et al., 2006).

Beppo-SAX Observatory

The *Beppo-SAX* observatory[2] is a high energy astrophysics mission by the Italian Space Agency and the Netherlands' Agency for Aereospace Programs. The observatory provides more than three decades of the energy range (∼0.1–300 keV) with a large effective area and moderate energy resolution during a period from 1996 to 2002. The satellite has several instruments in operation: Low Energy Concentrator Spectrometer (LECS), Medium Energy Concentrator Spectrometer (MECS), High pressure Gas Scintillator Proportional Counter (HPGSPC), Phoswich Detection System (PDS), and Wide Field Camera (WFC). More details of *Beppo-SAX* can be found in e.g., Boella et al. (1997).

- **X-ray Emission from U Scorpii :** The *Beppo-SAX* observed the recurrent nova U Sco around 19–20 days after the peak of the optical outburst in 1999 (Kahabka et al., 1999b). The X-ray spectrum up to ∼5 keV was interpreted by a combination of a non-local thermodynamic equilibrium (non-LTE) white dwarf atmosphere component and an optically-thin thermal plasma (Raymond & Smith, 1977) component convolved with a photoelectric absorption. The column density is estimated to be ∼3–5×10^{21} cm^{-2}. The temperature and the bolometric luminosity of the non-LTE white dwarf atmosphere component are respectively ∼9×10^5 K and ∼10^{35}–10^{36} erg s^{-1} assuming the distance of 1 kpc. Also, the temperature and the volume emission measure of the optically-thin thermal plasma component are respectively ∼0.2–0.5 keV and 0.4–3.2×10^{55} cm^{-3} at 1 kpc.

- **Hard-Thermal Emission from V382 Velorum :** The classical nova V382 Vel was observed with the *Beppo-SAX* around 15 and 184 days after the discovery (Orio et al., 2001a). The X-ray spectra were detected up to ∼30 keV from classical novae for the first time. On day 15, the X-ray flux is 1.8×10^{-11} erg cm^{-2} s^{-1} in the 0.1–10 keV energy band, and the 2-σ upper limit is 6.7×10^{-12} erg cm^{-2} s^{-1} in the 15–60 keV energy band. The spectra can be explained by an optically-thin thermal plasma model with a temperature of ∼6 keV convolved with a photoelectric absorption ($N_{\rm H}$ ∼ 1.7×10^{23}). The hard X-ray emission is attributed to shocks in the ejecta, which is a similar conclusion as the *ASCA* results (Mukai & Ishida, 2001). The deficiency of Fe is reported in the spectral fitting with the *Beppo-SAX*. On day 184, bright soft X-ray emission was seen in the spectra (Orio et al., 2002), which is explained by the non-LTE white dwarf atmosphere model with a temperature of ∼5×10^5 K convolved with a photoelectric absorption ($N_{\rm H}$ ∼ 10^{22} cm^{-2}).

2.4.2.6 Recent Progress in the X-ray Phenomena

***Chandra* and *XMM-Newton* Observatory**

Around the same time, two powerful X-ray observatories were successfully launched at the end of 20th century. One is the *Chandra X-ray Observatory*[2], which is the third of four satellites in the series of the Great Observatories program by NASA. The satellite was successfully launched in July 1999. The Advanced CCD Imaging Spectrometer (ACIS) onboard *Chandra* provides X-ray images with unprecedented spatial resolution with an order of $\sim 1''$ and also the spectral information. In addition, the Transmission Grating Spectrometers provide X-ray spectra with an extremely high energy resolution for bright X-ray sources. Details of *Chandra* can be found in e.g., Weisskopf et al. (2002).

The other is the *XMM-Newton* observatory[2], which is the second cornerstone mission of the Horizon 2000 Science Programme by the European Space Agency (ESA). The satellite was successfully launched in December 1999. The mission provides X-ray spectroscopy with unprecedentedly large effective area and a high energy resolution in the X-ray energy band. The satellite has three scientific instruments in operation: the European Photon Imaging Camera (EPIC), the Reflection Grating Spectrometer (RGS), and the Optical Monitor (OM). Details of the *XMM-Newton* mission and its instruments are described in section 4.2.

- **Major Progress with RS Ophiuchi :** The sixth recorded eruption of the recurrent nova RS Oph was discovered in 2006. During the eruption, the most intensive X-ray observations were performed with both *Chandra* and *XMM-Newton* (e.g., Ness et al. 2007b; Nelson et al. 2008). A total of twelve X-ray grating observations with *Chandra* and *XMM-Newton* were performed for RS Oph. In the early phase, hard-thermal emission was significantly detected in the grating observations. The emission lines from highly-ionized N, O, Mg, and Si were clearly resolved (figure 2.22), in which the emission lines were blue-shifted at velocities of $\sim$500–1300 km s^{-1} and broadened by $\sim$2000 km s^{-1} on day 14 (Nelson et al., 2008). Based on the asymmetric line features and a simple assumption, in which the blue-shifted components are brighter than the red-shifted components due to the circumstellar absorption, the mass of the ejecta was estimated (Drake et al., 2009). A multi-temperature optically-thin thermal plasma model was applied to explain the X-ray spectra in the early phase (Ness et al., 2009b). This revealed that hot and cool plasma components have different decay time-scales, in which the hot component is radiatively cooled, while the cool component is explained by the expansion of the ejecta. The elements of N, Ne, Mg, Si, and S are found overabundant in the plasma emission relative to Fe.

  In more later phases, the super-soft X-ray emission was detected in the grating observations on days 40 and 67 after the outburst with *Chandra* and on day 54 with *XMM-Newton* (e.g., Ness et al. 2007b). A periodicity of $\sim$35 s were confirmed in the X-ray light curve on day 54. Absorption features were clearly detected in the time-series spectra (figure 2.22), in which the absorption lines were also blue-shifted at a velocity of $\sim$1000 km s^{-1}. The collisionally excited emission lines from the radiatively cooling shock were also found in the spectra. In addition, the grating X-ray spectra

resolved He-like triplets, and anomalous line ratios were reported. Based on the results, Ness et al. (2007b) argued several mechanisms of the emission; e.g., bound-free absorption by neutral elements, resonance absorption lines plus emission-line components, collisionally excited emission lines, and He-like semi-forbidden (intersystem) lines.

About one and a half year after the outburst, X-ray nebula emission around RS Oph was found in the images of the ACIS with *Chandra* (Luna et al., 2009). The X-ray emitting region was extended by 1.″2, which implies the expanding ejecta at an average rate of more than ∼2 milli-arcsecond per year. Assuming the distance to RS Oph of 1.6 kpc, it corresponds to a velocity of greater than ∼6000 km s^{-1}. This expansion rate is comparable with the measured expansion rate for radio jet in the early phase. The spectrum of the nova-remnant emission is dominant in the soft X-ray band below ∼1 keV (Luna et al., 2009).

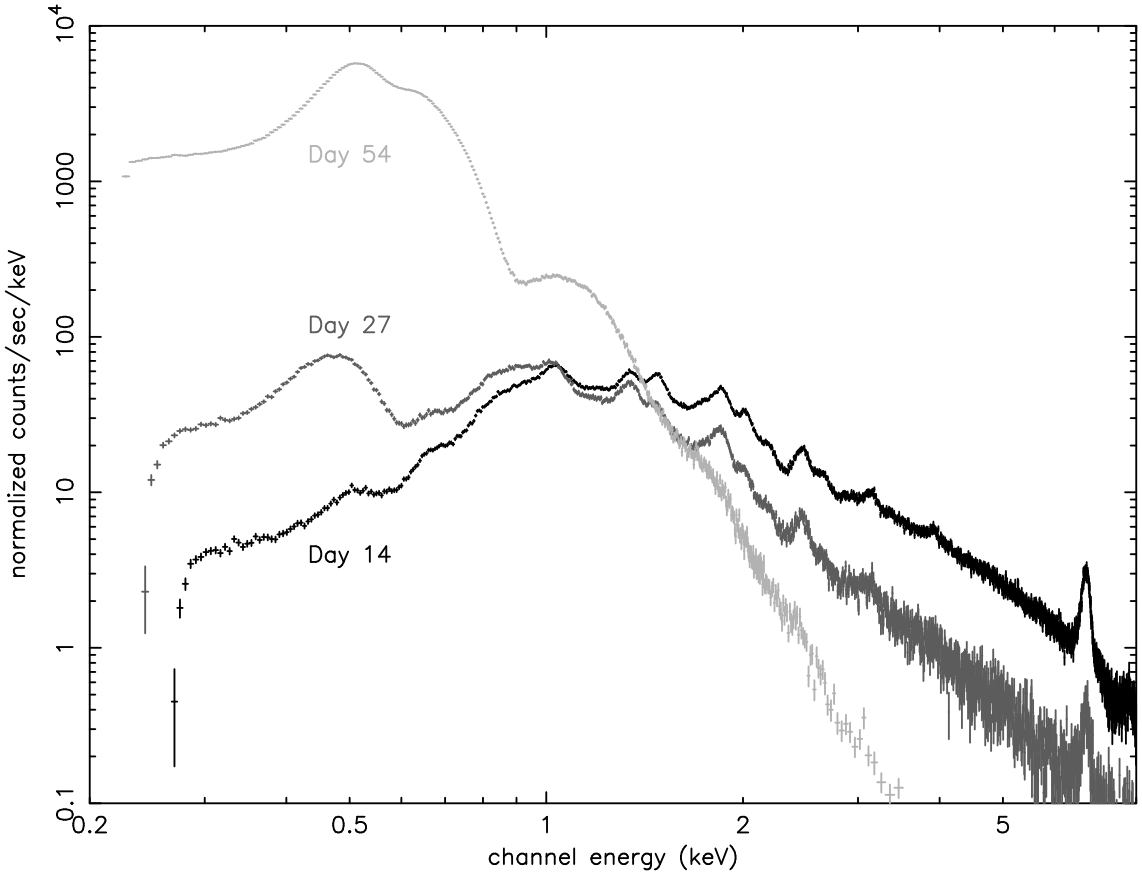

Figure 2.21: X-ray CCD spectra of the recurrent nova RS Oph with *XMM-Newton* (Nelson et al., 2008).

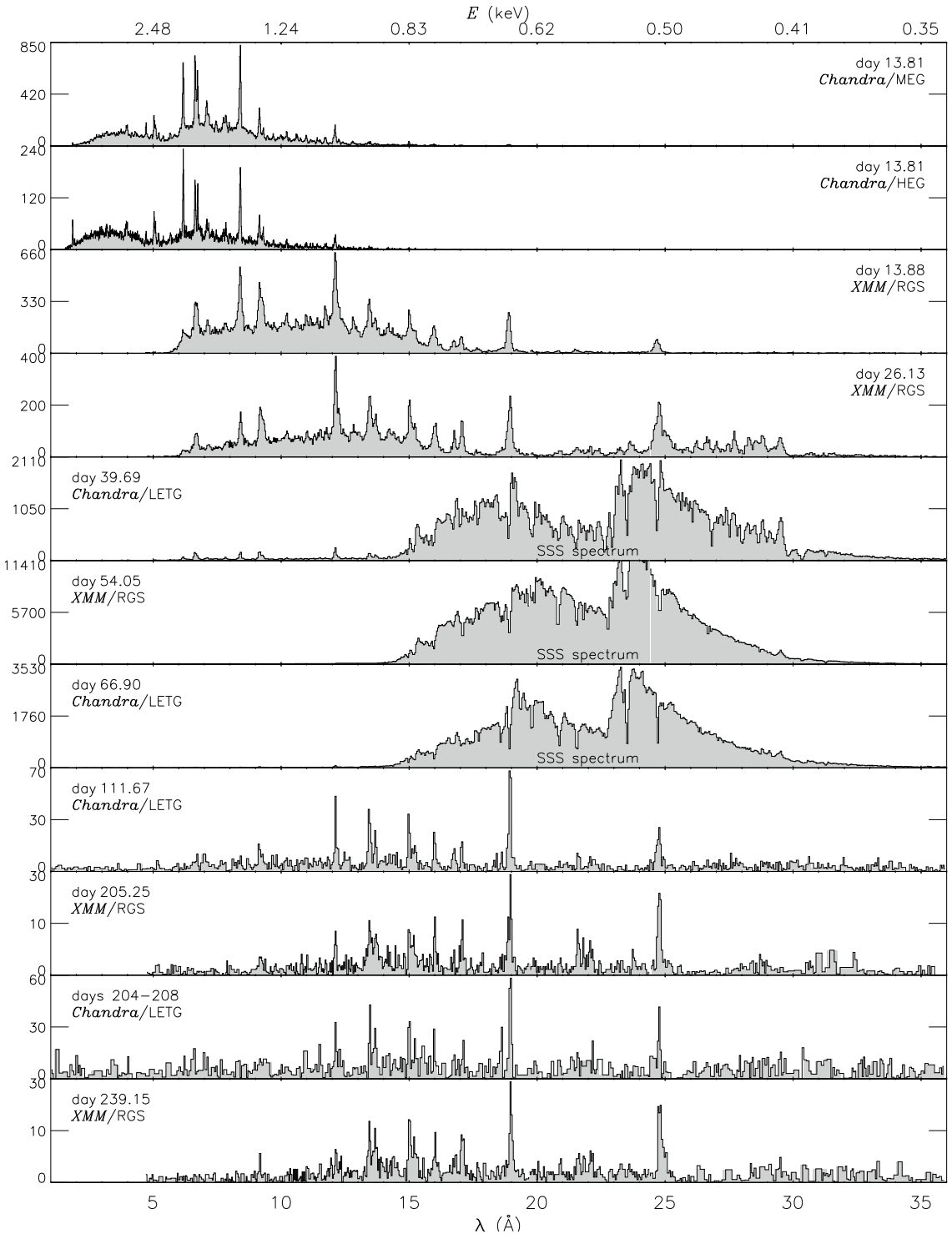

Figure 2.22: X-ray grating spectra of the recurrent nova RS Oph (Ness et al., 2007b).

- **Detailed Spectroscopy of Hard-Thermal Emission :** Hard-thermal emission was observed with *Chandra* from two classical novae (V1494 Aql; Rohrbach et al. 2009 and V382 Vel; Ness et al. 2005) and from three recurrent novae (RS Oph; e.g., Nelson et al. 2008, IM Nor; Orio et al. 2005 and CI Aql; Greiner & Di Stefano 2002). In the case of V1494 Aql, time-sliced X-ray spectroscopy was conducted using both grating and CCD instruments (Rohrbach et al., 2009). The emission lines from highly-ionized C, N and O were detected in the spectra, which is explained by an optically-thin thermal plasma model with large O and N abundances. In V382 Vel, the emission lines from highly-ionized C, N, O, Ne, Mg, and Si were detected on day 268 after the outburst (figure 2.23). While these metals were overabundant, the lack of Fe was seen in the spectra. The emission lines have broad profiles corresponding to a velocity of $\sim$2900 km s^{-1} in the FWHM (Ness et al., 2005). In IM Nor, X-ray observations were conducted twice one and six months after the outburst. The X-ray spectra were fitted by an optically-thin thermal plasma model with a temperature of several keV and a blackbody component (Orio et al., 2005). In CI Aql, weak X-ray emission was found after the super-soft X-ray emission phase (Greiner & Di Stefano, 2002). The X-ray spectrum was fitted by an optically-thin thermal plasma model with a temperature of $\sim$3 keV.

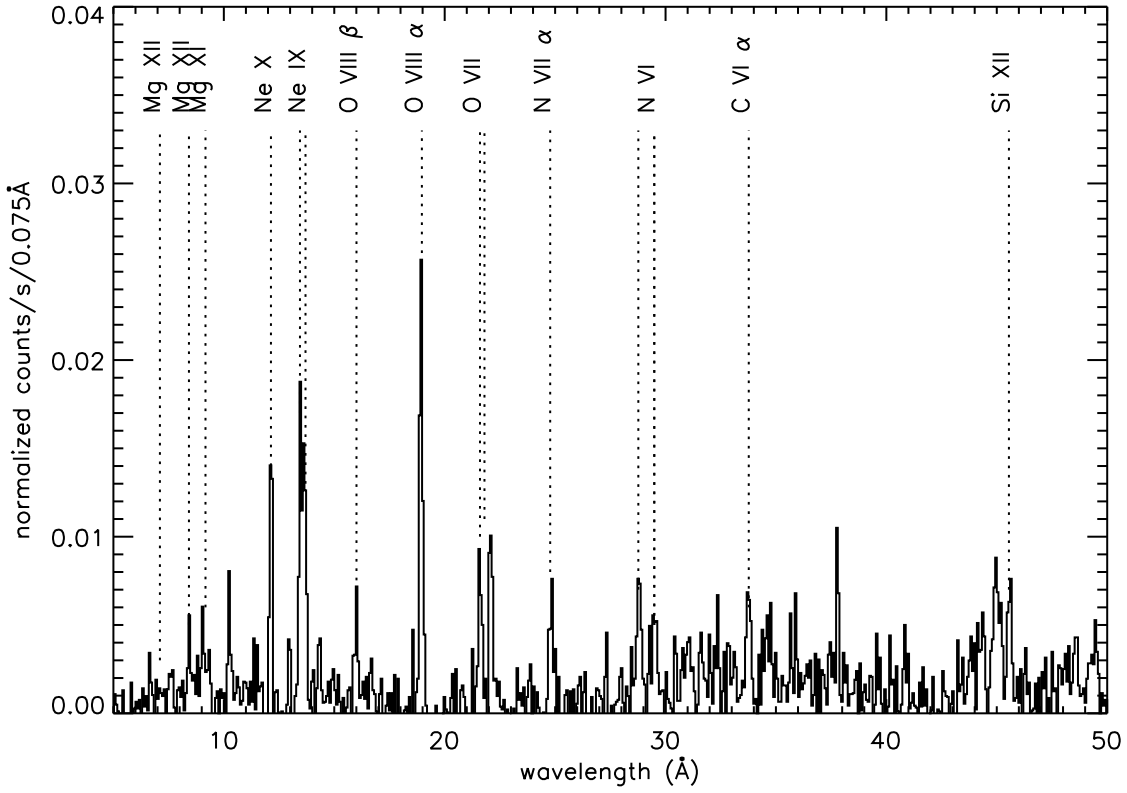

Figure 2.23: X-ray grating spectra of the classical nova V382 Vel (Nelson et al., 2008; Ness et al., 2005).

Hard thermal emission was also observed with *XMM-Newton* from two classical novae (V4633 Sgr; Hernanz & Sala 2005, 2007 and V5115 Sgr; Hernanz & Sala 2010) and the recurrent nova RS Oph (e.g., Nelson et al. 2008). In the case of V4633 Sgr, the spectra were explained by a multi-temperature optically-thin thermal plasma model 934, 1083, and 1265 days after the outburst. In V5115 Sgr, the X-ray spectra were explained by a combination of blackbody and optically-thin thermal plasma model with a temperature of respectively $\sim 6 \times 10^5$ K and $\sim$2.5 keV $\sim$18 month after the outburst. The volume emission measure of the optically-thin thermal plasma component is $\sim 4 \times 10^{55}$ cm^{-3}, and the luminosity of the blackbody emission is $\sim 10^{36}$ erg s^{-1} at an assumed distance of 10 kpc.

- **Studies of Super-Soft X-ray Emission :** The super-soft X-ray emission was clearly detected from two classical novae (V4743 Sgr; Ness et al. 2003b and V1494 Aql; Drake et al. 2003) and the recurrent nova RS Oph (e.g., Nelson et al. 2008) with *Chandra*. In the case of V4743 Sgr, large-amplitude oscillations with a period of 1325 s were found in the X-ray light curve (figure 2.24). The spectral hardness ratio changed from maximum to minimum in correlation with the flux oscillations. The X-ray spectrum is characterized by a soft blackbody-like continuum with absorption lines from both H-like and He-like C, N, and O (figure 2.25). The absorption lines were blue-shifted at velocities of ∼2400 km s^{-1}. To explain the X-ray spectra with the complex ionized absorption features, non-local thermodynamic equilibrium (non-LTE) atmosphere models were also applied (Rauch et al., 2010).

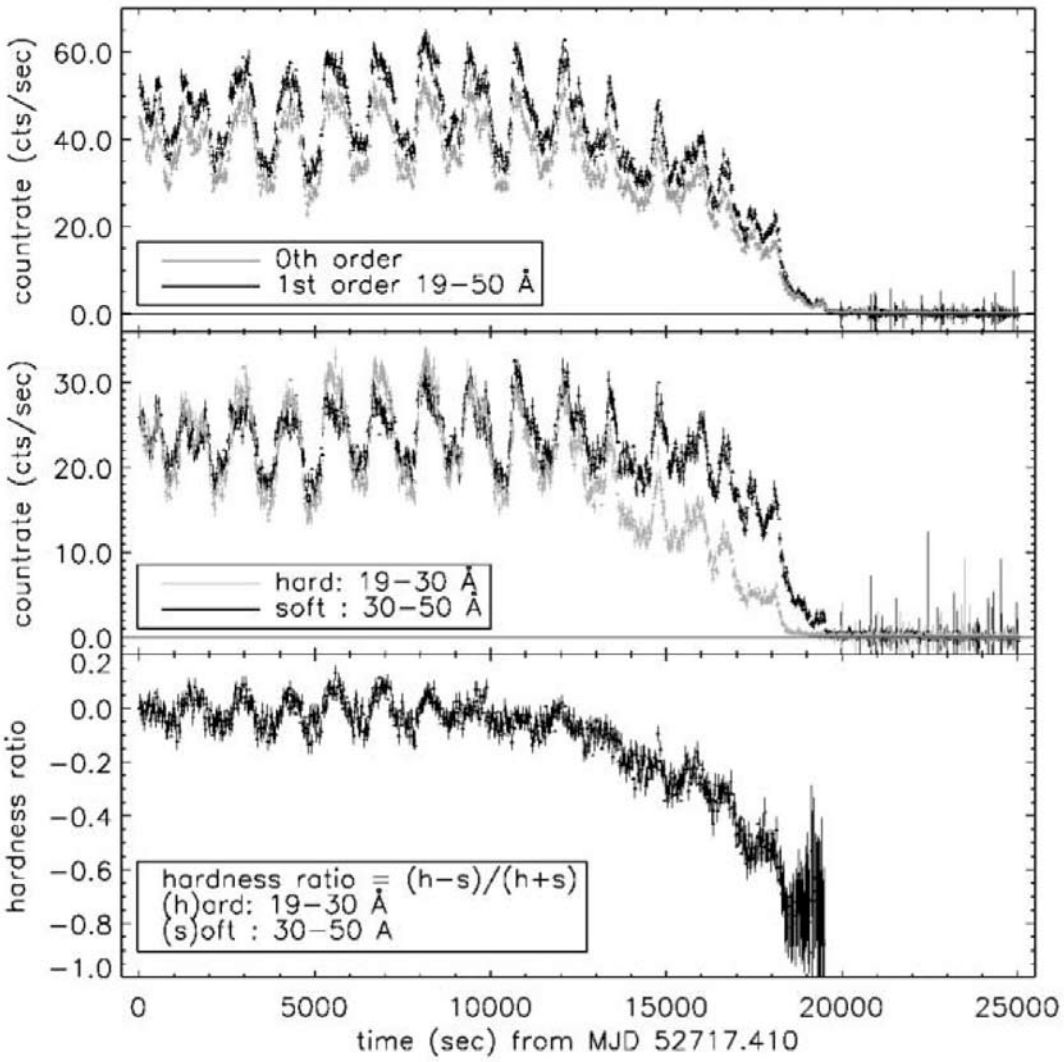

Figure 2.24: X-ray light curve of the classical nova V4743 Sgr with *Chandra* (Ness et al., 2003a,b).

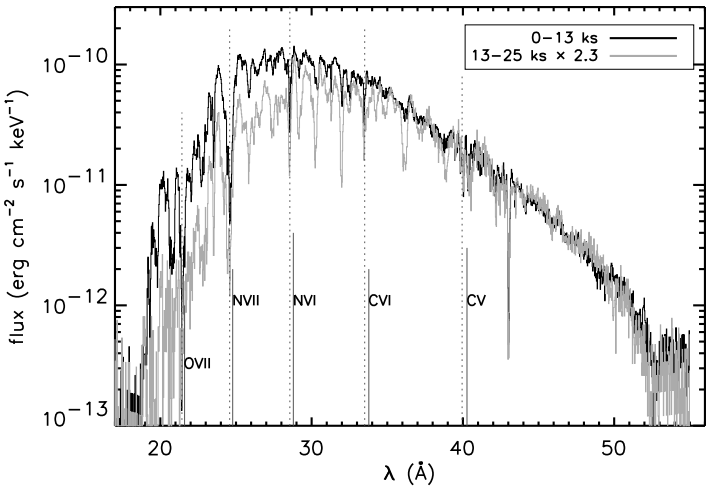

Figure 2.25: X-ray grating spectra of the classical nova V4743 Sgr with *Chandra* (Ness et al., 2003b,a).

In the case of V1494 Aql, a short time-scale amplification and oscillations were found in the super-soft X-ray emission (Drake et al., 2003). The X-ray count rate shows a complex rise and fall at a time scale of ∼1000 s (figure 2.26). The peak count rate is about a factor of six higher than the mean level before and after the X-ray amplification. A period of ∼2500 s was also found in the X-ray light curve with an amplitude of ∼15%. Drake et al. (2003) argued that the period occurs in nonradial g^+ mode pulsations in the hot white dwarf.

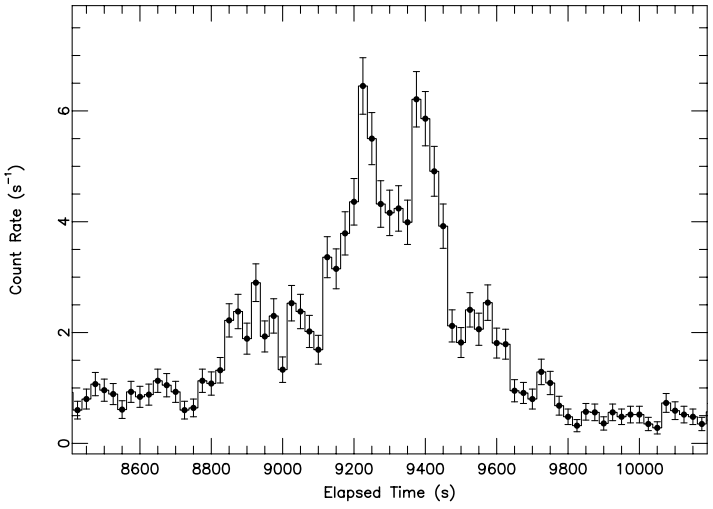

Figure 2.26: Shoft X-ray amplification of V1494 Aql (Drake et al., 2003).

The super-soft X-ray emission was also detected from three classical novae (V4743 Sgr; Leibowitz et al. 2006, V5116 Sgr; Sala et al. 2008, and V2491 Cyg; Ness 2010a) and the recurrent nova RS Oph (e.g., Nelson et al. 2008) with *XMM-Newton*. In the case of V4743 Sgr, the variability up to ∼40% of the total flux was found in the X-ray light curve in the super-soft X-ray emission, ∼196 days after the outburst (Leibowitz et al., 2006). Significant periods of ∼1310 and 1371 s were found in the X-ray light curve, and one of them is considered to be the spin period of the white dwarf. In V5116 Sgr, the flux variation by a factor of ∼8 was seen in the light curve in the super-soft X-ray emission. The periodicity is consistent with the orbital period of ∼3 hour. The X-ray spectra were explained by a blackbody component with a temperature of $\sim 6\times10^5$ K and a luminosity of $\sim 4\times10^{37}$ (distance/10kpc) erg s^{-1}. In all novae that have been observed with grating instruments (V2491 Cyg, V4743 Sgr, and RS Oph), the absorption lines in the super-soft X-ray emission were blue-shifted. The X-ray grating spectrum of V2491 Cyg is shown in figure 2.27. Therefore, Ness (2010a) argued the presence of expanding atmosphere. The results of V2491 Cyg are described in section 5.3 with the results of our observations in this thesis.

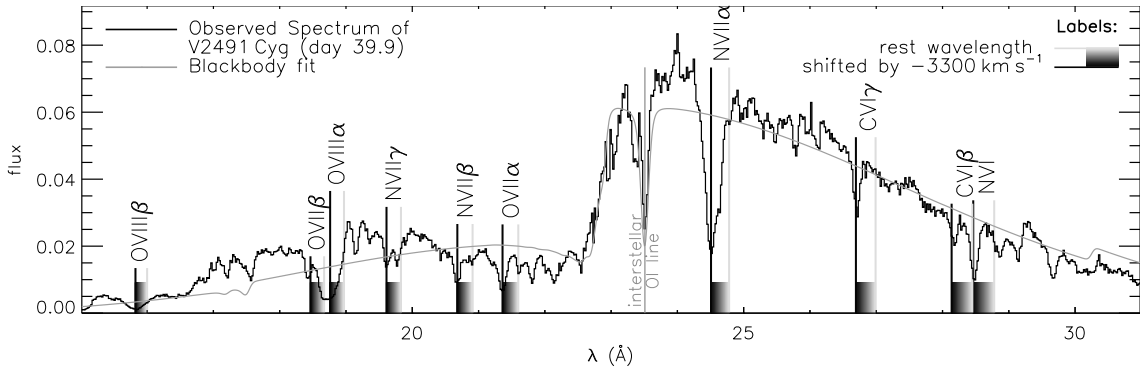

Figure 2.27: X-ray spectrum of the classical nova V2491 Cyg with textitXMM-Newton (Ness, 2010a).

- **Progress in Quiescent Emission :** Quiescent emission was detected from three binary systems causing a classical nova (V603 Aql; Mukai & Orio 2005, RR Pic; Pekön & Balman 2008, and GK Per; Hellier & Mukai 2004) with *Chandra*. In the case of V603 Aql, X-rays were detected ∼83 years after the outburst. The spectra were explained by a multi-temperature collisionally ionized plasma model (figure 2.28). V603 Aql is a highly variable X-ray source, but no period has been confirmed in the X-ray light curve, indicating that it is a non-magnetic system. The fluorescent emission line from Fe was detected at 6.4 keV (Mukai & Orio, 2005), which is a common signature from the accretion process in binary systems. In RR Pic, X-rays were detected ∼76 years after the outburst. The quiescent emission is also explained by a thermal bremsstrahlung model with a temperature of ∼1–2 keV. The presence of emission lines from C, O, Ne, Ca, S, and Fe as well as absorption lines from Na, Ne, and Fe were argued in the spectra. The orbital motions were also detected in the X-ray light curve (Pekön & Balman, 2008). In the case of GK Per, X-rays were detected ∼101 years after the outburst. A significant fluorescent emission line was also detected in the spectra with a red wing extending to 6.33 keV, which is consistent with a Doppler shift of ∼3700 km s^{-1}. Hellier & Mukai (2004) argued that this arises from pre-shock material.

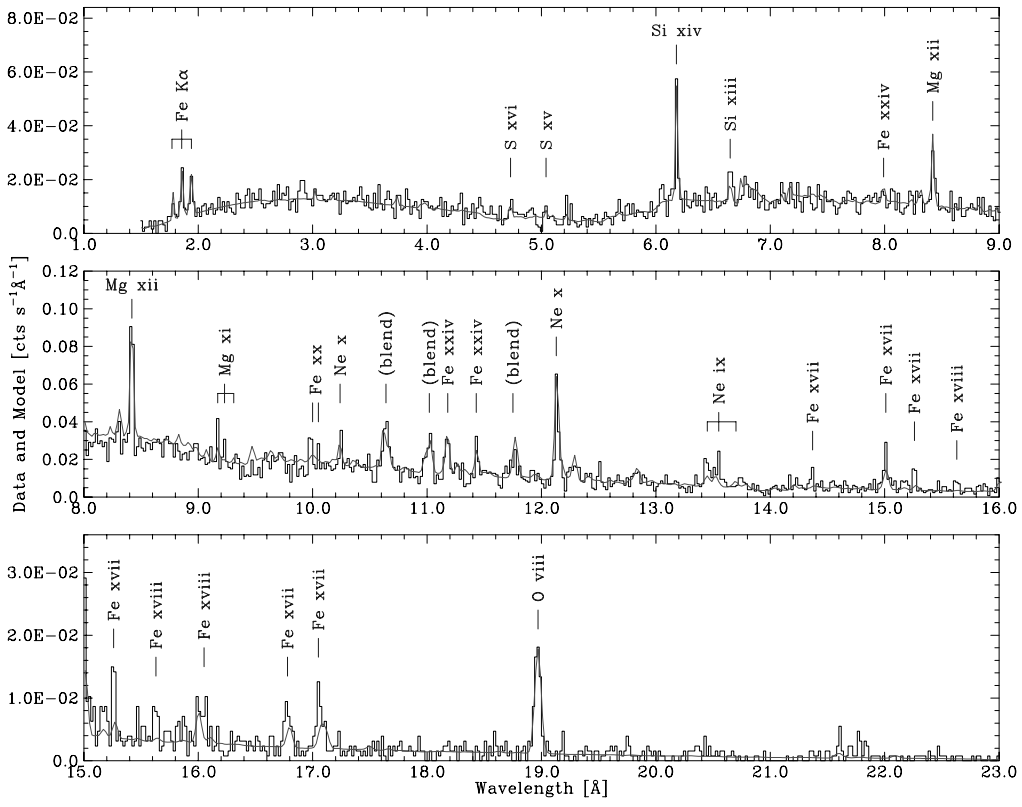

Figure 2.28: X-ray grating spectra of V603 Aql (Mukai & Orio, 2005).

XMM-Newton also observed quiescent emission from binary systems causing a clas-

sical nova (CP Pup; Orio et al. 2009 and V2487 Oph; Hernanz & Sala 2002). CP Pup was observed ∼63 years after the outburst. The X-ray spectra were explained by the optically-thin thermal plasma emission with a luminosity of $\sim 2\times10^{33}$ erg s^{-1} in the 0.15–10 keV energy band (figure 2.29). The fluorescent emission line from Fe was detected at 6.4 keV, and a Doppler-shifted red wing was confirmed in the emission line with a width of ∼200 eV. The origin of the wing is considered to be a Compton down-scattering process and pre-shock material falling at a near escape velocity (Orio et al., 2009). In the case of V2487 Oph, the quiescent emission has been confirmed as early as ∼3 years after the outburst. The spectra were explained by a multi-temperature optically-thin thermal plasma emission with a temperature of ∼0.2 keV and >48 keV. The volume emission measure is $\sim 1\times10^{57}$ cm^{-3}. An additional blackbody component with a temperature of ∼30 eV and a luminosity of $\sim 3\times10^{37}$ erg s^{-1} improves the spectral fitting. The fluorescent line at 6.4 keV was also detected in the quiescent emission, Hernanz & Sala (2002) argued that it is a magnetic system. Pre-nova X-ray activity was also found in *ROSAT* observations.

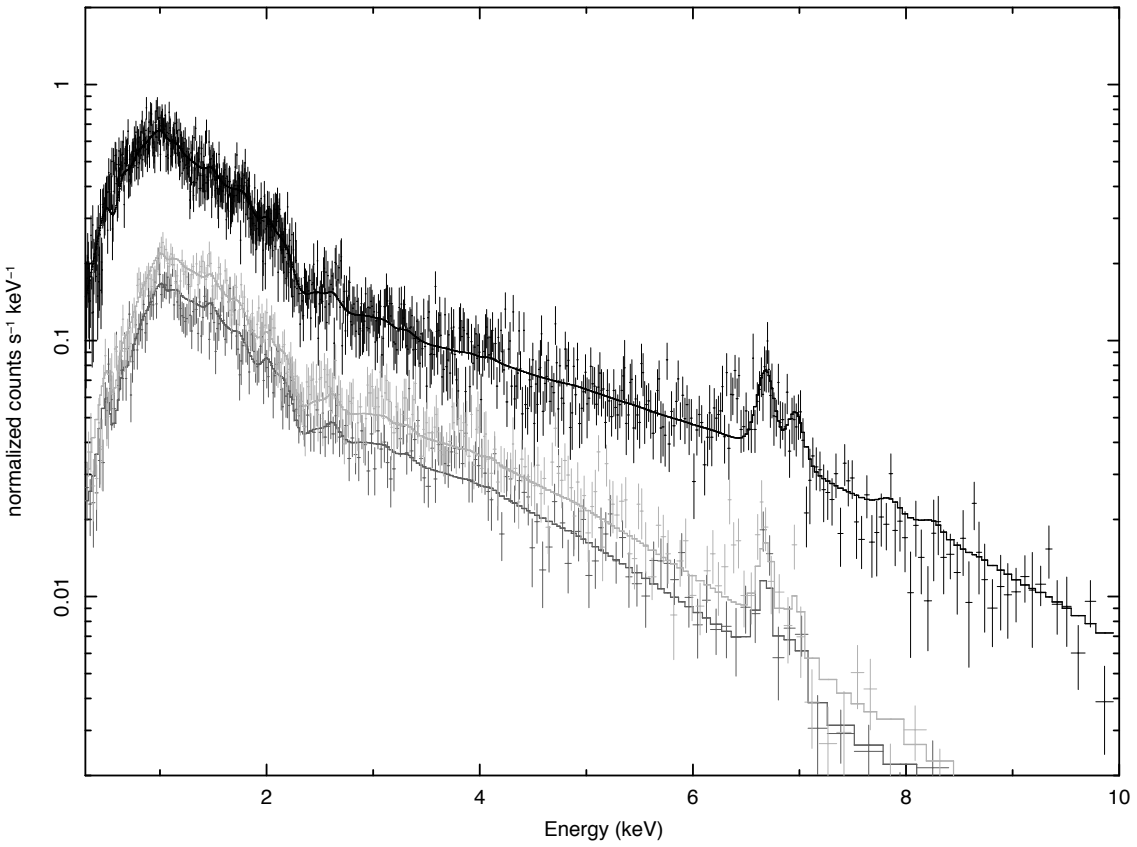

Figure 2.29: X-ray CCD spectra of CP Pup (Orio et al., 2009).

- **Imaging-Spectroscopy of Nova-Remnant Emission :** Finally, we review the results of diffuse X-ray emission around the systems causing a classical nova. The nova-remnant emission from the classical nova GK Per was detected with *Chandra*, ∼99 years after the outburst (Balman, 2005). An X-ray image with an extremely high spatial resolution revealed the presence of lumpy and asymmetric X-ray nebula around the GK Per (figure 2.30). The X-ray spectra were explained by a combination of soft optically-thin thermal plasma and hard power-law components with a photon index of ∼2.3. The luminosity was estimated to be $\sim 4.3 \times 10^{32}$ erg s^{-1}. The power-law emission suggests that the presence of particle acceleration in the expanding shell similar to those of supernova remnants.

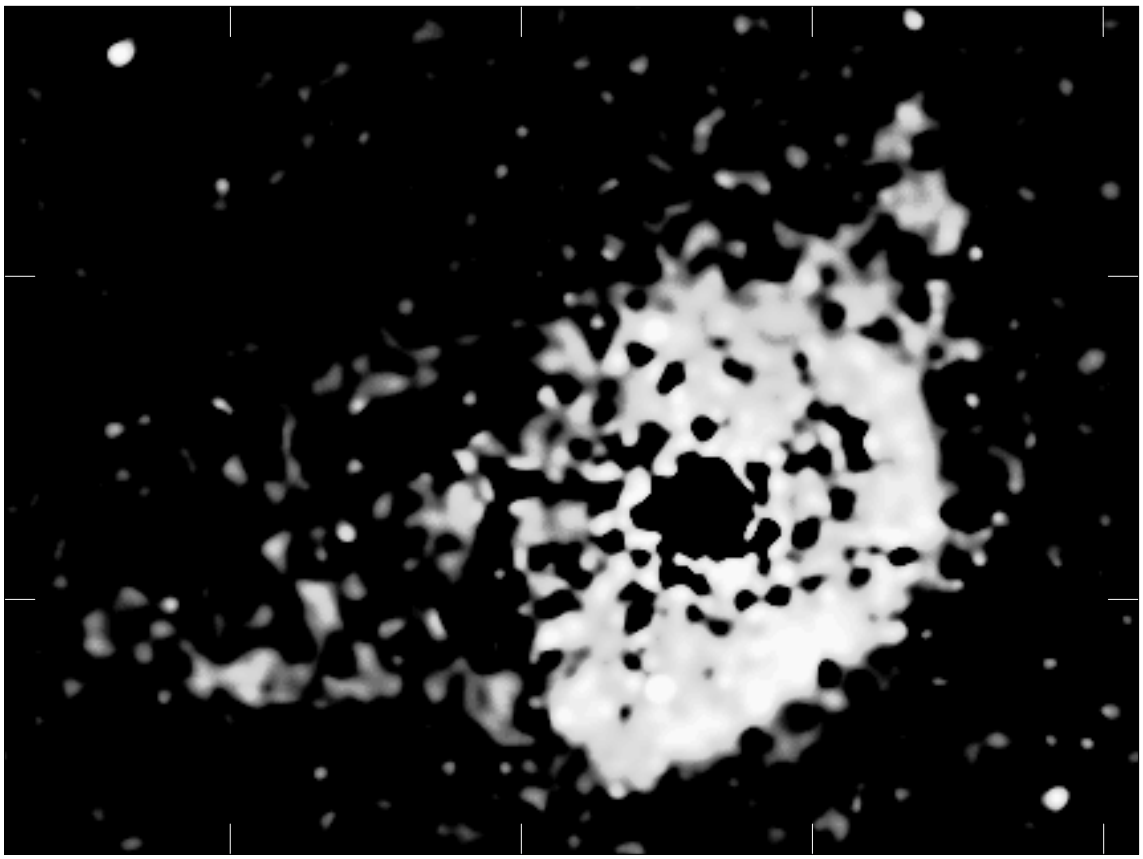

Figure 2.30: X-ray image of the classical nova GK Per with *Chandra* (Balman, 2005).

The nova-remnant emission in X-rays was also confirmed from the recurrent nova T Pyx with the *XMM-Newton* satellite (Balman, 2010). The X-ray nebula extended in an elongation from northeast to southwest in excess of ∼15″. The X-ray spectra were explained by a two-component optically-thin thermal plasma model with temperatures of ∼0.2 keV and 1.3 keV. The luminosity is 6×10^{32} erg s^{-1}. The shock velocity derived from the plasma temperature is consistent with the expansion velocity.

2.4.2.7 Dawn of the Golden Age for Transient X-ray Phenomena

***Swift* Observatory**

The *Swift* satellite[2] is a multi-wavelength observatory dedicated to the studies of gamma-ray burst. The mission is a Medium-sized Explorer (MIDEX) program by NASA, and *Swift* provides simultaneous observations in a wide-energy range from optical to γ-ray bands since 2004. The spacecraft has an ability to point swiftly and autonomously at a target position in less than approximately 90 s, which is a key requirement for the study of gamma-ray burst afterglow emission. More details of the *Swift* mission are described in section 4.3.

- **Systematic Observations for the X-ray Emission :** The *Swift* satellite provides intensive monitoring observations of bright X-ray emission from classical and recurrent novae (e.g., RS Oph; Bode et al. 2006, V723 Cas; Ness et al. 2008a, V2362 Cyg; Lynch et al. 2008b, V598 Pup; Page et al. 2009, V458 Vul; Ness et al. 2009c, and V2491 Cyg; Ibarra et al. 2009; Page et al. 2010). The snapshot observations were also performed in a number of classical novae with weak detections (e.g., V574 Pup, V382 Nor, V1663 Aql, V5116 Sgr, V1188 Sco, V1047 Cen, V476 Sct, V477 Sct, V723 Cas, V1494 Aql, and V4743 Sgr; Ness et al. 2007a). Based on the results, systematic and statistical studies have been conducted for comparing their X-ray light curves and spectra of each classical nova (Ness et al., 2007a). Systematic studies of X-ray luminosities have been performed using the results of *ROSAT*, *ASCA*, *Beppo-SAX*, *XMM-Newton*, and *Swift* (Mukai et al., 2008).

  The spectral evolution was followed by *Swift* in these bright novae, in which the observed X-ray spectra were typically explained by optically-thin thermal plasma and blackbody-like emission. In the recurrent nova RS Oph, the time-series X-ray spectra were explained by optically-thin thermal plasma emission, and they revealed that the plasma temperature declines from $\sim$9 to $\sim$2 keV between day $\sim$3 to $\sim$26 after the outburst. The time-development of the absorption column density was also constrained (Bode et al., 2006). In the case of V2362 Cyg, the broad-band light curves in infrared, optical and X-rays were compared in collaboration with *Swift*, the infrared satellite *Spitzer*, and ground-based observations (Lynch et al., 2008b). The X-ray spectra were explained by a multi-temperature optically-thin thermal plasma model with a temperature of 0.2 and 1.8 keV. In V723 Cas, the observations were performed 11–12 years after the outburst. The X-ray spectra were dominant below $\sim$2 keV, which is explained by a blackbody emission with a temperature of $\sim$3–4$\times10^5$ K and a luminosity of $\sim5\times10^{36}$ erg s^{-1}. Ness et al. (2008a) argued that the origin is a steady hydrogen burning due to the reestablished accretion process. In V598 Pup, monitoring observations were performed during day 147–255 after the outburst. The X-ray spectra were explained by a combination of an optically-thin thermal plasma component with a temperature of 0.2–0.6 keV and a blackbody component with a temperature of 40–70 eV Page et al. (2009).

  V458 Vul (Ness et al., 2009c) and V2491 Cyg (Ibarra et al., 2009; Page et al., 2010) were also observed at a high cadence with *Swift* in the post-outburst development. In

the case of V458 Vul, monitoring observations were performed during day 1–422 after the outburst, in which hard thermal emission was detected. In V2491 Cyg, X-rays were detected both before and after the outburst in *Swift* observations. These results are described in section 5.2 and 5.3 with the results of our observations in this thesis.

Table 2.2: List of classical (and recurrent) novae with X-ray detections (part 1).

Outburst date[a]	Name[b]	Observations[c]	Remarks	Reference
1848.04.27	V841 Oph	*Ei*:131 y	—	Orio et al. (2001b)
		RO:142 y	—	
		Ei:131 y	—	Becker & Marshall (1981b)
1860.05.21	T Sco	*RO*:132 y	—	Orio et al. (2001b)
1895.04.08	RS Car	*HE*:83 y	—	Cordova et al. (1981a)
1989.03.08	1059 Sgr	*Ei*:90 y	—	Becker & Marshall (1981b)
1901.02.21	GK Per	*RO*:91 y,95 y	—	Balman & Ögelman (1999)
		Ch:99 y	—	Balman (2005)
		Ei:78 y	—	Becker & Marshall (1981b)
		Ch:101 y	—	Hellier & Mukai (2004)
		Ei:78 y,79 y	—	Eracleous et al. (1991)
		Ei:78 y,79 y	—	Cordova & Mason (1984)
1906.02.14	AR Cir	*HE*:72 y	—	Cordova et al. (1981a)
1908	RR Tel	*Ei*:70 y,	—	Orio et al. (2001b)
		RO:82 y,84 y,85 y	—	
1918.06.08	V603 Aql	*Ei*:63 y,65 y	—	Orio et al. (2001b)
		EX:66 y	—	
		RO:72 y,73 y,75 y	—	
		RX:80 y,83 y	—	Mukai & Orio (2005)
		Ch:83 y	—	
		AS:78 y	—	
		Ei:61 y	—	Becker & Marshall (1981b)
		Ei:64 y	—	Drechsel et al. (1983)
		Ex:66 y	—	Haefner et al. (1988)
		Ei:61 y,64 y	—	Eracleous et al. (1991)
1925.05.25	RR Pic	*HE*:52–53 y	—	Cordova et al. (1981a)
		Ei:54 y	—	Orio et al. (2001b)
		RO:65 y,67–68 y	—	
		Ei:54 y	—	Becker & Marshall (1981b)
		Ch:76 y	—	Pekön & Balman (2008)
1927.07.30	EL Aql	*HE*:50–51 y	—	Cordova et al. (1981a)
1931.05.09	MT Cen	*HE*:47 y	—	Cordova et al. (1981a)
1934.12.12	DQ Her	*Ei*:45 y	—	Orio et al. (2001b)
		RO:58 y	—	
1936.06.18	CP Lac	*Ei*:43 y	—	Orio et al. (2001b)
		RO:57 y	—	
1936.09.18	V356 Aql	*HE*:41–42 y	—	Cordova et al. (1981a)
1942.11.09	CP Pup	*HE*:35–36 y	—	Cordova et al. (1981a)
		RO:51 y	—	Balman et al. (1995)
		RO:48 y,50 y	—	Orio et al. (2001b)
		Ei:37 y	—	Becker & Marshall (1981b)
		AS:56 y	—	Orio et al. (2009)
		Nw:63 y	—	
		Ei:37 y	—	Eracleous et al. (1991)
1943.09.05	V500 Aql	*HE*:34–35 y	—	Cordova et al. (1981a)
1953.04.08	RR Cha	*HE*:25 y	—	Cordova et al. (1981a)
1960.03.07	V446 Her	*RO*:30y,33y	—	Orio et al. (2001b)
1978.03.05	LW Ser	*HE*:−167–14 d	—	Cordova et al. (1981a)
1979.04.05	PU Vul	*Ei*:742 d	—	Eracleous et al. (1991)
1983.01.18	GQ Mus	*EX*:462 d	—	Oegelman et al. (1984)
		EX:462 d,547 d,707 d,914 d	—	Oegelman et al. (1987)
		RO:3325–3326 d	—	Oegelman et al. (1993)
		RO:3325–3326 d,3642–3646 d,3870–3642 d	—	Shanley et al. (1995)
		RO:3325–3326 d,3642–3646 d,3870–3642 d	—	Orio et al. (2001b)
		RO:3118 d,3322 d,3641 d,3871 d,4190 d	—	Balman & Krautter (2001)
1984.07.27	PW Vul	*EX*:8 d,107 d,313 d	—	Oegelman et al. (1987)
1984.12.18	QU Vul	*EX*:115 d,307 d	—	Oegelman et al. (1987)
		RO:5.3 y	—	Orio et al. (2001b)
		RO:2340 d	—	Balman & Krautter (2001)

Table 2.2: List of classical (and recurrent) novae with X-ray detections (part 2)

Outburst date[a]	Name[b]	Observations[c]	Remarks	Reference
1991.12.27	V351 Pup	*RO*:480 d	—	Orio et al. (1996)
		RO:480 d	—	Orio et al. (2001b)
		RO:480 d	—	Mukai et al. (2008)
		RO:480 d	—	Balman & Krautter (2001)
1991.03.24	V838 Her	*RO*:5 d	—	Lloyd et al. (1992)
		RO:5 d,370 d,576 d	—	Orio et al. (2001b)
		RO:5 d,370 d,576 d	—	Mukai et al. (2008)
		RO:5 d,365 d	—	Balman & Krautter (2001)
1992.02.19	V1974 Cyg	*RO*:63–653d (M18)	—	Krautter et al. (1996)
		RO:63–653d (M18)	—	Balman et al. (1998)
		RO:63–653d (M18)	—	Orio et al. (2001b)
		RO:63–653d (M18)	—	Mukai et al. (2008)
1995.08.24	V723 Cas	*Sw*:3698 d	—	Ness et al. (2007a)
		Sw:11–12 y (M)	—	Ness et al. (2008a)
1998.06.15	V2487 Oph	*Nw*:986 d,1178 d	—	Hernanz & Sala (2002)
1998.03.22	V4633 Sgr	*Nw*:934 d,1083 d,1265 d	—	Hernanz & Sala (2005)
		Nw:934 d,1083 d,1265 d	—	Hernanz & Sala (2007)
		Nw:934 d	—	Mukai et al. (2008)
1999.12.01	V1494 Aql	*Ch*:300 d,304 d	—	Drake et al. (2003)
		Sw:2289 d,2292 d,2359 d	—	Ness et al. (2007a)
		Ch:134 d,187 d,248 d,300 d,304 d,727 d	—	Rohrbach et al. (2009)
1999.05.22	V382 Vel	*RX*:6 d,31 d,35 d,50 d,59 d	—	Mukai & Ishida (2001)
		AS:20.5 d	—	
		Be:15 d,184 d	—	Orio et al. (2001a)
		Be:15 d,184 d	—	Orio et al. (2002)
		Ch:268 d	—	Ness et al. (2005)
		Ch:268 d	—	Mukai et al. (2008)
2002.09.20	V4743 Sgr	*Ch*:191 d	—	Ness et al. (2003b)
		Nw:196 d	—	Leibowitz et al. (2006)
		Sw:1265 d	—	Ness et al. (2007a)
		Ch:180 d,371 d	—	Ness (2010a)
2004.11.20	V574 Pup	*Sw*:175–264 d (M)	—	Ness et al. (2007a)
2005.08.01	V1047 Cen	*Sw*:66 d,141 d	—	Ness et al. (2007a)
2005.07.25	V1188 Sco	*Sw*:98 d,124 d	—	Ness et al. (2007a)
		Sw:98 d,124 d	—	Mukai et al. (2008)
2005.06.09	V1663 Aql	*Sw*:66 d,267 d	—	Ness et al. (2007a)
		Sw:66 d,267 d	—	Mukai et al. (2008)
2005.03.13	V382 Nor	*Sw*:313 d	—	Ness et al. (2007a)
		Sw:313 d	—	Mukai et al. (2008)
2005.09.30	V476 Sct	*Sw*:135 d	—	Ness et al. (2007a)
		Sw:135 d	—	Mukai et al. (2008)
2005.10.11	V477 Sct	*Sw*:117 d,125 d	—	Ness et al. (2007a)
		Sw:117 d,125 d	—	Mukai et al. (2008)
2005.03.28	V5115 Sgr	*Nw*:548 d	—	Hernanz & Sala (2010)
2005.07.04	V5116 Sgr	*Sw*:56 d	—	Ness et al. (2007a)
		Nw:609 d	—	Sala et al. (2008)
		Sw:56 d	—	Mukai et al. (2008)
2006.04.02	V2362 Cyg	*Sw*:195–486 d (M)	—	Lynch et al. (2008b)
2007.08.04	V458 Vul	*Sw*:1–422 d (M31)	—	Ness et al. (2009c)
		Sz:88 d	—	Tsujimoto et al. (2009)
2007.08.08	V598 Pup	*Sw*:147–255 d (M6)	—	Page et al. (2009)
		Nw:147 d	—	
2008.04.10	V2491 Cyg	*Sw*:−322–−100 d (M6)	—	Ibarra et al. (2009)
		RO:−6383 d,−5302 d	—	
		Nw:−517 d	—	
		Sz:9 d,29 d	—	Takei et al. (2009)
		Nw:40 d,50 d	—	Ness (2010a)
		Sz:29 d	—	Takei & Ness (2010)
		Sw:−322–236 (M)	—	Page et al. (2010)
2009.08.16	V2672 Oph	*Sw*:1–200 d (M)	—	section 5.4
		Sz:12 d,22 d	—	

Table 2.2: List of classical (and recurrent) novae with X-ray detections (part 3)

Outburst date[a]	Name[b]	Observations[c]	Remarks	Reference
1866.05.12	T CrB	*Ei*:113 y	—	Cordova & Mason (1984)
1999	U Sco	*Be*:19–20 d	—	Kahabka et al. (1999a)
1966	T Pyx	*Nw*:40 y	—	Balman (2010)
1985.01.26	RS Oph	*EX*:54 d,60 d,72 d	—	Mason et al. (1987)
		EX:83 d,91 d,250 d	—	
		RO:7 y	—	Orio (1993)
		EX:6 y,7 y	—	Orio et al. (2001b)
2006.02.12		*Sw*:3–26 d (M8)	—	Bode et al. (2006)
		RX:3 d,6 d,10 d,14 d,17 d,21 d	—	Sokoloski et al. (2006)
		Ch:40 d,67 d	—	Ness et al. (2007b)
		Nw:54 d	—	
		Ch:14 d,40 d,67 d,112 d	—	Nelson et al. (2008)
		Nw:14 d,26 d,54 d,205 d,239 d	—	
		Ch:14 d,40 d,67 d,112 d,204 d,207 d,208 d	—	Ness et al. (2009b)
		Nw:14 d,26 d,54 d,205 d,239 d	—	
		Ch:40 d,67 d	—	Ness (2010a)
		Ch:14 d	—	Drake et al. (2009)
		Ch:537 d	—	Luna et al. (2009)
1919.03.11	V1017 Sgr	*HE*:59 y	—	Cordova et al. (1981a)
		Ei:61 y	—	Cordova & Mason (1984)
2000.04.28	CI Aql	*Ch*:399 d,460 d	—	Greiner & Di Stefano (2002)
2002.01.03	IM Nor	*Ch*:40 d,148 d	—	Orio et al. (2005)

[a] http://www.cfa.harvard.edu/iau/nova_list.html
[b] Red sources are our data sets in this thesis.
[c] Existence of the observations with the *HEAO-1* (*HE*), the *Einstein* (*Ei*), the *EXOSAT* (*EX*), the *ROSAT* (*RO*), the *ASCA* (*AS*), the *RXTE* (*RX*), the *Beppo-SAX* (*Be*), the *Chandra* (*Ch*), the *XMM-Newton* (*Ne*), the *Swift* (*Sw*), and the *Suzaku* (*Sz*) observatories. "M" indicates that the monitoring observations were performed (with the following number).

2.4.2.8 Recent Progress in the Gamma-ray Observations

***Fermi* Observatory**

The *Fermi Gamma-ray Space Telescope* is an international and multi-agency space mission for a high energy astrophysics and particle physics[3]. The observatory provides an all-sky survey with unprecedented sensitivity in the γ-ray energy band. The satellite has two instruments in operation: the Large Area Telescope (LAT) and the GLAST Burst Monitor (GBM). The LAT is an imaging γ-ray detector sensitive in the energy range from 30 MeV to 300 GeV with a large field of view. The GBM consists of 14 scintillation detectors sensitive in the energy range from 8 keV to 1 MeV. Details of *Fermi* can be found in e.g., Atwood et al. (2009).

The detection of γ-ray emission from classical novae has been reported with *Fermi* for the first time (Abdo et al., 2010). In the symbiotic nova V407 Cyg, a marginal detection of a γ-ray signal was reported in 12–18 hours after the outburst, which was followed by a significant detection in 18–24 hours (figure 2.31). The peak flux was observed 3–4 days after the initial detection, and then it declined in 5 days. The γ-ray spectrum was explained by a π^0 decay emission model in the form of exponential cutoff power-law with a spectral index of -2.2 and a cut-off energy of 32 GeV (figure 2.32). Also, the spectrum is fitted by a leptonic model, which consists of an inverse Compton process plus a small contribution from bremsstrahlung emission, with a spectral index of -1.75 and a cut-off energy of 3.2 GeV.

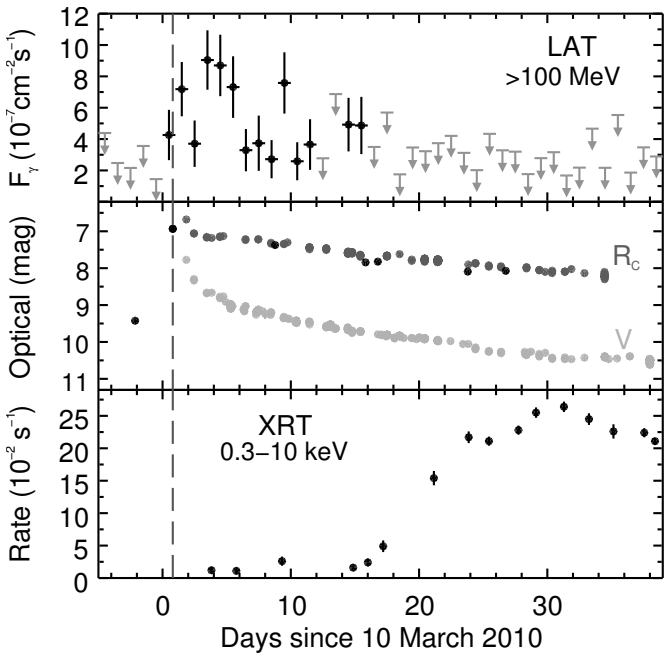

Figure 2.31: The time-development of the symbiotic nova V407 Cyg (Abdo et al., 2010) in γ-rays (top), optical (middle), and X-rays (bottom).

[3]See http://www.nasa.gov/mission_pages/GLAST/main/ for details.

The X-ray flux of V407 Cyg, which was also monitored with the *Swift* satellite, started to rise ∼2 weeks after the outburst. That is coincident with the γ-ray flux decline, and Abdo et al. (2010) proposed that the material of nova shell interacts with the dense circumstellar matter around a red giant companion, and that the particles can be accelerated to produce π^0 decay γ-rays from proton-proton interactions.

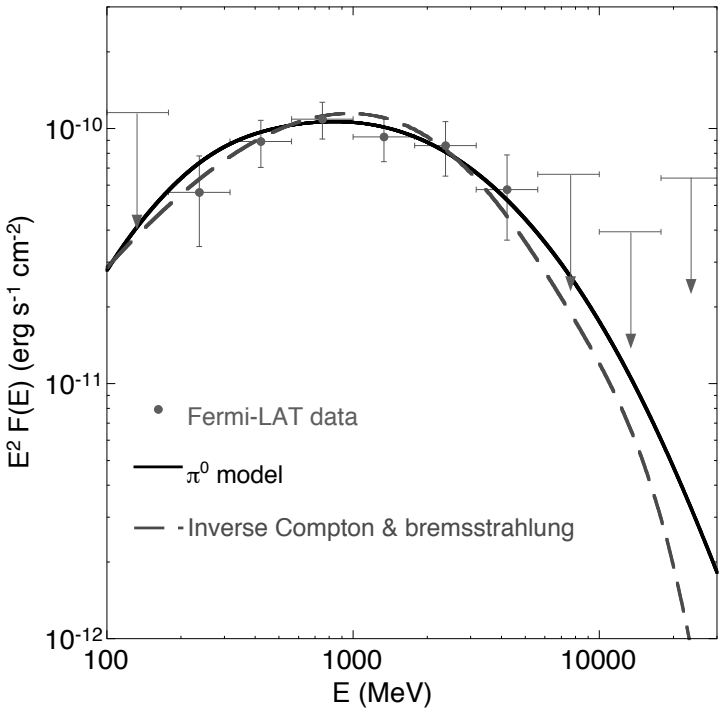

Figure 2.32: The spectral energy distribution in the γ-ray energy band (Abdo et al., 2010).

2.4.3 Summary of Previous X-ray Studies

After the launch of the *Swift* satellite, it became possible to take X-ray data of classical novae at a high cadence. Such systematic studies provide a basis to interpret the results obtained by individual pointing observations by other X-ray observatories such as *Suzaku*, *XMM-Newton*, and *Chandra*. We give such an example using the *Swift* satellite.

RS Oph is one of the best samples with quite a lot of snapshot X-ray observations with *Swift* in the post-outburst development (Bode et al., 2008). The X-ray light curve with *Swift* is shown in figure 2.33. We notice several X-ray characteristics in the light curve: (1) Hard X-rays emerged just after the outburst and declined continuously. (2) Soft X-rays emerged around day 30 fluctuated in the rising phase, leveled off for a while, and started to decline quickly around day 100. These phenomena as well as others are the topics of this thesis.

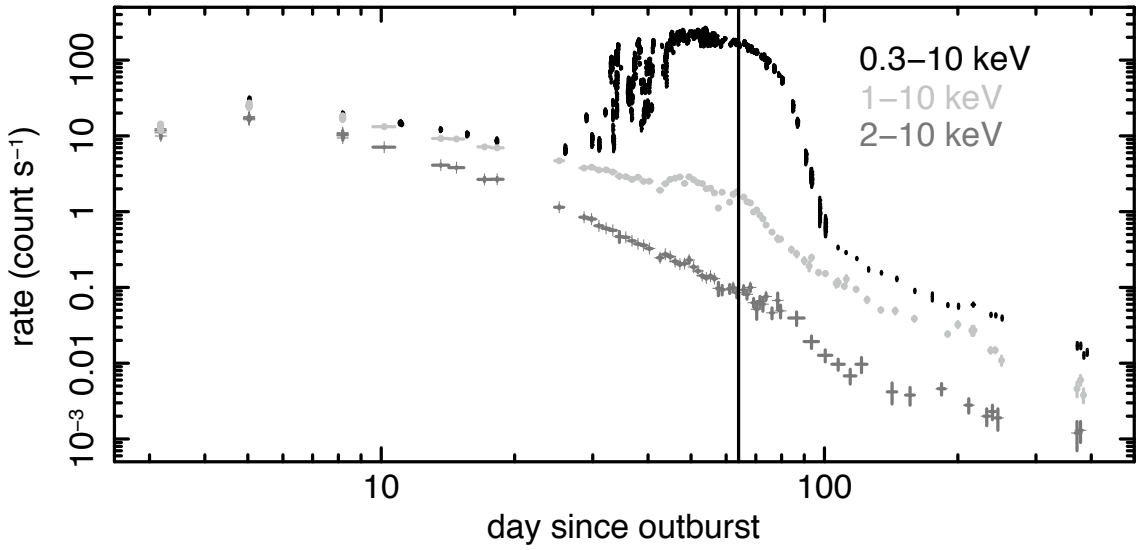

Figure 2.33: X-ray light curve of the recurrent nova RS Oph with *Swift* (Bode & Evans, 2008).

Chapter 3

Objectives and Strategy

In this chapter, we describe the objectives (section 3.1) and strategies (section 3.2) of this thesis. X-ray spectroscopy is a powerful tool to understand the nature of classical novae. However, they occur without any prior warning and disappear quickly. Conventional X-ray observations, which take more than one year to propose, review, schedule, and execute, do not work at all for studies of classical novae. We thus take two strategies in this research: archival search (section 3.2.1) and target-of-opportunity observations (section 3.2.2).

Contents

3.1 Objectives

Past X-ray observations revealed many important characteristics of high energy phenomena from classical novae. However, two items hinder to make more systematic and advanced study. One is the difficulty to conduct systematic observations due to the transient nature of classical novae. Most observational results so far were obtained either by (1) all sky surveys or (2) pointing observations with a target-of-opportunity program often at a risk of detecting nothing. The other is the performance of observing instruments. Especially, the advent of X-ray CCD imaging spectrometers onboard *Chandra*, *XMM-Newton*, *Swift*, and *Suzaku* made it possible to make sensitive observations with sufficient energy resolution for e.g., identifying absorption and emission features from the super-soft X-ray spectra and producing high signal-to-noise ratio spectra for spectral analysis in a time resolved manner. The low-background and narrow-field detector onboard *Suzaku* enabled the search for non-thermal emission in the super-hard X-ray band.

A suite of these instruments gives an excellent opportunity to overcome observational difficulties which existed in the previous decade. Armed with the advanced instruments and the expanded opportunities, we aim to address five issues (section 3.1.1–3.1.5) in this thesis, which are all independent but closely related to make a progress in our understanding of classical novae and the binary system.

3.1.1 X-ray Evolution in the Post-Outburst Phase

- **Objective:** Several types of X-ray emission have been reported in the post-outburst development by previous studies. We aim to classify different types of X-ray emission based on their X-ray production mechanisms and list observational features commonly seen in each type of emission.

- **Method:** We conduct time-sliced spectroscopy of several classical novae using X-ray CCD spectrometers and compare their features with those in literature. We propose a classification frame work based on our own results and those in literature.

- **Results:** Our observational results are presented in section 5.1–5.4, while the discussion can be found in section 6.1.1.

3.1.2 Diagnosis of White Dwarf Atmosphere

- **Objective:** The diagnosis of white dwarf atmospheric features gives vital clues to understand the basic properties of white dwarfs, in the same way as the diagnostics of stellar atmospheric features does for stars. We aim to give constrains of the white dwarf mass and radius by spectroscopy of atmospheric emission.

- **Method:** We conduct CCD spectroscopy of the super-soft X-ray emission of some classical novae. Even with a CCD resolution ($E/\delta E \sim 10$ at 1 keV), we can detect absorption features from some abundant species at different ionization stages. We

derive the plasma temperature of the atmosphere, estimate the mass and radius, and compare them with the values derived from other independent methods.

- **Results:** Observational results are presented in section 5.1 and 5.4, while the discussion can be found in section 6.1.2.

3.1.3 Ejecta Chemistry

- **Objective:** The mass ejection occurs in a classical nova explosion. The white dwarf loses a part of the accreted material as well as the material of its own, thus the abundance pattern of the ejecta reflects the chemical composition of the white dwarf core. In general, more massive white dwarf core is consists with more heavy metals in abundance. Therefore, the chemical composition of the ejecta provides a unique observational tool.

- **Method:** We conduct X-ray CCD spectroscopy in the $\sim$0.2–10 keV band. The energy band includes emission lines from abundant species including N, O, Mg, Si, S, Ar, and Fe. We obtain high signal-to-noise ratio spectra from several classical novae, conduct spectral fitting in a coherent format to derive relative abundance between metals.

- **Results:** Observational results are presented in section 5.2 and 5.3, while the discussion can be found in section 6.1.3.

3.1.4 Reestablishment of Accretion

- **Objective:** Classical novae occurs in a binary system in which matter provided by a companion accrets to the white dwarf. The accretion process is considered to be stopped after the classical nova, at which the radiation pressure exceeds the ram pressure of the accretion. The reestablishement of the accretion process is a major event after the classical nova, which affects the eventual fate of the binary system. Therefore, it is important to know how early the accretion is reestablished. We aim to address this question in this thesis.

- **Method:** We observe an intermediate polar after the classical nova at a high cadence and monitor Fe K fluorescence line. The fluorescence line is a signature of accretion in the intermediate polar system, and can be used as a probe for rekindled accretion.

- **Results:** Observational results are presented in section 5.3, while the discussion can be found in section 6.1.4.

3.1.5 Non-Thermal Process in Explosion

- **Objective:** A classical nova explosion is quite similar to a super-nova explosion, which is considered to be the dominant agent to accelerate charged particles in the Galaxy. The presence of high energy particles in classical novae are expected in the theoretical

contexts. The super-hard X-ray band ($\gtrsim$10 keV) is most suited for such purpose, as non-thermal emission dominates the spectrum without thermal contamination. However, super-hard X-ray emission has not been detected from any classical novae to date. We aim to discover such emission and derive its properties.

- **Method:** We use the Hard X-ray Detector onboard *Suzaku*, which has the highest sensitivity in the relevant energy band. We make ToO observations as quickly as possible of a classical nova, at which non-thermal emission is expected.
- **Results:** Observational results are presented in section 5.3, while the discussion can be found in section 6.1.5.

3.2 Strategies

3.2.1 Archival Search

3.2.1.1 Data Archives

In space astronomy, most observational data are released to public after a certain period (typically one year) of proprietary. Some observatories, such as the *Swift* satellite, release their data immediately after observations. These data are archived in a well-defined format and are accessible to anyone. Major web resources include the High Energy Astrophysics Science Archive Research Center (HEASARC)[1] by the National Aeronautics and Space Administration (NASA) for several high energy astrophysical missions, the Data ARchives and Transmission System (DARTS)[2] by the Japan Aerospace Exploration Agency (JAXA) for several Japanese astronomical missions, and the official web pages of the *Swift* satellite[3] for quick-look of data obtained with the satellite. In the ∼30 year history of the X-ray astronomy, a large number of observational data by many past and all current missions have been archived. Systematic search for unexpected transient sources including classical novae is possible by using the archival data.

3.2.1.2 Retrieved Data

In any astronomical instruments, the degradation of the performance in orbit is a major problem for correctly interpreting data sets. Therefore, routine calibration observations are necessary to check the status of instruments. Pre-installed standard calibration sources as well as stable astronomical objects are often employed for such purposes.

The lineup for the calibration targets includes famous astronomical object or lack thereof such as Crab, 1E 0102.2−7219, Lockman Hole, Cygnus Loop, Perseus, and RX J1856.5−3754. In particular, the super-nova remnant (SNR) 1E 0102.2−7219 is most frequently visited for routine calibrations by many missions. 1E 0102.2−7219 is the second brightest X-ray source in the Small Magellanic Cloud (SMC) at a distance of ∼60 kpc. It was discovered by the *Einstein* observatory (Seward & Mitchell, 1981). This source is particularly suited for monitoring the quantum efficiency, the absolute energy scale, and the energy resolution of X-ray instruments because of its soft and line-dominated spectrum, non-variable flux, and good visibility from satellites throughout a year. A large number of observations offer a unique opportunity to search for transient sources in the surrounding area and to monitor their long-term behavior without additional investments of telescope time.

[1] http://heasarc.gsfc.nasa.gov/docs/archive.html
[2] http://darts.isas.jaxa.jp/
[3] http://swift.gsfc.nasa.gov/cgi-bin/sdc/ql

3.2.2 Target of Opportunity Observations

3.2.2.1 Discovery of Classical Novae

In the past several years, ∼10 classical novae, including recurrent and symbiotic novae, were discovered every year (table 3.1). Almost all classical novae are discovered by amateur astronomers using small optical telescopes. In particular, discoveries by Japanese astronomers make a substantial contribution. These discoveries are circulated in electronic formats via e-mails and web pages, often within a few hours of discovery. Observations using a suite of observatories around the globe and in space follow, the results of which are also circulated in the same media.

Table 3.1: List of all classical novae discovered from 2007 to early 2010.

Date of outburst	Name[a]	Observation[b]				Reference[c]
		Sw	*Sz*	*Nw*	*Ch*	
2007.01.23	V1065 Centauri	X		X		[1],[2]
2007.02.04	V1280 Scorpii	O		X		[3],[4]
2007.02.19	V1281 Scorpii	O				[5],[6]
2007.03.15	V2467 Cygni	X		X		[7],[8]
2007.03.19	V2615 Ophiuchi	X		X		[9],[10]
2007.04.17	V5558 Sagittarii	O				[11],[12]
2007.06.15	V390 Normae	O				[13],[14]
2007.08.08	V458 Vulpeculae	O	O	X		[15],[16]
2007.10.08	V598 Puppis	O		O		[17],[18]
2007.11.14	V597 Puppis	O				[19],[20]
2007.12.25	V459 Vulpeculae	O				[21]
2008.03.07	V2468 Cygni	X				[22],[23]
2008.04.01	NR Trianguli Australis	X				[24]
2008.04.10	V2491 Cygni	O	O	O		[25],[26]
2008.04.18	V5579 Sagittarii	O				[27],[28]
2008.05.25	V2670 Ophiuchi	X				[29],[30]
2008.05.31	V2671 Ophiuchi	X				[31],[32]
2008.08.26	V1212 Centauri					[33]
2008.09.01	V466 Andromedae					[34]
2008.09.02	V1309 Scorpii	O				[35]
2008.09.22	V1721 Aquilae					[36]
2008.11.26	V679 Carinae	O				[37]
2008.11.29	V5580 Sagittarii					[38],[39]
2009.02.23	V5582 Sagittarii					[40]
2009.05.08	V1213 Centauri	O				[41],[42]
2009.05.28	V5581 Sagittarii					[43],[44]
2009.08.06	V5583 Sagittarii	O				[45],[46]
2009.08.16	V2672 Ophiuchi	O	O			[47]
2009.10.26	V5584 Sagittarii					[48],[49]
2009.11.08	V496 Scuti					[50]
2009.11.25	KT Eridani	O			O	[51]
2009.12.14	V1722 Aquilae					[52],[53]
2010.01.15	V2673 Ophiuchi					[54]
2010.01.20	V5585 Sagittarii					[55]
2010.01.28	U Scorpii	O	O	O	O	[56]
2010.02.18	V2674 Ophiuchi					[57],[58]
2010.02.20	V1310 Scorpii					[59],[60]
2010.04.23	V5586 Sagittarii					[61],[62]
2010.04.25	V1311 Scorpii					[63]

[a] Red sources are our data sets in this thesis.

[b] Existence of the observations with the *Swift* (*Sw*), the *Suzaku* (*Sz*) the *XMM-Newton* (*Nw*), and the *Chandra* (*Ch*) satellites. O and X mean that the first observation is performed within a year of discovery or not.

[c] [1] Liller et al. (2007b), [2] Samus (2007a), [3] Yamaoka et al. (2007b), [4] Samus (2007b), [5] Yamaoka et al. (2007a), [6] Samus (2007c), [7] Nakano et al. (2007e), [8] Samus (2007d), [9] Nakano et al. (2007c), [10] Samus (2007e), [11] Nakano et al. (2007d), [12] Samus (2007h), [13] Liller et al. (2007a), [14] Kazarovets (2007), [15] Nakano et al. (2007a), [16] Samus (2007f), [17] Read et al. (2007), [18] Samus et al. (2007), [19] Pereira et al. (2007), [20] Samus & Pereira (2007), [21] Nakano et al. (2008g), [22] Nakano et al. (2008c), [23] Samus (2008a), [24] Brown et al. (2008), [25] Nakano et al. (2008a), [26] Samus (2008b), [27] Nakano et al. (2008d), [28] Samus et al. (2008), [29] Nishiyama et al. (2008), [30] Samus (2008d), [31] Nakano et al. (2008e), [32] Samus (2008e), [33] Pojmanski et al. (2008), [34] Yamaoka et al. (2008a), [35] Nakano et al. (2008f), [36] Yamaoka et al. (2008b), [37] Waagen et al. (2008), [38] Liller (2008), [39] Samus & Kazarovets (2008), [40] Sun & Gao (2009), [41] Pojmanski et al. (2009), [42] Kazarovets & Samus (2009), [43] Kinugasa et al. (2009), [44] Samus (2009), [45] Nishiyama et al. (2009b), [46] Kazarovets et al. (2009), [47] Nakano et al. (2009b), [48] Kabashima et al. (2009), [49] Samus & Kazarovets (2009), [50] Nakano et al. (2009a), [51] Yamaoka et al. (2009), [52] Nishiyama et al. (2009a), [53] Kazarovets (2009), [54] Nakano et al. (2010a), [55] Kiyota et al. (2010), [56] Schaefer et al. (2010), [57] Nakano et al. (2010b), [58] Kazarovets & Samus (2010b), [59] Nishiyama et al. (2010a), [60] Kazarovets & Samus (2010a), [61] Nishiyama et al. (2010b), [62] Kazarovets (2010), [63] Nishiyama et al. (2010c)

3.2.2.2 Alert Notice and Monitoring

We describe the most frequently used media for alert notice of discoveries and the initial results of follow-up observations. These media are also used for transient events of astronomical objects besides classical novae.

- **International Astronomical Union (IAU)** : Both the International Astronomical Union Circulars (IAUCs) and the Central Bureau for Astronomical Telegrams (CBATs) are constructed for the dissemination of information on transient astronomical phenomena by the International Astronomical Union (IAU). Names of various celestial objects are assigned in the circulars. The IAUC is available in a series of printed postcard-sized announcements and of electronic forms via e-mail and web page[4], while the CBET is only in electronic forms[5].

- **Astronomer's Telegram (ATel)** : The Astronomer's Telegram (ATel) is constructed for the reporting and commenting on new astronomical observations of transient phenomena. The telegrams are available in the electronic forms via e-mail and web page[6].

- **American Association of Variable Star Observers (AAVSO)** : The American Association of Variable Star Observers (AAVSO) is an international organization for world-wide variable star observers. A lot of information for variable stars are circulated in public mailing lists associated with the AAVSO. Photometry data in optical and IR bands are taken by the observers, which is available in the official web page[7].

- **Variable Star Network (VSNET)** : The Variable Star Network (VSNET) is constructed by the Department of Astronomy, Kyoto University in Japan. Transcendent mailing lists and observed data for variable stars are available in the official web page[8].

- **Variable Star Observers League in Japan (VSOLJ)** : The Variable Star Observers League in Japan (VSOLJ) is constructed by Japanese amateur astronomers. Mailing lists and observed data for variable stars are available in the official web page[9].

- **Quick-look data of the *Swift* satellite** : The *Swift* satellite has an ability to point swiftly and to obtain the data in X-ray energy band (section 4.3). The quick-look data is released within a few hours from each observation. This observatory is suited for monitoring the X-ray behavior of classical novae. Intensive monitoring campaign of classical novae is conducted by the *Swift* Nova-CV group[10] including us. After the discovery of classical novae, snapshot observations are performed depending on the visibility, the optical brightness, and its behaviors.

[4]http://www.cfa.harvard.edu/iau/services/IAUC.html
[5]http://www.cfa.harvard.edu/iau/cbat.html
[6]http://www.astronomerstelegram.org/
[7]http://www.aavso.org/
[8]http://www.kusastro.kyoto-u.ac.jp/vsnet/
[9]http://vsolj.cetus-net.org/
[10]http://www.swift.ac.uk/nova-cv/

3.2.2.3 Target-of-Opportunity X-ray Observations

Many space observatories have quick response capability for transient targets, which is called Target-of-Opportunity (ToO) observations. Anyone can propose ToO programs and are conducted in a day to a week of notice if accepted. In case of *Suzaku*, two types of ToO programs are accepted. One is reserved ToOs, in which targets accepted in the normal proposal review system are observed by being triggered by pre-defined criteria, such as the X-ray count rates in all sky monitor programs. A part of the telescope times available for proposal-based observations is used. The other is non-reserved ToOs, in which observers request a short telescope time in response to unexpected events. A short notice is sent to the telescope managers and a part of the Director's Discretionary time is allocated if the proposal is accepted. Suzaku does not accept reserved ToO proposals for targets without a known position, so we use the non-reserved ToO slots for our observations of classical novae. Observatories normally require powerful motivation and feasibility for ToO proposals because these observations require human resources in operation.

Despite the rapid response and investment of human resources in operation, ToO observations are subject to failure by non-detection of X-rays. For this reason, systematic ToO observations of classical novae have not been made. The launch of the *Swift* satellite changed the situation entirely. It is a mission dedicated to transient events. The policy, the capability to respond rapidly, and the operation flexibility are ideal to make snapshot observations of classical novae repeatedly. In fact, such an effort has been made since the launch of the satellite by a group lead by Prof. Julian P. Osborne[11]. They trigger ToO programs for Galactic novae based on the following criteria: (1) If the maximum V-band magnitude is <5, observations are performed daily from 3 to 10 days after the outburst. (2) If the maximum V-band magnitude is <8, observations are performed around 3 mag below the maximum. (3) If X-rays are detected, subsequent monitoring observations are performed with frequency to depend on observed behavior. (4) If X-rays are not detected, an observation performs again in nebular phase.

We constructed an automated system to derive information necessary to judge whether we should request for a ToO observation with Suzaku. The information includes the visibility, X-ray flux at several energy bands, light curves of X-ray flux and color, and any curious features worthy of follow-up observations with a long exposure with observatory-type missions. Depending on the results, we propose ToO observations to an observatory suitable for the objective of the program. Each observatory has an area of specialty; i.e. the *Suzaku* satellite is suited for high signal-to-noise ratio spectroscopy in a wide X-ray energy band for moderately bright targets, while the *XMM-Newton* satellite for grating spectroscopy with unprecedented energy resolutions for bright targets. Therefore, we generally scheduled observations with *Suzaku* in the early hard X-ray phase and with *XMM-Newton* in the later super-soft X-ray phase, which is often bright enough for grating spectroscopy. As a result, we successfully obtained the data from three recent classical novae; V458 Vul, V2491 Cyg, and V2672 Oph.

[11]See http://www.swift.ac.uk/nova-cv/ for detail.

Chapter 4

Observing Facilities

In this chapter, we review three astronomical satellites used in this thesis; i.e., *Suzaku*, *XMM-Newton*, and *Swift* satellites. Their basic properties, X-ray optics, and the onboard instruments are described.

Contents

4.1 *Suzaku* Satellite

4.1.1 Overview of the mission

The *Suzaku* satellite is a joint mission between Japan and United States for the X-ray astronomy (figure 4.1). It was successfully launched on July 10, 2005 from the Uchinoura Space Center (USC) of the Japan Aerospace Exploration Agency (JAXA). The spacecraft orbits around the Earth once in ∼96 minutes at ∼570 km altitude with an inclination angle of ∼31°. The weight and the length of the spacecraft is ∼1.7 tons and ∼6.5 m, respectively. The electric power is ∼1700 W and ∼660 W for total and scientific instruments, respectively. The pointing accuracy of the spacecraft is ∼0.2′. The fixed solar panels onboard the spacecraft constrain the pointing direction of the telescope to be 65–110° from the Sun. Most targets are occulted by the Earth once in an orbit during the observations. In addition, scientific observations are not possible during the South Atlantic Anomaly (SAA) passages. Therefore, the average observing efficiency is ∼45%. For transient and unpredictable targets, *Suzaku* is prepared to perform ToO observations. The observation is typically conducted within a few days. More details of *Suzaku* can be found in the *Suzaku* Technical Description (*Suzaku* Science Working Group, 2009), the First Step Guide (*Suzaku* Help Desk Team, 2009), and the official web page[1].

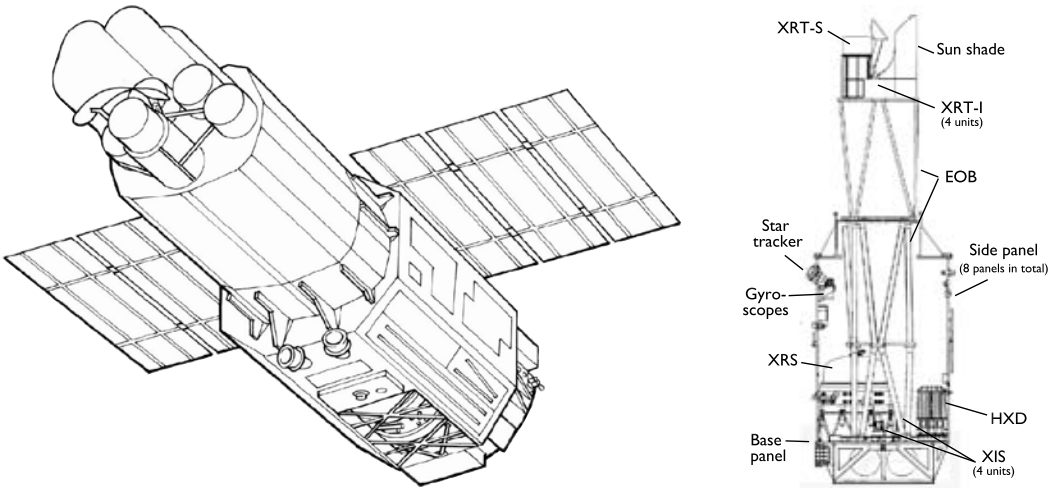

Figure 4.1: Schematic view of the *Suzaku* satellite (Mitsuda et al., 2007).

Suzaku has mirror assemblies and three scientific instruments for X-ray observations (Mitsuda et al., 2007): the X-Ray Spectrometer (XRS; Kelley et al. 2007), the X-ray Imaging Spectrometer (XIS; Koyama et al. 2007), and the Hard X-ray Detector (HXD; Takahashi et al. 2007; Kokubun et al. 2007). The XRS became unoperational by a thermal short between helium and neon tanks one month after the launch. However, simultaneous observations of the XIS and the HXD provide high signal-to-noise ratio (S/N) spectroscopy in broad energy band with a moderate energy resolution and a low background level.

[1]http://www.astro.isas.jaxa.jp/suzaku/

4.1.2 X-ray Optics

4.1.2.1 Mirror Assembly

The mirror assembly of *Suzaku* is composed of five light-weight X-Ray Telescope (XRT; Serlemitsos et al. 2007) modules (figure 4.2). Four of them (XRT-I0, 1, 2, and 3) are dedicated for the four XIS sensors, while the remaining one (XRT-S) for the XRS. All are grazing-incidence mirrors. Each XRT is composed of closely nested 175 thin-foil mirrors, which are conical approximation of the Wolter-I type geometry (figure 4.3). The focal length, the inner and outer diameters of the XRT-I are respectively ∼4.8 m, ∼0.1 m, and ∼0.4 m. A large number of reflectors in each module provides a large collecting efficiency with a moderate imaging capability in the energy range of ∼0.2–12 keV.

Figure 4.2: Picture of an XRT module onboard *Suzaku* (Serlemitsos et al., 2007).

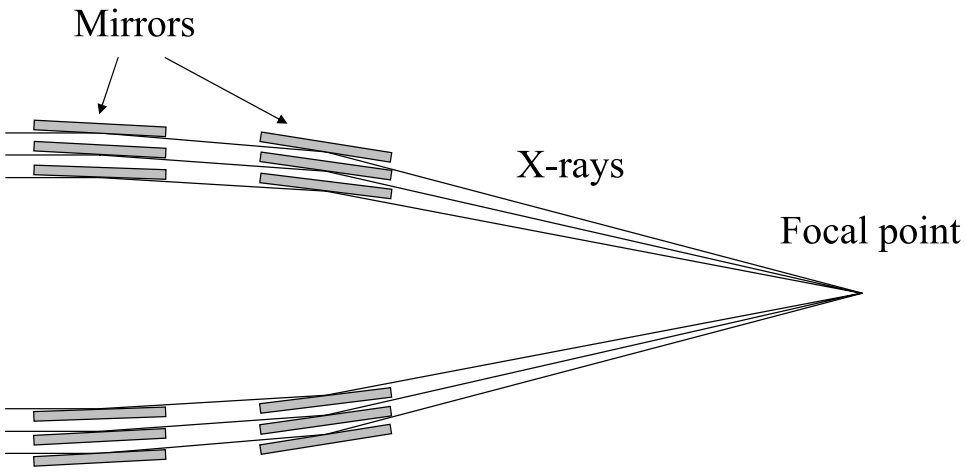

Figure 4.3: Schematic view of the Wolter-I type mirror (Hyodo, 2009)

4.1.2.2 Effective Area

The on-axis effective areas convolved with the transmissions of the thermal shield and the optical blocking filter, and with the detector quantum efficiency are shown in figure 4.4. The effective area decreases as the increasing off-axis angle depending on the photon energy (figure 4.5). The effective areas can be calculated based on Monte Carlo simulation (Ishisaki et al., 2007), and are tabulated as a function of incident X-ray energy, which is called an ancillary response file (ARF).

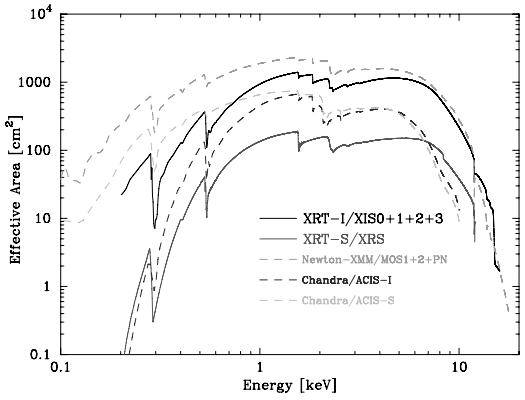

Figure 4.4: Total effective area of the four XRT modules combined with transmissions of the thermal shield and the optical blocking filter, and with the quantum efficiency of the CCD detectors (Serlemitsos et al., 2007). Those of other X-ray missions (*XMM-Newton* and *Chandra*) are shown for comparison.

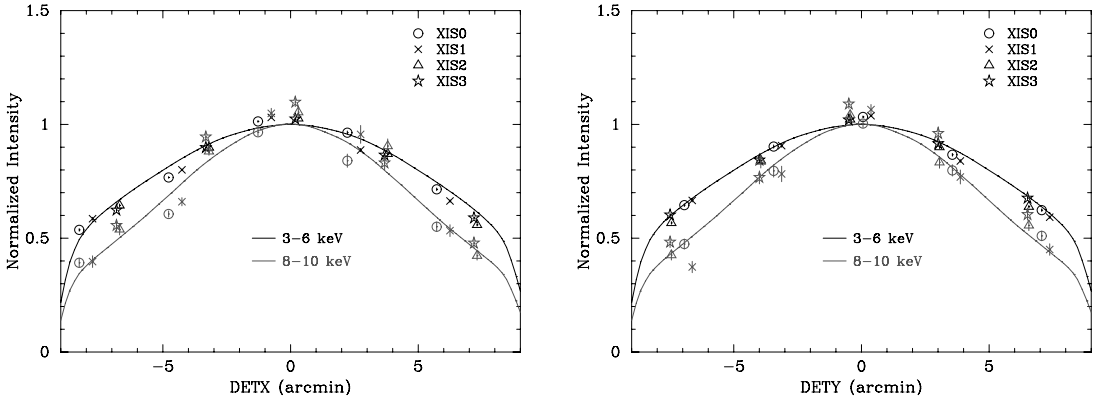

Figure 4.5: Off-axis angle dependence of the XRT modules along DETX (left) and DETY (right) axes in the 3–6 keV (black) and the 8–10 keV (red) energy band (Serlemitsos et al., 2007). Models and in-flight calibration data are shown with the solid lines and symbols, respectively (Serlemitsos et al., 2007).

4.1.2.3 Angular Resolution

Ths point spread function (PSF) is a spatial distribution function over the detector surface by a monochromatic X-ray point-like source at the infinity. In general, the sharpness of images is evaluated by the full width of half maximum (FWHM) and the encircled energy radius of the PSF. The XRT has an energy-independent half-power diameter (HPD) of ∼1′.8–2′.3, which is a diameter of the area including a half of the total flux of the focused X-rays. A typical X-ray image, the PSF, and the encircled energy function (EEF) of each XRT-I module are summarized in figure 4.6.

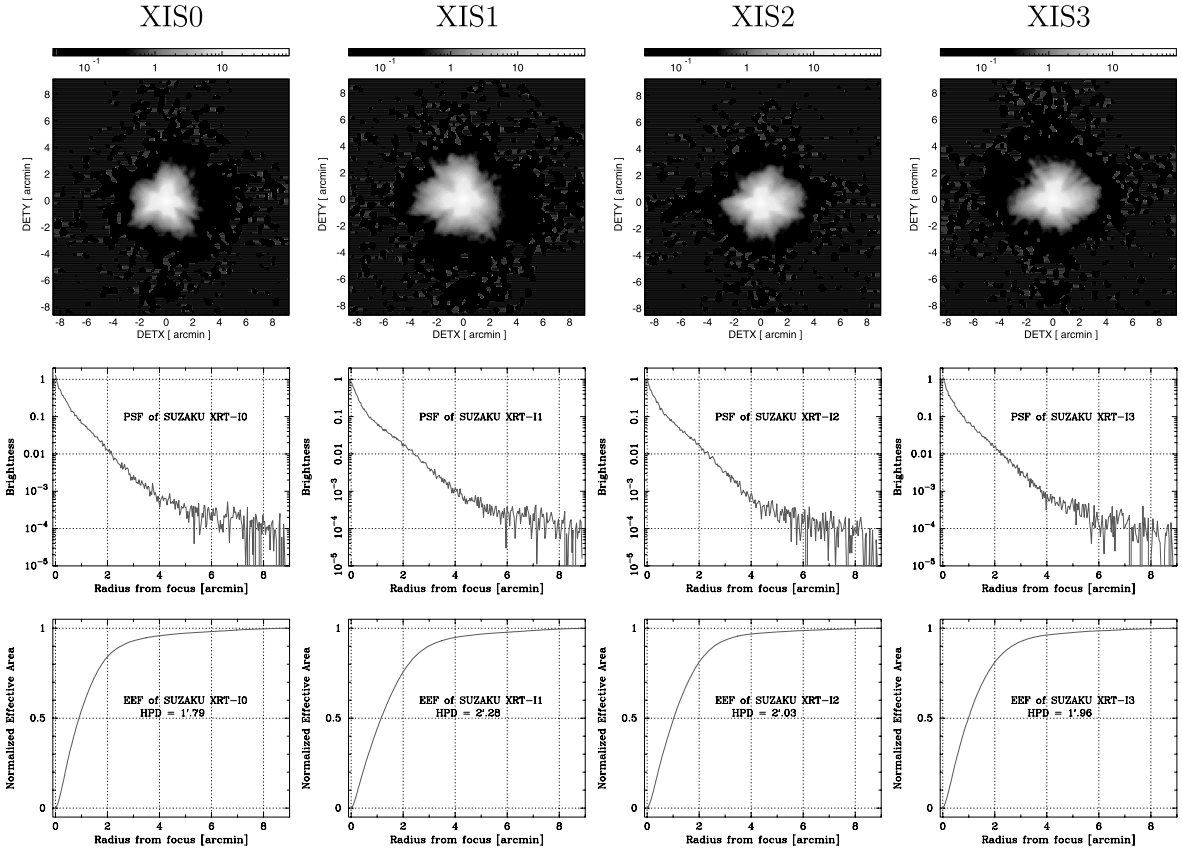

Figure 4.6: Typical X-ray image, the PSF, and the EEF of each XRT-I module at the focal plane (Serlemitsos et al., 2007).

4.1.2.4 Alignment Accuracy

When the satellite points a target for the XIS, its image is found at the focal position on each XIS sensor. The focal positions are located close to the detector center with a deviation of ∼0.3 mm from each other (figure 4.7). On the other hand, the maximum effective area is achieved to observe a target along the optical axis, which are expected for the XRT to scatter in an angular range of ∼1′ (figure 4.7).

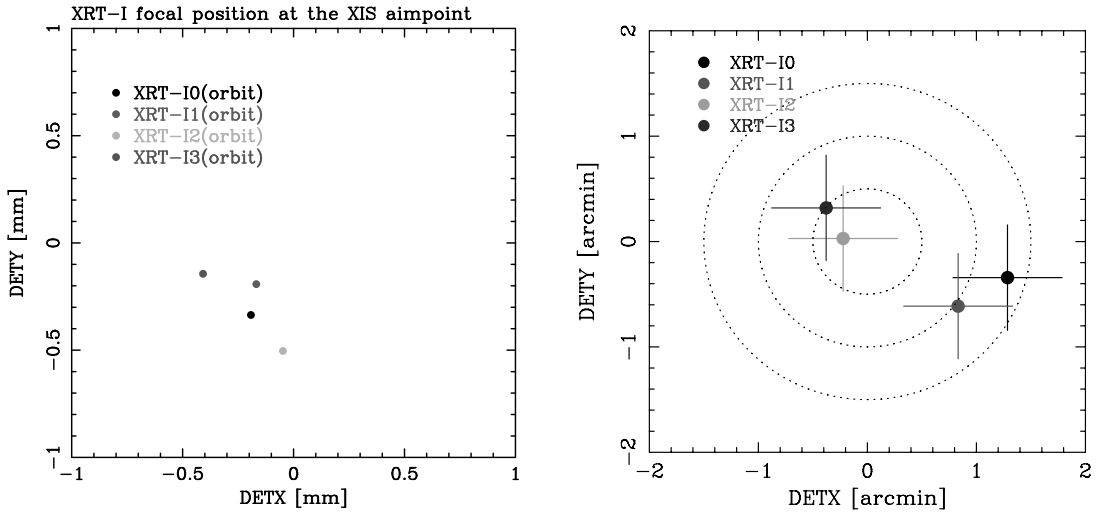

Figure 4.7: Positions of the focus (left) and the optical axis (right) in each XRT-I module. In the right panel, the image on each XIS detector becomes brightest when a target star is placed at the position of the corresponding cross. The dotted circles are drawn every 30′ in radius from the default position for the XIS.

The optical axis of the HXD deviates from that of the XIS by ∼5′ in the negative DETX direction. When the satellite points a target for the XIS, the effective area of the HXD is reduced to ∼93% of the value at its optical axis. In contrast, when the satellite points a target for the HXD, the effective area of the XIS is ∼88% of the value at its optical axis.

4.1.3 Instrument I : X-ray Imaging Spectrometer (XIS)

4.1.3.1 Overview

The XIS is equipped with four silicon X-ray Charge Coupled Devices (CCDs) at the foci of the four XRTs (figure 4.8). The combination of XRTs and XISs provides X-ray imaging-spectroscopic capability with a moderate energy resolution in the ∼0.2–12 keV energy range. The design parameters and the basic performance of the XIS are summarized in table 4.1 at section 4.1.5. More details can be found in e.g., Koyama et al. (2007).

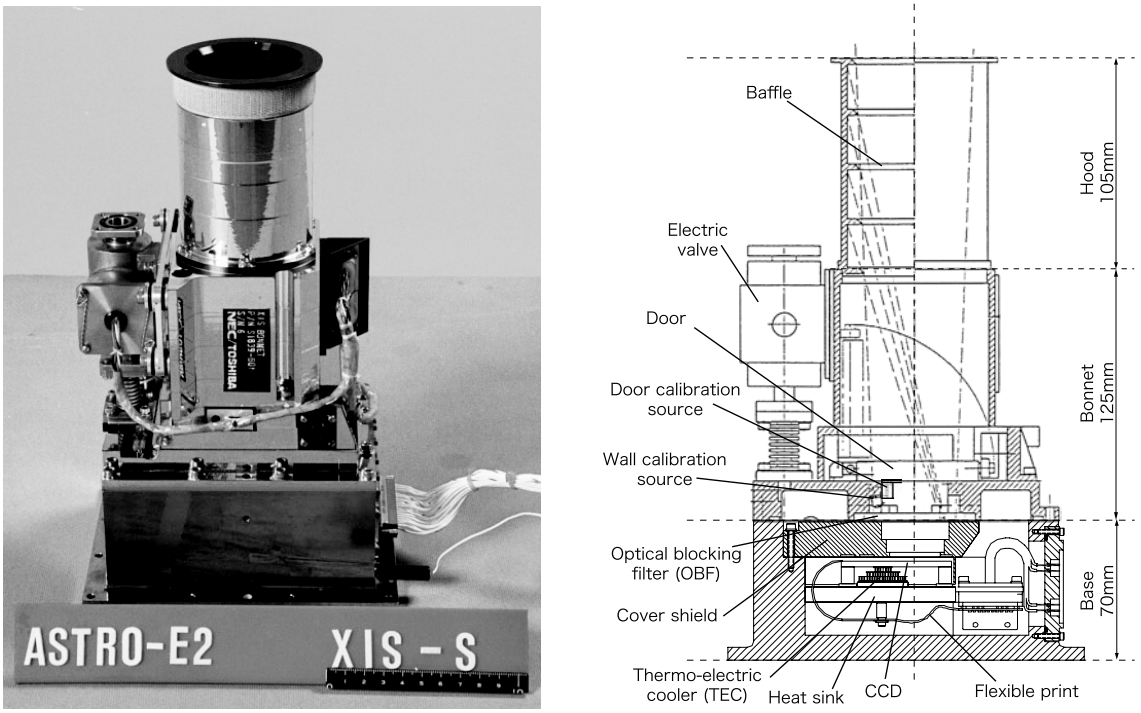

Figure 4.8: Picutre and cross section of the XIS onboard *Suzaku* (Koyama et al., 2007).

4.1.3.2 Systems of CCDs

The X-ray CCDs consist of a gate structure, an insulator, and a depletion layer. The XIS is Metal Oxide Semiconductor (MOS) type CCD, in which the gate structure, the insulator, and the depletion layer consist of Metal (poli-Silicon), Oxide (SiO_2), and Silicon, respectively. Incident photons are converted into an electron cloud by the photoelectric effect in the depletion layer. The electron cloud on each pixel are transferred into the output transistor of the gate structure. The amount of electrons is proportional to the energies of the incoming photons. X-ray CCDs are categorized as the front-illuminated (FI) or the back-illuminated (BI) chips based on the direction of incoming photons (figure 4.9). For the X-ray observations, Optical and UV photons are reduced by the Optical Blocking Filters (OBFs) in front of the CCDs. The charges are transferred from an imaging area to a framestore area after the exposure, and then read out into a serial register in the normal operation.

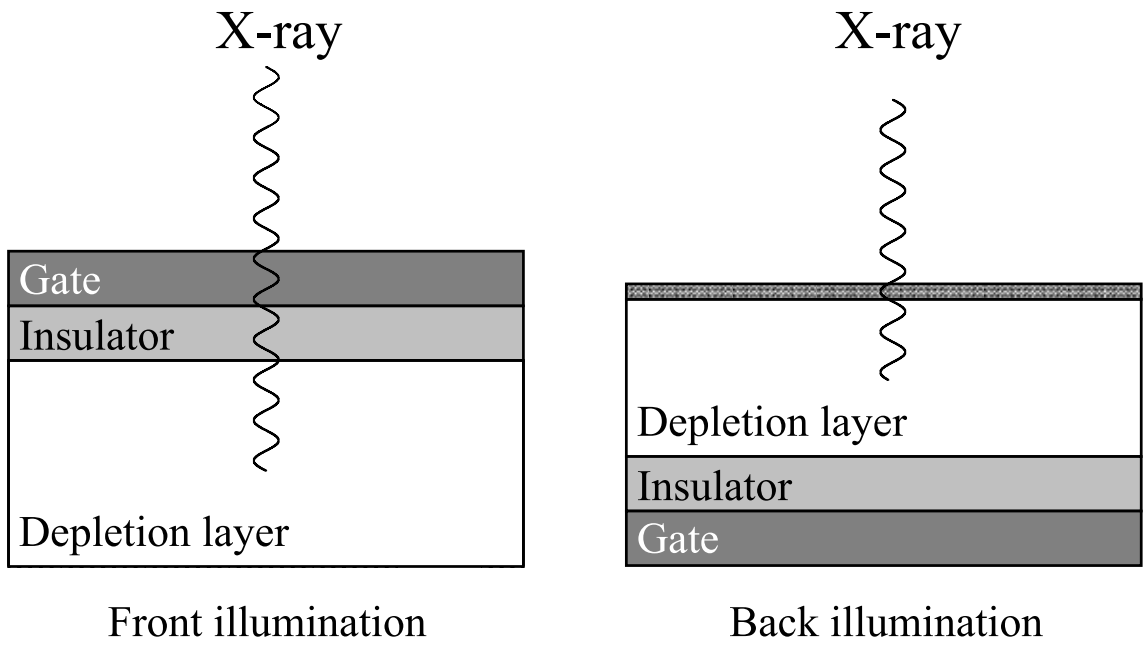

Figure 4.9: Schematic view of the FI (left) and BI (right) CCDs (Hyodo, 2009).

4.1.3.3 Configuration

A schematic view of the CCD chip is shown in figure 4.10. Each XIS sensor has a single CCD chip with the imaging area of 1024×1024 pixels, which covers a 18′×18′ field of view (FoV) at the focal plane of the XRT. The CCD chip consists of four segments (A, B, C and D) with 256×1024 pixels each of which has a readout node. Two radioactive sources of ^{55}Fe illuminate two corners of each CCD for in-flight calibration.

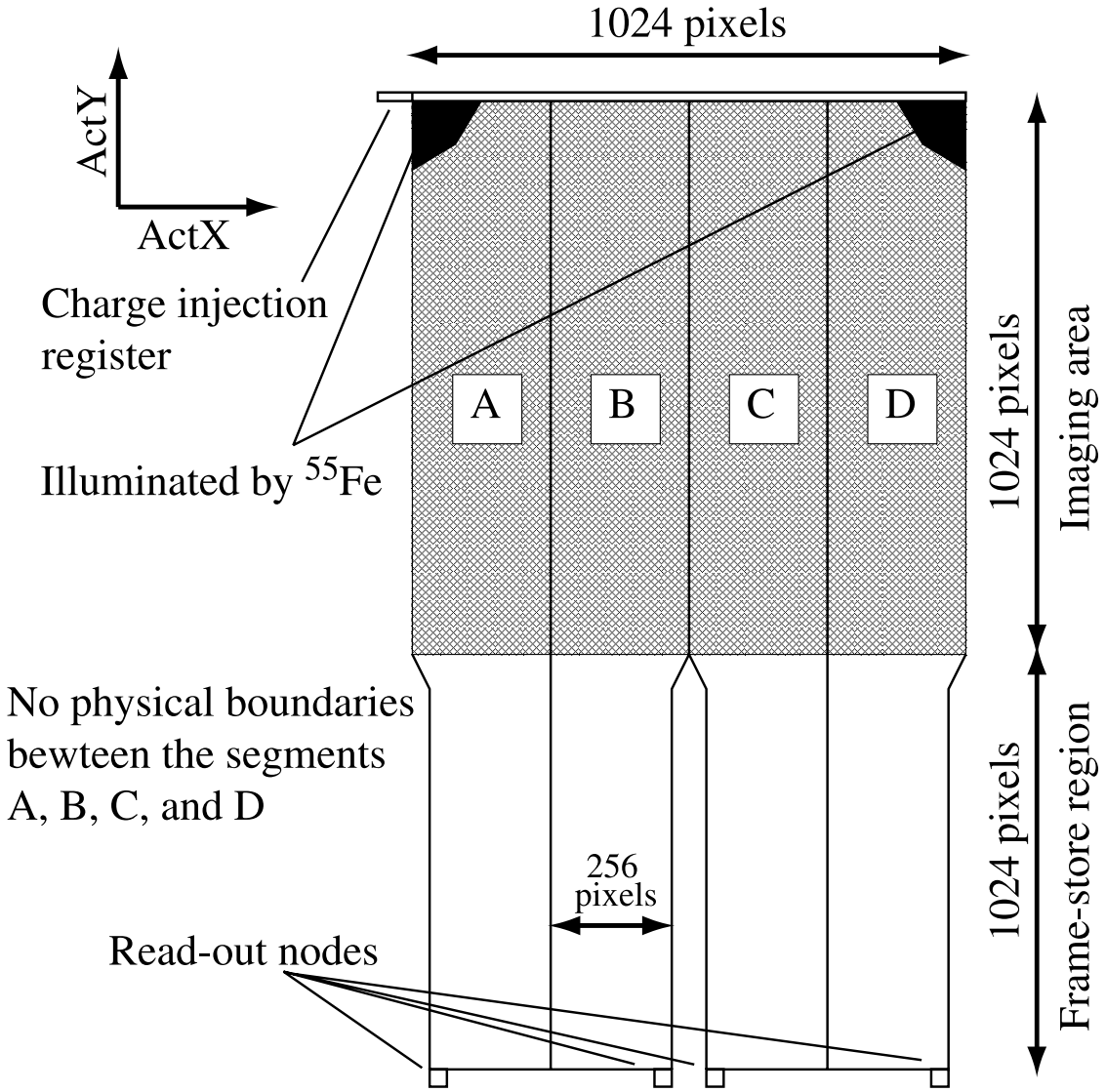

Figure 4.10: Schematic view of a CCD chip in the XIS (Koyama et al., 2007).

4.1.3.4 Effective Energy Range

The effective energy range and the quantum efficiency highly depend on the structure of the CCD chips. Three of the four XIS sensors (XIS0, 2, and 3) are front-illuminated (FI) CCDs sensitive in the 0.4–12 keV energy range, and the remaining one (XIS1) is a back-illuminated (BI) CCD sensitive in the 0.2–12 keV energy range. The FI CCDs detect photons that penetrate the gate structure, providing a low background observations. In contrast, the BI CCD detect photons that comes from a back side without the gate structures, providing a high quantum efficiency for low energy photons. The quantum efficiency is calibrated for each sensor (figure 4.11), which is used to generate the redistribution matrix function (RMF), a conversion table between channel and energy (Ishisaki et al., 2007).

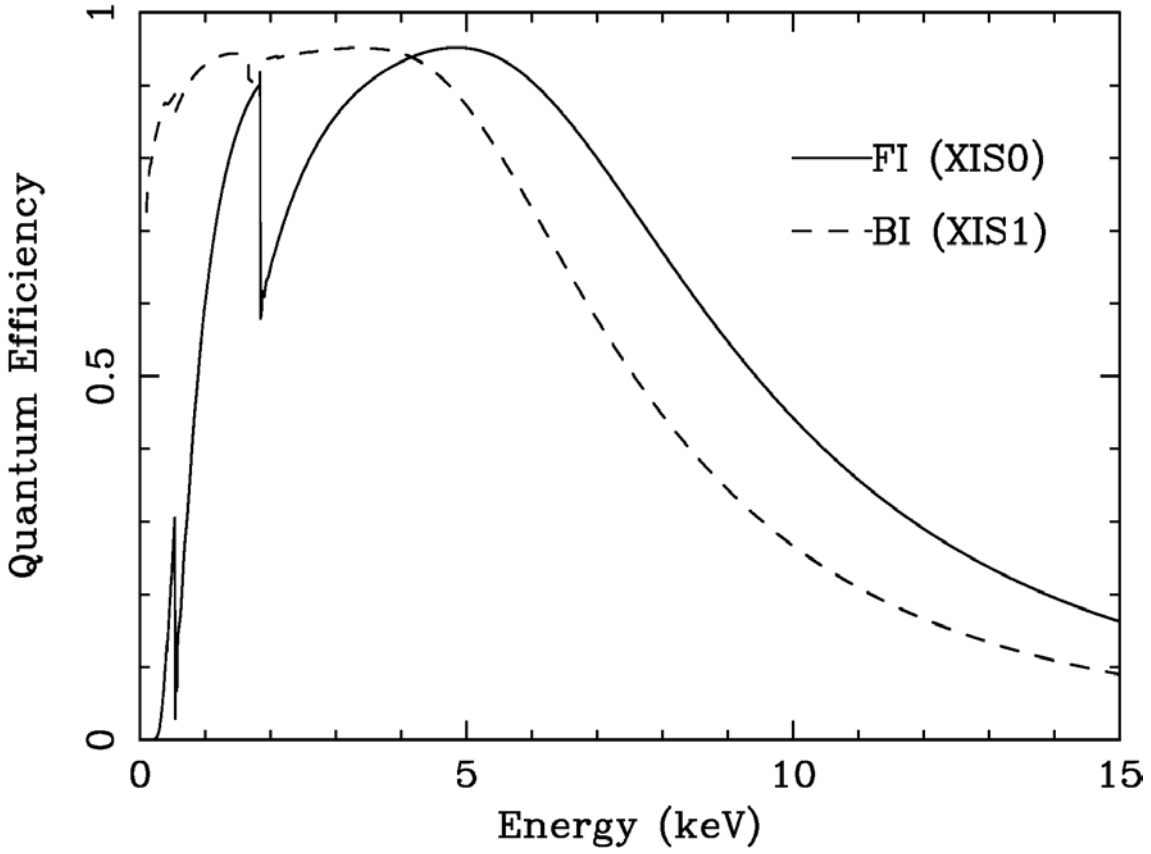

Figure 4.11: Quantum efficiency of the CCD chips in the XIS as a function of incident photon energy (Koyama et al., 2007). The FI (XIS0) and the BI (XIS1) CCDs are indicated with the solid and dashed lines, respectively.

4.1.3.5 Energy Resolution and Scale

The performance of the CCD chips is gradually degraded due to charge traps in pixels damaged by cosmic-ray radiation (e.g., Nakajima et al. 2008). Therefore, a spaced-row charge injection (SCI) technique was introduced in the XIS (Uchiyama et al., 2009). In this technique, sacrificial electrons are injected in the imaging area to fill the charge traps while observing. It prevents charges by X-rays from being captured by the traps. The SCI is applied for almost all observations since October 2006. The charge transfer efficiency (CTE) and the energy resolution were rejuvenated. The degradation of the energy resolution is shown in figure 4.12. The absolute energy scale is accurate to $\lesssim$0.2% and $\lesssim$5 eV at 5.9 keV and below 1 keV, respectively. They are also included in the RMF generator for the XIS (Ishisaki et al., 2007).

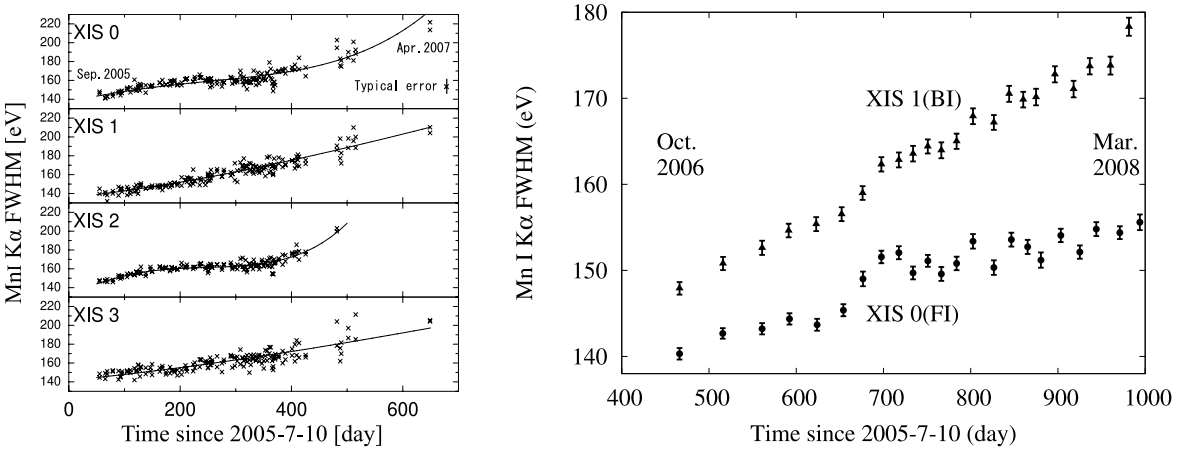

Figure 4.12: Trend of the energy resolution in the XIS with (left; Ozawa et al. 2009) and without (right; Uchiyama et al. 2009) the SCI technique.

4.1.3.6 Background Events

Two major sources of background for the XIS are the non X-ray background (NXB) and the cosmic X-ray background (CXB). The NXB is caused by interactions between cosmic-ray particles and the satellite. The intensity of the NXB depends on the strength of the geomagnetic field at the position of the spacecraft, which is called the cut-off rigidity (COR). A typical NXB spectrum of each XIS sensor is shown in figure 4.13, which is accumulated from observations pointed toward the night-Earth. In contrast, the intensity of the CXB depends on the target positions. In our observations of classical novae, the background intensity can be estimated from off-source regions within the same CCD.

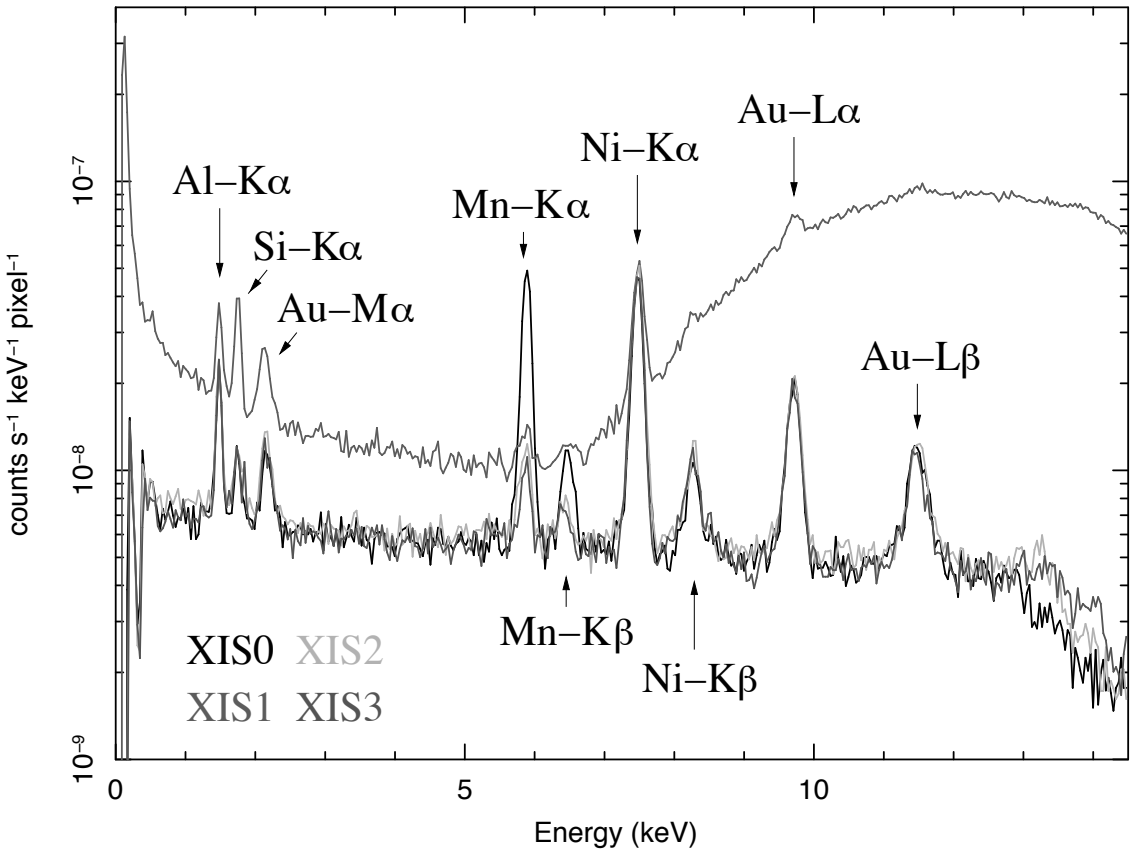

Figure 4.13: Typical NXB spectra of the XIS (*Suzaku* Science Working Group, 2009).

4.1.3.7 Contamination

The effective area below ∼2 keV degraded with unexpected contamination accumulated on the OBF after the launch (Koyama et al., 2007). The degradation is characterized by the additional absorption of mainly carbon, oxygen and hydrogen materials, which presumably stem from outgassing in the spacecraft. The time evolution of the contamination is estimated from the observations of stable X-ray sources (figure 4.14). The thickness of the absorber is different for different XIS sensors, and it decreases as the increasing off-axis angle. The effect of the contamination material are included in the ARF generator for the XIS (Ishisaki et al., 2007).

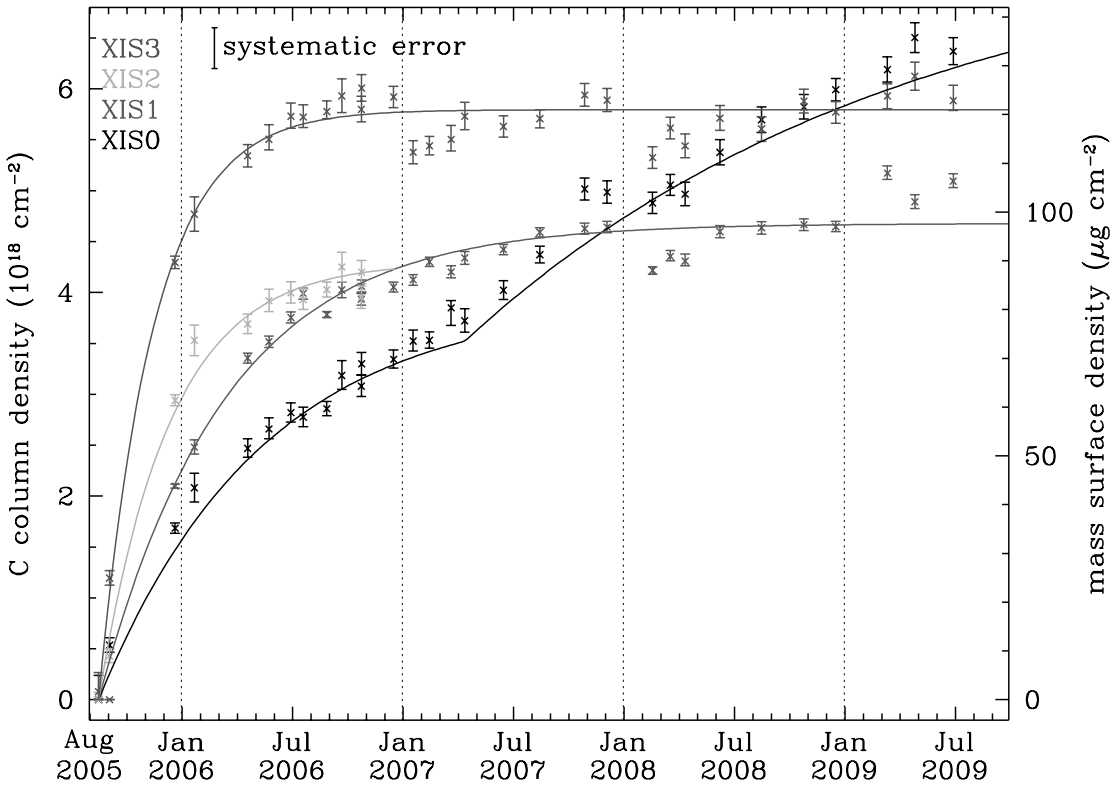

Figure 4.14: Evolution of the on-axis contamination with an empirical model assuming the constant chemical composition. Crosses indicate the column density of the Carbon estimated from regular observations for in-flight calibrations. Solid lines indicate the best fit empirical model to the time evolution of the contamination for each sensor.

4.1.3.8 Photon Pile-Up

The XIS is a position-sensitive integrating instrument. If more than one photon is injected in the same CCD pixel during the integration time, electron signals cannot be correctly detected as independent photons. Both images and spectra are distorted for the effect. This is called a photon pile-up, which is a big problem for the integrating instrument particularly in observations of bright targets. A pile-up fraction highly depends on a source flux, the PSF of the telescope, and a readout method of the CCD detector. In the normal mode of the XIS, the photon pile-up with 8 s integration time is negligible for objects with a lower flux than $\sim$12 count s^{-1}.

4.1.3.9 Anomalies

Sudden anomalies of XIS2 and XIS0 were respectively found in November 2006 and June 2009. The images of XIS2 were flooded with a large amount of charges over a wide region. Thus, XIS2 has not been used for scientific observations since this anomaly. In contrast, the anomaly of XIS0 is found in a small part of an off-axis area. Therefore, XIS0 is still functional for scientific observations. Although the cause of the anomalies is not well-understood, micro-meteoroid impacts are suspected. The decrease in the effective area due to decreased imaging area is included in the ARF generator for the XIS (Ishisaki et al., 2007).

4.1.4 Instrument II : Hard X-ray Detector (HXD)

4.1.4.1 Overview

The HXD is a non-imaging collimated instrument sensitive in the ∼10–600 keV energy range (figure 4.15). The sensor consists of 16 well-type main units and surrounding 20 scintillators for active anti-coincidence shielding. Thanks to the active anti-coincidence shields, a narrow field of view, and stable as well as low background environment in a low Earth orbit, unprecedented sensitivity is archived in the hard X-ray band. The design parameters and the basic performance are summarized in table 4.1 at section 4.1.5. More details can be found in e.g., Takahashi et al. (2007) and Kokubun et al. (2007).

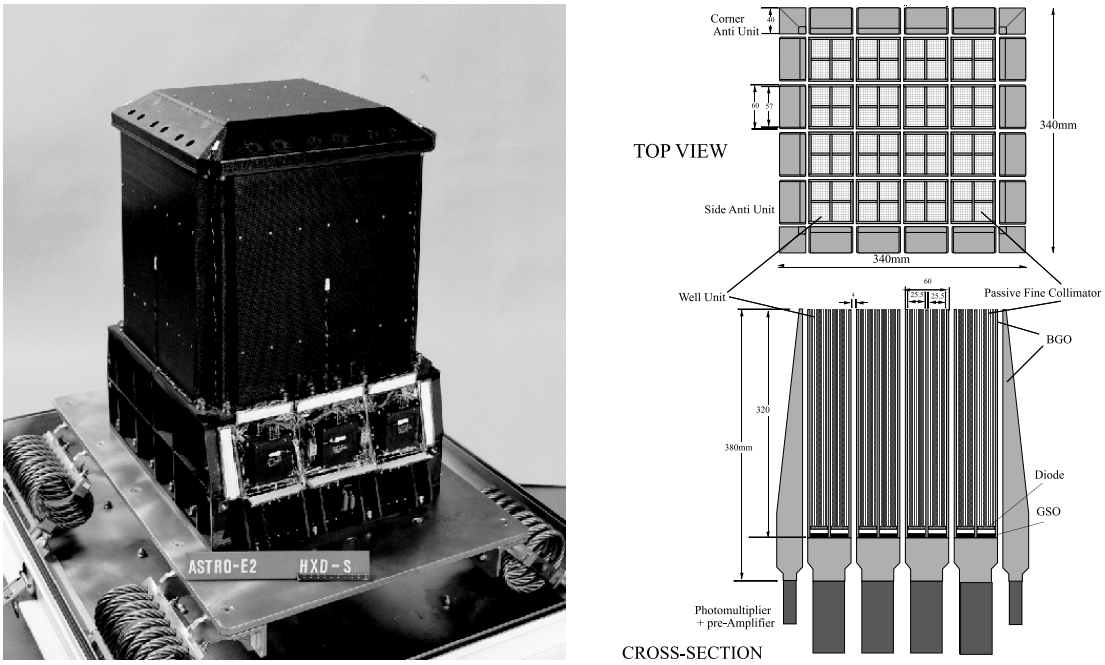

Figure 4.15: Picture and cross section of the HXD onboard *Suzaku* (Takahashi et al., 2007).

4.1.4.2 Configuration

The well-type units and the anti-coincidence shields have a compound-eye configuration to increase an effective area. The array configuration of the sensor units is shown in figure 4.16.

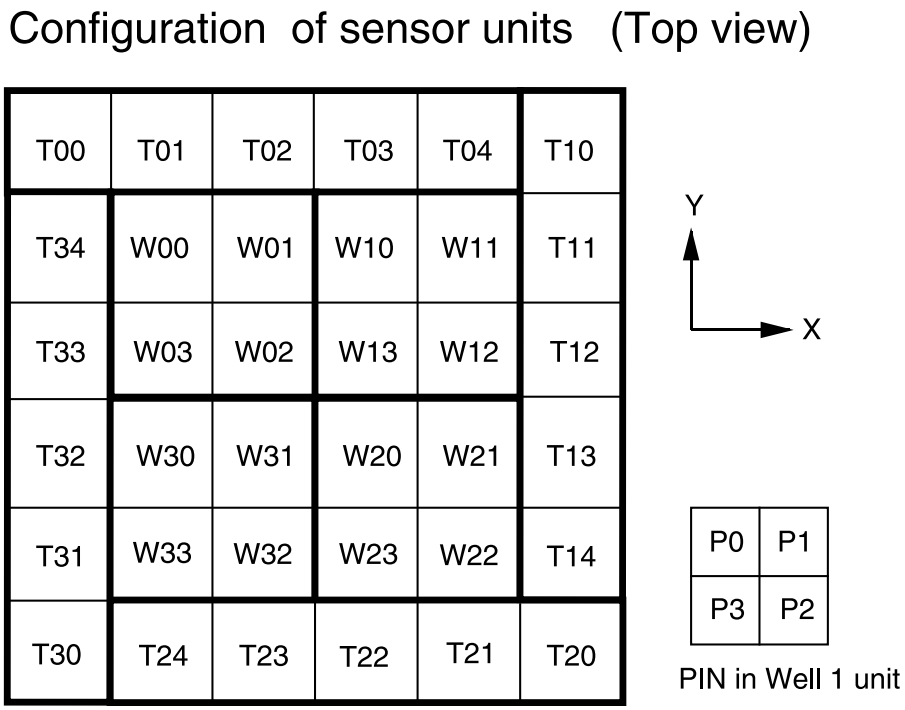

Figure 4.16: Array configuration and numbering of the sensor units in the HXD (Takahashi et al., 2007). The 16 well-type units and the surrounding 20 scintillators are identified from W00 to W33 and from T00 to T34, respectively.

Each well-type unit consists of two independent sensors: the gadolinium silicate (GSO) / bismuth germanate (BGO) phoswich counters and the PIN silicon diodes. A schematic view of the well-type unit is shown in figure 4.17. Each detector forms a 2×2 array with a layered structure at the bottom of the well. The lower energy response is provided by the PIN, which is located in front of the GSO and the BGO scintillators. The PIN has sensitivity in the ∼10–70 keV energy range, and gradually becomes transparent to higher energy photons. The transparent photons are detected with the GSO scintillators located in the middle layer, which has sensitivity in the ∼40–600 keV energy range. The bottom layer is the BGO scintillators, which work as a veto counter for both PIN and GSO detectors. Additionally, in order to reduce contamination from irrelevant emission, passive fine collimators are inserted in each well-type unit above the PIN. In the following section, we mainly concentrate on the PIN detector, which are used for our studies of classical novae.

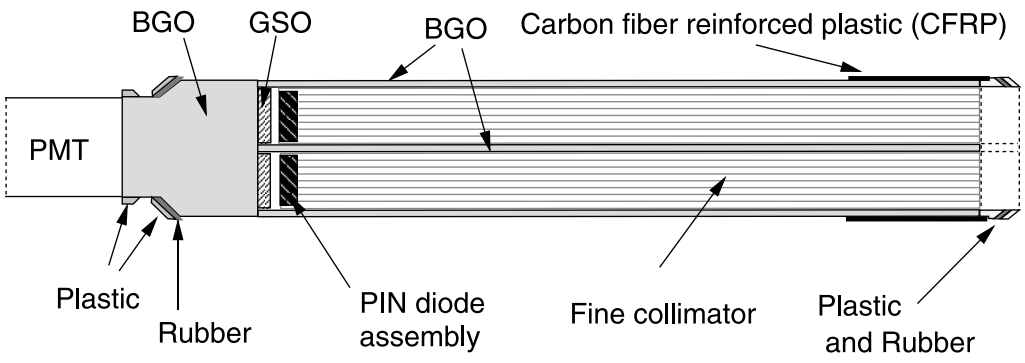

Figure 4.17: Schematic view of the well-type unit of HXD (Takahashi et al., 2007).

4.1.4.3 Effective Area

The total effective area is shown in figure 4.18. The values are convolved with the detector responses and with the photon absorption of the layered materials in front of the devices. Both the PIN and the GSO scintillators cover the ∼40–70 keV energy range.

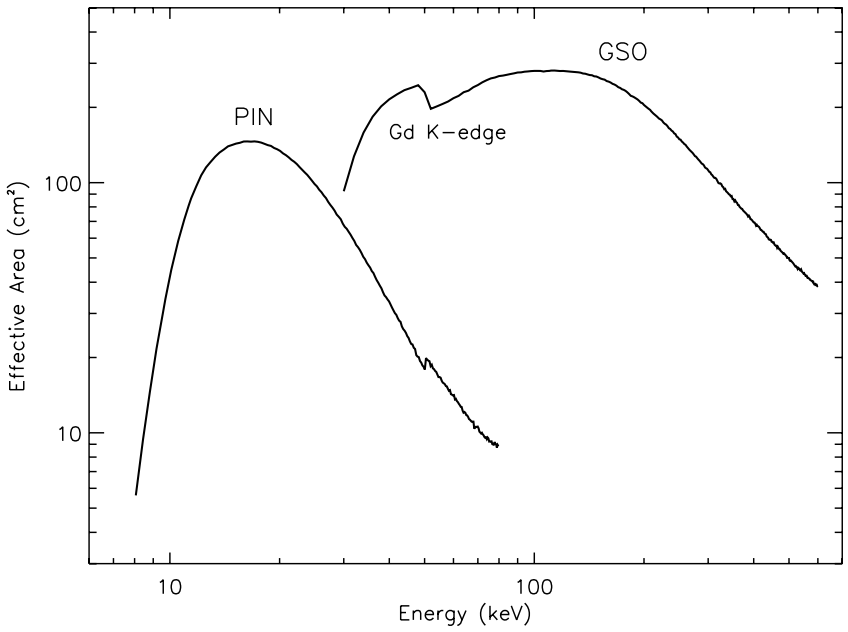

Figure 4.18: Total effective areas of the PIN and the GSO scintillators. The values are convolved with the detector responses and with the photon absorption of the layered materials in front of the devices (Takahashi et al., 2007).

4.1.4.4 Angular Resolution

With a combination of the surrounding BGO veto counters and the passive fine collimators, the angular response and the FoV highly depend on incoming photon energies. The low energy photons below ∼100 keV are restricted to a ∼34′×34′ in FWHM or ∼70′×70′ in full width at zero intensity (FWZI). As high energy photons are transparent to the fine collimators, the photons above ∼100 keV are restricted to a ∼4.5°×4.5° in FWHM only with the BGO shields.

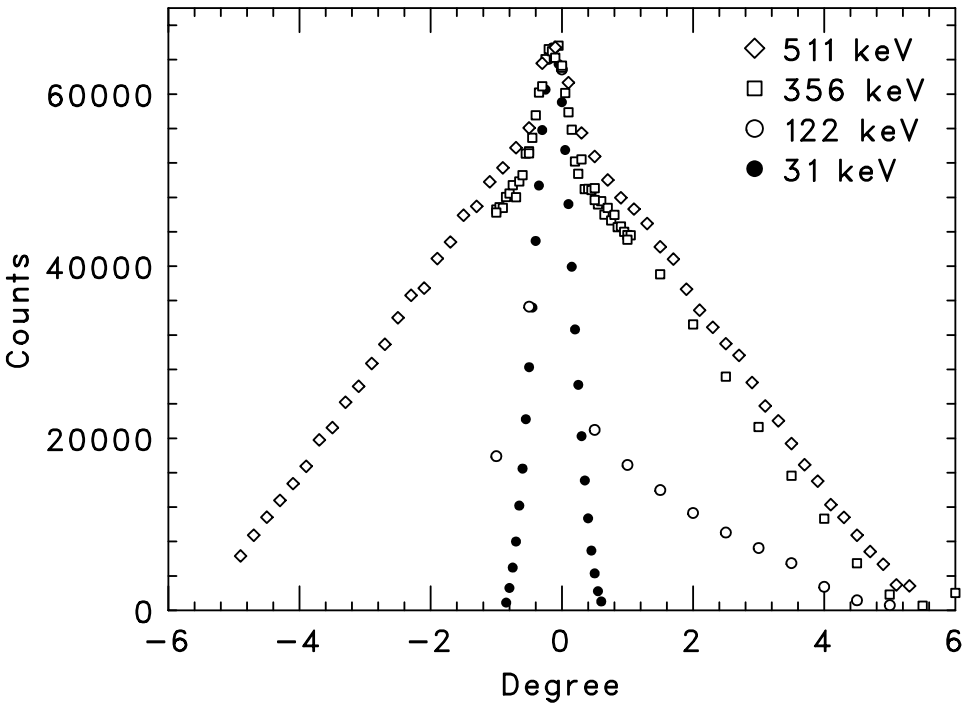

Figure 4.19: Angular responses of the well-type units measured with radio isotope sources at a finite distance (Takahashi et al., 2007).

4.1.4.5 Background Events

The HXD is designed to achieve an extremely low background level in operation. Most of the NXB for the PIN is considered to be caused by interactions between cosmic-ray particles and surrounding materials. A typical NXB of the PIN is shown in figure 4.20. No long-term variation of the NXB was confirmed during the first three years in operation. However, a significant short-term variability is seen in the NXB, which highly depends on the COR (figure 4.21).

As the HXD is a non-imaging instrument, the limiting sensitivity heavily depends on the reproducibility of background estimation. The background spectrum can be estimated from separate off-source observations or models. The NXB model spectra of the PIN are primarily based on the count rate of high-energy charged particles, which can be directly estimated

with the anti-correlation between the NXB and the COR. As an interaction of cosmic-ray particles causes large signals in the PIN, the upper discriminator (UD) is activated in the analog electronics. The background count rates can be generally estimated by the event rate above the UD. The NXB models are produced for each observation by the *Suzaku* HXD team. A reproducibility is better than 5% at a 90% confidence level. More details and the latest background models are available at the official webpage[2].

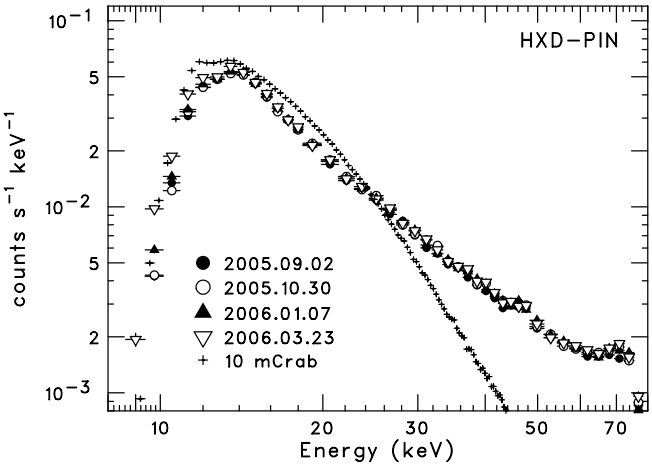

Figure 4.20: Comparison of the NXB spectra during the first three years (Kokubun et al., 2007).

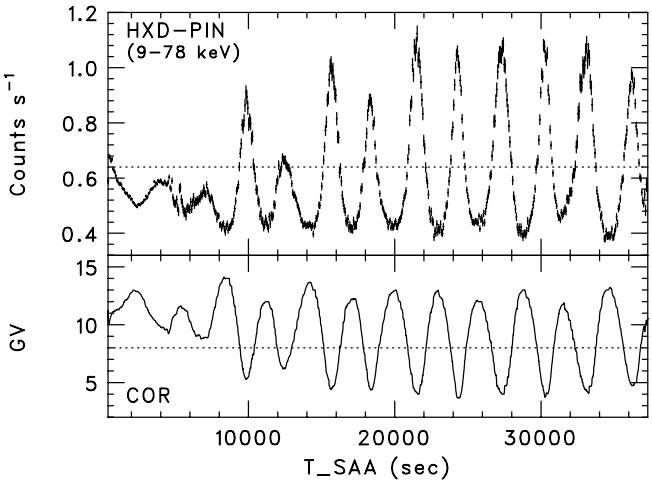

Figure 4.21: Short-term variability of the NXB (Kokubun et al., 2007). The upper panel shows a light curve of the NXB folded with an elapsed time from the SAA in the 9–78 keV energy range. The lower panel shows the corresponding COR values.

[2]http://www.astro.isas.jaxa.jp/suzaku/analysis/hxd/pinnxb/

4.1.5 Summary of the mission

The design parameters and the orbital information of the *Suzaku* spacecraft are summarized in table 4.1.

Table 4.1: Details of the *Suzaku* mission (*Suzaku* Science Working Group, 2009).

	Parameter	Value
Spacecraft	Orbit apogee	$\sim$568 km
	Orbital period	$\sim$96 m
	Observing efficiency	$\sim$45 %
XRT-I[a]	Focal length	4.75 m
	Substrate	Aluminium (152 μm)
	Reflector	Gold ($\lesssim$0.1 μm)
	Number of reflectors	175
	Inner diameter	118 mm
	Outer diameter	399 mm
	Incident angle	$0.^{\circ}18$–$0.^{\circ}60$
	Effective area (1.5 keV)	440 cm^2
	Effective area (8 keV)	250 cm^2
	Plate scale	$0.'724$ mm^{-1}
	FoV (1.5 keV)	$\sim17'$
	FoV (8 keV)	$\sim13'$
	Angular resolution	$\sim2'$ (HPD)
XIS[a]	FoV	$17.8'\times17.8'$
	Bandpass	0.2–12 keV
	Pixel grid	1024$\times$1024
	Energy resolution (6 keV)	$\sim$130 eV (FWHM)
	Effective area (1.5 keV)	$\sim$340 cm^2 (FI), $\sim$390 cm^2 (BI)
	Effective area (8 keV)	$\sim$150 cm^2 (FI), $\sim$100 cm^2 (BI)
	Timing resolution	8 s
HXD[a]	FoV ($\gtrsim$100 keV)	$4.5^{\circ}\times4.5^{\circ}$
	FoV ($\lesssim$100 keV)	$34'\times34'$
	Bandpass (PIN)	10–70 keV
	Bandpass (GSO)	40–600 keV
	Energy resolution (PIN)	$\sim$4.0 keV (FWHM)
	Energy resolution (GSO)	$\sim7.6/\sqrt{E_{\mathrm{MeV}}}$ % (FWHM)
	Effective area (20 keV)	$\sim$160 cm^2
	Effective area (100 keV)	$\sim$260 cm^2
	Timing resolution	61 μs

[a] Details of the XRT-I, the XIS, and the HXD are respectively described in section 4.1.2, 4.1.3, and 4.1.4.

4.2 *XMM-Newton* Satellite

4.2.1 Overview of the mission

The *XMM-Newton* satellite is the second cornerstone mission of the Horizon 2000 Science Programme by the European Space Agency (ESA). It was successfully launched on December 10, 1999. The spacecraft (figure 4.22) circulates around the Earth once in ∼48 hours in an elliptical orbit with the apogee and the perigee distances of ∼107000 km and ∼27000 km, respectively. It is three-axis stabilized and the absolute pointing accuracy is ∼1″. *XMM-Newton* has an ability to make long uninterrupted exposures with highly sensitive observations. For transient and unpredictable targets, *XMM-Newton* is prepared to perform ToO observations. The observation is typically conducted within a few hours to a few days. More details of the *XMM-Newton* mission can be found in the *XMM-Newton* Technical Description (*XMM-Newton* Science Operations Centre User Support Team, 2010), the Users Handbook (*XMM-Newton* Community Support Team, 2010), and the official web page[3].

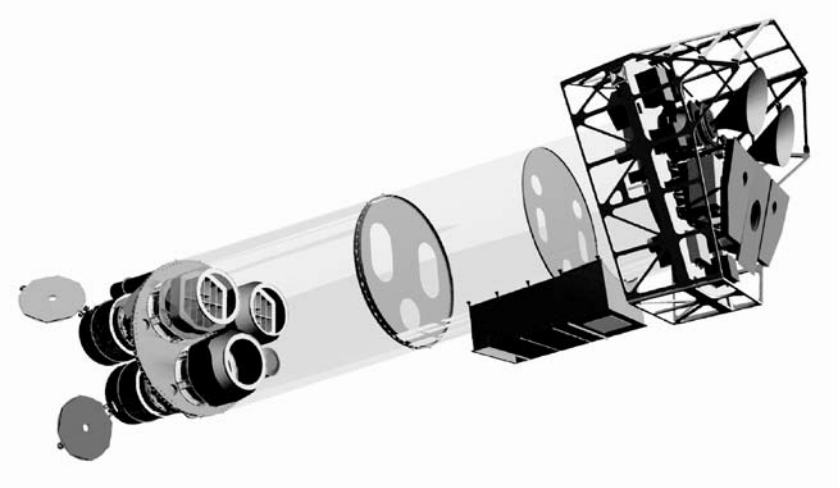

Figure 4.22: Schematic view of the *XMM-Newton* satellite (*XMM-Newton* Community Support Team, 2010).

XMM-Newton has three scientific instruments in operation (Jansen et al., 2001): the European Photon Imaging Camera (EPIC; Strüder et al. 2001; Turner et al. 2001), the Reflection Grating Spectrometer (RGS; den Herder et al. 2001), and the Optical Monitor (OM; Mason et al. 2001). The EPIC consists of two types of CCD arrays (EPIC-MOS and EPIC-PN), providing X-ray imaging-spectroscopic capability with unprecedentedly large effective areas. The RGS consists of two dispersive X-ray spectrometers, providing an extremely high spectral resolution. The OM consists of a modified Ritchey-Chretien telescope and a CCD detector, providing multiwavelength observations in UV and Optical bands. In the following section, we concentrate on the EPIC-PN module and its mirror systems, which are used in this thesis.

[3]http://xmm.esac.esa.int/

4.2.2 X-ray Optics

4.2.2.1 Mirror Assembly

The mirror assembly of *XMM-Newton* consists of three X-ray telescope modules (figure 4.23 and 4.24). Each telescope is composed of closely nested 58 grazing-incidence Wolter-I type mirrors, which are in a coaxial configuration. The focal length is 7.5 m, and the diameter of the largest mirror is 0.7 m. A moderate number of reflectors in each module provides a large effective area with a good imaging capability in the ∼0.2–15 keV energy range.

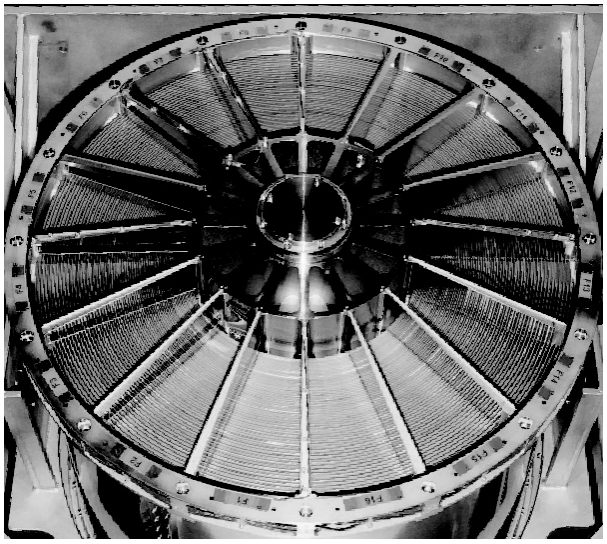

Figure 4.23: Picture of an X-ray telescope onboard *XMM-Newton*[3].

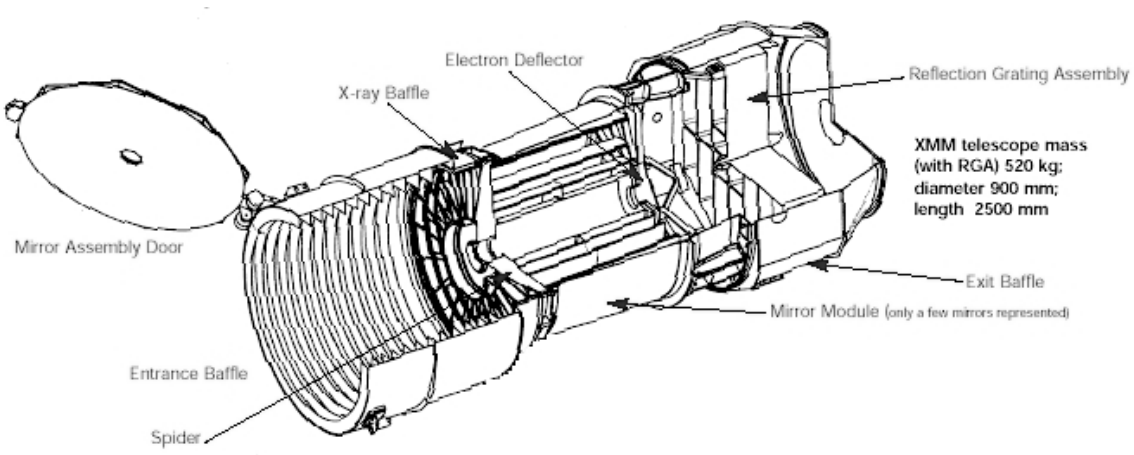

Figure 4.24: Shematic view of an X-ray telescope onboard *XMM-Newton*[3].

Two of the mirrors are designed for the two pairs of the EPIC-MOS and the RGS, in which the zero'th order X-rays are focused on the EPIC-MOS for non-dispersive spectroscopy and higher order X-rays on the RGS for dispersive spectroscopy using the reflection grating assemblies. Therefore, incoming photons are divided into ∼44 % and ∼40 % for the EPIC-MOS and the RGS, respectively. The remaining one is designed for only the EPIC-PN without a grating assembly, in which the maximum effective area is provided for the focal CCD detector. Schematic views of the two X-ray mirror systems are shown in figure 4.25.

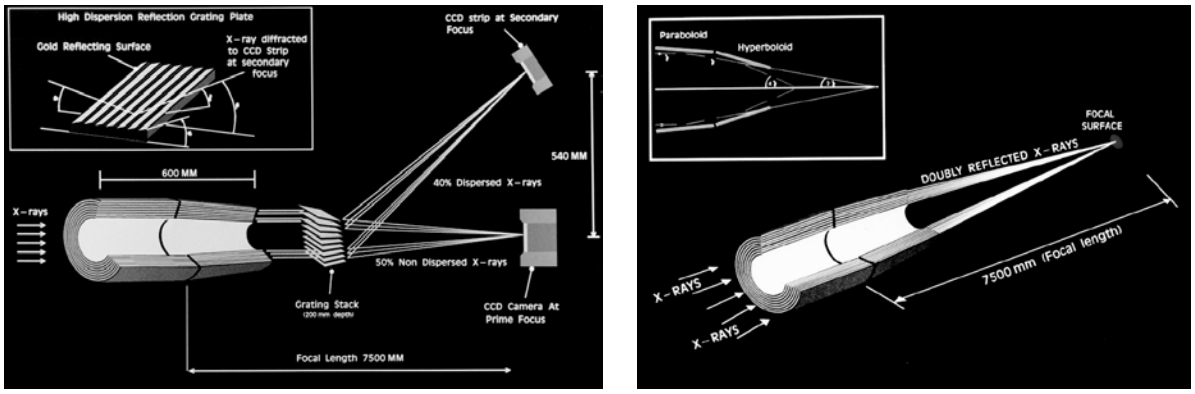

Figure 4.25: Schematic view of the mirror systems onboard *XMM-Newton* (*XMM-Newton* Community Support Team, 2010).

4.2.2.2 Optical Blocking Filter

For the EPIC instruments, three types of OBFs are installed for suppressing the optical contamination from the targets. The thick filter provides a capability of minimizing the optical contamination instead of a small effective area in the soft X-ray band. This is able to suppress efficiently the optical contamination for a point-like target with the V-band magnitudes of 1–4 mag and −2–1 mag for the EPIC-MOS and the EPIC-PN. The medium filter is less efficient than the thick filter about 10^3, which is able to suppress the optical contamination for a point-like target with the V-band magnitudes of 6–9 mag. The remaining one, the thin filter, is used for the targets with the V-band magnitudes of >12 mag.

4.2.2.3 Effective Area

The on-axis effective areas for the EPIC-PN convolved with the responses of each OBF and focal detectors are shown in figure 4.26. The effective area decreases as the increasing off-axis angle depending on the incoming photon energy (figure 4.27).

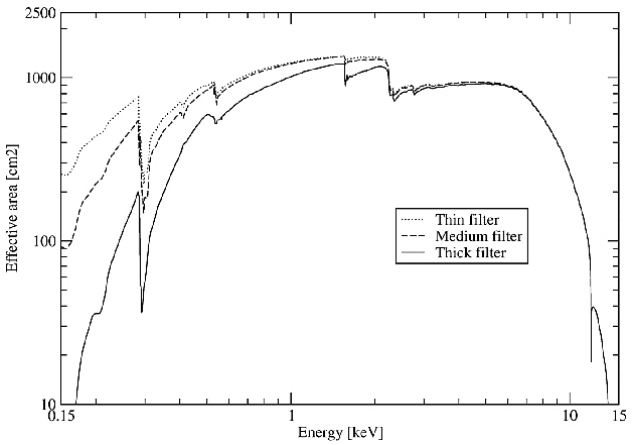

Figure 4.26: Effective areas for the EPIC-PN with each OBF (*XMM-Newton* Community Support Team, 2010).

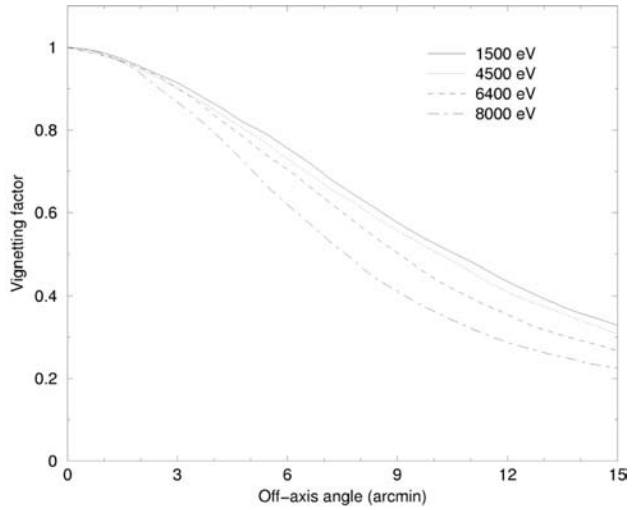

Figure 4.27: Off-axis angle dependence of the effective area with respect to the value at the on-axis for the EPIC-PN (*XMM-Newton* Community Support Team, 2010).

4.2.2.4 Angular Resolution

The mirror system for the EPIC-PN has a HPD of $\sim 15''$ at the optical axis. The PSF of the mirror system is basically approximated by a King function. The EEF of the mirror system is shown in figure 4.28.

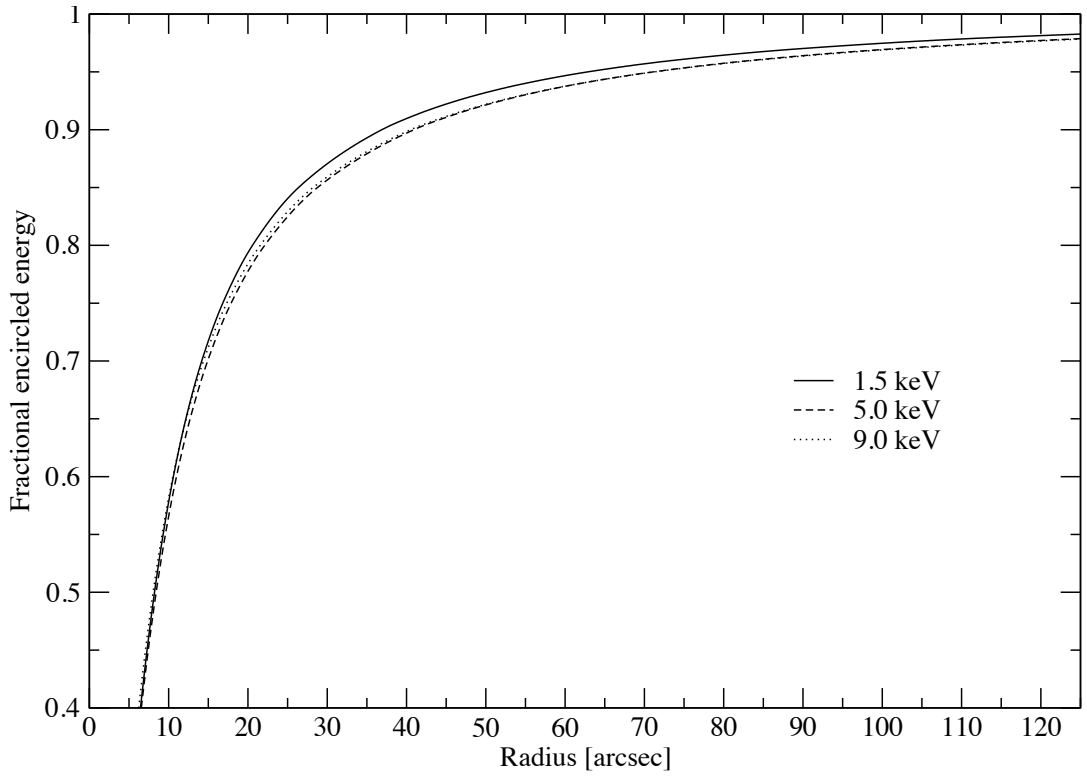

Figure 4.28: EEF of the mirror system for the EPIC-PN at different energies (*XMM-Newton* Community Support Team, 2010).

4.2.3 Instrument I : European Photon Imaging Camera (EPIC)

4.2.3.1 Overview

The EPIC is equipped with three X-ray CCD arrays at the foci of the corresponding X-ray mirror systems. Two of them (EPIC-MOS1 and EPIC-MOS2; Turner et al. 2001) consists of seven MOS-type CCDs sensitive in the ∼0.15–12 keV energy range, and the remaining one (EPIC-PN; Strüder et al. 2001) consists of twelve pn-type CCDs sensitive in the ∼0.15–15 keV energy range. In particular, the combination of the mirror system and the EPIC-PN module (figure 4.29) provide large effective area and a moderate energy resolution in the hard X-ray band. The design parameters and the basic performance are summarized in table 4.2 at section 4.2.4. More details can be found in e.g., the *XMM-Newton* Technical Description (*XMM-Newton* Science Operations Centre User Support Team, 2010).

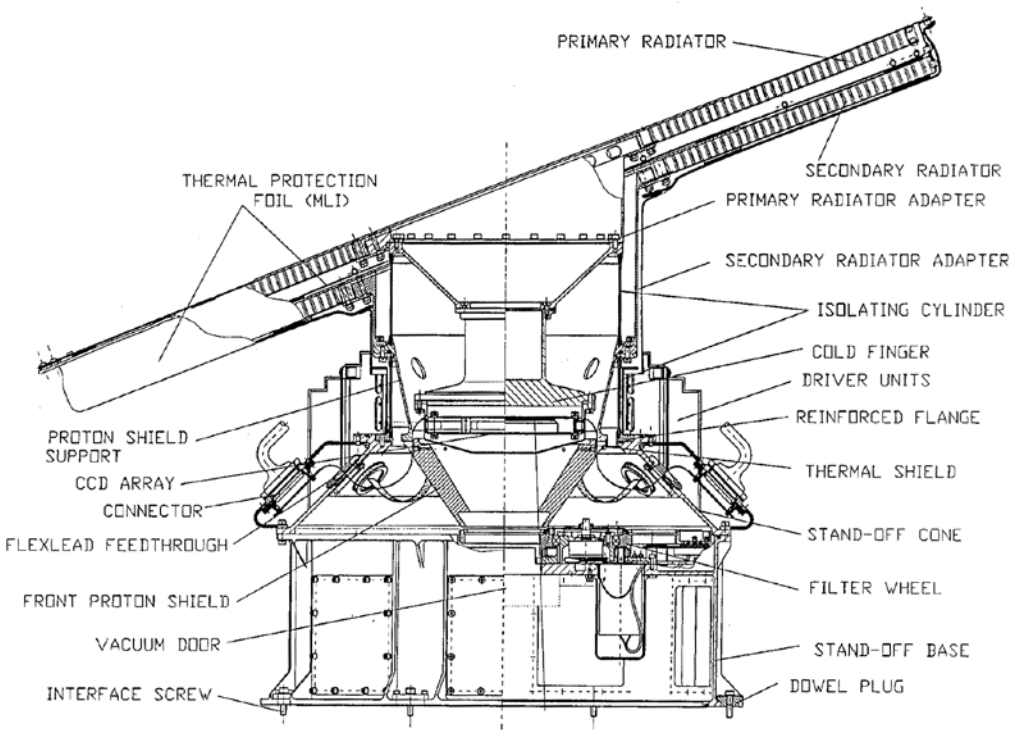

Figure 4.29: Shematic view of the EPIC-PN camera (Strüder et al., 2001).

4.2.3.2 Systems of CCDs

In the pn-type CCD chips, incident photons are converted into electrons and holes, which are quickly separated by strong electric fields before they recombine. Resultant charges are drifted to the potential minimum and stored under the transfer registers. Finally, the signals are read out from each CCD line with a readout amplifier. A schematic view of the pn-type CCD is shown in figure 4.31.

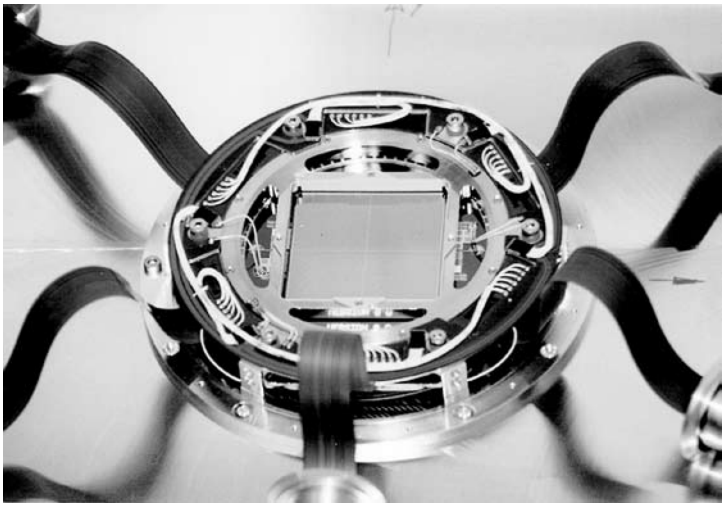

Figure 4.30: Picture of the EPIC-PN onboard *XMM-Newton*.

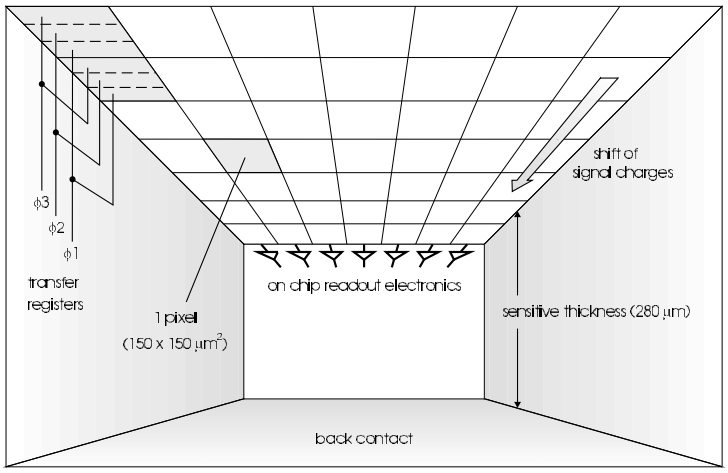

Figure 4.31: Schematic view of the inside of the pn-type CCD (Strüder et al., 2001).

4.2.3.3 Configuration

The EPIC-PN consists of twelve pn-type CCD chips (§ 4.1.3) on a single wafer. Each CCD has an imaging area of 200×64 pixels. The array of the total twelve chips covers a ∼30′ FoV at the focal plane of the X-ray mirror system. Four individual quadrants each having three CCD chips are operated in parallel. The configuration of the CCD chips on the EPIC-PN is shown in figure 4.32.

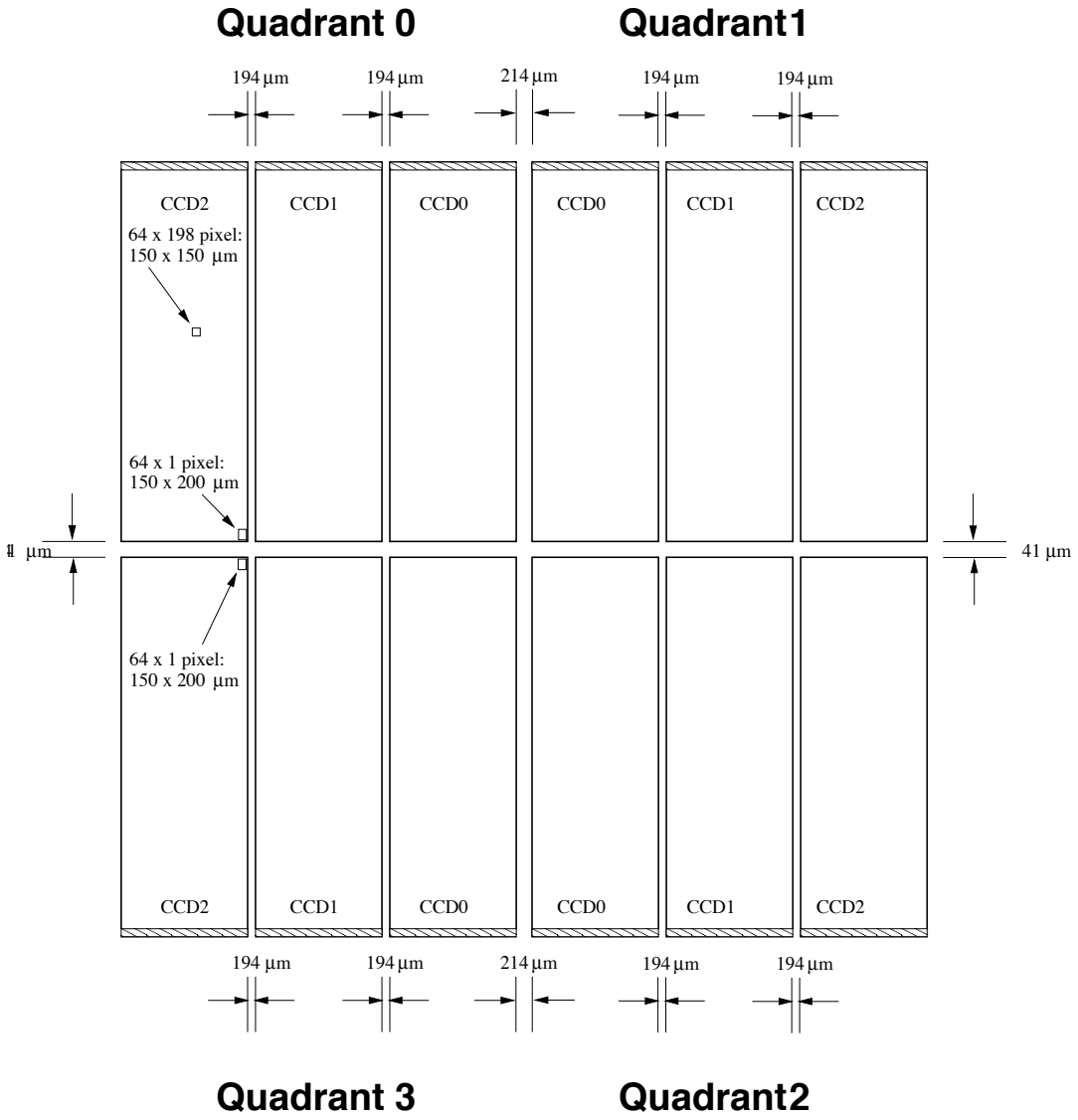

Figure 4.32: Layout of the internal boundaries of the EPIC-PN (Strüder et al., 2001).

4.2.3.4 Effective Energy Range

The thick depletion layer of the EPIC-PN provides a high quantum efficiency particularly in the high energy band. The quantum efficiency of the EPIC-PN is shown in figure 4.33. An absorption structure at the ∼528 eV energy is caused by an absorption of a SiO_2 insulator. A typical X-ray absorption fine structure is also seen at ∼1.8 keV by the Si K edge.

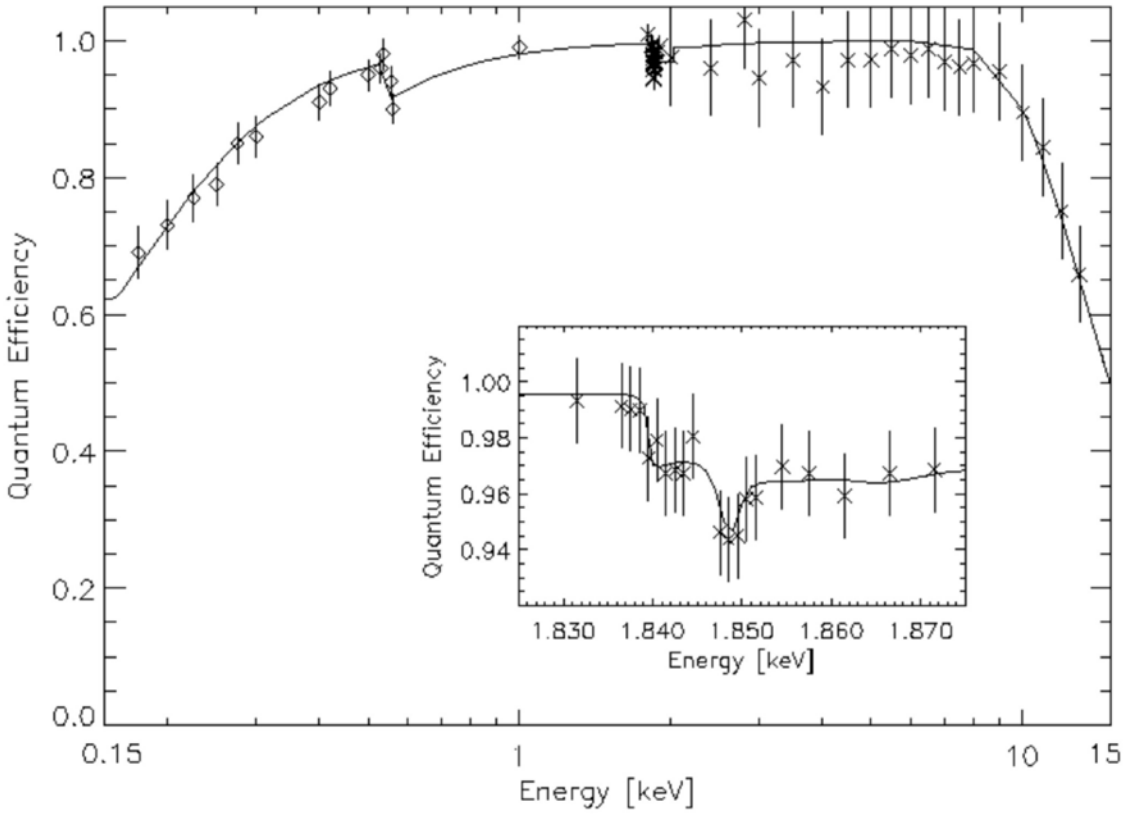

Figure 4.33: Quantum efficiency of the EPIC-PN as a function of incident photon energy (*XMM-Newton* Community Support Team, 2010).

4.2.3.5 Energy Resolution and Scale

A typical energy resolution of the EPIC-PN is shown in figure 4.34. A constant degradation of the energy resolution is found at a rate of $\simeq$2.5 eV yr^{-1}. The absolute energy scale is accurate to $\sim$10–50 eV for the EPIC-PN.

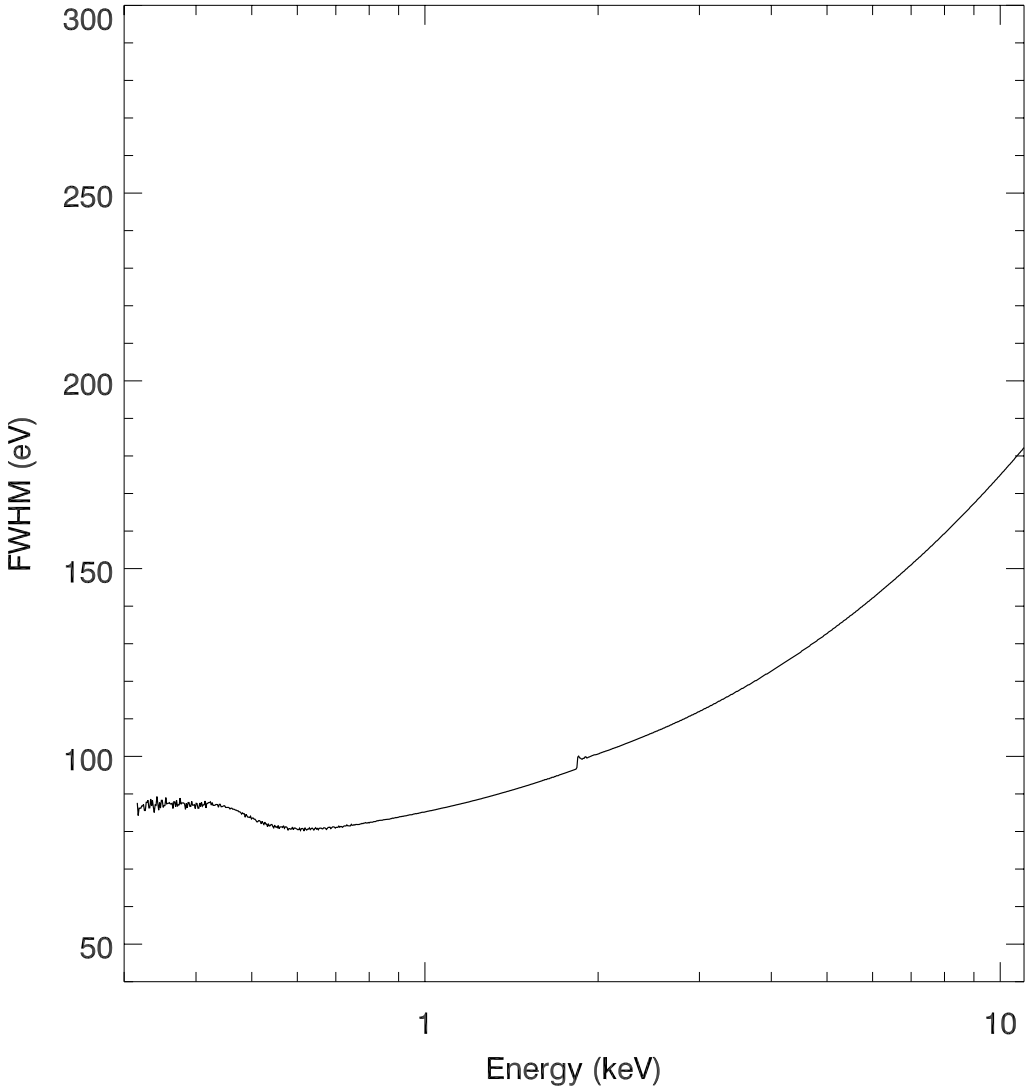

Figure 4.34: Typical energy resolution of the EPIC-PN (*XMM-Newton* Community Support Team, 2010), which is simulated with the science analysis software (SAS) for *XMM-Newton* released on 2007.

4.2.3.6 Observation Modes

Both the EPIC-MOS and the EPIC-PN have several readout modes in operation: A full frame mode is the standard operation, in which all pixels of all CCDs are read out. A large window, a small window, and a timing mode can also be selected for each observation. A reduced number of read-out pixels provide a high-resolution light curves with a stronger resistance to pile-up for bright targets. Typical images obtained in each mode are shown in figure 4.35.

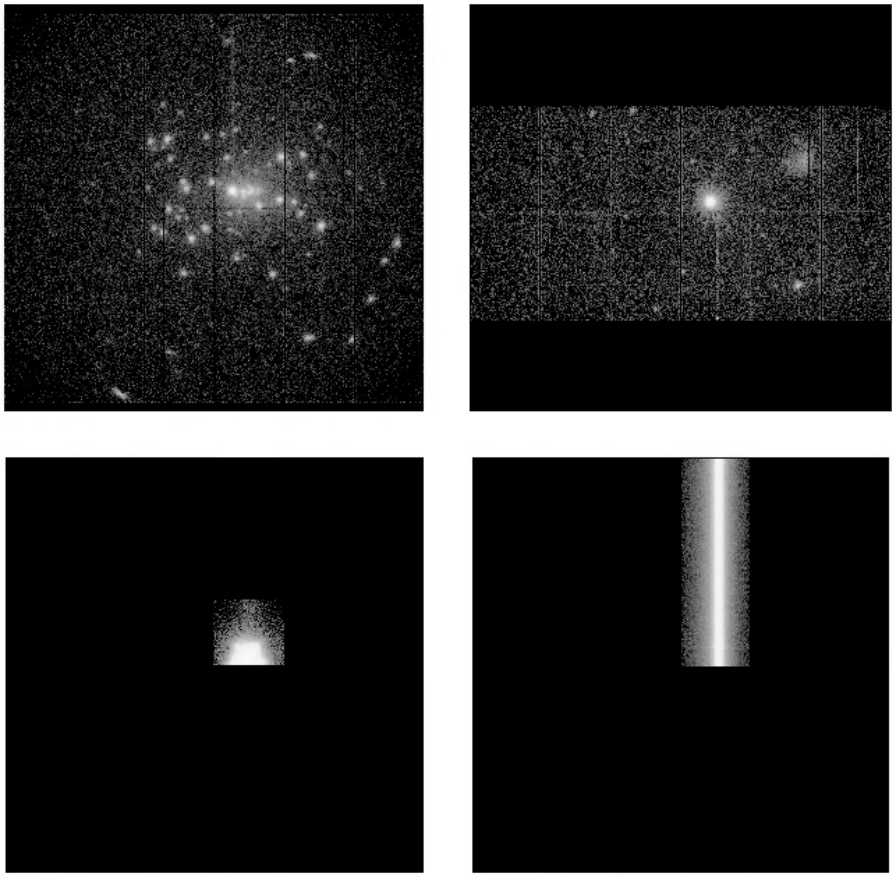

Figure 4.35: Typical images of four readout modes for the EPIC-PN (*XMM-Newton* Community Support Team, 2010). A full frame, a large window, a small window, and a timing mode are respectively shown in the top left, the top right, the bottom left, and the bottom right panels.

In our observations, we chose the timing mode for the EPIC-PN. This mode is suited for observing a point-like bright X-ray target. The window is restricted to 64×200 pixels on the CCD. In the timing mode, events from a predefined area on the CCD chip are stacked into an one-dimension image to obtain a fast read-out. The timing resolution is 0.03 ms, and the effect of the photon pile-up is negligible for the source fluxes below ∼800 count s^{-1} in general observations (*XMM-Newton* Community Support Team, 2010).

4.2.3.7 Background Events

The quiescent NXB of the EPIC mostly originates from Cosmic-Ray particles interacting with the surrounding structures. The intensity of the NXB is monitored regularly by closed filter observations. No large variation is found in the long-term NXB spectra, in which the intensity during any given observation is within ∼10 % of the mean value. A quiescent NXB spectrum of the EPIC-PN is shown in figure 4.36.

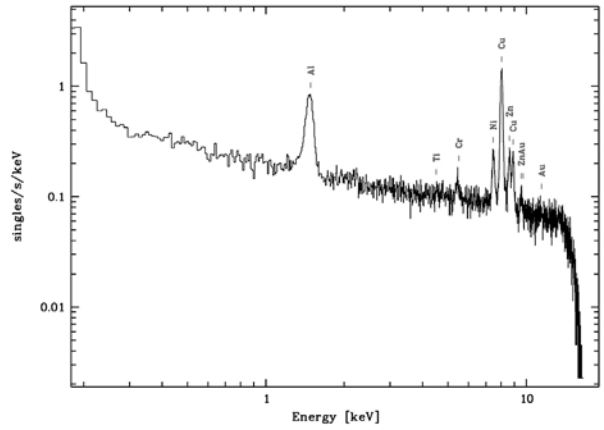

Figure 4.36: Typical NXB spectrum for the EPIC-PN (*XMM-Newton* Community Support Team, 2010).

The NXB is characterized by a flat continuum with a number of fluorescence emission lines (figure 4.36). In particular, intense Kα emission lines from Al (∼1.5 keV), Ni (∼7.5 keV), Cu(∼8.0 keV), and Zn (∼8.6 keV) are seen in the spectrum. The intensity of the emission lines depends on the structure of the detectors, which is not constant over the CCD chips of the EPIC-PN. The spatial inhomogeneity of typical intense NXB emission lines is shown in figure 4.37.

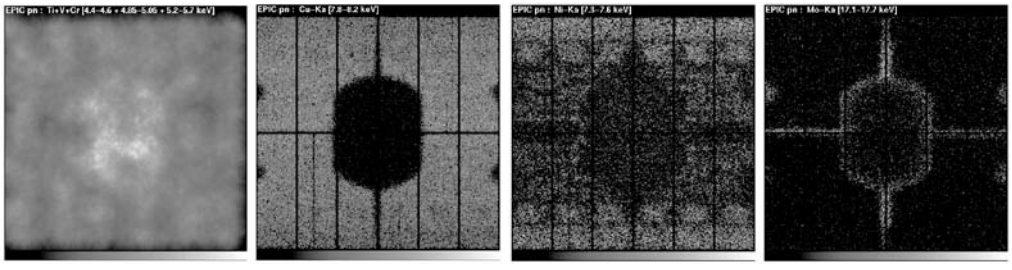

Figure 4.37: Spatial inhomogeneity of typical intense NXB emission lines for the EPIC-PN (*XMM-Newton* Science Operations Centre User Support Team, 2010). The Kα lines from Ti+V+Cr, Co, Ni, and Mo are shown in the first, second, third, and fourth images, respectively.

4.2.4 Summary of the mission

The design parameters and the orbital information of *XMM-Newton* spacecraft are summarized in table 4.2.

Table 4.2: Details of the *XMM-Newton* mission (*XMM-Newton* Community Support Team, 2010).

	Parameter	Value
Spacecraft	Apogee distance	$\sim$107000 km
	Perigee distance	$\sim$27000 km
	Orbital period	$\sim$48 h
	Launch date	December 10, 1999
	Spacecraft weight	$\sim$3800 kg
EPIC-PN[a]	Telescope	Wolter I (7.5 m focal length)
	Detector format	200×64 pixels (twelve CCDs)
	Pixel size	150×150 μm
	Pixel scale	$4.1'' \times 4.1''$ pixel^{-1}
	FoV	$\sim 30'$
	Energy range	0.15–15 keV
	Telescope PSF	$\sim 15''$ (HPD)
	Sensitivity	$\sim 10 \times 10^{-14}$ erg cm^{-2} s^{-1} in 10^4 s

[a] Details of the EPIC-PN are described in section 4.2.2 and 4.2.3.

4.3 *Swift* Satellite

4.3.1 Overview of the Spacecraft

The *Swift* satellite is a Medium-sized Explorer (MIDEX) program by the National Aeronautics and Space Administration (NASA). This is a multi-wavelength observatory dedicated to the studies of Gamma-Ray burst (GRB). *Swift* was successfully launched on November 20, 2004. The spacecraft (figure 4.38) orbits around the Earth once in ∼95 minutes in a low-Earth orbit at a ∼600 km altitude with an inclination angle of ∼21°. More details of *Swift* can be found in the *Swift* Technical Handbook (*Swift* Science Center, 2009) and the official webpage[4].

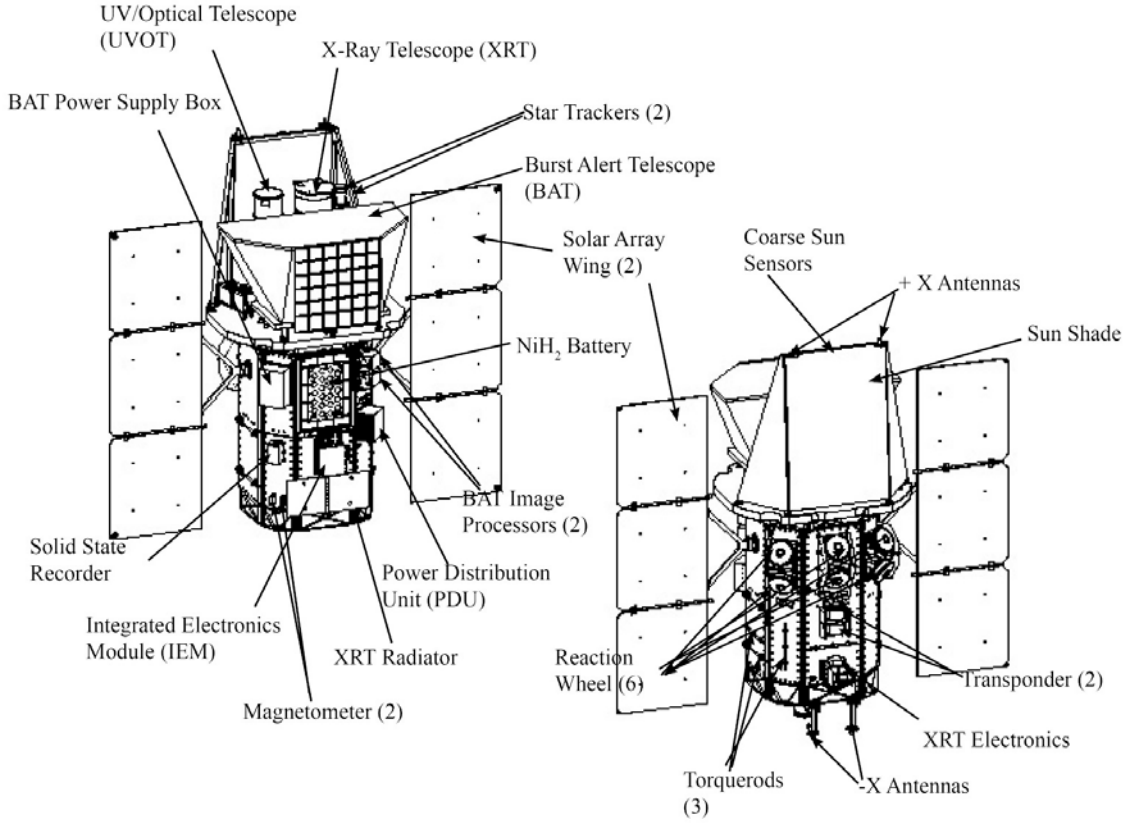

Figure 4.38: Shematic view of the *Swift* satellite (*Swift* Mission Participants, 2004).

[4]http://swift.gsfc.nasa.gov/

Swift has three scientific instruments in operation (Gehrels et al., 2004): the Burst Alert Telescope (BAT; Barthelmy et al. 2005) in gamma-ray, the X-Ray Telescope (XRT; Burrows et al. 2005) in X-ray, and the Ultra-Violet/Optical Telescope (UVOT; Roming et al. 2005) in ultra-vioret and optical bands. Three independent instruments provide simultaneous observations in a wide-energy range. The spacecraft has an ability to point swiftly and autonomously a target position in less than approximately 90 s, which is a key requirement for the study of GRB afterglow emission. All data products are promptly available in a public archive.

Also, the quick response and autonomous maneuver with a suite of wide-band instruments are well-suited to observe transient and highly variable targets such as classical novae. In fact, the Swift Nova-CV Group[5] leads intensive monitoring observations in classical novae bright enough in X-ray using the XRT. We use a part of the data in this thesis. In the following section, we concentrate on the in-flight performances of an X-ray telescope and a CCD detector in the XRT.

[5]http://www.swift.ac.uk/nova-cv/

4.3.2 X-ray Optics

4.3.2.1 Mirror Assembly

Swift has an X-ray telescope module (Burrows et al., 2005) to focus X-rays onto a focal detector (figure 4.39). We first describe the properties of the mirror system in the XRT. The mirror was originally built and calibrated as a flight spare for the *JET-X* telescope onboard the *Spectrum-X*-Γ satellite (e.g., Citterio et al. 1996; Wells et al. 1997), which was eventually aborted. In the X-ray telescope, the Wolter-I type geometry is employed for 12 concentric gold-coated electroformed Ni shells, reflecting X-rays at small grazing angles. The focal length, the overall instrument, and the diameter of the telescope are ∼3.5 m, ∼4.7 m, and ∼0.5 m, respectively. A moderate number of reflectors provides a collecting efficiency with a good imaging capability in the 0.2–10 keV energy range. More details of the module can be found in Burrows et al. (2005).

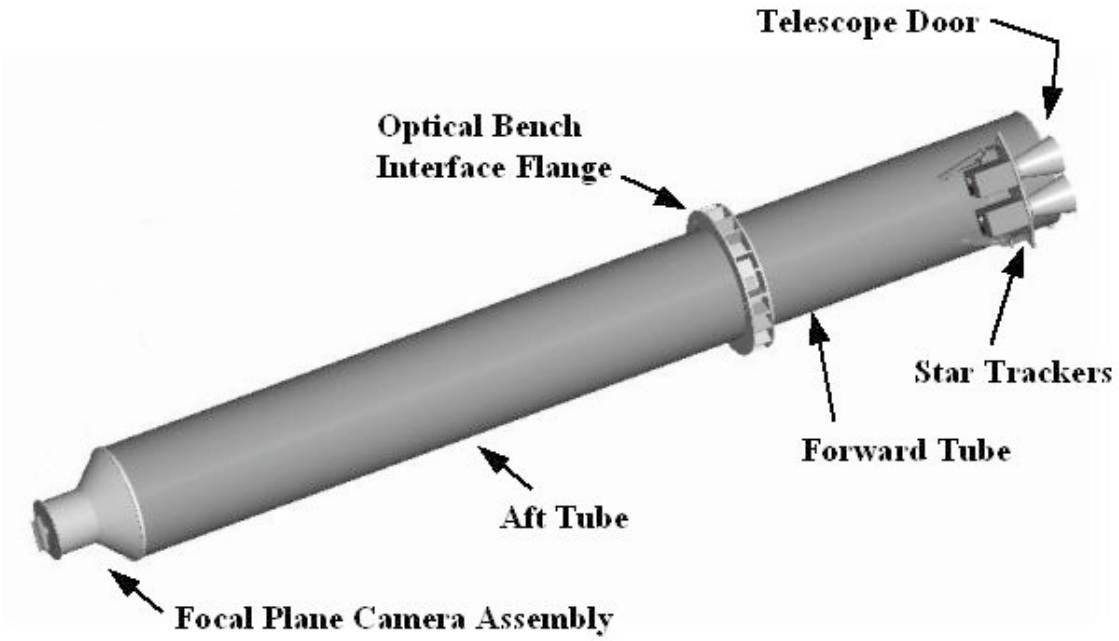

Figure 4.39: Design of the X-ray telescope onboard *Swift* (Burrows et al., 2005).

4.3.2.2 Effective Area

The on-axis effective area convolved with a focal CCD detector response is shown in figure 4.40 (Mukerjee et al., 2004). The X-ray telescope has a total effective area of $\sim$110 cm^2 over a 0.2–10 keV energy range.

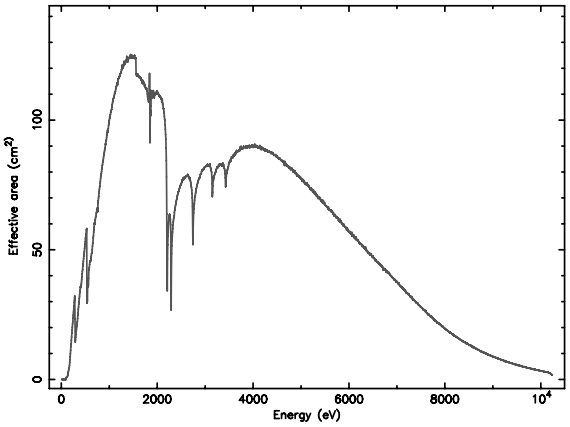

Figure 4.40: Effective area of the X-ray telescope (Mukerjee et al., 2004).

4.3.2.3 Angular Resolution

A typical radial profile of a point source is shown in figure 4.41 (Moretti et al., 2005). Although the shape of the PSF is complex, the radial profile can be approximated by a King function as PSF(r) $= (1 + (r/r_c)^2)^{-\beta}$, where r is the radius, r_c is the core radius, and β is the slope. The X-ray telescope has a HPD of $\sim$18″.

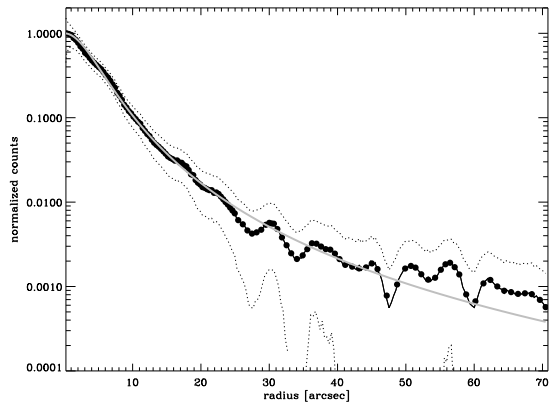

Figure 4.41: An example of mean radial profile of XRT (black symbols) in the 2–10 keV energy range at the off-axis angle of 1′ (Moretti et al., 2005). The best-fit model with a King function and error at the 90% confidence level are shown with the gray and the dotted lines, respectively.

4.3.3 Instrument I : X-Ray Telescope (XRT)

4.3.3.1 Overview

The XRT is equipped with a single CCD chip at the focus of the X-ray telescope module (Burrows et al., 2005). We next describe the properties of the detector in the XRT. The CCD chip is originally designed for the EPIC-MOS instruments onboard *XMM-Newton* (§ 4.2). The XRT provides X-ray imaging-spectroscopic capability in the 0.2–10 keV energy range. The design parameters and the basic performance are summarized in table 4.3 at section 4.3.4. More details can be found in e.g., Burrows et al. (2005), and the *Swift* XRT Data Reduction Guide (Capalbi et al., 2005).

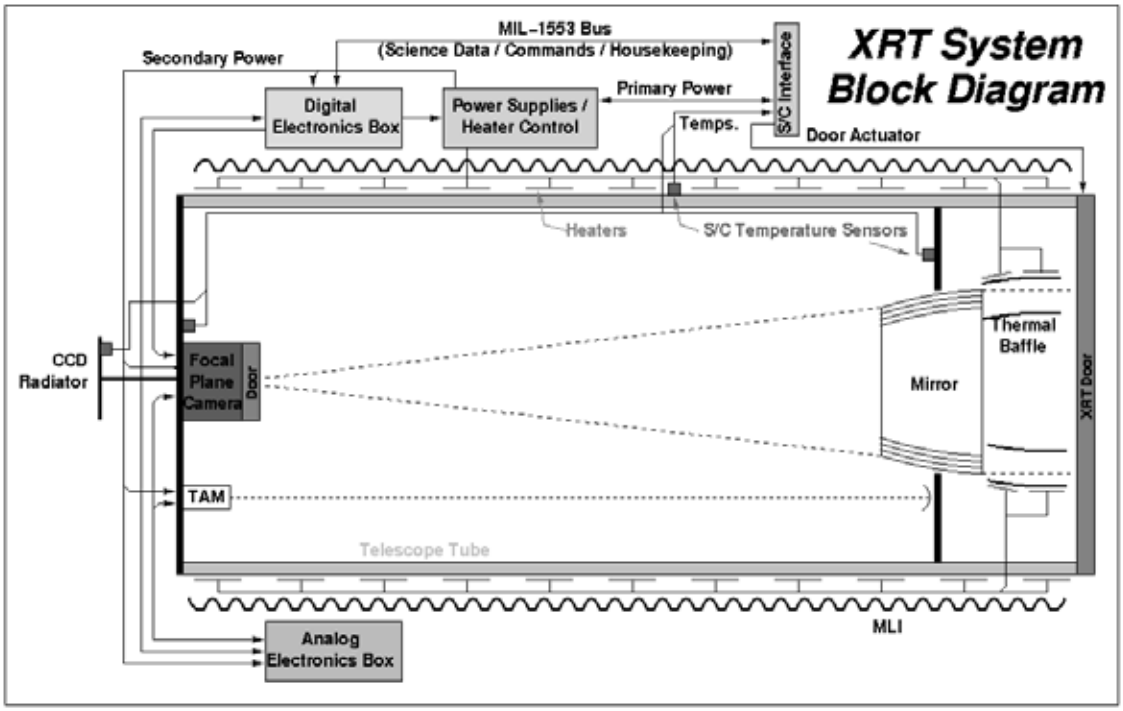

Figure 4.42: Block diagram of the XRT (Burrows et al., 2004).

4.3.3.2 Configuration

The focal CCD detector is a three phase frame-transfer device. It has an imaging area of 600×600 pixels with a pixel size of 40 μm pixel^{-1} corresponding to a pixel scale of 2.36″ pixel^{-1}. Data of the imaging area is transferred to a framestore region of 600×600 array, and then it is read out according to an operating readout mode.

4.3.3.3 Effective Energy Range

The XRT has an FI CCD at the focal plane of the X-ray telescope. The quantum efficiency of the CCD chip is shown in figure 4.43 (Mukerjee et al., 2004).

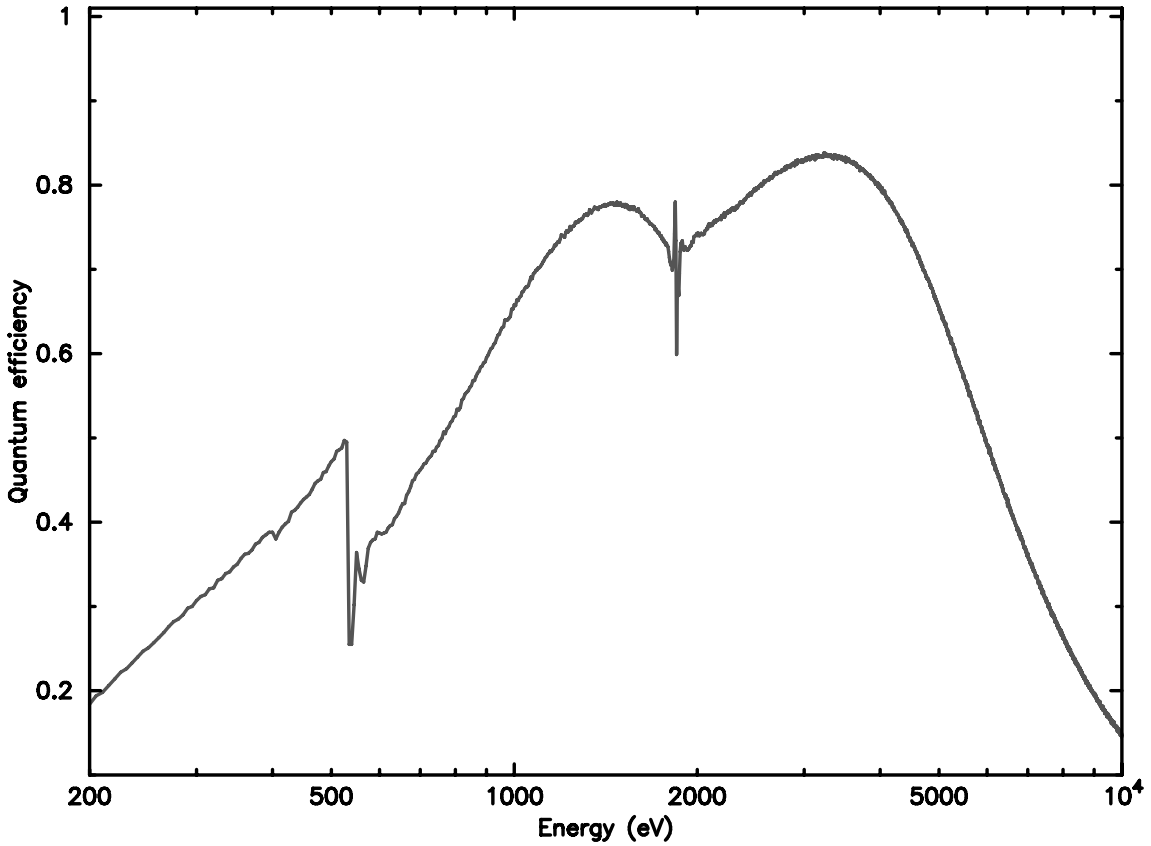

Figure 4.43: Quantum efficiency of the CCD in the XRT (Mukerjee et al., 2004).

4.3.3.4 Energy Resolution

The energy resolution of the CCD is shown in figure 4.44. It decreases from ∼190 eV (FWHM) at 10 keV to ∼50 eV (FWHM) at 0.1 keV.

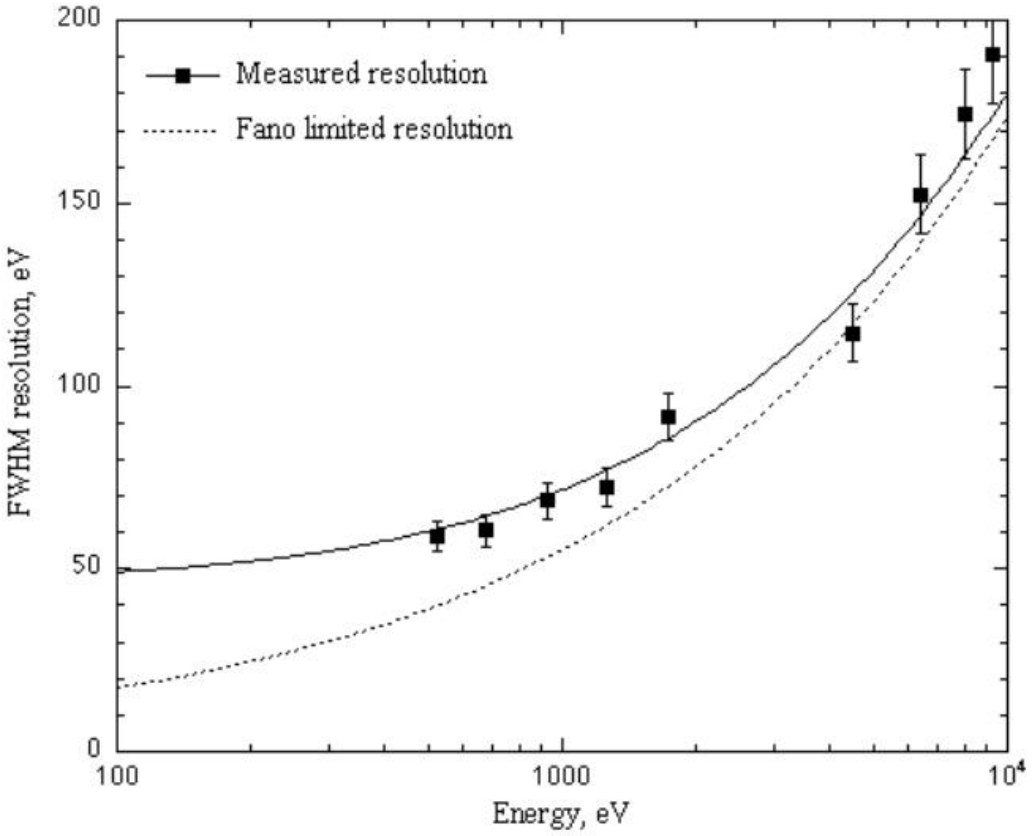

Figure 4.44: Energy resolution of the CCD detector (figure 16 in Burrows et al. 2005). The filled squares with error bars indicate the data from a flight device. Predicted and ideal (Fano-limited) resolutions for the EPIC-MOS instruments are respectively shown in the solid and the dotted lines.

4.3.3.5 Observation States and Modes

The XRT has two observation states in operation: Auto and Manual states. In the Auto state, a readout mode of the CCD is automatically selected according to the source count rates. In the Manual state, the readout mode can be commanded for given observations. Four readout modes are prepared in both states: (1) the Image-Long and Short (IM) mode, (2) the Low Rate (LR) and Piled-up Photodiode (PU) mode, (3) the Windowed-Timing (WT) mode, and (4) the Photon-Counting (PC) mode. The Auto state is selected for the normal operation. The observations used in the thesis were also conducted in this state. As a result, the PC and the WT modes were used for our targets.

The PC mode :

This mode is a traditional frame transfer operation. Each CCD frame is transferred into the frame store area. The signals are read out from a serial register. It retains full imaging and spectroscopic resolution of the detector. A typical image with the PC mode is shown in the left panel of figure 4.45. The read-out time for a full frame is 2.5 s. The PC mode is only used for objects with a lower flux then $\sim$10 count s^{-1} in the Auto state. We need to consider the photon pile-up for the measured count rates above $\sim$0.5 count s^{-1} in general observations.

The WT mode :

This mode is suited for observing a moderately bright X-ray source. A read-out window is restricted to 200 columns on the CCD, which cover the central $8'$ of the FoV. The telemetered information is divided into the frames. The narrow window and the restricted read-out provide a high-resolution X-ray light curves, spectra, and one-dimension images. A typical image with the WT mode is shown in the right panel of figure 4.45. The timing resolution is 1.7 ms. The WT mode is used for medium fluxes above 10 count s^{-1} in the Auto state. The photon pile-up is negligible for objects with a lower flux then $\sim$100 count s^{-1} in general observations (Romano et al., 2006).

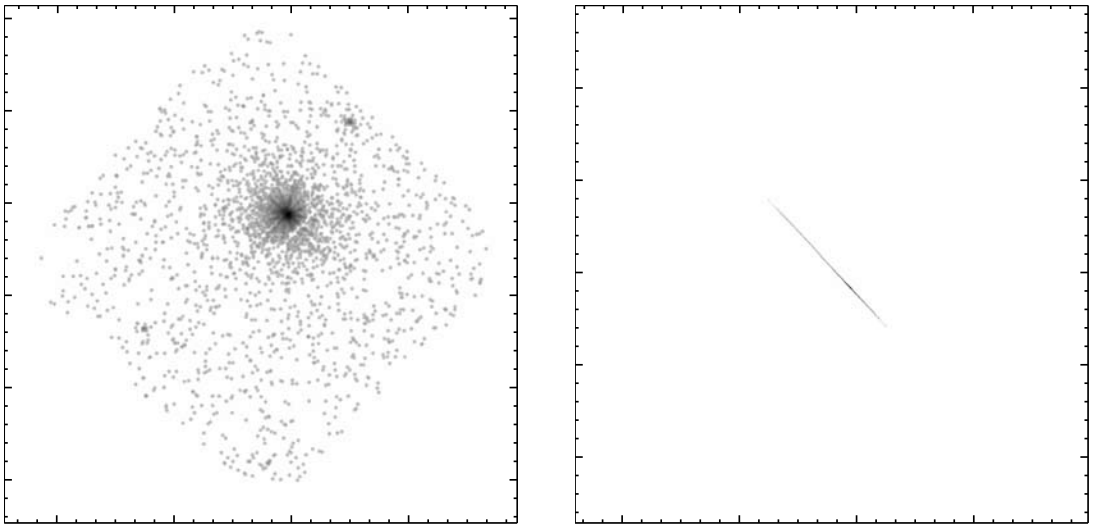

Figure 4.45: Typical images with the PC (left) and the WT (right) modes.

4.3.4 Summary of the mission

The design parameters and the orbital information of the *Swift* spacecraft are summarized in table 4.3.

Table 4.3: Details of the *Swift* mission (*Swift* Science Center, 2009; Burrows et al., 2005).

	Parameter	Value
Spacecraft	Orbit	∼600 km
	Inclination angle	20.6°
	Launch date	November 20, 2004
	Launcher	Delta II 7320
	Spacecraft weight	1470 kg
XRT[a]	Telescope	Wolter I (3.5 m focal length)
	Detector	E2V CCD-22
	Detector format	600×600 pixels
	Pixel size	40×40 μm
	Pixel scale	2.36″×2.36″ pixel^{-1}
	FoV	23.6′×23.6′
	Energy range	0.2–10 keV
	Effective area (1.5 keV)	∼125 cm^2
	Effective area (8.1 keV)	∼20 cm^2
	Position accuracy	∼3″
	Telescope PSF (1.5 keV)	∼18″ (HPD)
	Telescope PSF (8.1 keV)	∼22″ (HPD)
	Sensitivity	$\sim 2\times10^{-14}$ erg cm^{-2} s^{-1} in 10^4 s

[a] Details of the XRT are described in section 4.3.2 and 4.3.3.

Chapter 5

Observations and Analysis

Contents

5.1 Suzaku J0105–72

5.1.1 Summary

Based on the strategy of archival search (see section 3.2.1), we first developed analysis programs to extract X-ray images automatically for searching a new source from these archival data. Then, we intensively checked these X-ray images. As a result, we successfully discovered a transient X-ray source toward the small Magellanic cloud (SMC) with the *Suzaku* satellite. The X-ray source was detected at the edge of an XIS image in the routine observation of a calibration source 1E 0102.2−7219, a super-nova remnant in the SMC. We named the transient X-ray source Suzaku J0105−72.

We extracted high signal-to-noise ratio spectra for the transient source, and confirmed the long-term behavior using a huge amount of archived data at this position using various X-ray satellites. X-ray spectra can be explained by a single blackbody with a temperature of $\sim$72 eV convolved with an interstellar absorption. An additional absorption edge structure at $\sim$0.74 keV from helium-like oxygen ions is also found in the soft X-ray spectra. Based on the behavior, we concluded that the transient source is super-soft X-ray emission caused by a classical nova explosion. In this section, we describe the results of our spectroscopic as well as long-term flux studies and discuss the nature of the target. This results have already been published in Takei et al. (2008).

5.1.2 Observations and Data Reduction

The sixteen observations of 1E 0102.2−7219 were performed using the *Suzaku* satellite by 2007 March from its launch (table 5.1). In the routine calibration observation, we found a transient source at the edge of XIS images obtained on 2005 August 31. In this research, we concentrate on the XIS data for the transient X-ray source.

As of the observation dates, when the transient source was detected, the absolute energy scale was accurate to $\lesssim$5 eV. The energy resolution is respectively $\sim$63 and $\sim$71 eV at 1.0 keV in the full width at half maximum for the FI and BI CCDs. All of the XIS data were taken with the normal clocking mode with a frame time of 8 s. The net exposure times are also listed in table 5.1. The first two observations were aimed at (R.A., Dec.) = ($01^h04^m02^s$, $-72°02'00''$), while the others were at (R.A., Dec.) = ($01^h04^m02^s$, $-72°01'53''$) in the equinox J2000.0.

The data were processed with the standard pipeline version 1.2, in which events were removed during the South Atlantic anomaly passages, the earth elevation angles below 5°, or the day Earth elevation angle was below 20° (Fujimoto et al., 2007). For reduction of the data, we used the High Energy Astrophysics Software (HEASoft) package version 6.1[1].

Table 5.1: *Suzaku* observation log.

Sequence number	Start date	$t_{\rm exp}$[a] (ks)
100001020	2005-08-13	4
100014010[b]	2005-08-31	24
100044010	2005-12-16	71
100044020	2006-01-17	42
100044030	2006-02-02	21
101005010	2006-04-16	22
101005020	2006-05-21	19
101005030	2006-06-26	22
101005040	2006-07-17	22
101005050	2006-08-25	49
101005060	2006-09-19	11
101005070	2006-10-21	37
101005090	2006-12-13	28
101005100	2007-01-15	24
101005110	2007-02-10	36
101005120	2007-03-18	18

[a] Averaged exposure time of the operating CCDs.
[b] The transient source was detected in this observation.

[1]See http://heasarc.gsfc.nasa.gov/docs/software/lheasoft/ for detail.

5.1.3 Analysis

5.1.3.1 Image Analysis

Figure 5.1 shows XIS images obtained on 2005 August 31. Events taken with the four detectors were merged. XIS detected four sources. Three of them were identified as 1E 0102.2−7219, RX J0103.6−7201, and 2E 0101.5−7225 using the SIMBAD database [2]. These sources were detected in all images taken during the other epochs. The remaining one is a transient source detected only in the soft-band image on 2005 August 31. The position of the transient source is very close to the edge of the detector, and its image is truncated. In order to constrain the position as precisely as possible, we took the following procedure. Throughout this thesis, we used ray-tracing software designed for the *Suzaku* XRT (`xissim`; Ishisaki et al. 2007) to simulate XIS images. Simulation was conducted only for the XIS1; the source is quite soft and most of the events were recorded in the XIS1.

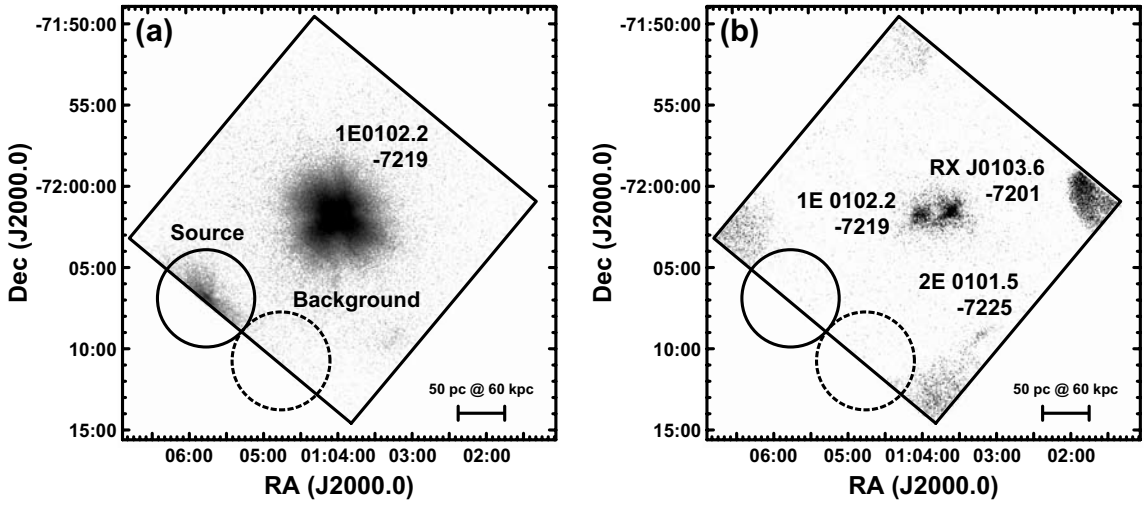

Figure 5.1: XIS images in the (a) 0.2–2.0 keV and (b) 2.0–12 keV bands. Events taken with the four XIS were merged in the data on 2005 August 31. The bright spots in the four corners in (b) are the calibration sources. The solid and the dashed circles indicate the source and background accumulation regions, respectively. The names of the three persistent sources are given. The XIS frame was registered to match the observed position of 1E 0102.2−7219 with the *Chandra* position.

First, we registered the astrometry of the XIS images by matching the position of 1E 0102.2−7219 with that of the *Chandra* satellite. The astrometry of the *Chandra* images is accurate to $\sim 0\farcs6$[3]. We simulated XIS images based on the *Chandra* image (ObsID = 5139), and constructed R.A. and Dec. projections of the surface brightness in the 0.2–2.0 keV band. The observed profile was fitted to the simulated profile by shifting $13''$ and $19''$ in the R.A. and Dec. directions, respectively. The uncertainty of the fitting is estimated to be $\sim 1''$ in

[2] http://simbad.u-strasbg.fr/

[3] See http://asc.harvard.edu/proposer/POG/ for details.

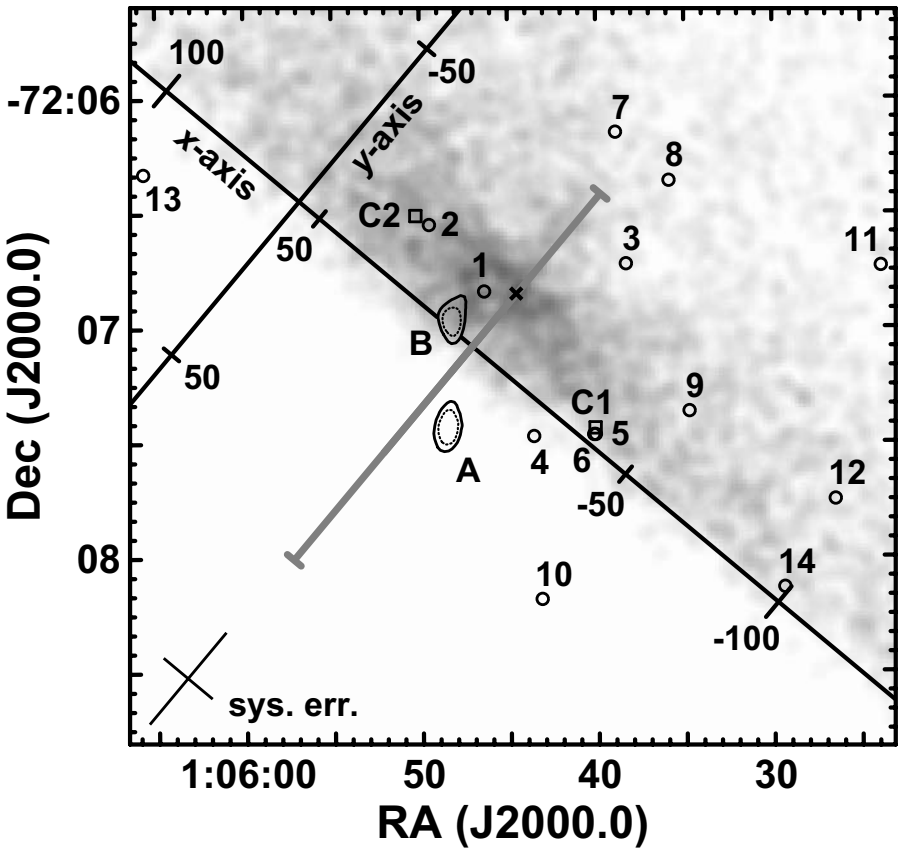

Figure 5.2: Close-up image of the transient source in gray scale. The observed peak position is shown by a cross. The open circles are the positions of the nearby sources with the labels given in table 5.3, while the open squares are the positions of the two faint sources (C1 and C2; also in table 5.3) found in the archived *Chandra* images. The range of initial positions of the simulated source is given by the gray line. The contours indicate 90% and 99% confidence ranges of the transient source position. The systematic uncertainty of the position determination is indicated as a cross at the bottom left.

both directions, which is inherited to the uncertainty of the position determination of the transient source.

Second, we simulated XIS images of a point source at various positions toward the inside and outside of the field of view from the observed peak of the source. Figure 5.2 shows the layout of the simulated positions. We define the axes parallel and perpendicular to the detector edge as x and y, respectively. The origin of the x-axis is defined so that the observed peak of the transient source is 0. The origin of the y-axis is placed at the field edge, and negative and positive values of y indicate that the position is inside and outside of the field, respectively. The unit of the coordinate is pixels. The apparent peak of the source is at (x, y) = (0, −17).

We simulated XIS images at positions along the line between (x, y) = (0, −50) and (0, 70) with a step of $\Delta\, y = 1$ (the gray line in figure 5.2). For the simulated two-dimensional image at each position, we constructed a one-dimensional surface brightness profile inside the field

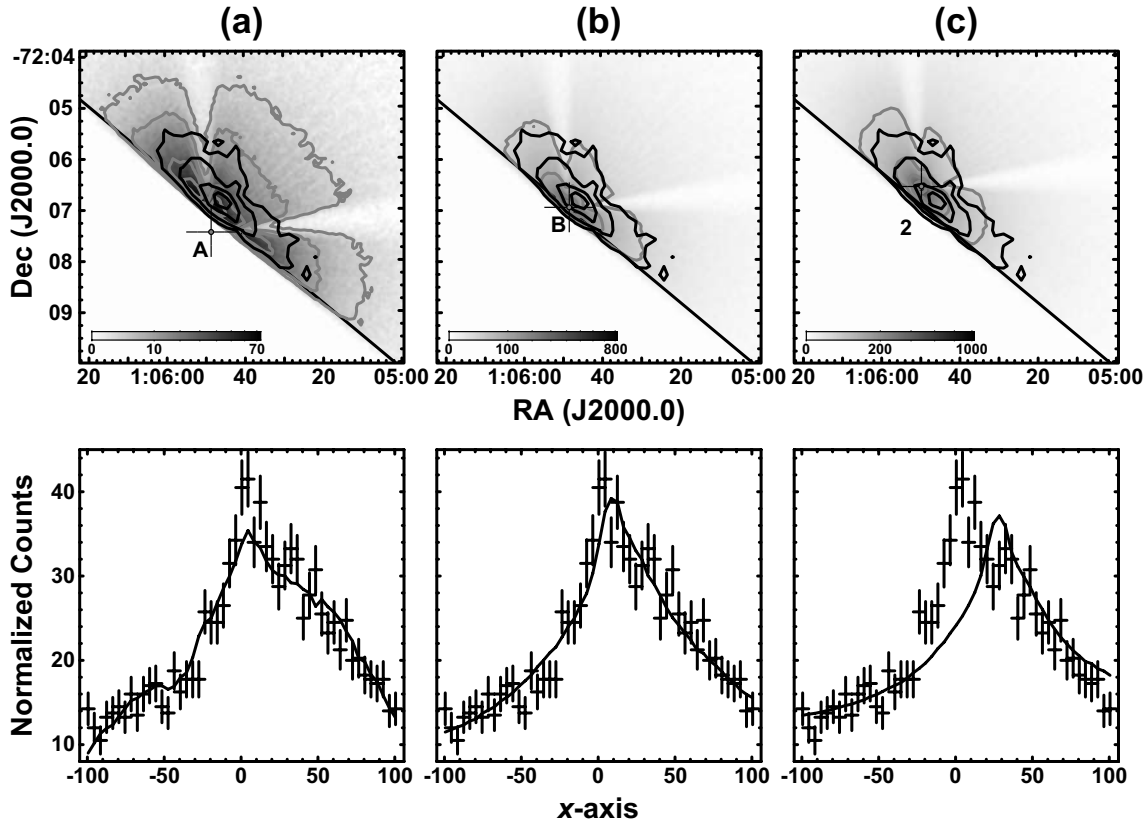

Figure 5.3: Simulated images and profiles at three different positions; (a) the local minimum A, (b) the local minimum B, and (c) the second closest source in table 5.3. The upper panels show the simulated images in gray scale. The intensities of simulated and observed images in an arbitrary unit are shown with gray and black contours, respectively. The assumed positions are shown with pluses. The lower panels show the projected profiles of the simulated (lines) and the observed (pluses) images.

of view of the detector to match with the observed profile. The profiles were projected on the x-axis and the counts in the range of $y > -183$ were accumulated, so that it would cover the entire extent of the observed image. In the fitting, the simulated profile was allowed to move along the x-axis, so that its peak would match with that of the observed profile.

With the x-projected profile, we can constrain both the x and y positions of the transient source. On one hand, the peak position of the profile is sensitive to the assumed x position of the transient source. On the other hand, the width of the profile is sensitive to the assumed y position; this is because the width of the simulated profile becomes narrower as the assumed y position moves away from the edge. We do not use the y-projected profiles, because their peaks and widths are insensitive to the assumed position of the source.

After this procedure for every point along the gray line in figure 5.2, we obtained the 90% and 99% confidence ranges of the source position, which are shown as contours in figure 5.2. We have two islands of local minimum; one (A in figure 5.2) is outside of the field of view at (x, y) = (-8.5, 20) or (R.A., Dec.) = ($01^h05^m49^s$, $-72°07'26''$), and the other (B in

figure 5.2) is inside of the field of view at (x, y) = (8.5, −2) or (R.A., Dec.) = ($01^h05^m48^s$, $-72°06'57''$). The former has a smaller χ^2 value of the fit. The simulated images and the best-fit profiles at the two local minima are shown at the panels (a) and (b) in figures 5.3.

The systematic uncertainty of this procedure was assessed using a different XIS observation of the blazar 0836+714 (ObsID = 700010010). A bright source is found in the image close to the edge but well within the detector. We artificially truncated the image of the source, and derived the displacement of the real and reconstructed peak positions. The derived uncertainty of $\sim 8''$ and $\sim 15''$, respectively, for the x and y directions is shown as a cross at the bottom left in figure 5.2. We designate the source as Suzaku J0105−72.

5.1.3.2 Temporal Analysis

We constructed a background-subtracted light curve of the transient source (figure 5.4). The source and background photons were accumulated from the solid and dashed circles truncated by the field edge in figure 5.1. The source circle around the observed peak has a radius of 3′, which would include ∼90% of the photons from a point source if the whole region is inside the field of view. The background region was selected from a region devoid of X-ray emission at the edge does have the same radius and the same truncated fraction as the source region.

We found a decline of the count-rate in the light curve. We fitted the curve with a constant count rate model, which was rejected by a χ^2 test with a χ^2/d.o.f value of ∼93/10. No such trend was found in the background light curve, which indicates that the decline is intrinsic to the transient source. We also searched for any periodicity of signals using the Lomb method (Lomb, 1976) and the epoch folding search technique. We found no significant periodicity, except for those related to the *Suzaku* orbit.

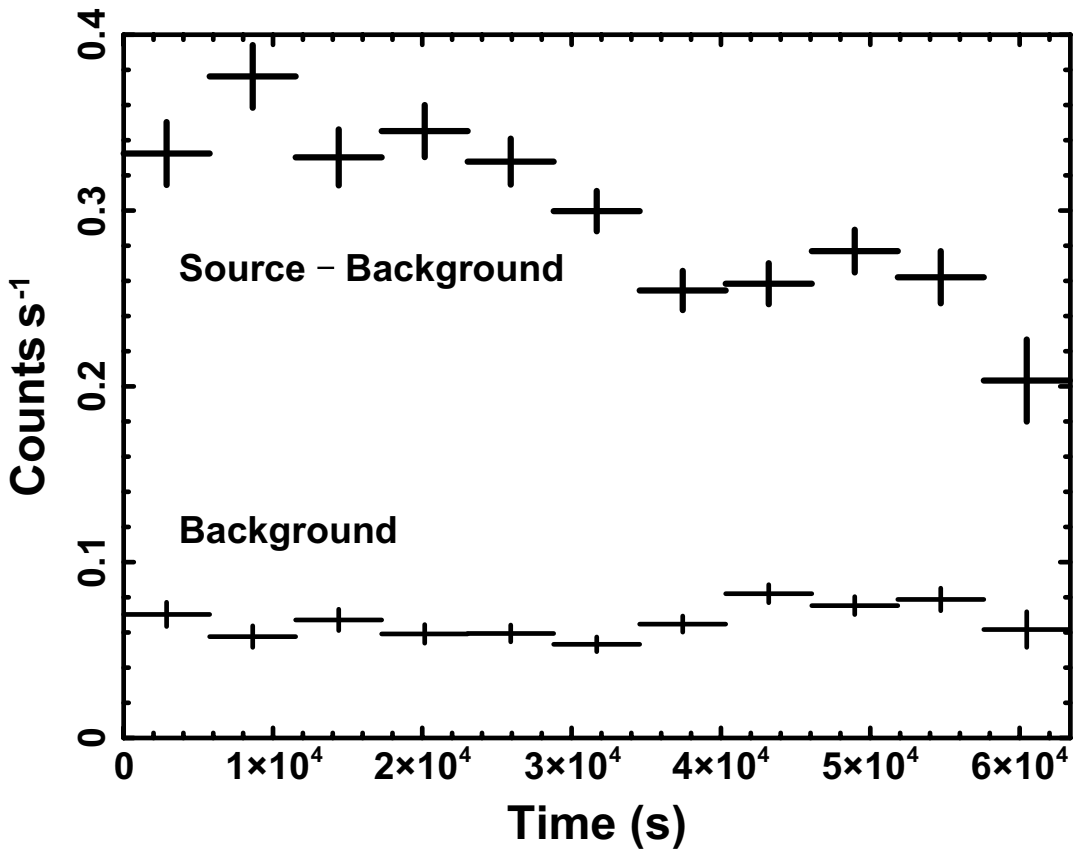

Figure 5.4: Background-subtracted source (thick pluses) and background (thin pluses) light curves with a binning size of 5760 s, the period of the *Suzaku* orbit. Events taken with the four XIS in 0.2–2.0 keV were merged. The origin of the time is the start time of the observation.

5.1.3.3 Spectral Analysis

We constructed the background-subtracted spectrum in 0.4–2.0 keV for the FI chips and 0.2–2.0 keV for the BI chip (figure 5.5). The source and the background signals were integrated from the same regions with the temporal analysis. The spectrum is very soft, with almost all photons below 2 keV, and shows no conspicuous emission lines. In order to fit the spectrum, we created the detector and mirror responses on the observation date at two local minima (A and B in figure 5.2) using the `xisrmfgen` and `xissimarfgen` tools. The spectra and responses were constructed independently for the four CCDs, and the fitting trials were conducted simultaneously for the set of four spectra. In order to account for the possible normalization differences among the four CCDs, we added normalization parameters relative to XIS1.

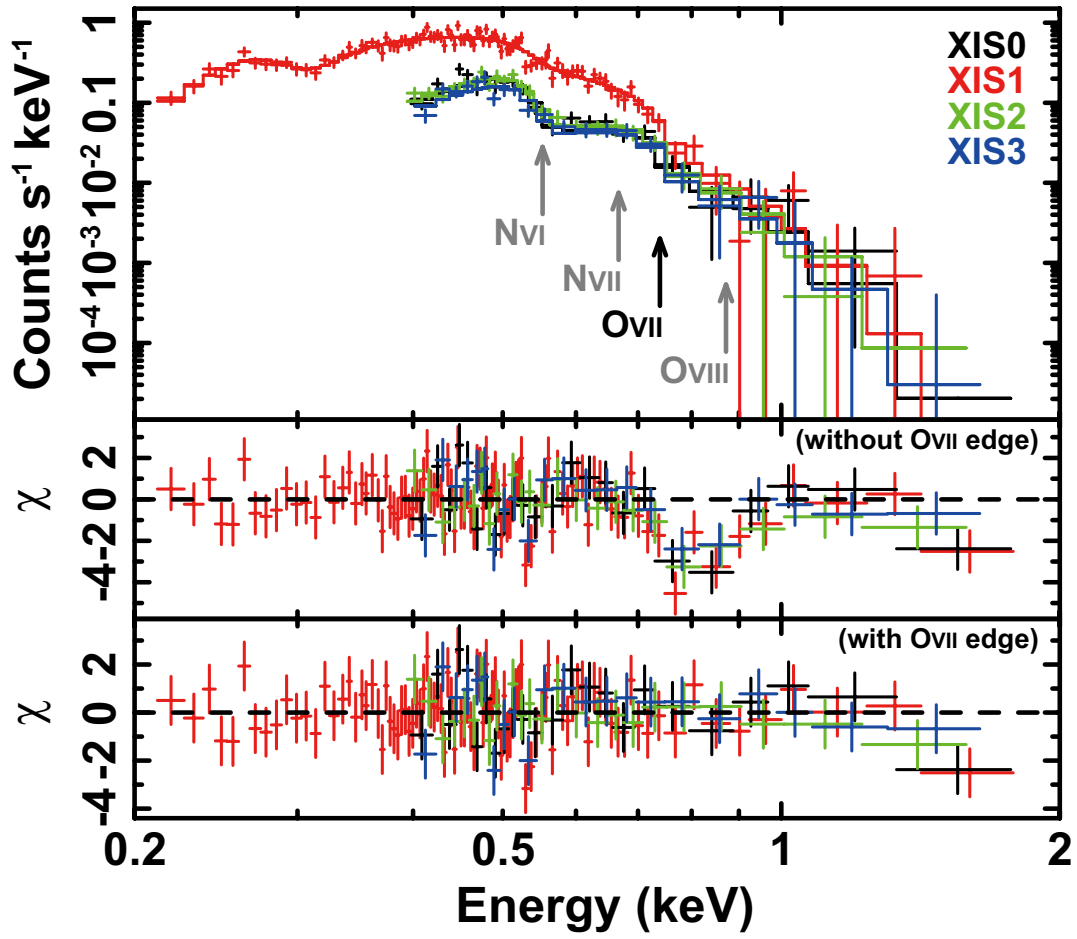

Figure 5.5: XIS spectrum and the best-fit model. The background-subtracted spectra are shown with pluses in the upper panel in different colors for the four censors (black, red, green, and blue for XIS 0–3). The best-fit model (absorbed blackbody with an edge) is shown by solid lines. The energies of the K edges are indicated by arrows. The lower two panels show the residuals from the absorbed blackbody models with and without the O_{VII} edge.

We fitted the spectra with several continuum (blackbody, bremsstrahlung, and power-law) models with interstellar absorption. The blackbody model with a temperature of $k_{\rm B}T$ $\sim$ 72 eV and the interstellar extinction of $N_{\rm H}$ $\sim$ 4.9×10^{20} H atoms cm^{-2} yielded the best-fit result, which explains the global spectral shape quite well. The amount of interstellar extinction is consistent with the value toward the SMC (Dickey & Lockman, 1990). However, we see an edge-like residual at $\sim$0.74 keV, as shown in the middle panel of figure 5.5. We therefore modified the blackbody model by adding an edge model with two more free parameters, the edge energy (E) and the optical depth at the edge (τ), and obtained an improved acceptable fit. Based on the F-test, we found that the improvement is statistically significant ($<10^{-6}$ of a chance probability).

The best-fit parameters are given in table 5.2 separately for positions A and B. X-ray flux ($F_{\rm X}$) and luminosity ($L_{\rm X}$) were derived in the 0.2–2.0 keV band. A distance of 60 kpc was assumed for the luminosity. The best-fit model is given in figure 5.5 for position A. The parameters for the spectral shape ($N_{\rm H}$, $k_{\rm B}T$, E, and τ) do not differ very much between positions A and B. This is because the half-power diameter and the vignetting function of the telescopes do not depend on energy at <5 keV. On the other hand, the parameters for the normalization ($F_{\rm X}$) are different. This is because A is further away from the observed peak, and thus requires a brighter intrinsic flux.

Table 5.2: Best-fit parameters of the fitting model for Suzaku J0105−72.

Components	Par.	Units	Values (at pos. A)[a]	Values (at pos. B)[a]
Absorption	$N_{\rm H}$	(cm^{-2})	$4.87\ ^{+0.44}_{-0.42}\times10^{20}$	$4.86\ ^{+0.44}_{-0.42}\times10^{20}$
Blackbody	$k_{\rm B}T$	(eV)	$71.6\ ^{+2.1}_{-2.0}$	$71.6\ ^{+2.1}_{-2.0}$
	$F_{\rm X}$[b]	(erg s^{-1} cm^{-2})	$1.02\ ^{+0.04}_{-0.06}\times10^{-11}$	$4.66\ ^{+0.31}_{-0.45}\times10^{-12}$
	$L_{\rm X}$[b]	(erg s^{-1})	$1.35\ ^{+0.05}_{-0.07}\times10^{37}$	$6.14\ ^{+0.37}_{-0.30}\times10^{36}$
Edge	E	(keV)	$0.74\ ^{+0.02}_{-0.02}$	$0.74\ ^{+0.02}_{-0.02}$
	τ		$1.22\ ^{+0.52}_{-0.39}$	$1.22\ ^{+0.43}_{-0.39}$
Constant	XIS0		$0.98\ ^{+0.07}_{-0.07}$	$1.00\ ^{+0.07}_{-0.07}$
	XIS1		1.00 (fixed)	1.00 (fixed)
	XIS2		$0.81\ ^{+0.06}_{-0.05}$	$0.94\ ^{+0.07}_{-0.06}$
	XIS3		$0.98\ ^{+0.08}_{-0.07}$	$1.05\ ^{+0.08}_{-0.08}$
χ^2/d.o.f ($\chi^2_{\rm red}$)			187.13/161 (1.16)	187.29/161 (1.16)

[a] The uncertainties are for the 90% confidence ranges, which do not include systematic uncertainties in the instrumental calibration. See http://www.astro.isas.jaxa.jp/suzaku/doc/suzaku_td/ suzaku_td.html for details.

[b] Flux and luminosity are estimated in a range of 0.2–2.0 keV. The distance to the SMC (60 kpc) is assumed to derive the luminosity.

5.1.4 Results

5.1.4.1 Counterpart Search and Long-Term Behavior

First, in a search for possible bursts of this source in the past, we retrieved all of the available archived data taken in the vicinity by *Einstein*, *ROSAT*, *ASCA*, *Beppo-SAX*, *Chandra*, and *XMM-Newton*. We inspected a total of 133 observation that spanned ∼28 years with an integrated exposure time of ∼2 Ms. No source was found in the error region at a comparable brightness with the *Suzaku* source.

Next, in a search for the quiescent X-ray emission of this source and the counterpart in other wavelengths, we further retrieved the SIMBAD database as well as the published X-ray source lists using *Einstein* (Inoue et al., 1983; Seward & Mitchell, 1981; Wang & Wu, 1992), *ROSAT* (Kahabka et al., 1999b; Haberl et al., 2000; Sasaki et al., 2000), and *ASCA* (Yokogawa et al., 2003). Table 5.3 lists the sources within 2′ of the observed peak of the *Suzaku* source.

Table 5.3: List of nearby sources of Suzaku J0105−72.

ID	Source name[a]	R.A. (J2000.0)	Dec. (J2000.0)	Sep.[b]	Object types[a]	References[c]
1	2dFS 2064	$01^h05^m46^s$	$-72°06'51''$	0.14′	Star (B0)	[1]
2	MA93 1554	$01^h05^m50^s$	$-72°06'33''$	0.48′	Emission-line star	[2]
3	FBR2002 J010538−720643	$01^h05^m38^s$	$-72°06'43''$	0.50′	Radio source	[3]
4	2dFS 2059	$01^h05^m44^s$	$-72°07'28''$	0.63′	Star (F0)	[1]
5	RX J0105.7−7207	$01^h05^m40^s$	$-72°07'28''$	0.70′	X-ray source	[4]
6	HFP2000 135	$01^h05^m40^s$	$-72°07'28''$	0.70′	X-ray source	[5]
7	MA93 1542	$01^h05^m39^s$	$-72°06'09''$	0.83′	Emission-line star	[2]
8	OGLE SMC−SC10 106764	$01^h05^m36^s$	$-72°06'22''$	0.83′	Star	[6]
9	OGLE SMC−SC10 104288	$01^h05^m35^s$	$-72°07'22''$	0.91′	Unknown	[7]
10	MA93 1548	$01^h05^m43^s$	$-72°08'11''$	1.34′	Emission-line star	[2]
11	2dFS 2011	$01^h05^m24^s$	$-72°06'44''$	1.59′	Star (B5)	[1]
12	MA93 1531	$01^h05^m27^s$	$-72°07'45''$	1.65′	Emission-line star	[2]
13	2dFS 2110	$01^h06^m06^s$	$-72°06'20''$	1.70′	Emission-line star	[1]
14	IRAS F01038−7224	$01^h05^m29^s$	$-72°08'08''$	1.73′	Infra-red source	[8]
C1	CXOU J010540.1−720726	$01^h05^m40^s$	$-72°07'26''$	0.68′	X-ray source	this work
C2	CXOU J010550.3−720631	$01^h05^m50^s$	$-72°06'31''$	0.55′	X-ray source	this work

[a] The names and object types follow the SIMBAD designation except for C1 and C2. The spectral types are given for stars in the object type when they are available.
[b] Separation from the observed peak.
[c] [1] Evans et al. (2004), [2] Meyssonnier & Azzopardi (1993), [3] Filipović et al. (2002), [4] Filipović et al. (2000), [5] Haberl et al. (2000), [6] Udalski (1998), [7] Ngeow & Kanbur (2006), [8] Moshir & et al. (1990).

We supplemented the list with two faint X-ray sources, which we found during a visual inspection of the archived images. These two sources appear most significantly in a series of *Chandra* images. We determined their positions, named them CXOU J010540.1−720726 and J010550.3−720631, and refer to them as C1 and C2 hereafter. Four X-ray sources (sources 5, 6, C1, and C2) are listed in table 5.3. From the positional coincidence, we consider that the two *ROSAT* sources (sources 5 and 6) and a *Chandra* source (C1) are the same.

Among the sources in table 5.3, source 1 is the only likely counterpart of the *Suzaku*

source for its positional coincidence, including the systematic uncertainty. Other sources, including the two X-ray sources, are displaced too far from both islands A and B, and thus are unlikely to be the counterpart. At the position of source 2, the closest source, except for source 1, the simulated X-ray profile is inconsistent with the observed one (figure 5.3c).

To reinforce our claim that the *Suzaku* source is different from the two nearby X-ray sources, we reduced 26 data sets taken by the Advanced CCD Imaging Spectrometer (ACIS; Garmire et al. 2003) onboard *Chandra* (Weisskopf et al., 2002) to reveal their nature. The exposure times of all ACIS observations were too short to construct spectra. We derived the photometric flux as the mean energy times the net count rate divided by the accumulation area (Tsujimoto et al., 2005b) in the soft-band at each epoch, and found that both C1 and C2 are faint persistent sources (figure 5.6). By combining all of the data sets, we constructed composite X-ray spectra (figure 5.7).

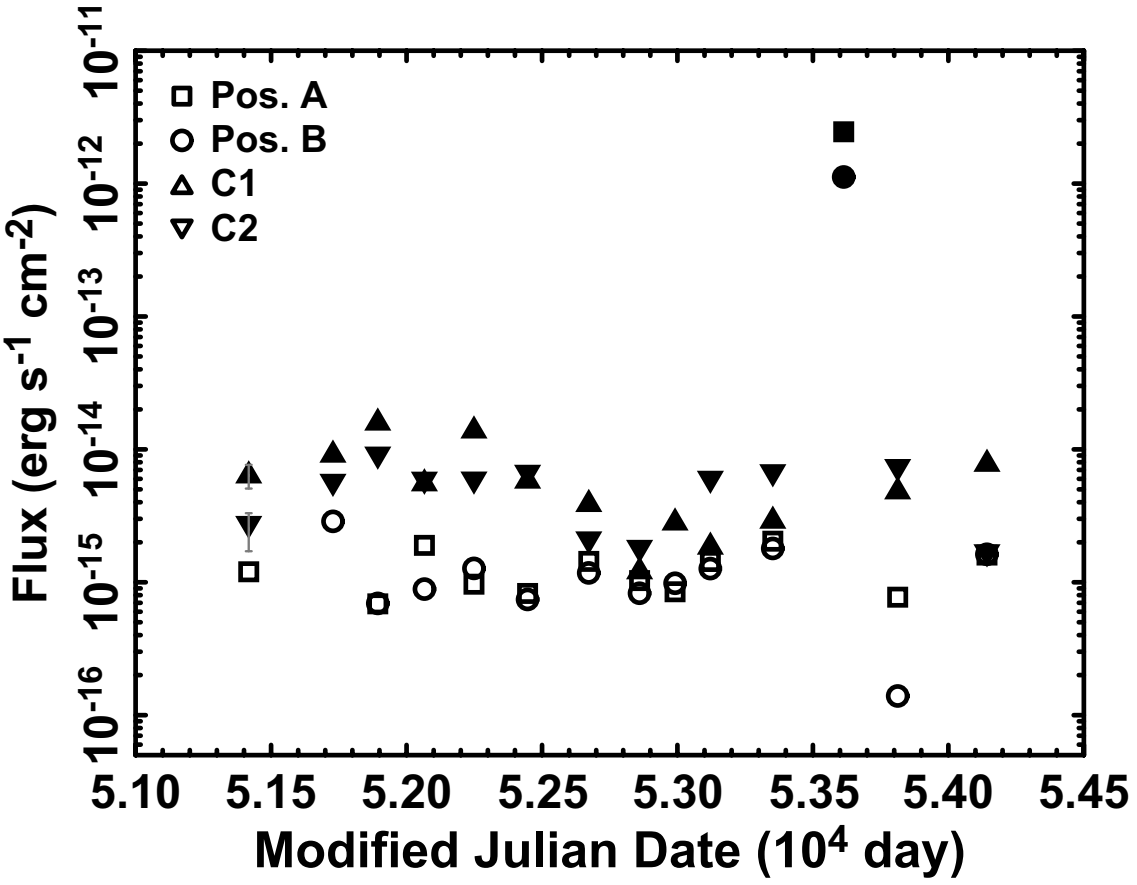

Figure 5.6: Long-term flux (0.5–2.0 keV) variation of the Suzaku and the neighboring *Chandra* sources. The *Suzaku* transient flux at positions A and B are plotted by filled squares and circles, respectively. The 3 σ upper limits at these positions by *Chandra* are also plotted with open symbols. The flux of the two *Chandra* sources (C1 and C2) are shown with upward and downward triangles, respectively. The typical uncertainty for these sources are given for the first data points. *Chandra* data within ten days were grouped.

The two sources show very similar spectra with hard and featureless emission. The absorbed power-law model well explains these spectra. The best-fit index of power, 0.5–2.0 keV flux, and the amount of extinction are 1.3–1.7, 4–5$\times10^{-15}$ erg s^{-1} cm^{-2}, and 0.8–2.2$\times10^{21}$ cm^{-2}, respectively. The hard spectra extending beyond $\sim$5 keV and the amount of absorption larger than that of the *Suzaku* source comprise a sharp contrast with the *Suzaku* spectra, indicating that C1 and C2 are not the *Suzaku* counterpart. We examined a Digitalized Sky Survey (DSS) image at C1 and C2, and found no optical source. From all of these properties, both C1 and C2 are likely to be background active galactic nuclei.

Using the same *Chandra* data sets, we can derive the flux upper limits at the *Suzaku* position for the last seven years and a half. Figure 5.6 shows a long-term trend of the *Suzaku* and the two *Chandra* sources. The figure indicates that the transient source experienced a burst during the *Suzaku* observation, and the flux was amplified by more than 10^3 times compared to the undetected quiescent level.

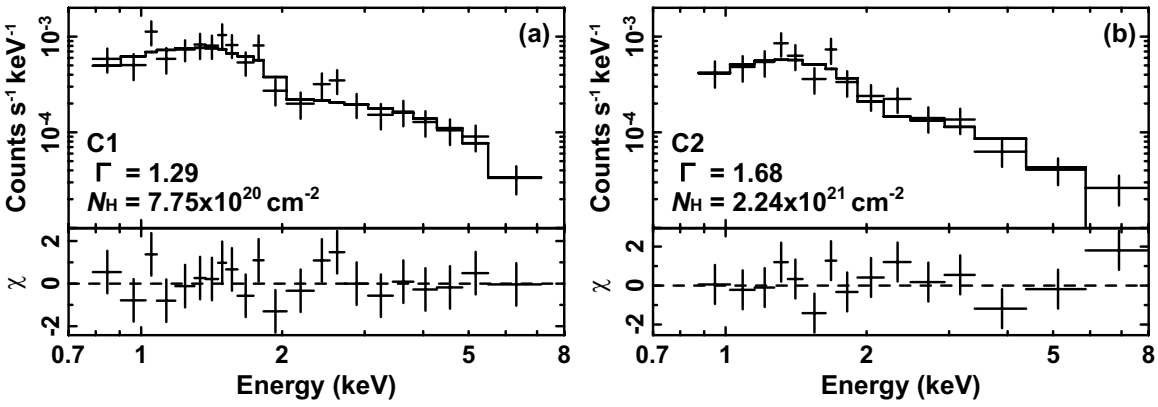

Figure 5.7: ACIS spectra of the two *Chandra* sources (C1 and C2). The upper panels show the background-subtracted spectra combining all the data sets (pluses) and the best-fit absorbed power-law models (solid lines). The lower panels show the residuals to the fit.

5.1.4.2 Nature of Suzaku J0105–72

The transient source has a very soft spectrum of a blackbody temperature of $\sim$72 eV (figure 5.5). Assuming a distance of 60 kpc, the bolometric luminosity is $\sim10^{37}$ erg s^{-1} and the blackbody sphere has a radius of $\sim10^8$ cm. The light curve (figure 5.4) shows a gradual decline of the X-ray flux. The long-term behavior (figure 5.6) indicates that the source was in a burst with an amplified flux of more than 10^3 times the undetected quiescent level.

All of these properties are commonly seen among supersoft X-ray sources (SSSs). SSSs are considered to be a binary of a white-dwarf and a companion star (van den Heuvel et al., 1992) in the SSS phase, in which mass accretion from the companion star fuels hydrogen burning on the white dwarf surface. The X-ray spectra observed by CCD or proportional counter spectrometers are fitted by a blackbody model of $k_{\rm B}T \lesssim 100$ eV and a bolometric luminosity of 10^{36}–10^{38} erg s^{-1} (Greiner, 2000). We therefore conclude that the nature of

the transient source is a white-dwarf binary, which was in the declining end of the SSS phase during the *Suzaku* observation.

SSSs show a variety of temporal behaviors. Some sources are constant supersoft X-ray emitters fueled by continuous mass inflow and steady nuclear burning (e.g., CAL 87; van den Heuvel et al. 1992) with occasional off-states (e.g, CAL 83; Kahabka 1998). Others have an eruptive nature, recognized as classical novae (e.g., RX J0513.9−6951; Reinsch et al. 1999), which can be recurrent (e.g., RS Oph; Hachisu et al. 2007). The transient nature of the Suzaku J0105−72 indicates that the source is in the latter group.

The possible optical counterpart, source 1, is a spectroscopically-identified B0 star. This source may be the companion star of the *Suzaku* source. We caution, however, that many anonymous DSS sources can be found in the positional confidence range of the *Suzaku* source. Follow-up studies are necessary to identify the companion star.

5.1.4.3 White Dwarf Mass

Although the observational data are limited, we can obtain a rough estimate of the mass of the white dwarf. Two independent estimates can be derived from the X-ray light curve and the plasma temperature, both of which indicate that the mass is $\approx$1.2 $M_{\odot}$.

First, the duration of the supersoft phase is a function of mass (figure 3 in Hachisu & Kato 2006). The supersoft phase is seen at a later stage of bursts in classical novae. In the optically thick wind model (Hachisu & Kato 2006 and references therein), the supersoft phase emerges when the wind stops and the inflated photosphere shrinks after the optical burst and ends when the hydrogen shell burning is extinguished. As the mass increases, the duration of the supersoft phase becomes shorter. This is because for a larger mass, and hence for a stronger surface gravity, the accreting mass can be smaller to ignite the thermonuclear process, resulting in a shorter time scale to exhaust the fuel (Hachisu & Kato, 2005).

In the light curve of the supersoft burst (figure 5.6), the *Chandra* observation $\sim$200 days after the *Suzaku* burst gives a strong flux upper limit at the source position. Besides, we do not find any significant emission at the position in the *Suzaku* image obtained $\sim$110 days after the burst on 2005 December 16 (table 5.1), despite the facts that the image was exposed for three-times longer, and that the observation has a roll angle to cover the source well within the XIS field of view. These suggest that the supersoft phase faded out quickly in less than $\sim$3.5 months. We compared the duration with the calculation for the smallest metallicity value (figure 3 and table 8 in Hachisu & Kato 2006), and found that the mass is estimated to be larger than $\sim$1.2 $M_{\odot}$. The rapid decay is reminiscent to the recent supersoft burst from the recurrent nova RS Oph (Osborne et al., 2006), which faded out in $\sim$60 days.

Second, the effective temperature of the soft X-ray blackbody emission is also a function of mass (figure 13 in Ebisawa et al. 2001), in which the temperature becomes higher as the mass increases. This is because for a larger mass, hence for a stronger surface gravity, the plasma electron density increases, which suppresses the ionization. To achieve the observed level of ionization, the plasma temperature has to be higher (Ebisawa et al., 2001). We observed a color temperature of 72$\pm$2 eV, which we assume is similar to the effective temperature. The mass is estimated to be $\sim$1.0–1.2 $M_{\odot}$ for the plasma at a local thermal equilibrium.

5.1.4.4 Absorption Edge

Some SSSs show absorption features in their blackbody spectra, which is thought to arise from absorption by the atmosphere of the white dwarf (Heise et al., 1994; van Teesellng et al., 1996; Hartmann & Heise, 1997). These features provide valuable tools to diagnose the physical status of the atmospheric plasma.

The *Suzaku* spectra show a conspicuous edge feature at ∼0.74 keV with an optical depth of ∼1.2 (figure 5.5 and table 5.2). We consider that this is the O_{VII} K edge at 0.7393 keV (Scofield, 2001). In contrast, we do not see significant features of other K absorption edges by O_{VIII} at 0.8714 keV, N_{VI} at 0.5521 keV, and N_{VII} at 0.6671 keV (Scofield, 2001). The 90% confidence upper limits to the optical depth of these features were measured to be ∼1.18, ∼0.06, and ∼0.25, respectively.

The presence of the O_{VII} K edge and the upper limit of the O_{VIII} K edge set an upper limit to the temperature of the atmosphere. Ebisawa et al. (2001) calculated the fractional density of ions at various ionization stages for several elements (C, N, O, Ne, and Fe), as a function of plasma temperature (0–150 eV), and two electron densities ($n_e = 10^{18}$ and 10^{19} cm^{-3}). The K edge absorption cross sections for O_{VII} and O_{VIII} are $\sim 2.4\times10^{-19}$ and $\sim 1.2\times10^{-19}$ cm^2, respectively (Lang, 2006). The ratio of the optical depth (< 1.42) is converted to the ratio of the column density (< 2.84) of O_{VIII} to O_{VII}. From the ratio and figure 1 in Ebisawa et al. (2001), the atmospheric plasma temperature is constrained to be $\lesssim$58 and $\lesssim$68 eV for the electron density of 10^{18} and 10^{19} cm^{-3}, respectively.

The lack of N absorption edges does not necessarily indicate that the nitrogen is deficient in terms of the N/O ratio from the solar abundance. The metallicity of the SMC is deficient from the solar value by several times (Russell & Dopita, 1992), which we cancelled by using the ratio N/O. From the upper limits of the N_{VI} K edge, the relative abundance of N/O is $\lesssim 0.46$ assuming $k_BT = 60$ eV and $n_e = 10^{18}$ cm^{-3}, which does not contradict with the solar value of ∼0.14 (Anders & Grevesse, 1989).

Finally, we mention that the blackbody plus edge model may be an oversimplification. Using a grating X-ray spectrometer, Orio et al. (2004) showed that the spectrum of a SSS (CAL 87) has in fact a complex of emission lines and absorption edges, which appears as a blackbody spectrum in a study using a CCD spectrometer with a lower resolution by ∼10 times (Ebisawa et al., 2001). Higher resolution spectroscopy observations need be conducted in the future to confirm these results.

5.2 V458 Vulpeculae

5.2.1 Summary

In this section, we describe the observation and results of the classical nova V458 Vul. We performed an X-ray spectroscopic study of this source based on a target-of-opportunity observation (see section 3.2.2) with the *Suzaku* satellite. A 20 ks *Suzaku* observation yielded high signal-to-noise ratio light curves and spectra with the XIS on 88 days after the outburst.

The X-ray spectra show Kα emission lines from N, Ne, Mg, Si, and S, and L-series emission from Fe in highly ionized states. The spectra can be explained by a single temperature ($\sim$0.64 keV) thin-thermal plasma model convolved with a photoelectric absorption. This results have already been published in Tsujimoto et al. (2009).

5.2.2 Target

5.2.2.1 Ground-based monitoring

On 2007 August 8.54 UT, an optical nova reaching a visual magnitude of $\sim$9.5 mag was spotted in the constellation Vulpecula at (R.A., Dec.) = ($19^h54^m24.^s66$, $+20^\circ52'51.''7$) in the equinox J2000.0 (Nakano et al., 2007b). The variable star was fainter by $\sim$8 mag before the explosion if a cataloged source (USNO-A2.0 1050-15545600; Monet et al. 1998) is its precursor. Optical spectroscopic observations on the following day revealed hydrogen and helium emission lines with P-Cygni profiles with a full width at half maximum (FWHM) of 1750–1900 km s^{-1} (Buil & Fujii, 2007), establishing the classical nova nature of this source. The nova was named V458 Vul (Samus, 2007g).

Subsequent ground-based observations were made both photometrically and spectroscopically. The light curve of the nova (Bianciardi et al., 2007b,a; Broens et al., 2007; Casas et al., 2007; Labordena et al., 2007; Nakamura et al., 2007; Scarmato, 2007) declined from the maximum V-band magnitude of 7.65 mag on day 1.42 to $\sim$14 mag in five months with time scales of $t_2 \sim 7$ day (Poggiani, 2008), where t_2 is the time of decline from the optical maximum by 2 mag. The declining trend is globally monotonic, but with several exceptions of local brightening at around 68 and 95 days after the explosion (figure 5.8). The earliest spectra (Kiss & Sarneczky, 2007; Lynch et al., 2007; Munari et al., 2007; Prater et al., 2007; Skoda et al., 2007; Tarasova, 2007) are characterized by P Cygni profiles in H Balmer series, He_I, and Fe_{II} lines. From all these data, the nova was initially classified as a very fast (Gaposchkin, 1957) and a Fe_{II}-type (Williams, 1992) nova. However, subsequent observations obtained approximately one month after the outburst show that the Fe lines have faded and the N_{II} and N_{III} lines have gained prominence, indicating an evolution toward a He/N class nova (Poggiani, 2008). Wesson et al. (2008) found that this nova occurred inside a planetary nebula with Hα imaging, a second such case after GK Per.

We adopt the distance to V458 Vul to be 13 kpc (Wesson et al., 2008). In a series of Hα images taken in May 2008, a bright circumstellar knot was discovered at $3.''5$ away from the central source. By assuming that the knot is illuminated by the flash of the nova, the distance of $\sim$13 kpc was derived. This is consistent with two other distance estimates. The one is derived from a maximum-magnitude versus rate-of-decline relation (MMRD; Downes

& Duerbeck 2000), an empirical relation that intrinsically bright novae fade our fast. The other is derived from the assumption that the measured radial velocity stems only from the Galactic rotation (Wesson et al., 2008).

The interstellar extinction ($A_{V,\mathrm{ISM}}$) was estimated to be 1.76 ± 0.32 mag (Poggiani, 2008). This converts to an interstellar hydrogen-equivalent absorption column density ($N_{\mathrm{H,ISM}}$) of $3.15 \pm 0.57 \times 10^{21}$ cm^{-2} using the relation $\mathrm{N_{H,ISM}/A_{\mathit{V},ISM}} = 1.79 \times 10^{21}$ cm^{-2} mag^{-1} (Predehl & Schmitt, 1995). The line-of-sight extinction integrated through our Galaxy toward V458 Vul is estimated from $\mathrm{H_I}$ maps to be 3.7×10^{21} cm^{-2} (Kalberla et al., 2005) or 4.0×10^{21} cm^{-2} (Dickey & Lockman, 1990), which is consistent that the nova is within in our Galaxy.

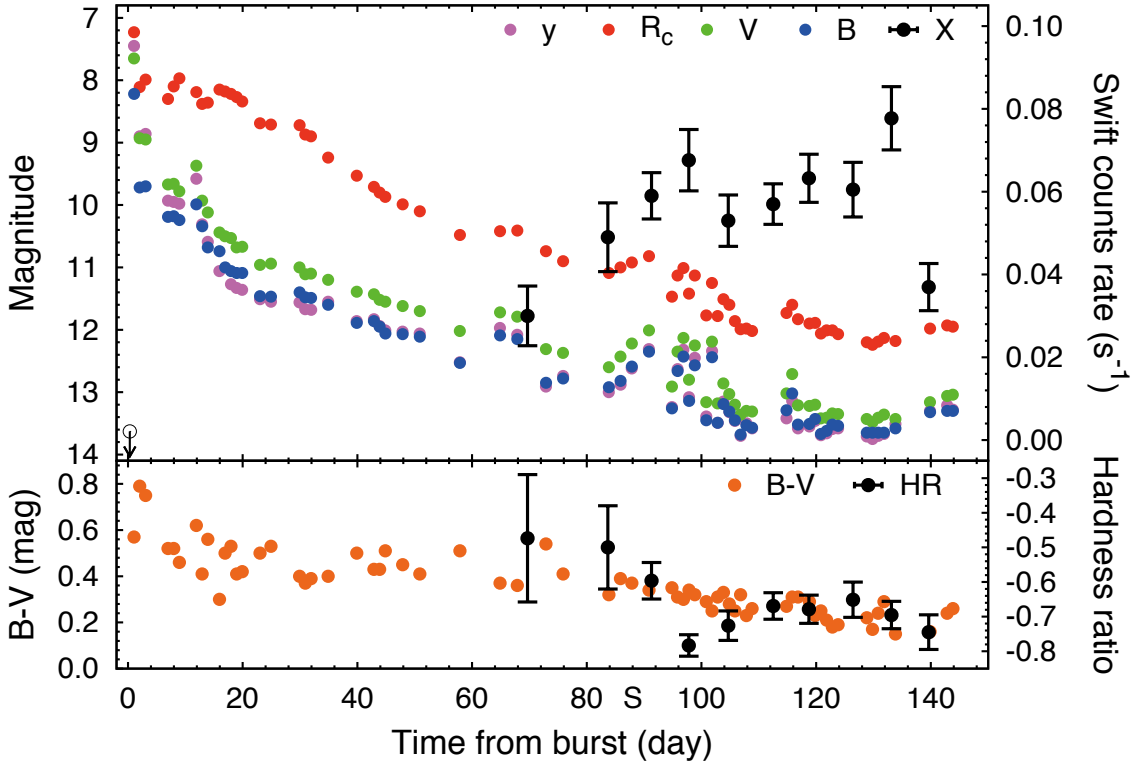

Figure 5.8: Evolution of V458 Vul in brightness and color (upper and lower panels, respectively). The origin of the abscissa is day 54320.54 in modified Julian date when the nova was first spotted (Nakano et al., 2007b). The epoch of the *Suzaku* observation is indicated with "S" on the abscissa. In the upper panel, the *y*-, *Rc*-, *V*-, and *B*-band magnitudes (private communication with K. Nakajima) are respectively shown in magenta, red, green, and blue, while the *Swift* X-ray count rate (0.3–10.0 keV) is shown in black with 1-σ errors (Ness et al., 2009a). The 95.5% upper-limit for non-detected X-rays on day 1 is indicated by an open circle. In the lower panel, the $B-V$ color is shown in orange, while the *Swift* hardness ratio is in black with 1-σ errors. Hardness ratio is defined by (H−S)/(H+S), where S and H are the *Swift* count rates in the 0.25–1.5 keV and 1.5–10 keV band, respectively.

5.2.2.2 Space-based monitoring

Monitoring observations were also conducted with space-based facilities. The XRT onboard Swift was employed to take an immediate follow-up image on day 1 and repeated snapshots from day 71 to 140 (figure 5.8). The X-ray emission was not detected on day 1, but it started to emerge on day 70 during the first optical rebrightening. A total of 192 X-ray counts were accumulated in a short observation of ∼6.7 ks, which is at least 10 times brighter than the upper limit to the X-ray counts on day 1 (Drake et al., 2007). The X-ray flux continued to increase until the peak on day ∼100, showed a stable flux for ∼30 days, then decreased in flux quite sharply on the last *Swift* visit on day 140.

The XRT spectrum on day 70 has significant signal above 1 keV, indicating that hard X-ray emission component was present in addition to any soft emission typical of the SSS phase (Drake et al., 2007). No detailed spectroscopy was possible due to the paucity of counts. We therefore requested a director's discretionary time for the *Suzaku* telescope to obtain an X-ray spectrum of better statistics and resolution. A ∼20 ks observation was conducted on day 88. *Swift* resumed its observing campaign on day 315. In this later phase, the hard X-ray flux is highly variable and is anti-correlated with the UV flux. The *Swift* results, including the later observations, are presented in Drake et al. (2008) and Ness et al. (2009a).

5.2.3 Observations and Data Reduction

Suzaku observed V458 Vul on 2007 November 4 from 7:51 UT to 21:00 UT. We concentrate on the XIS data, which has sensitivity for the energy range of interest. The spaced-row charge injection technique yields an improved FWHM resolution of 145–174 eV at 5.9 keV in the observation. The observation was conducted using the normal clocking mode with a frame time of 8 s. Data were cleaned using the processing version 2.1 to remove non–X-ray events and those taken during South Atlantic Anomaly passages, at elevation angles below 5° from the Earth rim, and at elevation angles below 20° from sunlit Earth rim. After filtering, the net integration time is ∼19.6 ks. We used HEASoft version 6.4.1[4] for the data reduction and the X-ray Spectral fitting package (Xspec) version 11.3.2[5] for the X-ray spectral analysis.

[4]See http://heasarc.gsfc.nasa.gov/docs/software/lheasoft/ for detail.
[5]See http://heasarc.gsfc.nasa.gov/docs/xanadu/xspec/index.html for detail.

5.2.4 Analysis

5.2.4.1 Image and Timing

Figure 5.9 shows the XIS image in the 0.2–5.0 keV band obtained by merging the events recorded by all the three CCDs. Four sources were detected by visual inspection. The brightest one at the center is V458 Vul based on astrometric consistency with the *Swift* data. We fine-tuned the coordinate of the XIS image using this source as a reference. The resulting positions, X-ray count rates (CR), and hardness ratio (HR) of the four sources are summarized in table 5.4. None of the sources except for V458 Vul has records in the SIMBAD or the NASA/IPAC Extragalactic Database, leaving their natures unclear.

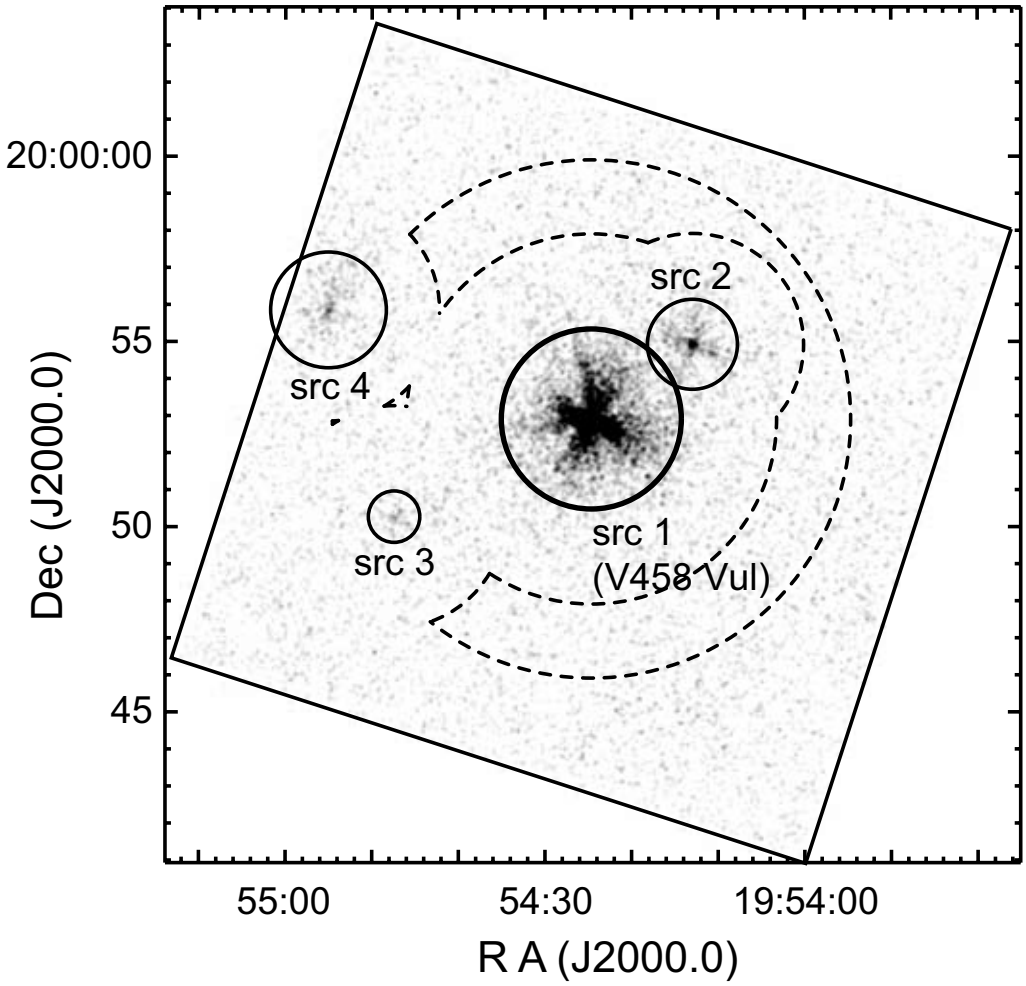

Figure 5.9: Smoothed XIS image in the 0.2–5.0 keV band. Three CCD images were merged and a Gaussian smoothing was applied. V458 Vul (source 1) and three faint sources (sources 2–4) were detected. The source regions are shown with solid circles around each source, while the background region for V458 Vul is shown with broken annulus with masks.

Table 5.4: List of nearby sources.

Source	R.A. (J2000.0)	Dec. (J2000.0)	CR[a] (s^{-1})	HR[b]
1[c]	$19^h54^m25^s$	$+20°52'52''$	9.8×10^{-2}	-0.55
2	$19^h54^m13^s$	$+20°54'53''$	7.9×10^{-3}	$+0.43$
3	$19^h54^m47^s$	$+20°50'13''$	2.7×10^{-3}	$+0.40$
4	$19^h54^m55^s$	$+20°55'48''$	5.2×10^{-3}	-0.34

[a] The background-subtracted count rate in the 0.2–5.0 keV averaged over the three CCDs. The values are normalized to the circular aperture of a $3'$ radius.
[b] The hardness ratio defined as (H−S)/(H+S), where H and S are background-subtracted count rates in the hard (1.5–5.0 keV) and soft (0.2–1.5 keV) band, respectively.
[c] V458 Vul. The contamination by source 2 is not corrected in the CR and HR values.

The background was subtracted to compute CR and HR. Source counts were integrated in circles with adaptively-chosen radii to maximize the ratio against background for all sources (solid circles in figure 5.9). Background counts were accumulated in a different method for V458 Vul and the others. For V458 Vul, background was taken from an annular region with inner and outer radii of $5'$ and $7'$, respectively. For the other sources, it was from annuli around V458 Vul with the inner circle circumscribed to and the outer circle inscribed to the source extraction circle of each source. The $3'$ circles around all sources were masked in these annuli. In this way, we cancelled the contamination to the faint three sources by the dominantly bright source 1. The background was corrected for the vignetting before subtracting from the source. The contamination of source 1 by source 2 is considered later. We constructed a light curve of V458 Vul and found no significant changes. The curve was fitted with a constant flux model with a null hypothesis probability of 53%.

5.2.4.2 Spectrum

Figure 5.10 shows the background-subtracted XIS spectra of V458 Vul in a linear scale at the 0.4–3.5 keV band. We see conspicuous Kα line emission from N_{VII}, Ne_{IX}, Ne_{X}, Mg_{XI}, Mg_{XII}, Si_{XIII}, and S_{XV}. We also see some emission from Fe_{XVII} L-series lines.

In order to model the spectrum, we generated the redistribution matrix functions and the auxiliary response functions using `xisrmfgen` and `xissimarfgen` (Ishisaki et al., 2007), respectively. The difference in effective area arising from different off-axis angles between the source and the background regions were compensated following the procedure described in Hyodo et al. (2008).

The contamination by the nearby source 2 was considered by including an additional absorbed power-law model (7.8×10^{21} cm^{-2} for the absorption column and 2.1 for the photon index) that best describes its spectrum. From a ray-tracing simulation, we found that $\sim$1.5% of the emission from source 2 is in the source extraction region of source 1. Fortunately, sources 1 and 2 have different spectral hardness (table 5.4) and the contamination by source 2 is almost negligible.

We fitted the 0.3–3.0 keV spectrum of source 1 using an optically-thin thermal plasma model in collisional equilibrium (the APEC model; Smith et al. 2001) convolved with an interstellar absorption assuming the cross sections and the chemical abundance in Wilms et al. (2000). The plasma temperature ($k_{\rm B}T$) and its emission measure as well as the hydrogen column density ($N_{\rm H}$) were allowed to vary.

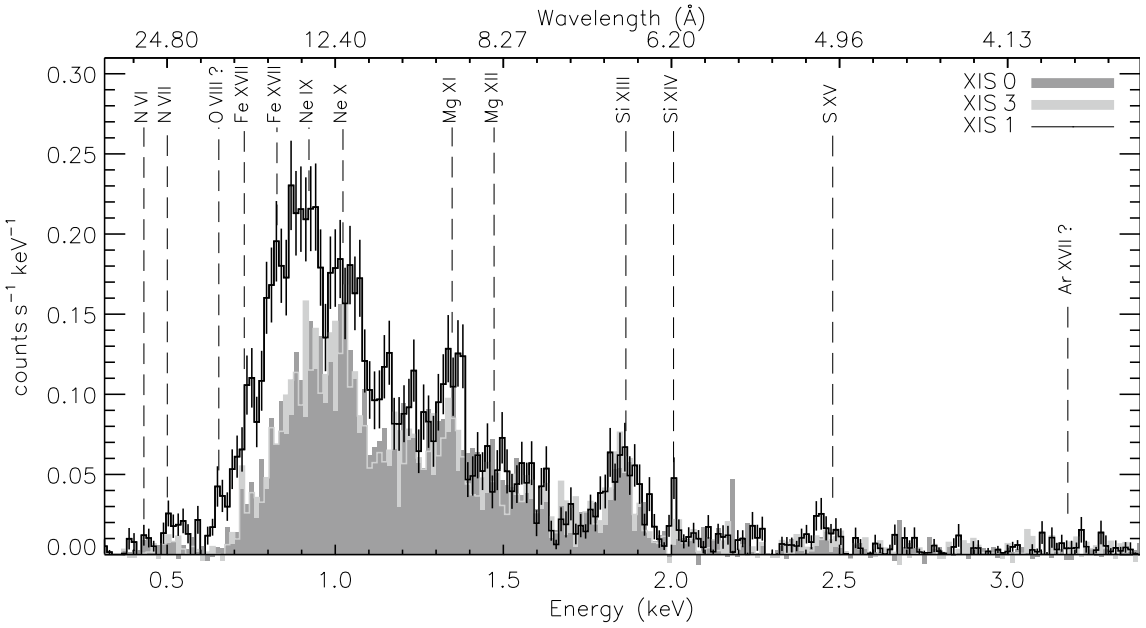

Figure 5.10: X-ray spectra of V458 Vul (background subtracted) in a linear scale observed with the XIS0 and XIS3 (both FI devices; dark and light gray shadings, respectively) and with the XIS1 (BI device; solid line). The energies of plausible emission lines are labeled.

For the chemical composition of the plasma, we tried four models with different constraints on the abundance of elements (Model 1–4). The base-line model is the Model 1, in which the abundance of elements with noticeable Kα emission (N, Ne, Mg, Si, and S) were allowed to vary individually. Also, the abundance of Fe was also varied, as the Fe L series emission is necessary to explain the spectrum between the O_{VIII} Kα (0.65 keV) and Ne_{IX} Kα (0.92 keV) features. The abundance of Ni, which also contributes through its L series emission, was tied to that of Fe at the solar ratio. Other elements were fixed to the solar abundance. Here, we assumed the solar values by Anders & Grevesse (1989). The spectrum and the best-fit model is shown in figure 5.11, and the best-fit parameters are summarized in table 5.5. Additional components are not statistically required to explain the spectra.

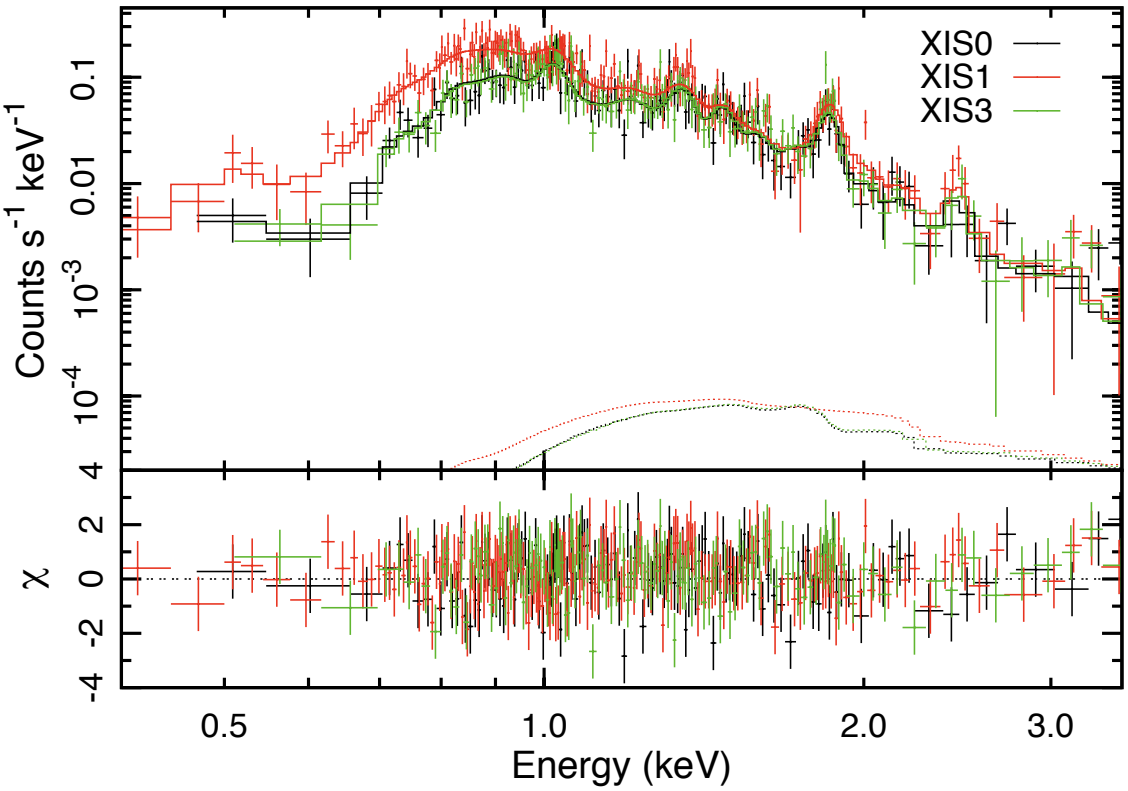

Figure 5.11: Best-fit models to the background-subtracted spectra in a logarithmic scale. Different colors are used for each CCD. The top panel shows the data with crosses and the best-fit model with solid lines. The contamination by the nearby source 2 is included as dotted lines. The bottom panel shows the residuals to the fit.

For the other models, we put additional constraints on the Model 1 for the purpose of reducing the statistical uncertainties. In the Model 2, we tied the abundance of intermediate-mass elements (Ne, Mg, Si, S) after confirming that the abundance of these elements is consistent with each other in the Model 1. In the Model 3, we fixed the N abundance to be 1 solar. In the Model 4, we fixed the abundance of less constrained elements (N, O, and S) than the others to be 1 solar. The best-fit parameters for these models are also tabulated in

table 5.5. The results are consistent among all these models except for the Model 4, in which the estimate of $N_{\rm H}$ and the abundance values are higher and the χ^2-fitting is worse than the others with significant residuals in the N–O Kα energy range. We therefore consider that this is not an appropriate model, and interpret the spectrum based on the result of the other three models.

Table 5.5: Best-fits spectral parameters of V458 Vul.

Param.	Unit	Model 1[ab]	Model 2[ab]	Model 3[ab]	Model 4[ab]
$N_{\rm H}$	10^{21} (cm^{-2})	2.8 (1.8–4.6)	2.8 (1.8–4.4)	2.8 (1.9–4.1)	3.8 (2.9–4.8)
$k_{\rm B}T$	(keV)	0.64 (0.57–0.71)	0.65 (0.60–0.71)	0.64 (0.60–0.70)	0.64 (0.59–0.69)
$Z_{\rm N}$	(solar)	1.0 (0.0-45)	1.3 (0.0–35)	1 (fixed)	1 (fixed)
$Z_{\rm O}$	(solar)	0.0 (0.0–1.6)	0.0 (0.0–1.1)	0.0 (0.0–0.8)	1 (fixed)
$Z_{\rm Ne}$	(solar)	0.6 (0.3–1.8)	0.5 (0.3–1.1)	0.6 (0.3–1.2)	1.2 (0.6–1.9)
$Z_{\rm Mg}$	(solar)	0.4 (0.2–1.3)	0.5 (0.3–1.1)	0.4 (0.2–0.9)	0.9 (0.5–1.4)
$Z_{\rm Si}$	(solar)	0.5 (0.3–1.3)	0.5 (0.3–1.1)	0.5 (0.3–0.9)	0.9 (0.5–1.5)
$Z_{\rm S}$	(solar)	0.6 (0.0–1.5)	0.5 (0.3–1.1)	0.6 (0.0–1.3)	1 (fixed)
$Z_{\rm Fe}$	(solar)	0.2 (0.1–0.8)	0.2 (0.1–0.6)	0.2 (0.1–0.4)	0.5 (0.3–0.7)
$Z_{\rm Ni}$	(solar)	0.2 (0.1–0.8)	0.2 (0.1–0.6)	0.2 (0.1–0.4)	0.5 (0.3–0.7)
$F_{\rm X}$[c]	10^{-12} (erg s^{-1} cm^{-2})	1.1 (0.5–1.7)	1.1 (0.7–1.5)	1.1 (0.7–1.6)	1.1 (0.8–1.5)
$L_{\rm X}$[cd]	10^{34} (erg s^{-1})	5.9	5.7	5.9	7.2
χ^2/d.o.f.	.....	385.2/456	391.0/449	385.3/447	403.3/449

[a] The statistical uncertainties are indicated by the 90% confidence range.
[b] Fitting with constraints with $Z_{\rm Fe} = Z_{\rm Ni}$ (Model 1), $Z_{\rm Fe} = Z_{\rm Ni}$ and $Z_{\rm Ne} = Z_{\rm Mg} = Z_{\rm Si} = Z_{\rm S}$ (Model 2), $Z_{\rm Fe} = Z_{\rm Ni}$ and $Z_{\rm N} = 1$ (Model 3), and $Z_{\rm Fe} = Z_{\rm Ni}$ and $Z_{\rm N} = Z_{\rm O} = Z_{\rm S} = 1$ (Model 4).
[c] The X-ray flux in the 0.3–3.0 keV band.
[d] A distance of 13 kpc is assumed.

In a transient plasma like that characterizing our V458 Vul spectra, electrons and ions may not have reached a collisional ionization equilibrium. For non-equilibrium ionization (NEI) plasma, low levels of ionization of ions can be seen for the temperature determined from the electron bremsstrahlung emission (e.g., Mewe 1999). As a result, the energies of dominant emission features appear shifted toward lower energies in X-ray CCD spectra by $\gtrsim$10 eV, which is detectable by XIS (Miyata et al., 2007; Bamba et al., 2008). The degree of the shifts is parameterized by the ionization parameter $\int_0^t dt'\ n_{\rm e}(t')$, where $n_{\rm e}(t)$ is the electron density as a function of time t. We fitted the XIS spectra using an NEI model (Hamilton et al., 1983; Borkowski et al., 1994; Liedahl et al., 1995; Borkowski et al., 2001) and found a 90% lower limit to the ionization parameter of 1.4×10^{12} s cm^{-3}. Finding a value higher than $\approx10^{11}$–10^{12} s cm^{-3} implies that the XIS spectrum is consistent with being at a collisional equilibrium (Mewe, 1999).

5.2.5 Results

5.2.5.1 Interstellar and Circumstellar Absorption

From our spectral fitting, we derived a neutral hydrogen column density of $N_{\rm H}$ = (1.8–4.6) $\times$ 10^{21} cm^{-2} along the line of sight to V458 Vul (table 5.5). The value is consistent with the interstellar absorption estimated by Poggiani (2008). By the time of the *Suzaku* observation, the color index (B–V) of the nova has plateaued from the initial redder values. Therefore, most of the observed absorption stems from the interstellar medium, not from the material local to the nova.

The average interstellar hydrogen density ($n_{\rm H,ISM}$) in the line of sight is then estimated as $\sim$0.1 cm^{-3}, which is smaller by an order of magnitude than the canonical value of $n_{\rm H,ISM}$ = 1 cm^{-3}. We suspect that this is due to the off-plane location of the nova at $-$3.6 degree in the Galactic latitude (Schlegel et al., 1998).

5.2.5.2 Chemical Abundance

Previous Abundance Studies

White dwarfs causing novae can have two different chemical compositions depending on their initial mass; CO-type for sources less than $\sim$1.2 $M_\odot$ and ONe-type for those more than 1.1–1.2 $M_\odot$ (Iben & Tutukov, 1989). With a less mass, the gravitational potential on the white dwarf surface is smaller and the peak temperature in the thermo-nuclear runaway is lower. Together with a different core composition, the two types of novae yield different species of elements in runaways. The major nuclear reaction in CO novae does not go beyond elements heavier than O, while that in ONe novae reaches up to Si and S. Theoretical calculations show that intermediate-mass species are enhanced in the ejecta from ONe novae (Starrfield et al., 2008; Jose & Hernanz, 1998; José & Hernanz, 2007). Also, the ratio of C and N against O increases as the white dwarf mass increases (Jose & Hernanz, 1998; José & Hernanz, 2007). The chemical pattern of nova ejecta thus provides important clues to guess the type of the white dwarf that hosts the nova.

Three novae have been studied to discuss the chemical abundance in their hard X-ray plasma. V382 Vel was observed by medium-resolution gas scintillation proportional counters aboard *Beppo-SAX* on day 15 (Orio et al., 2001c) and by a high-resolution grating spectrometer aboard *Chandra* on day 268, after the nova had turned off (Ness et al., 2005). V4633 Sgr was observed by medium-resolution CCD spectrometers aboard *XMM-Newton* 2.6 and 3.5 years after the explosion (Hernanz & Sala, 2007). RS Oph was observed by high-resolution grating on *Chandra* and *XMM-Newton* (Nelson et al., 2008; Drake et al., 2008; Ness et al., 2009a) ten times from day 14 to day 239.

In the high-resolution grating spectra of the early hard X-rays in RS Oph (Ness et al., 2009a), bremsstrahlung continuum emission and line emission are resolved. N is found overabundant as a fingerprint of the CNO cycle for the H fusion. High N abundances thus point to the ejected material from the white dwarf as the source for the X-ray emission. However, in the specific case of RS Oph, the abundances must be compared to those of the accreted material from its giant companion (thus the composition of the companion) in

order to confirm that the observed X-rays originate from the white dwarf ejecta. In a grating spectrum of V382 Vel, a high N abundance was also found (Ness et al., 2005). However, the observation was conducted well after the nova had turned off, thus reflecting the late nebular emission rather than the early hard emission.

In the medium-resolution studies, the chemical pattern is murkier for being unable to derive the abundances element by element. Nevertheless, Orio et al. (2001c) found a hint of significant iron depletion in V382 Vel. Hernanz & Sala (2007) tried two thermal models with different chemical patterns to fit the V4633 Sgr spectra, one with all elements fixed to the solar values and the other fixed to those of a CO nova shell. Both models can explain the data.

Abundance of V458 Vul

We observed V458 Vul with the medium-resolution spectrometer aboard *Suzaku*. A high signal-to-noise ratio spectrum allows us to constrain the abundance of metals individually for seven elements (table 5.5). The abundance values are subject to change due to the unconstrained He abundance. He, along with H, contributes to the continuum emission in the observed band. We fixed the He abundance to the solar value in our fitting procedures, but an increased abundance of He leads to an increased estimate of metal abundances. Therefore, the best-fit abundance values of metals should be considered only in a sense relative to each other.

Using the result of the Model 2, we define the metal abundance, $Z_{\rm m} = 0.5 \times Z_{\odot}$, which we derived by collectively thawing Ne, Mg, Si, and S abundances. With respect to this value, the best-fit parameters of the spectrum shows an enhanced N abundance with $Z_{\rm N}/Z_{\rm m} \sim 2.6$ and deficient O and Fe abundances with $Z_{\rm O}/Z_{\rm m} \sim 0$ and $Z_{\rm Fe}/Z_{\rm m} \sim 0.4$.

We note here that systematic uncertainties can arise from possible inaccurate modeling. First, the uncertainty in the $N_{\rm H}$ estimate amplifies the uncertainty of the N and O abundances, although we consider it unlikely that the both elements have the solar abundance from the result of the Model 4. Second, a single temperature model may be an oversimplification. This leads to particularly high uncertainties in elements formed far away from the isothermal temperature. For example, in a 0.65 keV plasma, the lines of S and Si (the peak formation temperature ∼1.4 keV) have to be formed in the wings of their line emissivity functions. Small changes in temperature require large changes in abundance, because the slope of the line emissivity functions is steeper in their wings than near the peak. This explains the increasing uncertainties of Mg, Si, to S in the Model 1. The same arguments apply for the low-temperature lines of N and O (the peak formation temperature ∼0.3 keV). If the plasma is not isothermal and additional components with temperatures of 0.3 and 1.4 keV are present, significantly lower abundances for N, O, Si, and S will be obtained. Without a knowledge of the true emission measure distribution such as that determined by Ness et al. (2005), it is impossible to determine the accurate abundances. We speculate, however, that contributions from plasma with temperatures below 0.3 keV and above 1.4 keV are minor, judging from a high ratio of $\rm N_{VII}$ to $\rm N_{VI}$ and a low ratio of $\rm Si_{XIV}$ and $\rm Si_{XIII}$ (figure 5.10).

With these uncertainties in mind, it is interesting to note that an N enhancement and a Fe deficiency in hard X-ray emission are seen in all novae with a $Z_{\rm N}$ and a $Z_{\rm Fe}$ measurement,

respectively, including the present work (Mukai & Ishida, 2001; Orio et al., 2001c; Ness et al., 2005, 2009a). We speculate that this typical pattern in the X-ray spectra is a consequence of these novae belonging to the ONe-type. The deficiency of the Fe abundance with respect to the intermediate-mass elements is consistent with the theoretical understanding that ONe-type novae produce elements up to Si and S. The N enhancement can be interpreted as an outcome of the H fusion on the white dwarf surface, where the CNO cycle produces abundant N by the N to O conversion as the rate-determining process The abundance of N with respect to O increases for more massive ONe-type novae. A quantitative comparison with theoretical work (Starrfield et al., 2008; Jose & Hernanz, 1998; José & Hernanz, 2007) is hampered by a relatively large uncertainty in our fitting results, but the overall abundance pattern in V458 Vul indicates that this is an ONe-type nova.

5.2.5.3 Plasma Origin and Parameter Constraints

We first argue that the X-ray emission observed from V458 Vul is most likely to be the internal shock of the nova ejecta, and not due to other processes. The hard spectrum exceeding 1 keV shows that it is neither the SSS emission nor the reprocessed emission of it. The possible N enhancement is consistent with the plasma mostly composed of the ejecta. Shocks might occur externally between the ejecta and swept-up interstellar matter, but the total mass of the swept-up matter by the time of the *Suzaku* observation is too small compared to the ejected mass. The ejecta mass is estimated to be in the range of $\sim 10^{-3}$–10^{-6} $M_\odot$ (Gehrz et al., 1998), whereas the swept-up mass is $\sim 4\pi/3(v_0 t_{\rm S})^3 m_{\rm p} n_{\rm H,ISM}$ $\sim 10^{-11}$ $M_\odot$ where $m_{\rm p}$ is the proton mass, $n_{\rm H,ISM} = 1$ cm^{-3} is the ISM density, $v_0 = 1.8 \times 10^3$ km s^{-1} is the initial speed of expanding shell (Buil & Fujii, 2007), and $t_{\rm S}$ is the time of the *Suzaku* observation elapsed from the explosion. If we adopt $n_{\rm H,ISM} = 155$ cm^{-3}, the densest value in the surrounding planetary nebula (Wesson et al., 2008), the swept-up mass is far smaller than the typical ejecta mass.

In the case of symbiotic novae like RS Oph, early hard emission can be produced by external shocks between the expanding ejecta and the stellar wind of the giant companion (Bode et al., 2006). This does not work for classical novae, in which the secondary is a main sequence star and the stellar wind is not dense enough (O'Brien et al., 1994). While no observational evidence exists that V458 Vul is not a symbiotic nova, shock emission by collisions between the expanding ejecta and the stellar wind of the companion is not likely. In RS Oph, the shock itself occurred over a relatively short time scales, and the hard X-ray emission quickly faded afterwards (Bode et al., 2006), while the X-ray count rate in V458 Vul rises with no indication of a decline. It is most likely that the X-rays from V458 Vul originate in shocks internal to the expanding system, presumably between slower and earlier pre-maximum ejecta and faster and later nova winds (Friedjung, 1987; Mukai & Ishida, 2001). However, in the later *Swift* observations one year after the nova, this hard X-ray emission still remains and exhibits highly variable flux in anti-correlation with the UV flux (Ness et al., 2009a). Elaborated theoretical work is necessary to explain all these properties to see if the internal shock interpretation is valid.

From the spectral fits, the absorption-corrected X-ray luminosity at the *Suzaku* observation is $L_{\rm X}(t_{\rm S}) = 6{\times}10^{34}$ erg s^{-1} in the 0.3–3.0 keV band at an assumed distance of 13 kpc.

The luminosity is in a typical range for classical novae (Mukai et al., 2008). The X-ray volume emission measure at the same time is $EM(t_{\rm S}) = n_{\rm e}^2(t_{\rm S})V_{\rm X}(t_{\rm S}) \sim 7{\times}10^{57}$ cm^{-3}, where $V_{\rm X}(t)$ and $n_{\rm e}(t)$ represent the X-ray-emitting volume and the plasma density as a function of time t.

With these measurements and several simplifying assumptions, a crude estimate can be obtained for the lower and upper bounds of the plasma density at $t_{\rm S}$. Assuming that the plasma density is uniform and that the expansion velocity v_0 has not changed since the outburst, the X-ray emitting volume cannot exceed the volume of the expanding shell; i.e., $V_X(t_{\rm S}) < 4\pi/3(v_0 t_{\rm S})^3$. The observed $EM(t_{\rm S})$ thus implies that the density must be $n_{\rm e}(t_{\rm S})$ $> 8{\times}10^5$ cm^{-3}. If we further assume that the plasma was created at one epoch and not heated repeatedly, the plasma density cannot be too high to cool radiatively too soon. The cooling time $t_{\rm rc}$ at $t_{\rm S}$ is approximated as $3n_{\rm e}(t_{\rm S})k_{\rm B}T(t_{\rm S})V_X(t_{\rm S})/L_{\rm X}(t_{\rm S})$. With $t_{\rm rc} > 100$ day, which is an approximate duration of the detected X-ray coverage by *Swift*, the upper bound is estimated as $n_{\rm e}(t_{\rm S}) < 4{\times}10^7$ cm^{-3}. The lower and upper bounds put $n_e(t_{\rm S})$ within a range of two orders around $\approx 10^6$ cm^{-3}. Orio et al. (1996) derived a similar density of $n_{\rm e}$ $\sim 2{\times}10^6$ cm^{-3} assuming $V_{\rm X}(t) = 4\pi/3(v_0 t)^3$ for V351 Pup observed 16 month after its explosion.

5.3 V2491 Cygni

5.3.1 Summary

We performed X-ray spectroscopic studies of V2491 Cyg based on target-of-opportunity observations with the *Suzaku* and *XMM-Newton* satellites as well as archived data with the *Swift* satellite. Time-sliced X-ray spectra were obtained at several post-nova time intervals on days 9, 29, 40, 50, and 60–150 in addition to a pre-nova interval between days −322 and −100 all relative to the time when the classical nova was spotted.

On day 9, super-hard X-ray (> 10 keV) spectra was obtained with the quite a high absorption column density ($\sim 10^{23}$ cm^{-2}) and continuum emission up to ∼70 keV, which was the highest energy photons ever detected from a classical nova. On day 29, a completely different soft spectra were obtained, which can be explained by a combination of a blackbody (temperature of ∼30 eV) and a two-component thin-thermal plasma (temperatures of ∼0.4 and ∼2 keV) model. In the time series of the spectra, we also found remarkable changes in emission lines at the Fe K complex; the 6.7 keV line from Fe_{XXV} was significantly detected on days 9, 40, 50, 60–150, and in the pre-nova spectra. Both the 7.0 keV Lyα line from Fe_{XXVI} and the 6.4 keV fluorescence line from Fe_I were detected on days 50 and 60–150. The results have already been published in Takei et al. (2009) and Takei & Ness (2010), and submitted in Takei et al. (2011).

5.3.2 Target

5.3.2.1 Ground-based observations

An optical nova was discovered on 2008 April 10.728 UT (54566.73 d in modified Julian date) in the constellation Cygnus at (R.A., Dec.) = ($19^h43^m01.96^s$, $-32°19'13.8''$) in the equinox J2000.0 (Nakano et al., 2008b). We define the epoch of the discovery as the origin of time throughout this research. The optical nova showed a brightness of 7.7 mag at the discovery and 7.1 mag at the peak one day later using an unfiltered CCD camera (Nakano et al., 2008b). In the United States Naval Observatory catalogue (USNO-B1.0; Monet et al. 2002), a very faint infrared source 1223-0482965 was found near this position (Henden & Munari, 2008) with an R-band magnitude of 15.5 mag, which disappeared below $R = 18.6 \pm 0.5$ mag in the images taken from 2007 July to November (Balman et al., 2008). The variable star suddenly increased its brightness at the outburst by 5–10 mag (Jurdana-Sepic & Munari, 2008). The nova was named V2491 Cygni (Samus, 2008c).

Photometric and spectroscopic studies of the nova were conducted with subsequent ground observations (Ashok et al., 2008; Ayani & Matsumoto, 2008; Lynch et al., 2008a; Naik et al., 2009; Rudy et al., 2008; Tomov et al., 2008b,a). The development of brightness and color is shown in figure 5.12. In early observations, P-Cygni absorption profiles were found in Hβ and Hγ profiles (Tomov et al., 2008b), establishing a nature of a classical nova on this source. Broad emission lines with complex profiles from the H Balmer series, He_I, O_I, and Fe_{II} were also found in the optical spectra (Ayani & Matsumoto, 2008; Tomov et al., 2008b,a). Strong emission lines from N_I and N_{II} were found in the infrared spectra (Lynch et al., 2008a; Naik et al., 2009). Based on these results, V2491 Cyg was classified as a He/N

type nova (Williams et al., 1991). O_I emission lines indicate a reddening of $E_{B-V} = 0.3$ (Lynch et al., 2008a) and 0.43 mag (Rudy et al., 2008) on days 2 and 7, respectively. A periodic flux modulation was found in the V-band and R-band with a period of 0.09580 d (Baklanov et al., 2008). In the following months of the outburst, the velocity width of the Hα line continued to decline, while that of the Hβ line increased (Helton et al., 2008). Prominent emission lines from N_{II} and N_{III} emerged in the spectrum, supporting the conclusion that this is a He/N nova (Helton et al., 2008). Using all these emission and absorption features, the ejecta velocity was measured with a mean value of $\sim$4000 km s^{-1}. The spectral characteristics are similar to recurrent novae such as U Sco and V394 CrA (Tomov et al., 2008a).

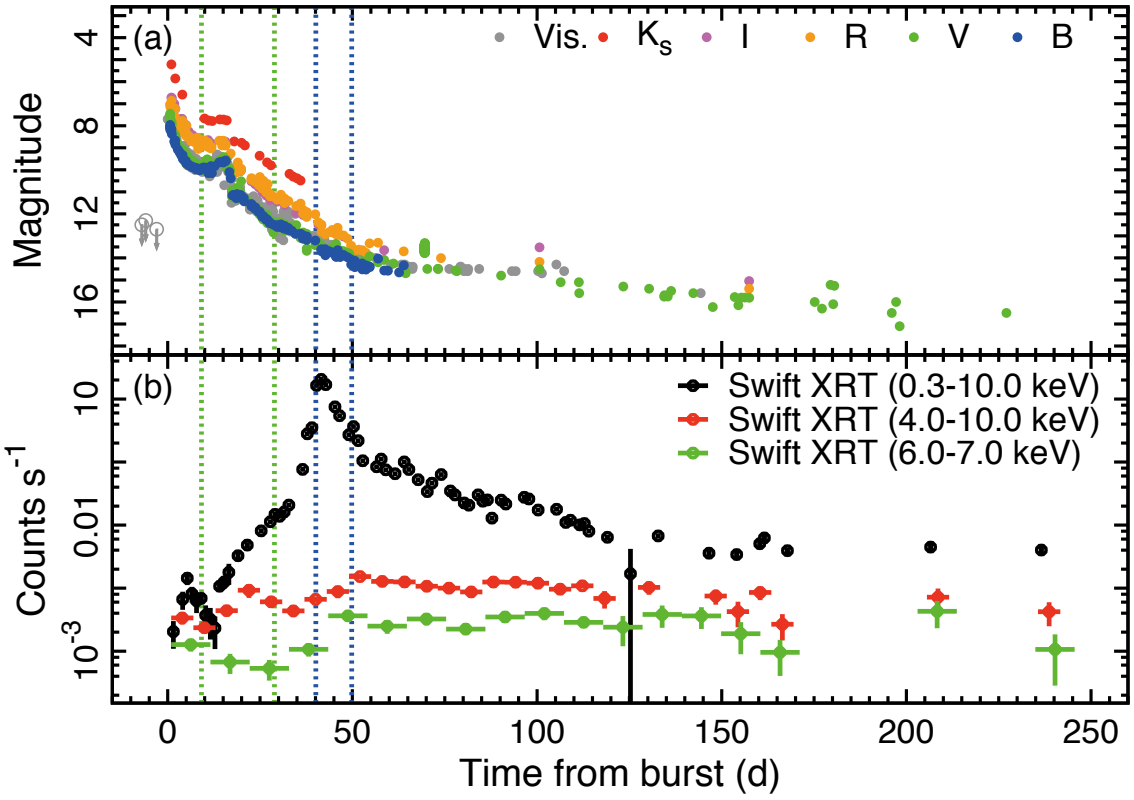

Figure 5.12: Development of the (a) optical and (b) X-ray brightness. The origin of the abscissa is 54566.73 d (MJD) when the classical nova was spotted (Nakano et al., 2008b). The time of the *Suzaku* and *XMM-Newton* observations are indicated by dotted lines with green and blue colors, respectively. (a) The *B*-, *V*-, *R*-, *I*-, *K*s-band, and visual magnitudes are shown with different colors. The upper limit for visual magnitudes before the outburst (Nakano et al., 2008b) is indicated by open circles and arrows. (b) The background-subtracted X-ray count rates with *Swift* in the broad band (0.3–10 keV), the hard band (4.0–10 keV), and the Fe K band (6.0–7.0 keV) with different colors. The optical photometry data are taken from the American Association of Variable Star Observers (AAVSO) International Database, the Variable Star Observers League in Japan (VSOLJ) Observation Database, and other ground-based observations (Nakano et al., 2008b; Lynch et al., 2008a; Ashok et al., 2008; Tomov et al., 2008b,a; Rudy et al., 2008; Helton et al., 2008). The infrared photometry data are taken by the Kanata TRISPEC team.

Assuming the maximum V-band magnitude of 7.54 mag obtained on 2008 April 11.36 (Nakano et al., 2008b), the classical nova declined at a rate of $t_2 \sim 4.6$ d (Tomov et al., 2008a), where t_2 is the time to decline by 2 mag from the optical maximum. The rapid decline makes V2491 Cyg an extremely fast nova (Tomov et al., 2008b). We adopt a distance of 10.5 kpc (Helton et al., 2008) based on the MMRD relation (della Valle & Livio, 1995).

In general, classical novae show a monotonic decline after the outburst in the optical brightness. However, V2491 Cyg exhibited a clear rebrightening followed by a sudden fading around day 15 (figure 5.12). A similar rebrightening was found only in two other classical novae to date; V1493 Aql (Venturini et al., 2004) and V2362 Cyg (Kimeswenger et al., 2008; Lynch et al., 2008c). Hachisu & Kato (2009) speculated that the rebrightening in these novae can be explained by a sudden release of magnetic energy.

5.3.2.2 Space-based observations

The discovery of V2491 Cyg triggered an intense monitoring campaign with *Swift*, which continued for more than half a year (Kuulkers et al., 2008; Osborne et al., 2008; Page et al., 2008, 2010). Subsequent follow-up observations were also made by *Suzaku* and *XMM-Newton*. We present the result of these data sets in this research. Below, we summarize other results published to date.

Before the outburst, *Swift* observed the area including V2491 Cyg between days -322 and -100. An X-ray source was significantly detected in five *Swift* observations (Swift J194302.1+321913; Ibarra & Kuulkers 2008; Ibarra et al. 2008, 2009; Page et al. 2010). At the position of V2491 Cyg, X-ray emission was also detected in the *ROSAT* all-sky survey faint source catalogue (1RXS J194259.9+321940; Voges et al. 2000), the second *ROSAT* PSPC catalogue[6] (2RXP J194302.0+321912), and the *XMM-Newton* slew survey catalogue (XMMSL1 J194301.9+321911; Saxton et al. 2008). The spectral shape changed dramatically among the *Swift* observations (Ibarra et al., 2009).

After the outburst, an intense monitoring campaign was conducted by *Swift* for more than half a year (Kuulkers et al., 2008; Page et al., 2008; Osborne et al., 2008). No significant X-ray emission was detected on day 1, but the X-rays emerged clearly on day 5. The *Swift* spectra exhibited extremely hard continuum emission (Kuulkers et al., 2008). Then, *Swift* recorded a soft and bright X-ray spectra on 2008 May 16 (day 36; Osborne et al. 2008). The nova continued to increase its brightness to the level at which grating observations became feasible. *XMM-Newton* observations were conducted to obtain grating spectra on 2008 May 20.6 (day 40) and 30.3 (day 50), when the nova turned into a typical super-soft X-ray phase (Ness et al., 2008b,c; Ness, 2010b; Ness et al., 2011). The RGS yielded blackbody-like spectra with broad absorption lines from N_{VI}, N_{VII}, O_{VII}, and O_{VIII}, as well as emission lines from Ne_{IX}, Ne_{X}, and Mg_{XII}. The large majority of absorption lines were blue-shifted by $\sim$3000 km s^{-1} (Ness et al., 2011).

[6]See ftp://ftp.xray.mpe.mpg.de/rosat/catalogues/2rxp/pub for detail.

5.3.3 Observations and Data Reduction

5.3.3.1 *Suzaku*

We made two target-of-opportunity observations using the *Suzaku* satellite on 2008 April 19 and May 9 (days 9 and 29; table 5.6). Two observations were aimed to put V2491 Cyg at the XIS field center with different roll angles. As of the observation dates, the absolute energy scale of the XIS is accurate to $\lesssim$10 eV, and the energy resolution is 160–190 eV (FWHM) at 5.9 keV. XIS2 has not been functional since 2006 November, thus we used the remaining three CCDs in our observations. The XIS was operated in the normal clocking mode with a frame time of 8 s.

We used HEASoft version 6.6.2 for data reduction. The data were processed with the pipeline version 2.2, in which events were removed during South Atlantic anomaly passages, the earth elevation angles below 5°, and the day earth elevation angles below 20°. As a result, the net exposure times of $\sim$21 and $\sim$25 ks were obtained for days 9 and 29, respectively.

Table 5.6: List of our target-of-opportunity observations for V2491 Cyg.

Mission	Observation number	Start time (UT)	End time (UT)	$t_{\rm b}$[a] (d)	Δt[b] (ks)
Suzaku	903001010	2008-04-19 15:21	2008-04-20 02:00	9.13	21
	903001020	2008-05-09 08:39	2008-05-09 21:30	28.90	25
XMM-Newton	0552270501	2008-05-20 14:24	2008-05-21 00:58	40.09	29
	0552270601	2008-05-30 08:41	2008-05-30 17:05	49.81	27

[a] Elapsed days in the middle of the observation from the discovery of V2491 Cyg (54566.73 d in MJD; Nakano et al. 2008b).
[b] Net exposure time averaged over the operating CCDs.

5.3.3.2 *XMM-Newton*

Following the flux increase in the soft X-ray band about a month after the nova outburst, two target-of-opportunity observations were also carried out using the *XMM-Newton* satellite on 2008 May 20 and 30 (days 40 and 50; table 5.6). The results obtained from the RGS data can be found in Ness et al. (2008b), Ness et al. (2008c), Ness (2010b), and Ness et al. (2011). We concentrate on the EPIC data focusing on the hard X-ray evolution in this research.

The EPIC-MOS was operated in the small window mode, while the EPIC-PN was in the timing mode. We do not use the EPIC-MOS spectra of V2491 Cyg here for the following reasons: (1) they suffered severe pile-up, and (2) a lower signal-to-noise dataset resulted because of the smaller effective area than that of the EPIC-PN by a factor of $\sim$4 at the Fe K band. Annulus source extraction does not work to mitigate the pile-up issue in this case; the pile-up is caused by intense soft X-ray band emission and it is difficult to obtain a sufficiently strong signal for the fainter, harder emission in annular regions.

We used the Science Analysis Software (SAS) version 8.0.0 in data reduction. In the background light curve constructed using the 10–12 keV band events, several spikes were recognized as flares. We removed events taken during these flare intervals. The intervals

were defined as time bins with background count rates of more than 0.36 and 0.95 s^{-1} respectively for the observations on days 40 and 50. The criteria were derived in an iterative process to remove time bins having more background counts than the average by 3-σ. As a result, the net exposure times of ∼29 and ∼27 ks were obtained for days 40 and 50, respectively.

5.3.3.3 *Swift*

We retrieved the archived data taken by the *Swift* satellite. *Swift* conducted monitoring observations after the nova. It also observed the sky area of V2491 Cyg before the nova for different purposes. The XRT and UVOT results were presented in Page et al. (2010) and Ibarra et al. (2009) for the post-nova and pre-nova data, respectively. We reanalyze the XRT data focusing on the hard X-ray band in this research.

The XRT was operated in the state that selects the clocking mode automatically depending on the source count rate. The present data were mainly taken with the PC and the WT modes. We used HEASoft version 6.9 for data reduction. The data were processed using the `xrtpipeline` tools to produce level 2 event files with standard screening criteria. As a result, the total net exposure times of ∼18 ks and ∼185 ks were obtained in the pre-nova and post-nova phases.

5.3.4 Analysis

5.3.4.1 Constructing spectra and light curves

***Suzaku*/XIS**

Figure 5.13 shows the smoothed XIS image in the 0.2–12.0 keV energy band obtained on days 9 and 29. The source events were accumulated from a circle with a radius of 120 pixels (2.1′) to maximize the signal-to-noise ratio (solid circle in figure 5.13), while the background events were from an annulus region with inner and outer radii of 4′ and 7′, respectively. 3′ radius circles were masked around other detected sources in the background region.

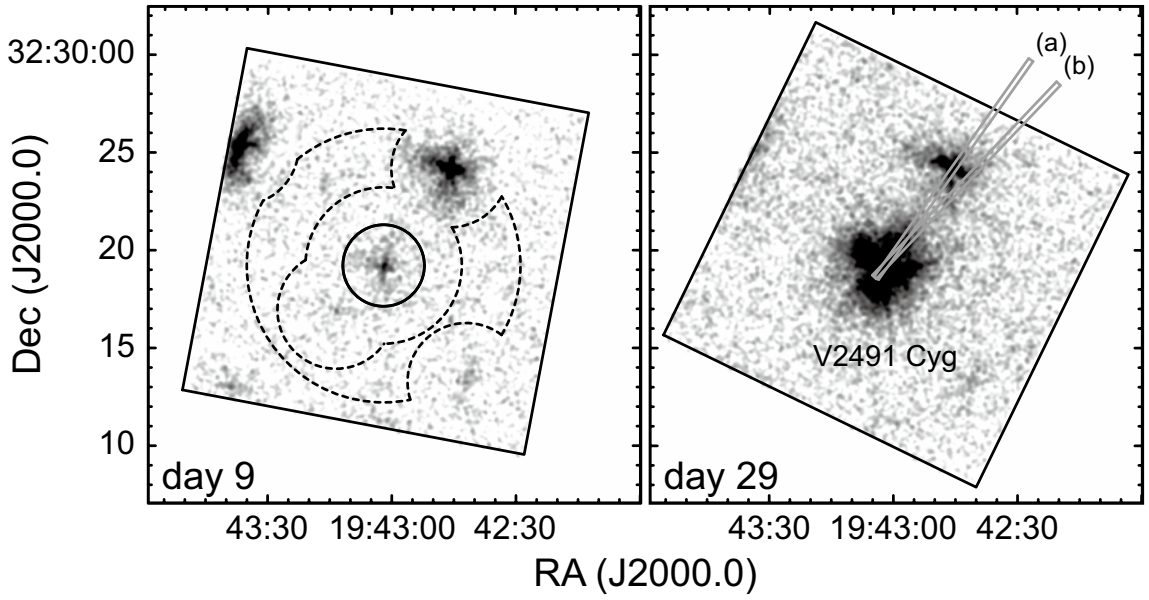

Figure 5.13: Smoothed *Suzaku* XIS images on days 9 and 29. Events recorded by the three CCDs in the 0.2–12.0 keV range were used, excluding those in the 5.0–7.0 keV range to eliminate the signals from the calibration sources at the corners. In the left panel, the XIS source extraction region is shown as a solid circle, while the background extraction region is shown using dashed lines. In the right panel, the source extraction regions for the EPIC-PN data are shown for days (a) 40 and (b) 50 as gray rectangles.

The background-subtracted XIS spectra were constructed separately for days 9 and 29. The top panel of figure 5.14 shows the broad-band spectra of the Fi chip in the 0.4–10 keV. The detector and mirror responses were generated using the `xisrmfgen` and `xissimarfgen` tools (Ishisaki et al., 2007), respectively. The two XIS-FI spectra with nearly identical responses were merged, while the XIS BI spectrum was treated separately. The difference of the effective area due to different off-axis angles were compensated between source and background regions using a method described in Hyodo et al. (2008). The fraction of a photon pile-up is negligible ($\lesssim$0.1 %) in both observations.

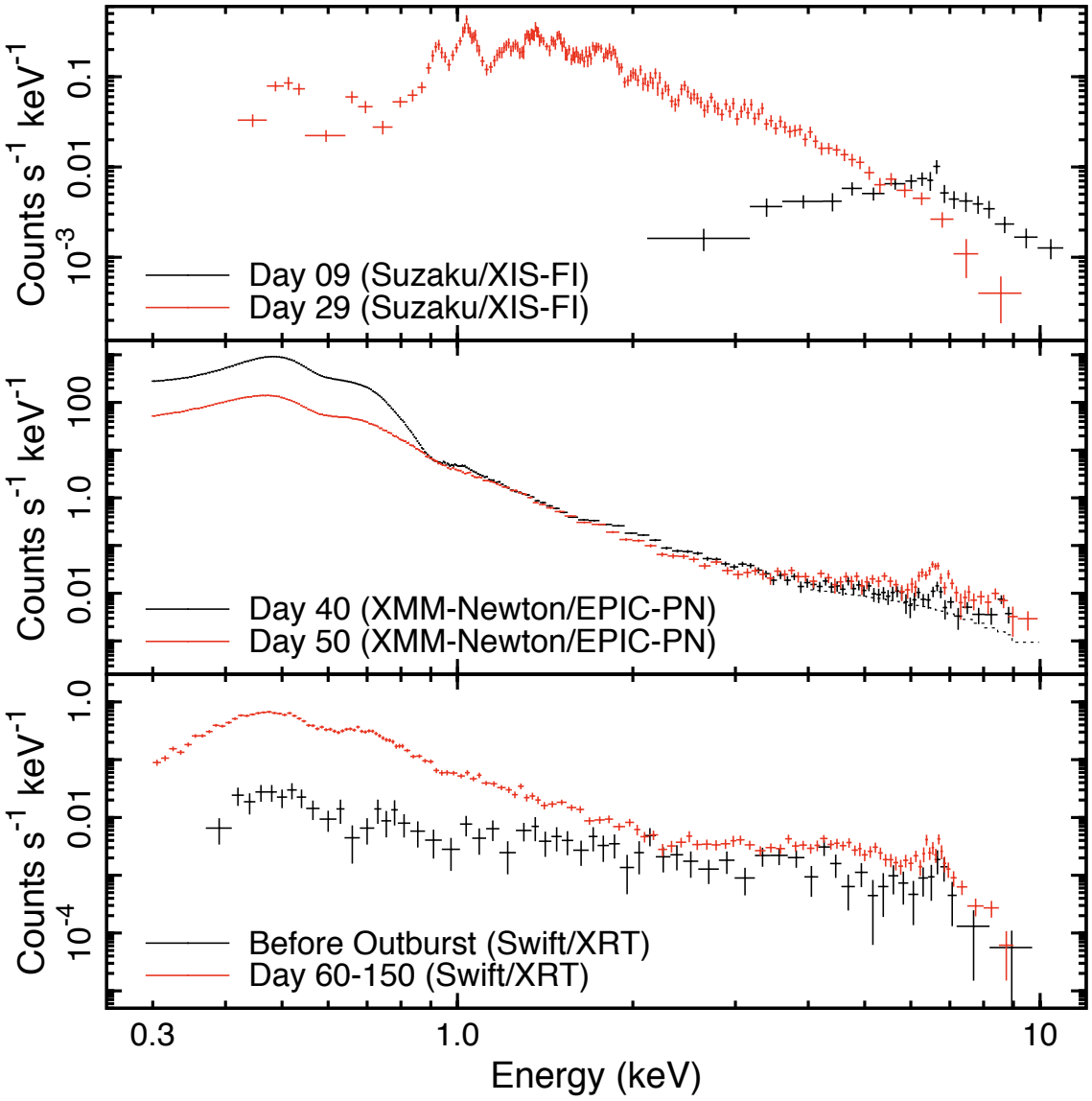

Figure 5.14: Background-subtracted broad-band (0.3–10 keV) X-ray spectra of V2491 Cyg at six different epochs. The top, middle, and bottom panels show the spectra with *Suzaku*/XIS-FI, *XMM-Newton*/EPIC-PN, and *Swift*/XRT, respectively. The contamination by the nearby source in the *XMM-Newton*/EPIC-PN spectra on day 40 is shown as the dotted line in the middle panel.

Suzaku/PIN

We see a high prospect of PIN detection on day 9, in which the XIS spectrum shows very flat continuum emission extending beyond 10 keV (the top panel of figure 5.14). We examine the signal against the background, which is a combination of the instrumental non–X-ray background (NXB) and the X-ray background. The X-ray background consists of the Cosmic X-ray background (CXB) emission and the Galactic ridge X-ray emission (GRXE). The majority of the background is the NXB; the CXB is $\sim$2 orders smaller than the NXB, and the GRXE is totally negligible with $\gtrsim$1 order smaller than the CXB toward V2491 Cyg (Revnivtsev et al., 2006).

In figure 5.15, we compare the observed signal against the model background. The NXB model was simulated by taking account of the cut-off-rigidity history and the elapsed time from South Atlantic anomaly passages during the observation. The 1-σ reproducibility of the NXB is $\lesssim$1.8 % in flux (Fukazawa et al., 2009). The CXB model was constructed by convolving the detector responses with the CXB model derived by *HEAO-1* observations (Boldt, 1987). A significant signal up to 70 keV was detected at $\gtrsim$3 σ level on day 9. The detection is also significant even when subtracting the maximum allowable NXB model. The detection is further confirmed by subtracting another NXB model constructed differently by accumulating the PIN data of our own observation during the earth occultation. In contrast, no significant PIN emission was detected on day 29.

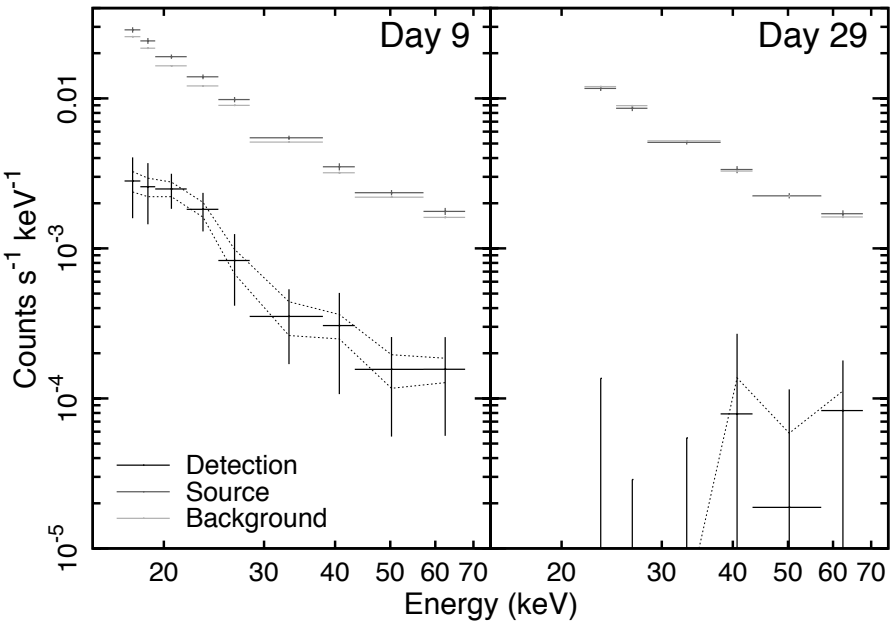

Figure 5.15: Comparison of the observed signal (red) against the model background (green) of the PIN data on days 9 (left) and 29 (right). The background includes both the NXB and the CXB. The background-subtracted spectrum is shown in black. The dotted band indicates the uncertainty stemming from the inaccuracy of the reproducibility in the NXB model. On day 29, the data are not used below 20 keV due to high detector temperatures.

We attribute the PIN emission on day 9 to V2491 Cyg for the following reasons: (1) the flux of the PIN emission is consistent with the extrapolated flux of the flat hard continuum in the hard end of the XIS spectrum, (2) no other X-ray source with a comparable hardness was found around the source, (3) no super-hard X-ray source is known within the PIN field of view by the *INTEGRAL* observatory (Ebisawa et al., 2003) and the quick-look data by the All-Sky Monitor in the *RXTE* observatory, and (4) the absence of the PIN emission on day 29 is consistent with the fact that the extrapolated XIS emission is too weak for any PIN detection.

XMM-Newton/EPIC

In the one dimensional image of the EPIC-PN data obtained in the timing mode, V2491 Cyg is centered near columns 36–37. The source events were accumulated from columns 35–38, while the background events were from columns 3–4 and 61–62. We show background-subtracted spectra both in the broad band (0.3–10 keV) separately for days 40 and 50 (figures 5.14). The detector and mirror responses were generated using standard SAS tools.

The V2491 Cyg spectrum on day 40 was unfortunately contaminated by a nearby source in the source region (figure 5.13). In the timing mode data, the image is stacked in the readout direction, so their overlapping signals cannot be separated. Therefore, we extracted the EPIC-MOS spectrum from the contaminating source and evaluated the level of contamination. The hard-band (4.0–10 keV) spectrum was fitted by a power-law model, and a statistically-acceptable fit was obtained for a photon index of 1.5 ± 0.7 and an X-ray flux of $(7.6 \pm 1.5) \times 10^{-13}$ erg cm^{-2} s^{-1} (90% statistical uncertainty). We show the contribution of the nearby source for the V2491 Cyg spectrum on day 40 in figures 5.14, in which we normalized the spectrum of the contaminating source by taking into account the reduced effective area at an off-axis position. The X-ray flux of the contamination source was estimated to be comparable with that of V2491 Cyg in the hard band (4.0–10 keV). We checked all data sets from *Suzaku*, *XMM-Newton*, and *Swift* observations, and no emission line was detected in the Fe K band. Therefore, the emission line in the V2491 Cyg spectrum on day 40 is entirely attributable to V2491 Cyg itself. Hereafter, we remove the contamination by including the best-fit model of the contaminating source in the spectral fitting of V2491 Cyg on day 40. We note here that the signals of V2491 Cyg and the contamination source on day 50 can be clearly separated in the one dimensional image with different roll angles.

Swift/XRT

The source events were accumulated from a circle with a radius of 20 pixels (47″), while the background events were from an annulus with inner and outer radii of 50 and 70 pixels (118″ and 165″), respectively. For several data sets affected by pile-up with a pile-up fraction of more than 1%, we masked the core with an adaptively chosen radius in the source extraction circle for each snapshot observation. The light curves were constructed both in a broad band (0.3–10 keV) and a narrow band (6.0–7.0 keV), which are shown in figure 5.12. We grouped several snapshot observations for each epoch. The telescope vignetting, the reduced aperture due to pile-up masking and bad pixels were taken into account for the aperture photometry.

In order to investigate the spectral development with sufficient photon statistics, we stacked the pre-nova data between −322 and −100 into one and the post-nova data between days 60 and 150 into another. We made the broad-band spectra in figures 5.14 both for the pre-nova and the post-nova phases.

5.3.4.2 Spectral Modeling

Super-hard X-ray Emission on day 9

First, we fit the resultant background-subtracted XIS and PIN spectra on day 9 simultaneously. We start with the Fe Kα feature between 6 and 7 keV. We fitted the feature locally with a Gaussian line and obtained the best-fit energy and equivalent width of 6.6$\pm$0.1 keV and $\sim$240 eV, respectively. The detection of the line was found significant at a >3 σ level both by the F-test and a Monte Carlo simulation (Protassov et al., 2002). We attribute the feature to the Fe_{XXV} Kα emission line at 6.7 keV. We further examined the presence of possible accompanying lines at 6.4 keV by Fe_{I} Kα and at 7.0 keV by Fe_{XXVI} Kα, but these lines were found insignificant.

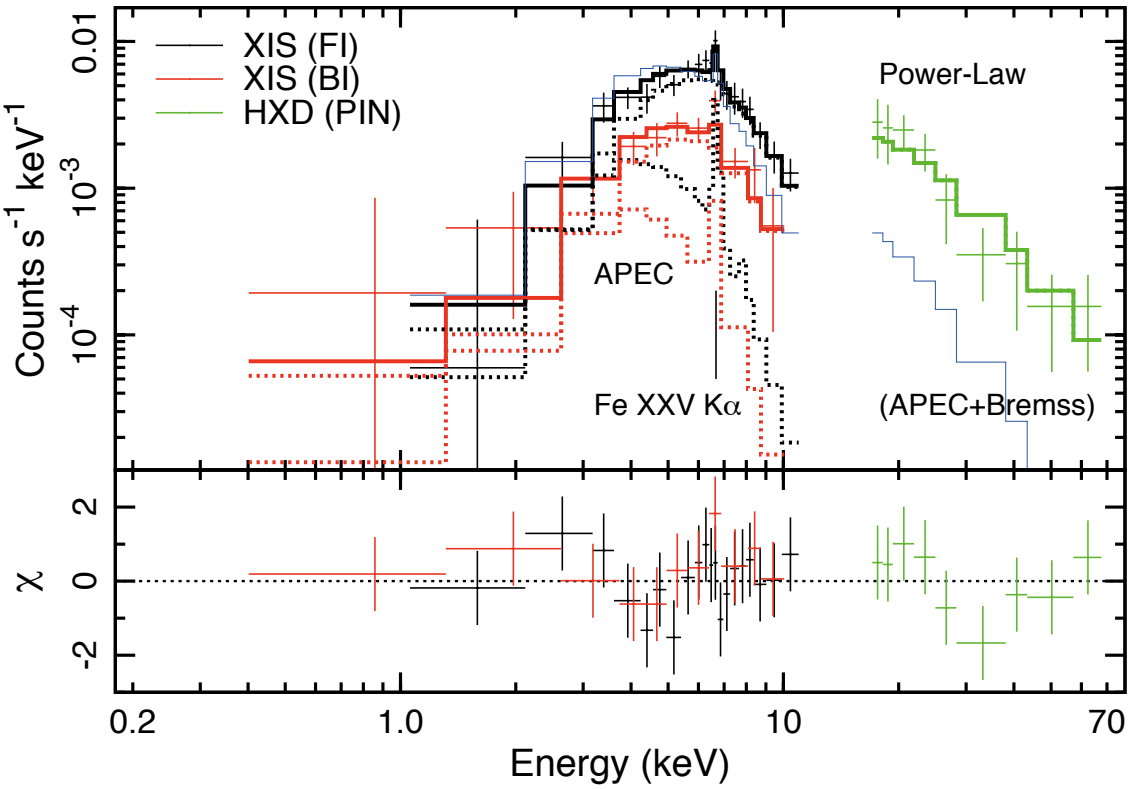

Figure 5.16: Background-subtracted XIS and PIN spectra on day 9 and the models. The two XIS FI spectra with nearly identical responses were merged, while the BI spectrum was treated separately. The best-fit model (APEC + power-law) is shown with thick lines (solid for total and dashed for each component) for FI, BI and PIN in different colors. The alternative unsuccessful model (APEC + 100 keV bremsstrahlung) is shown with thin blue lines for FI and PIN. The lower panel shows the residual from the best-fit.

The presence of the Fe_{XXV} Kα line and the absence of the Fe_{XXVI} Kα line indicate a thermal origin of the emission by plasma with a temperature of $\lesssim$10 keV. The plasma at this temperature is incapable of producing the flat super-hard continuum, so an additional harder

spectral component is required. We fitted the entire spectrum with two different combinations of models. The first one is optically-thin thermal plasma (APEC; Smith et al. 2001) plus a power-law model, which is respectively for the thermal features in the hard band and the flat continuum across both bands. The second combination employs a bremsstrahlung model in place of the power-law model. These models are attenuated by an interstellar extinction model (TBabs; Wilms et al. 2000). The Fe abundance relative to H in the plasma model was not constrained well by the data, and we therefore fixed it at solar (Anders & Grevesse, 1989).

We obtained a statistically acceptable fit for the first combination. The best-fit parameter values are compiled in Table 5.7 for the amount of extinction ($N_{\rm H}$), the thermal plasma temperature and flux ($k_{\rm B}T$ and $F_{\rm X}^{\rm th}$), and the power-law photon index and flux (Γ and $F_{\rm X}^{\rm pl}$). The extinction-corrected luminosity at 10.5 kpc was also derived for each component ($L_{\rm X}^{\rm th}$ and $L_{\rm X}^{\rm pl}$). For the second combination of models, the electron temperature of the bremsstrahlung emission is constrained to be >100 keV, which is much higher than the post shock temperature in a strong shock by the ejecta propagating at $\sim$4000 km s^{-1} (e.g., Tomov et al. 2008b,a). We therefore conclude that the spectrum on day 9 is better explained by a combination of 3 keV thermal plasma and power-law emission with a photon index of 0.1 attenuated by a heavy extinction. The systematic uncertainty in the NXB reproducibility for the PIN brings little change in the result by about $\pm$0.3 keV in $k_{\rm B}T$, $\pm$0.08 in Γ, and $\pm$15% both in $F_{\rm X}^{\rm th}$ and $F_{\rm X}^{\rm pl}$.

Table 5.7: Best-fit parameters of V2491 Cyg on day 9.

Comp.	Par.	Unit	Value[a]
Absorption	$N_{\rm H}$	(cm^{-2})	$1.4^{+0.9}_{-0.4}\times10^{23}$
Power-law	Γ		$0.1^{+0.2}_{-0.2}$
	$F_{\rm X}^{\rm plb}$	(ergs s^{-1} cm^{-2})	$4.8^{+0.7}_{-1.3}\times10^{-11}$
	$L_{\rm X}^{\rm plb}$	(ergs s^{-1})	$6.4^{+0.9}_{-1.7}\times10^{35}$
Thermal	$k_{\rm B}T$	(keV)	$2.9^{+4.3}_{-2.6}$
	$F_{\rm X}^{\rm thb}$	(ergs s^{-1} cm^{-2})	$1.4^{+12}_{-1.1}\times10^{-13}$
	$L_{\rm X}^{\rm thb}$	(ergs s^{-1})	$1.9^{+16}_{-1.4}\times10^{33}$
χ^2/d.o.f.			22.8/35

[a] The statistical uncertainties indicate the 90% confidence ranges.
[b] The values are in 1.0–12.0 and 15–70 keV respectively for the thermal and power-law emission. The luminosities are at 10.5 kpc (Helton et al., 2008).

Plasma model fitting on day 29

The Suzaku XIS spectra taken on day 29 exhibit emission lines from several elements at various ionization stages, including Kα and some hints of Kβ emission lines from O_{VIII}, Ne_{IX}, Ne_{X}, Mg_{XI}, Mg_{XII}, Si_{XIII}, Si_{XIV}, S_{XV}, and Ar_{XVII} (figure 5.17). High signal-to-noise ratio spectra with a continuum and many emission lines put constraints on the chemical abundance.

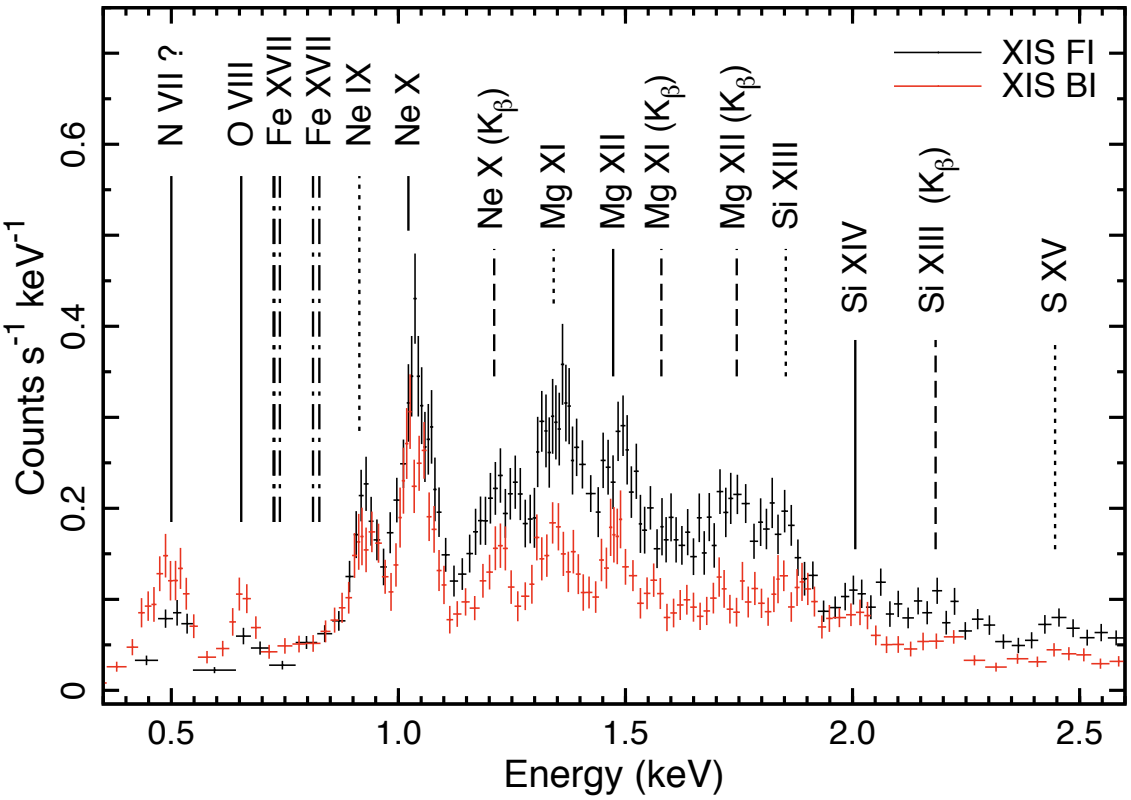

Figure 5.17: Background-subtracted XIS spectra on day 29 in a linear scale. Pluses indicate the spectra for the two instruments (black and red for XIS FI and XIS BI, respectively). The energies of plausible emission lines from H-like Kα, He-like Kα, and Kβ are labeled with solid, dotted, and dashed lines, respectively. Most intense five emission lines in a Fe L-series are labeled with dashed-and-dotted lines, assuming the typical plasma density of 10^7 cm^{-3} for the ejecta of classical novae.

First, we fitted the spectra with the sum of one or more isothermal thin-thermal plasma models (APEC; Smith et al. 2001) convolved with the interstellar absorption model (TBabs; Wilms et al. 2000). At least two components with different temperatures are necessary to reproduce the spectra between 0.6–10 keV. A large absorption column density ($N_{\rm H} \sim 5{\times}10^{21}$ cm^{-2}) is necessary to explain the spectrum with a cut-off at $\sim$0.8 keV. Rich statistics allowed us to constrain the abundance for major metals ($Z_{\rm O}$, $Z_{\rm Ne}$, $Z_{\rm Mg}$, $Z_{\rm Si}$, $Z_{\rm S}$, $Z_{\rm Ar}$, and $Z_{\rm Fe}$). In addition to the previously defined parameters, we derived the X-ray fluxes ($F_{\rm X}^{\rm th1}$ and $F_{\rm X}^{\rm th2}$) and extinction-corrected luminosities ($L_{\rm X}^{\rm th1}$ and $L_{\rm X}^{\rm th2}$) of the hotter and cooler

plasma components, respectively, assuming the distance of 10.5 kpc (Helton et al., 2008). Additional fitting parameters (offset for XIS FI and XIS BI) were also introduced to account for an additional systematic uncertainty from the energy gain calibration. The resultant best-fit parameters are summarized in table 5.8. The Fe abundance was constrained to be less than ∼0.01 solar by the lack of K and L series emission on day 29. In particular, the lack of the Fe_{XXV} Kα emission feature at 6.7 keV gives a stringent upper limit as the line achieves the maximum equivalent width at a temperature of ∼2 keV by Rothenflug & Arnaud (1985).

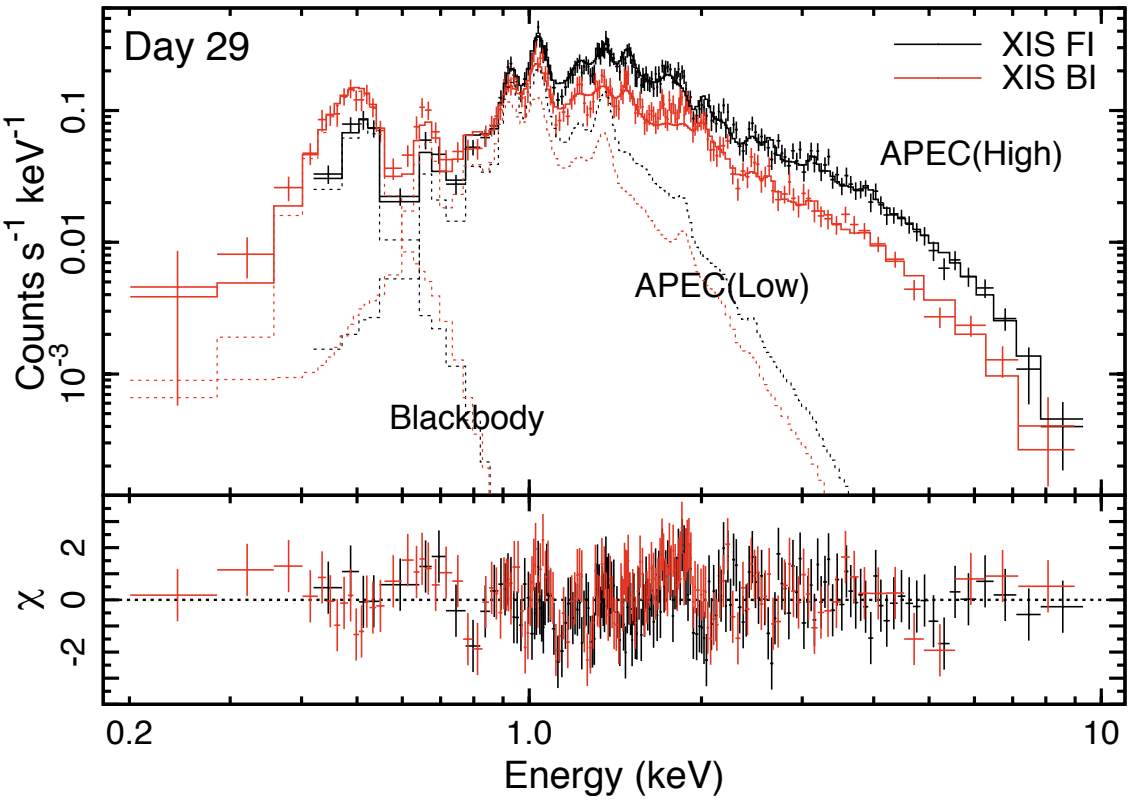

Figure 5.18: Background-subtracted spectra and the best-fit models of V2491 Cyg on day 29. The symbols follow figure 5.17. The best-fit models are shown by the solid (total) and dashed (each component) histograms. The lower panels show the residual from the best-fit models.

Next, we inspected the soft-band excess emission peaking at ∼0.5 keV. This broad feature cannot be explained by a simple Gaussian model, and a statistically-acceptable fit was obtained by an additional blackbody model. However, the best-fit parameters indicate that the resultant bolometric luminosity exceeds the Eddington limit of a white dwarf with Chandrasekhar mass. It has to be noted that blackbody fits to the SSS spectra on classical novae have a tendency to overestimate the bolometric luminosity and thus the radius (Krautter et al., 1996). Also, we have other solutions by increasing a degree of freedom of these models. For example, if we introduce a partial covering absorber model assuming that the circumstellar material have a continuous distribution in $N_{\rm H}$, the effective attenuation is reduced

in the soft band as photons can penetrate through thin parts of the absorber. Thus, the luminosity of the blackbody model can be small. Both blackbody and thin-thermal plasma models can also make statistically-acceptable fit to the soft excess (Takei & Ness, 2010). These results mean that the spectral quality in the very soft range is not high enough to distinguish between these models, and we cannot constrain the best solution from our data. We decided to use the blackbody model to fit the soft portion of the spectrum, yielding a good fit to the entire spectra that allows us to estimate the X-ray flux.

Table 5.8: Best-fit parameters of V2491 Cyg on day 29.

Component	Parameter	Unit	Value[a]
Absorption	$N_{\rm H}$	($\rm cm^{-2}$)	$5.2^{+0.3}_{-0.3}\times10^{21}$
APEC	$k_{\rm B}T^{\rm th1}$	(keV)	$2.08^{+0.07}_{-0.07}$
	$F_{\rm X}^{\rm th1b}$	(erg $\rm s^{-1}$ $\rm cm^{-2}$)	$2.6^{+0.9}_{-0.5}\times10^{-12}$
	$L_{\rm X}^{\rm th1bd}$	(erg $\rm s^{-1}$)	$3.4^{+1.6}_{-0.8}\times10^{34}$
	$k_{\rm B}T^{\rm th2}$	(keV)	$0.39^{+0.02}_{-0.02}$
	$F_{\rm X}^{\rm th2b}$	(erg $\rm s^{-1}$ $\rm cm^{-2}$)	$3.8^{+1.0}_{-1.2}\times10^{-13}$
	$L_{\rm X}^{\rm th2bd}$	(erg $\rm s^{-1}$)	$1.1^{+0.3}_{-0.3}\times10^{34}$
	$Z_{\rm O}$	(solar)	$6.2^{+2.6}_{-2.1}$
	$Z_{\rm Ne}$	(solar)	$4.7^{+2.3}_{-1.1}$
	$Z_{\rm Mg}$	(solar)	$2.5^{+0.6}_{-0.6}$
	$Z_{\rm Si}$	(solar)	$0.8^{+0.2}_{-0.2}$
	$Z_{\rm S}$	(solar)	$0.7^{+0.3}_{-0.3}$
	$Z_{\rm Ar}$	(solar)	$1.2^{+0.7}_{-0.7}$
	$Z_{\rm Fe}$	(solar)	< 0.01
Blackbody	$k_{\rm B}T^{\rm bb}$	(keV)	$3.0^{+0.2}_{-0.3}\times10^{-2}$
	$F_{\rm X}^{\rm bbcd}$	(erg $\rm s^{-1}$ $\rm cm^{-2}$)	$6.8^{+16.0}_{-3.4}\times10^{-13}$
	$L_{\rm X}^{\rm bbcd}$	(erg $\rm s^{-1}$)	$1.9^{+4.4}_{-0.9}\times10^{38}$
Response	Offset (XIS-FI)	(eV)	$11.0^{+3.6}_{-1.3}$
	Offset (XIS-BI)	(eV)	$4.6^{+1.4}_{-1.9}$
χ^2/d.o.f.			330.0/310

[a] The statistical uncertainties and the upper limits indicate the 90% confidence ranges.
[b] The values are derived in 1.0–10.0 keV energy bands for the thin-thermal plasma components.
[c] The values are derived in 0.2–1.0 keV energy bands for a blackbody component.
[d] A distance of 10.5 kpc (Helton et al., 2008) is assumed for the absorption-corrected luminosities.

Evolution of Fe emission lines

In the time series of the spectra, we found remarkable changes in emission lines at the Fe K complex (figures 5.14). We also show the narrow-band (5.2–8.6 keV) spectra of V2491 Cyg at six time intervals around the Fe K complex with the three observatories (figure 5.19).

We first characterize line emission in the hard-band spectra. For identifying the three lines in the Fe K complex (figure 5.19), we fitted the 4–10 keV band spectra using a phenomenological model composed of a power-law continuum and three Gaussian line components. The Gaussian energy of each line was tied among the six different spectra such that the line energies were not allowed to vary between them. The Gaussian width was fixed to 0 for all lines for all spectra, the expected widths being negligible compared with the instrumental resolution. Other parameters were allowed to vary independently for each spectrum.

We obtained statistically acceptable results for the fitting, with the null hypothesis probability for the χ^2 value of >0.05. The best-fit energy centers for the three Gaussian components are 6.41±0.05, 6.66±0.02, and 6.96±0.05 keV (90% statistical uncertainty), which are consistent respectively with the energies of the Kα fluorescent line from $\mathrm{Fe_I}$, the $1s^1S_0$–$2p^1P_1$ resonance line from $\mathrm{Fe_{XXV}}$, and the Lyα line from $\mathrm{Fe_{XXVI}}$. The flux and the equivalent width of each line are tabulated in table 5.9, in which 90% upper limits are given for undetected lines. The flux and the equivalent width on day 40 are subject to further uncertainty due to the propagated uncertainty from the fitting of the contaminating source, which is estimated as 2×10^{-7} photons cm^{-2} s^{-1} and 400 eV, respectively.

Table 5.9: Best-fit parameters of V2491 Cyg from the phenomenological line fitting[a].

t_b[b]	—— Flux (10^{-6} cnts cm^{-2} s^{-1}) ——			—— Equivalent width (10^2 eV) ——		
(d)	Fe_I	Fe_{XXV}	Fe_{XXVI}	Fe_I	Fe_{XXV}	Fe_{XXVI}
{−322, −100}	< 9.7	10.4 (2.0–19.0)	< 14.3	< 5.7	5.2 (0.8–18.5)	< 13.3
9.13	1.9 (0.2–3.5)	3.3 (1.7–4.9)	< 1.3	1.0 (0.05–2.0)	2.0 (0.8–3.1)	< 2.2
28.90	< 2.7	< 1.7	< 1.8	< 4.6	< 1.0×10^2	< 2.4×10^2
40.09[c]	< 1.3	3.0 (1.4–4.6)	< 1.6	< 5.2	7.0 (1.6–10.3)	< 4.0
49.81	6.2 (3.7–8.7)	10.3 (7.6–13.0)	4.4 (1.4–7.1)	1.6 (0.9–2.3)	2.7 (1.9–3.8)	1.2 (0.5–2.2)
{60, 150}	10.2 (6.0–14.5)	13.4 (8.8–18.0)	5.4 (1.7–9.2)	2.3 (1.3–3.7)	3.0 (1.8–4.7)	1.4 (0.4–2.8)

[a] The statistical uncertainties and upper limits indicate the 90% confidence ranges.
[b] Elapsed days from the discovery of V2491 Cyg (54566.73 d in MJD; Nakano et al. 2008b). Times as shown in the style of X, Y indicate combined observations between days X and Y.
[c] Increased uncertainty due to the contaminating source is not included.

We next characterize the continuum and line emission using a thermal plasma emission model. We fitted the hard-band (4.0–10 keV) spectra using an optically-thin isothermal plasma component (APEC; Smith et al. 2001). This plasma component accounts for the continuum as well as the emission lines from highly ionized Fe and other metals. We fixed the chemical abundance to be solar (Anders & Grevesse, 1989) for all the elements other than Fe for all the six different spectra. A narrow Gaussian component accounting for the 6.4 keV emission line due to the Fe fluorescence was also included. The combined model was multiplied with an interstellar absorption model (TBabs; Wilms et al. 2000). The X-ray spectrum on day 9 was excluded from the plasma model analysis due to severe contamination by non-thermal emission of V2491 Cyg that renders diagnosis of the softer thermal component difficult.

We obtained statistically acceptable results for all the fitting. The best-fit plasma temperature ($k_{\rm B}T$), the Fe abundance relative to solar ($Z_{\rm Fe}$), the detected X-ray flux ($F_{\rm X}$), and the absorption-corrected luminosity ($L_{\rm X}$) in the hard band (4.0–10 keV) are summarized in table 5.10. A distance of 10.5 kpc was assumed (Helton et al., 2008). The absorption column density ($N_{\rm H}$) was fixed to be 2.2×10^{21} cm^{-2} based on the analysis of the quiescent phase data by Ibarra et al. (2009). By extrapolating the best-fit model, we estimated the X-ray luminosity in the 2.0–10 keV energy band to be in the order of $\sim10^{34}$ erg s^{-1}. The fitting results on day 40 are again subject to increased uncertainty in the fitting uncertainty of the contaminating source. It is estimated that ±1.6 keV in $k_{\rm B}T$, ±2.5 solar in $Z_{\rm Fe}$, $\pm1.0\times10^{-13}$ erg cm^{-2} s^{-1} in $F_{\rm X}$, and 1.3×10^{33} erg s^{-1} in $L_{\rm X}$.

Table 5.10: Best-fit parameter of V2491 Cyg from plasma model fitting[a].

$t_{\rm b}$[b] (d)	$k_{\rm B}T$ (keV)	$Z_{\rm Fe}$ (solar)	$F_{\rm X}$[c] (10^{-13} erg cm^{-2} s^{-1})	$L_{\rm X}$[cd] (10^{33} erg s^{-1})	χ^2/d.o.f.
{−322, −100}	7.5 (2.9–18.2)	2.6 (0.8–7.0)	7.4 (1.7–9.0)	9.9 (2.3–11.9)	0.62 (12)
9.13	(Plasma fitting omitted estimate because of dominant continuum from non-thermal emission.)				
28.90	2.1 (1.6–2.7)	< 0.2	5.5 (3.6–5.9)	7.4 (4.8–7.8)	0.50 (17)
40.09[e]	6.1 (2.9–10.7)	1.3 (0.5–2.7)	2.4 (0.5–3.2)	3.2 (0.6–4.2)	0.85 (32)
49.81	9.6 (7.8–12.0)	1.4 (1.0–1.8)	14.3 (12.7–15.4)	18.9 (16.9–20.4)	1.38 (37)
{60, 150}	7.2 (5.5–9.3)	1.1 (0.8–1.6)	16.8 (14.4–18.0)	22.2 (19.1–23.9)	0.64 (30)

[a] The statistical uncertainties and upper limits indicate the 90% confidence ranges.
[b] Elapsed days from the discovery of V2491 Cyg (54566.73 d in MJD; Nakano et al. 2008b). The time {X, Y} indicates the time interval between days X and Y.
[c] These values are derived in the 4.0–10.0 keV energy band.
[d] A distance of 10.5 kpc (Helton et al., 2008) is assumed for the luminosity.
[e] Increased uncertainty due to the contaminating source is not included.

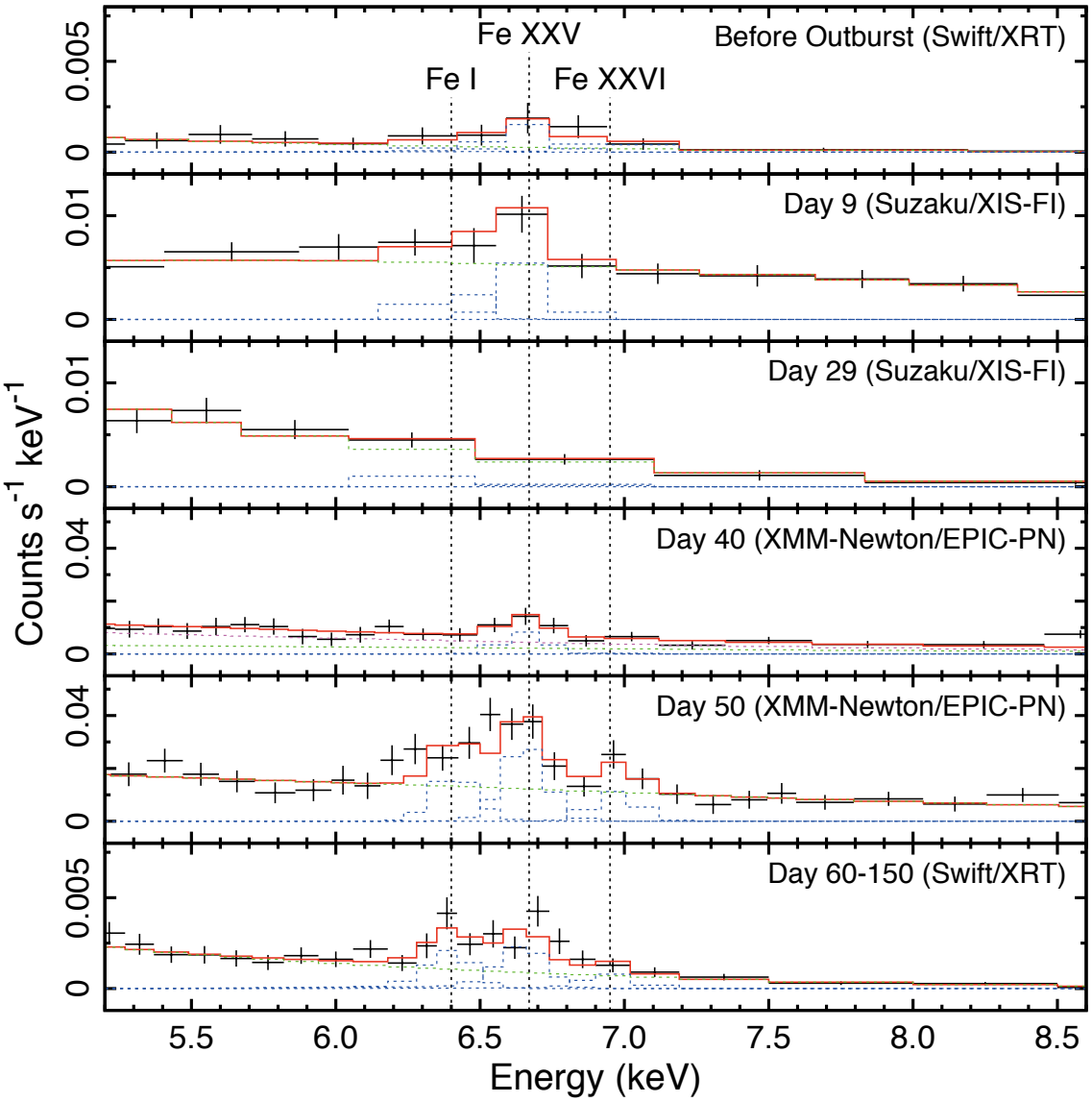

Figure 5.19: Background-subtracted narrow-band (5.2–8.6 keV) X-ray spectra of V2491 Cyg, including the Fe K complex, at six different epochs. The center energy of the three emission lines are indicated by dashed lines. Black pluses indicate the data, while the red solid histograms indicate the best-fit model. The model is decomposed into the power-law continuum (green dotted) and the three Gaussian line (blue dotted) components. The contamination by the nearby source in the XMM-Newton/EPIC-PN spectra on day 40 is shown as the dotted line in magenta.

5.3.5 Results

5.3.5.1 Absorption

The hydrogen-equivalent column density is $\sim 1.5\times10^{23}$ cm^{-2} on day 9 (Takei et al., 2009). It is decreased drastically to be $\sim 5\times10^{21}$ cm^{-2} on day 29. Here, the absorption integrated through our Galaxy toward V2491 Cyg is $\sim 4\times10^{21}$ cm^{-2} from H$_{\rm I}$ maps (Dickey & Lockman, 1990; Kalberla et al., 2005), which is an upper limit for the interstellar absorption as the nova is a Galactic source. Both of the observed absorptions are larger than this value. The large absorption and the time variation suggest the presence of an additional circumstellar absorption by surrounding material such as the ejecta. Therefore, we can decompose the observed column density as $N_{\rm H}(t) \sim N_{\rm H,ISM} + N_{\rm H,CSM}(t)$, where $N_{\rm H,ISM}$ and $N_{\rm H,CSM}(t)$ are respectively the constant interstellar absorption and the circumstellar extinctions as a function of time t. $N_{\rm H,ISM}$ is estimated as $\sim 2\times10^{21}$ cm^{-2} based on the optical and X-ray observations before and long after the outburst (Ibarra et al., 2009). As a result, $N_{\rm H,CSM}(t_9)$ is $\sim 1.5\times10^{23}$ cm^{-2} and $N_{\rm H,CSM}(t_{29})$ is $\sim 3\times10^{21}$ cm^{-2}, where t_9 and t_{29} are the time on days 9 and 29, respectively.

5.3.5.2 Mass loss with the outburst

As $N_{\rm H,CSM}(t)$ is caused by the ejecta, the ejecta mass can be estimated as $M_{\rm ejecta} \sim 4\pi R^2_{\rm system}(t)$ $N_{\rm H,CSM}(t)$ $m_{\rm H}$ X^{-1} assuming a spherical symmetry, where $R_{\rm system}(t)$ is the radius of the expanding system as a function of time t, $m_{\rm H}$ is the hydrogen mass, and X is the hydrogen mass fraction. $R_{\rm system}$ is derived as $v_{\rm ejecta}t$, in which $v_{\rm ejecta} \sim 4000$ km s^{-1} is the median value among optical and X-ray results (Ashok et al., 2008; Ayani & Matsumoto, 2008; Helton et al., 2008; Lynch et al., 2008a; Ness et al., 2008b; Tomov et al., 2008b,a). We further assume the solar abundance for the ejecta composition ($X \sim 0.7$; Däppen 2000). As a result, $M_{\rm ejecta}$ is estimated to be $\sim 10^{-4}$ $M_\odot$ based on the spectra of day 9, when the CSM extinction is dominant. Based on the spectra of day 29, $M_{\rm ejecta}$ is also estimated to be $\sim 10^{-5}$ $M_\odot$. Both of these results are a typical value for nova ejecta (Pietsch et al., 2007), and the difference is possibly caused by a complex geometry of circumstellar absorption.

5.3.5.3 Super-hard X-ray emission on day 9

We have found the super-hard X-ray emission extending up to 70 keV from V2491 Cyg on day 9. The spectrum cannot be explained by a simple bremsstrahlung model with a reasonable temperature. The best-fit power-law model is very flat with a photon index of 0.1 ± 0.2. The emission was absent on day 29 in an observation with the same exposure. The 15–70 keV flux decreased from 4.8×10^{-11} ergs s^{-1} cm^{-2} on day 9 to $\lesssim 1.5\times10^{-11}$ ergs s^{-1} cm^{-2} on day 29 (a 90% confidence upper limit assuming the same spectral shape). The rapid decay rules out the possibility of Comptonization of nuclear γ-ray lines from radioactive species such as ^{22}Na (Livio et al., 1992).

Super-hard X-ray emission was studied in two other classical novae to date; V382 Vel by *BeppoSAX* (Orio et al., 2001c), and RS Oph by *RXTE* (Sokoloski et al., 2006) and *Swift* (Bode et al., 2006). Similarly to V2491 Cyg, these observations were conducted a short time

after the outburst (days 3 and 15 for RS Oph and V382 Vel, respectively). However, neither of the two other cases shows clear evidence of non-thermal signature of the emission. In RS Oph, *RXTE* detected photons only below ∼20 keV, which is attributable to thermal plasma with a reasonable temperature of $\lesssim$10 keV (Sokoloski et al., 2006). *Swift* reported weak 25–50 keV detection but no spectrum was obtained in the super-hard X-ray band (Bode et al., 2006). In V382 Vel, *BeppoSAX* only constrained a 2-σ upper limit in the 15–60 keV band (Orio et al., 2001c). On the contrary, in V2491 Cyg, the spectrum is clearly seen up to 70 keV, which is not explained by a simple bremsstrahlung model with a reasonable temperature but by an extremely flat power-law model.

The power-law emission from V2491 Cyg suggests the presence of an accelerated population of electrons with non-thermal energy distribution. Non-thermal particles in classical nova explosions are suggested in some radio observations and theoretical studies of RS Oph. Rupen et al. (2008) found evidence of synchrotron emission in a high-resolution radio interferometer observation. Tatischeff & Hernanz (2007) argued for the presence of diffusive shock acceleration based on the fact that the blast wave decelerated at a much faster rate than that predicted by the standard adiabatic shock model. Our result is the first to claim a non-thermal signature from classical nova explosions in the X-ray band.

The extremely flat photon index of 0.1±0.2 in the power-law radiation poses a challenge to understand the radiation mechanism as well as the acceleration mechanism of electrons to produce the radiation. If the dominant radiation is inverse Compton or synchrotron emission and the electrons lose energy radiatively, the electron population has a number index from -0.8 to -1.8 in the power-law energy distribution at injection. If bremsstrahlung emission is the dominant radiation and the non-relativistic electrons lose energy via ionization losses with ambient matter, the injected electrons have a number index from -0.4 to 1.1. These values are too hard for standard diffusive shock acceleration, in which a number index of 2.0 is expected (Blandford & Ostriker, 1980). Additional explanations, such as multiple scattering in the inverse Compton process or the acceleration by magnetic reconnections, would be necessary.

Alternative interpretations to the non-thermal model for the super-hard emission include a multiple temperature hot ($\gtrsim$10 keV) plasma with an extreme extinction ($\gtrsim 10^{25}$ cm^{-2}) and Comptonized blackbody emission (Nishimura et al., 1986). The former is unlikely due to the lack of reprocessed emission (e.g., Fe$_{\rm I}$ Kα) and the fact that such a large extinction cannot be realized by the typical amount of ejecta ($\sim 10^{-5}$ $M_\odot$; e.g., Pietsch et al. 2007). The latter requires blackbody emission of ∼5 keV, which is too hot for the white dwarf surface emission.

5.3.5.4 Plasma diagnosis on day 29

On day 29, the spectrum shows many emission lines from O, Ne, Mg, Si, S, and Ar without serious contamination by SSS emission. In addition, we found enhanced O, Ne, and Mg abundances with a fitting result by the multi-temperature thin-thermal plasma emission model (table 5.8). If the white dwarf lost mass by the outburst, the abundance pattern of the ejecta reflects the chemical composition of the white dwarf itself, and the metal abundances should be higher than that of the accreted material. The underlying white dwarf can have two different sets of chemical composition; a CO-type and an ONe-type. In the case of

V2491 Cyg, the enhanced O, Ne, and Mg abundances suggest that the white dwarf has an ONe-type core and its material was ejected by the outburst.

In contrast, the iron abundance was constrained to be less than 0.01 solar by the lack of K and L series emission in the spectrum on day 29. Such an iron deficiency is widely seen in the hard X-ray emission of classical novae (e.g., Mukai & Ishida 2001; Orio et al. 2001b; Tsujimoto et al. 2009; Ness et al. 2009a). Possible causes for the deficiency include the intrinsically low abundance of iron, iron depletion to the dust, and the overionization (recombination) of plasma. The first case is not supported by the clear detection of iron emission lines on the other days.

5.3.5.5 Phases of X-ray emission

V2491 Cyg shows completely different light curves for the soft and hard parts of the X-ray band (figure 5.12; see also figures 1 and 4 in Page et al. 2010). The soft-band flux was negligible immediately after the outburst, but continued to increase to reach a peak at day ∼40, then faded rapidly until day ∼50 and more slowly thereafter. This behavior is commonly seen in the soft X-ray light curves of other classical novae. The increase in soft-band brightness before the peak is interpreted in terms of an increasing plasma temperature (e.g., Osborne et al. 2011) and/or a decreasing extinction column as the ejecta expands, while the decrease in brightness after the peak is interpreted as the shrinkage of the photosphere after the fuel, in the form of H-rich accreted material, is consumed.

In contrast to the soft band, the hard-band light curve is relatively stable (figure 5.12; see also figures 1 and 4 in Page et al. 2010). Despite the overall stability, however, we argue that the hard-band development can be divided into two phases (earlier and later phases hereafter) separated at day ∼40 based on the following lines of evidence: (1) In the Fe K band light curve (figure 5.12), the flux changes gradually in the earlier phase with a minimum on day ∼30, whereas the flux is stable in the later phase. (2) In the narrow-band spectra (table 5.10), the Fe_I Kα fluorescent line at 6.4 keV is only detected with a significance greater than the 3σ level in the later phase. (3) In the plasma model fitting results (table 5.10), the Fe abundance relative to H is different between the two phases. In the earlier phase, a stringent upper limit to the Fe abundance was obtained for the spectra on day 29 of $Z_{\rm Fe} < 0.2$, which is reasonable from the lack of 6.7 keV lines despite the plasma temperature (∼2.1 keV) being close to the maximum formation temperature of the line (e.g., Rothenflug & Arnaud 1985). In the later phase, the two lines from highly ionized Fe are clearly detected (figure 5.19) with a corresponding Fe abundance of $Z_{\rm Fe} \sim 1$. Here, we note that the Fe abundance values are subject to change with the unconstrained chemical composition of other elements, which contribute to continuum emission in the X-ray band. However, we consider that the comparative values between two different spectra are valid as long as the chemical abundance of the plasma is assumed to be the same.

The earlier and later phases are distinctive in the flux changes and the evolution of Fe features. The only exception to this view is the presence of a discernible 6.7 keV emission line and a 2-σ detection of 6.4 keV feature on day 9 (Takei et al., 2009), for which we currently have no interpretation. Additional explanations, such as another X-ray source of hot thin-thermal plasma with sufficient Fe abundance, would be necessary to account for

these lines on day 9.

5.3.5.6 Origins of the X-ray emission

The two distinctive phases in the hard-band evolution of V2491 Cyg suggest that there are two different production mechanisms operating in each phase. We consider that plasma generated by shocks in the ejecta is responsible for the earlier phase, while emission by accretion shocks in the rekindled accretion process is responsible for the later phase.

Hard components from classical novae were first reported in V838 Her (Lloyd et al., 1992). Such hard emission has been established as a common phenomenon among classical novae by recent intensive monitoring observations with Swift and subsequent follow-up observations with *XMM-Newton*, *Suzaku*, and others (e.g., Ness et al. 2009c; Page et al. 2010, 2009; Tsujimoto et al. 2009). Viable interpretations for the hard components include the plasma produced by internal shocks; i.e., ejecta with different velocities collide with each other (Friedjung, 1987; Mukai & Ishida, 2001). The X-ray spectra are represented by optically-thin thermal plasma emission with a plasma temperature of several keV (e.g., Lloyd et al. 1992; Mukai & Ishida 2001; Orio et al. 2001c; Tsujimoto et al. 2009). For unknown reasons, Fe is often depleted in the chemical composition (e.g, V382 Vel; Orio et al. 2001c, V458 Vul; Tsujimoto et al. 2009). These features are quite similar to those found in the hard component in the earlier phase of V2491 Cyg.

On the other hand, the hard component in the later phase is more similar to that commonly seen in IPs. The defining characteristics of IP X-ray emission include the following (e.g., Ezuka & Ishida 1999): (1) The Fe emission lines are clearly seen at 6.4, 6.7, and 7.0 keV respectively from Fe_{I}, Fe_{XXV}, and Fe_{XXVI}. (2) The continuum emission is very flat, which is represented by thermal bremsstrahlung of a temperature of $\sim$10 keV. (3) The X-ray luminosity in the 2.0–10 keV energy band is $\sim 10^{33}$ erg s^{-1} (e.g., Chanmugam et al. 1991; Norton & Watson 1989; Warner 2003), which is much brighter than that of non-magnetic or weakly magnetized white dwarfs and polars (e.g., Mukai & Shiokawa 1993; Warner 2003; Baskill et al. 2005; Byckling et al. 2010). The hard-band luminosity of V2491 Cyg ($\sim 10^{34}$ erg s^{-1}) is even larger than the typical IPs. This may be due to a higher accretion rate in the system. (4) The harder band (>2 keV) emission dominates the spectrum in IPs. In contrast, the softer band (<2 keV) emission dominates the spectrum in polars. (5) The modulation due to the white dwarf spin and orbital motions are shown in the X-ray light curve (see Ness et al. 2011 for results of the timing analysis for V2491 Cyg). In IPs, the high temperature plasma responsible for the flat continuum and the highly ionized Fe lines is caused by a shock at the base of the accretion funnel. The plasma illuminates the white dwarf surface, which produces a prominent Fe_{I} Kα fluorescent line. All these features are seen in the hard-band emission in the later phase of V2491 Cyg.

It is important to note three things in the results. The first is the equivalent width of the Fe_{I} line found in the later phase. The observed equivalent width ($\gtrsim$100 eV) is comparable to those observed in IPs (e.g., Ezuka & Ishida 1999). It can be explained by fluorescence at the white dwarf surface, or at the surface of the accretion disk, by X-ray emitting plasma at the base of the accretion funnel in the proximity of the white dwarf (e.g., Ishida et al. 1991; George & Fabian 1991). It corresponds to the "infinite plane" fluorescence included

in the calculations by Drake et al. (2008). However, such a large equivalent width cannot be explained for cases in which (1) the plasma heated by ejecta shocks illuminates the white dwarf surface, or (2) the plasma heated by ejecta or accretion shocks illuminates cold material in the ejecta. In case (1), the subtended angle of the white dwarf surface is too small ($\Delta\Omega/4\pi \sim 10^{-12}$, assuming that the X-ray emitting region has expanded for 50 d at a constant speed of 3000 km s^{-1}). In case (2), the cold material is too thin to produce the Fe fluorescence with a large equivalent width. Although the cold matter subtends the entire sphere (4π steradian), the ejecta with a hydrogen column density of $\sim 10^{21}$ cm^{-2} (Page et al., 2010) can yield the equivalent width of only $\lesssim$10 eV for $\sim$10 keV thermal plasma X-rays (see equation 4 in Tsujimoto et al. 2005a). This is in line with our interpretation that the hard component in the later phase is from the accretion process in the white dwarf.

The second is that the hard-band features in the pre-nova phase of V2491 Cyg resemble those in the later phase of the post-nova spectra more than those in the earlier phase regarding the presence of Fe emission lines (figure 5.19) and the spectral hardness (table 5.10). This suggests that the origin of dominant X-ray emission is the same between the pre-nova and the later post-nova phases. A notable difference can be found in the hard-band flux. It is significantly higher in the late post-nova phase after day 50 than in the pre-nova phase. We speculate that the accretion rate in the late post-nova phase may have been higher than that in the pre-nova phase, which might be expected due to the heating of the secondary star by the outburst and the heated white dwarf (Schaefer, 2010).

The third is that V2487 Oph (Hernanz & Sala, 2002), GK Per (Hellier & Mukai, 2004), and CP Pup (Orio et al., 2009), which are the other three among four classical novae with a Fe_I fluorescence detection in the post-nova phase, also share characteristics with IPs such as high X-ray luminosity in the quiescent phase (e.g., Cordova et al. 1981a; Balman et al. 1995; Hernanz & Sala 2002) and the rapidity of the optical decline (t_3 is $\sim$8 d for V2487 Oph; Liller & Jones 1999; Pagnotta et al. 2009, $\sim$13 d for GK Per; Downes & Duerbeck 2000, and $\sim$6.5 d for CP Pup; Payne-Gaposchkin 1957; Orio et al. 2009).

5.3.5.7 Time-scale of accretion process

Using the Fe emission lines, we argued that the accretion process in V2491 Cyg was reestablished by at least $\sim$50 days after the outburst. Page et al. (2010) argued that the accretion was rekindled no later than day 57 using the X-ray flux flickering method. These independent methods lead to the same conclusion on the time scale for the accretion process to resume after the nova.

The time for the reestablishement of the accretion process coincides with the time when the soft-band emission starts to decline (figure 5.12). This is consistent with the following scenario. The accretion disk was likely destroyed by the blast (Drake & Orlando, 2010). Immediately after the outburst, the strong radiation pressure inhibits rejuvenation of the accretion disk and likely exceeds the ram pressure of the accretion flow once reestablished, thereby preventing accretion to occur. When the H-rich fuel had been consumed on the white dwarf surface by nuclear burning and the radiation pressure started to drop, the accretion resumed. We further speculate that the magnetic field on the white dwarf is responsible for the short time scale of rekindled accretion. When mass accretion from the companion

star was switched on after a post-nova interval, the viscous time scale of the accretion disk would have to elapse before gas could again reach the white dwarf surface (e.g., Frank et al. 1992). For a magnetized white dwarf, accretion could resume earlier as less disk spreading is required. The scenario will be tested by examining the coincidence of the decline in the soft-band flux and the emergence of the Fe_I line by high-cadence X-ray observations of classical novae in the future.

5.4 V2672 Ophiuchi

5.4.1 Summary

We conducted an X-ray spectroscopic study of V2672 Oph based on target-of-opportunity observations (§3.2.2) with the *Suzaku* satellite. Two ∼25 ks *Suzaku* observations yielded high signal-to-noise ratio light curves and spectra with the XIS on 12 and 22 days after the outburst.

On day 12, a rapid flare-like X-ray flux amplification was seen in the soft X-ray band below ∼2 keV. Time-sliced spectra are characterized by the growing soft excess and relatively stable hard X-ray continuum with intense emission lines from highly-ionized silicon. On day 22, the flux of both the soft and hard components decreased, and the energies of dominant emission from the soft component shifted toward lower energies. We found that the time-variable spectra are explained by a development of a soft blackbody and hard thin-thermal plasma model convolved with a photoelectric absorption. In this section, we introduce characteristics of the X-ray emission and its evolution of V2672 Oph. This results are also scheduled for publication by Takei et al. (2011, in prep.).

5.4.2 Target

5.4.2.1 Ground-based observations

An optical nova was discovered on 2009 August 16.515 UT (55059.52 d in the MJD) in the constellation Ophiucus at (R.A., Dec.) = ($17^h38^m19.68^s$, $-26°44'14.0''$) in the equinox J2000.0 (Nakano et al., 2009d). We define the epoch of the discovery as the origin of time throughout this research. This nova showed a visual brightness of 10.0 mag at the discovery using an unfiltered CCD camera (Nakano et al., 2009d). Nothing brighter than an R-band magnitude of 20.8 mag was recognized at the position in the Digitized Sky Survey images from 1991 to 1996 (Nakano et al., 2009d,c), indicating that the source suddenly increased its brightness by more than ∼10 mag. The nova was named V2672 Ophiuchi (Nakano et al., 2009c).

Photometric and spectroscopic studies were subsequently performed based on the ground-based observations (Nakano et al., 2009d,c; Nissinen et al., 2009; Ayani et al., 2009a,b; Munari et al., 2009). The time development of the optical brightness is shown in the top panel of figure 5.20. Assuming the maximum V-band magnitude of 11.9 mag on 2009 August 17.134 UT (Nakano et al., 2009d), the nova declined at the rate of $t_2 \sim 3$ day, where t_2 is the time to decline by 2 mag from the optical maximum, indicating that V2672 Oph is an extremely fast nova. The $B-V$ color is 1.81 mag on 2009 August 17.47 UT (Munari et al., 2009). In the early phase of the outburst, optical spectra exhibited Hα, Hβ, O$_{\rm I}$, and possibly He$_{\rm I}$ emission lines (Munari et al., 2009). The velocity width of the Hα line was ∼8000 km s^{-1} on day 1 (Ayani et al., 2009a). The rapid decline of the brightness and the extremely high velocity of the ejecta suggest that this is a classical nova with a massive white dwarf (Munari et al., 2009). In the radio regime, synchrotron emission with a flat spectral index ($\alpha \lesssim 1.2$) was detected on day 15.61 using the Very Large Array in its C configuration, indicating the

presence of strong shocks with relativistic electrons and magnetic fields (Krauss Hartman et al., 2009).

5.4.2.2 Space-based observations

In the pre-nova phase, no significant emission was found in X-ray images obtained with *ROSAT*, *ASCA*, and a slew survey of *XMM-Newton* (Schwarz et al., 2009). After the discovery, intensive monitoring observations were performed with *Swift* (Schwarz et al., 2009). The developments of the band-limited X-ray count rates are shown in the bottom panel of figure 5.20. X-rays were first detected on day 1.43 with a count rate of $\sim$0.017 s^{-1} by the XRT onboard *Swift*. Significant ultraviolet emission was also found with the UVOT onboard *Swift*, whereas no γ-ray emission was detected with the *INTEGRAL* satellite on days 4 and 7 (Schwarz et al., 2009). X-ray spectra exhibited hard continuum emission with a heavy absorption (Schwarz et al., 2009).

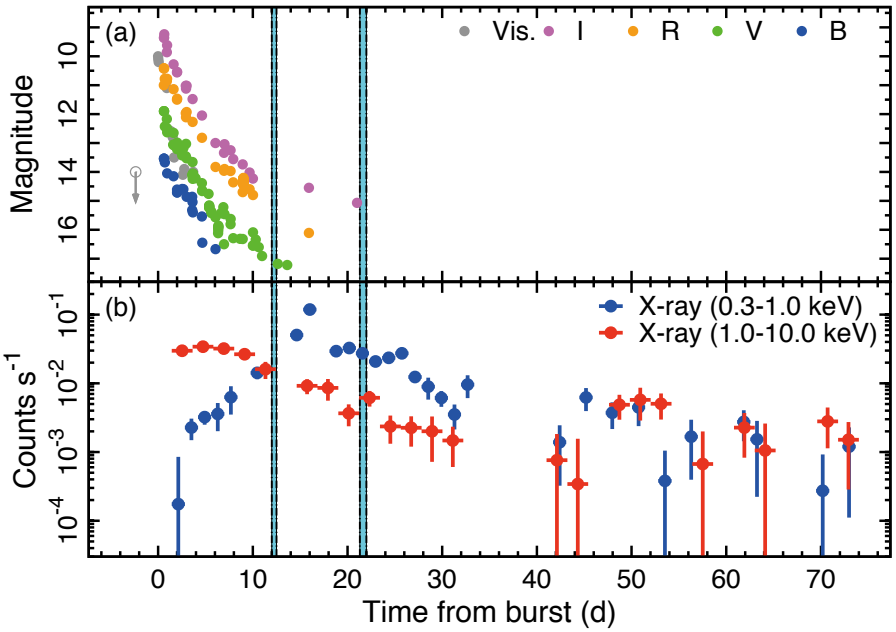

Figure 5.20: Developments of the optical magnitudes and the X-ray count rates are shown in panel (a) and (b), respectively. The origin of the abscissa is 55059.52 d in modified Julian date when the nova was discovered (Nakano et al., 2009d). The durations of the two *Suzaku* observations are indicated with cyan regions. (a) *B*-, *V*-, *R*-, *I*-band, and visual magnitudes are shown with different colors. The upper-limit for the visual magnitude before the outburst is indicated by the open circle and the downward arrow. As the optical brightness quickly faded, no ground-based observation was performed beyond day $\sim$20. (b) The background-subtracted X-ray count rates with Swift in the soft (0.3–1.0 keV) and hard (1.0–10.0 keV) energy band with different colors. The optical photometry data are taken from the American Association of Variable Star Observers (AAVSO) International Database, the Variable Star Observers League in Japan (VSOLJ) Observation Database, Nakano et al. (2009d), Nakano et al. (2009c), Nissinen et al. (2009), Ayani et al. (2009b), and Munari et al. (2009). The X-ray photometry data are from Swift observations conducted by G. Schwarz and the *Swift* Nova-CV Group.

5.4.3 Observations and Data Reduction

V2672 Oph was observed with *Suzaku* twice (table 5.11) on 2009 August 28 and September 6 (12 and 22 days after the outburst, respectively). Two observations were aimed to put V2672 Oph at the center of the XIS field with almost the same roll angle. As the signals of the HXD are seriously contaminated by neighboring hard X-ray sources, we concentrate on the XIS data in this paper.

Table 5.11: *Suzaku* observation log of V2672 Oph.

Mission	Observation number	Start time (UT)	End time (UT)	$t_{\rm b}$[a] (d)	Δt[b] (ks)
Suzaku	904002010	2009-08-28 12:20	2009-08-29 00:00	12.2	23.1
	904002020	2009-09-06 19:38	2009-09-07 11:30	21.6	25.1

[a] Elapsed days in the middle of the observation from the discovery of V2672 Oph (55059.52 d in the MJD).
[b] Net exposure time averaged over the operating CCDs.

The absolute energy scale is accurate to $\lesssim$10 eV as of the observation dates. The energy resolution is 180 and 230 eV at 5.9 keV in the full width at half maximum for respectively the FI and BI CCDs. XIS2 and a part of XIS0 are not functional, thus we used the remaining part of the data. The XIS was operated in the normal clocking mode with a frame time of 8 s. The net exposure times are 23 and 25 ks for the observations on days 12 and 22, respectively. The data were processed with the standard pipeline version 2.4, in which events were removed during the South Atlantic anomaly passages, the earth elevation angles below 5°, and the day-earth elevation angles below 20°. For reduction of the data, we used the HEASoft package version 6.7.

5.4.4 Analysis

5.4.4.1 Images

Figure 5.21 shows smoothed XIS images in the 0.2–12.0 keV energy band obtained on days 12 and 22. The astrometry of each image was registered by matching the position of V2672 Oph with that of the optical observation by Nakano et al. (2009d). For the following temporal and spectral analyses, the source events were accumulated from a circle with an adaptively chosen radius to maximize the ratio against background events (solid circle), while the background events were accumulated from an annulus with the inner and outer radii of $4'$ and $7'$, respectively (dashed annulus).

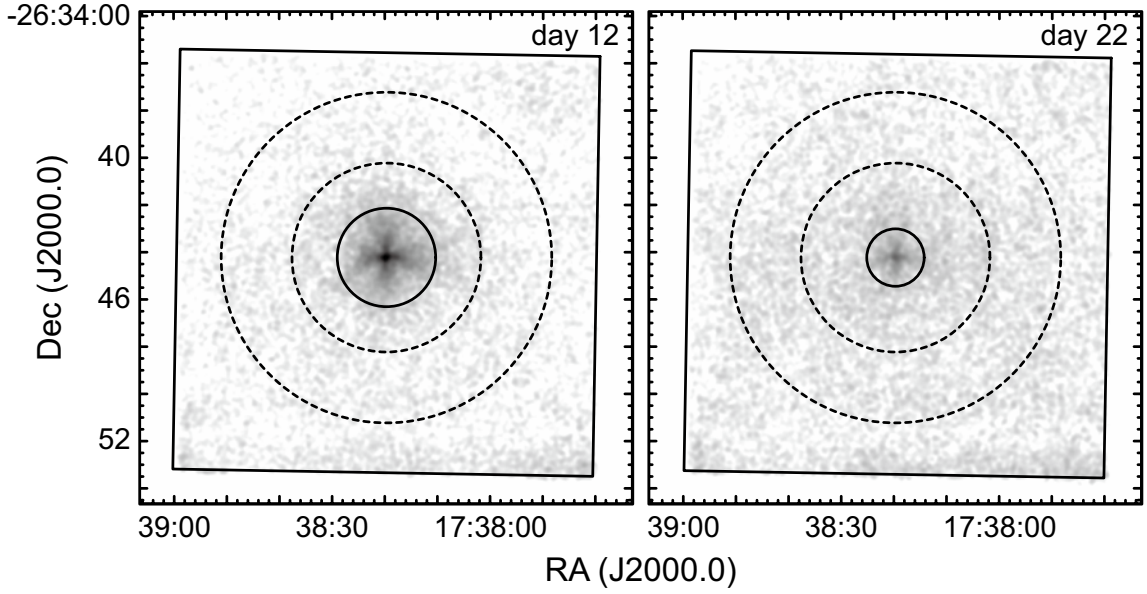

Figure 5.21: Smoothed XIS images obtained on days 12 and 22. Events recorded by the three CCDs in the 0.2–12.0 keV energy band were used. The source and background extraction regions are respectively shown with the solid circle and the dashed annulus for each observation.

5.4.4.2 Light curves

We constructed source and background light curves in the 0.2–12.0 keV band separately on day 12 and 22 (figure 5.22). On day 12, the X-ray count rate remains constant in the former half, but it shows a prominent flare-like event in the latter half. On day 22, the light curve is relatively stable with a count rate smaller than that in the former half of the day 12. In accordance with this development, we defined four time phases (figure 5.22) for time-sliced spectroscopy: (A) the stable phase on day 12, (B) earlier half of the flare on day 12, (C) latter half of the flare on day 12, and (D) day 22.

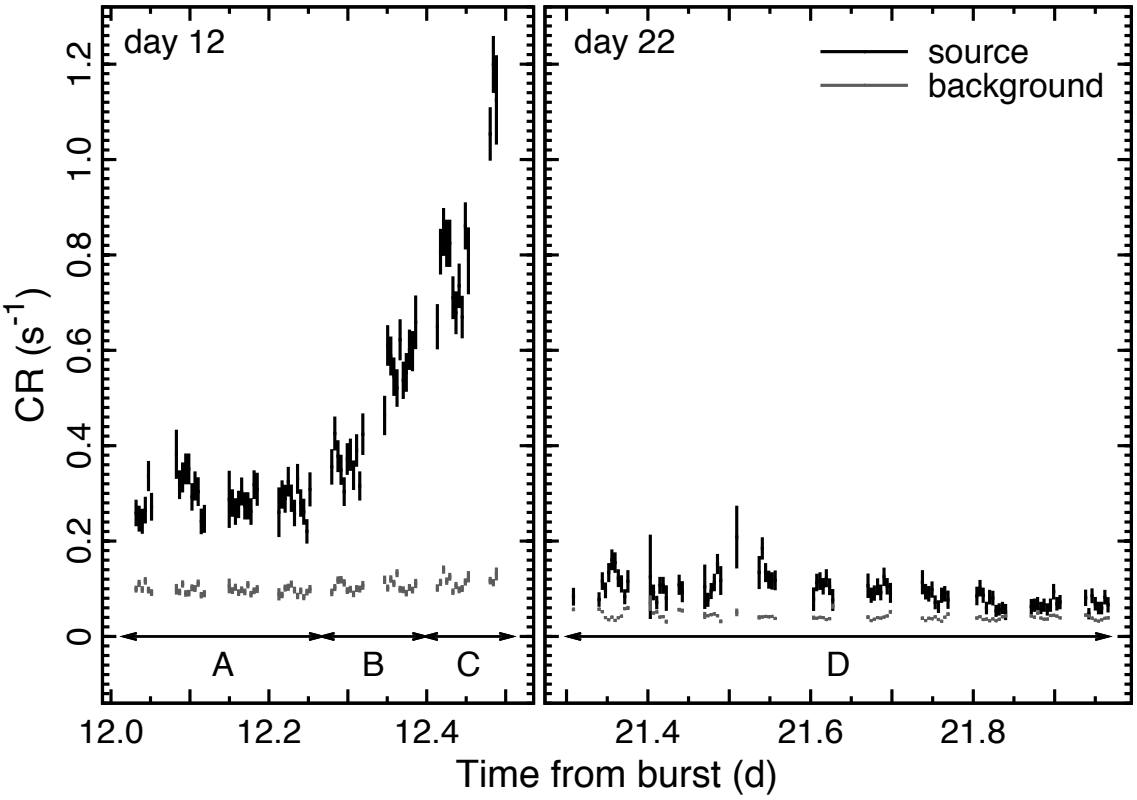

Figure 5.22: Source (black) and background (red) light curves of the count rates on days 12 (left) and 22 (right). Events recorded by the three CCDs in the 0.2–12.0 keV energy band were used. We defined four time intervals (phases A, B, C, and D) according to the development for time-sliced spectroscopy. The background count rate is normalized to the source extraction area.

5.4.4.3 Spectra

Figure 5.23 shows the background-subtracted BI spectra with time slices of A–D. The detector and mirror responses were generated using the `xisrmfgen` and `xissimarfgen` tools (Ishisaki et al., 2007), respectively. For the following spectral analysis, two FI spectra with nearly identical responses were merged, while the BI spectrum was treated separately.

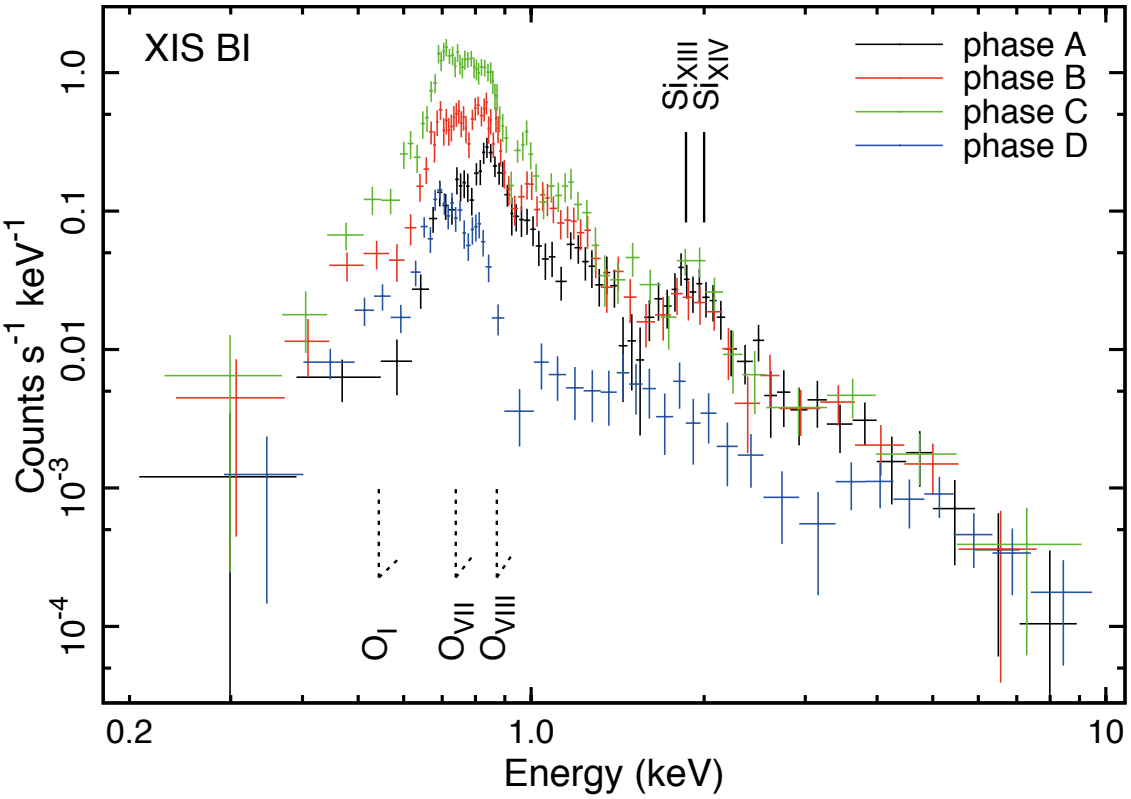

Figure 5.23: Background-subtracted BI spectra during the phases A, B, C, and D. Pluses indicate the spectra with different colors (black, red, green, and blue for the phases A, B, C, and D, respectively). The energies of significant Kα emission lines and K absorption edges are respectively labeled with solid and dashed lines.

The spectral shape is highly variable particularly in the soft X-ray band. In order to parameterize the time-varying complex spectra, we conducted fitting trials for the set of eight spectra on the four time-slices with both FI and BI CCDs, simultaneously. The Xspec version 11.3.2 in HEASoft was used for the spectral analysis. We make a simplifying assumption that all four time-sliced spectra are explained by the same set of spectral components; i.e., their differences are attributable to the changes of the parameters in these components.

We start with the hard emission above 1 keV, which remains relatively stable in the four slices. In slices A–C, the obtained spectra are characterized by a hard continuum up to $\sim$10 keV with an intense Kα emission line from Si_{XIII} stronger than Si_{XIV} (figure 5.23), indicating that an optically-thin thermal plasma component is necessary to explain the

hard X-ray emission. We therefore introduced an optically-thin collisionally-ionized thermal plasma (APEC; Smith et al. 2001) component with a temperature of $k_{\rm B}T^{\rm th}$. The elemental abundance of Si ($Z_{\rm Si}$) is thawed, while those of the other metals were fixed to the solar value (Anders & Grevesse, 1989). These models are attenuated by an interstellar absorption model.

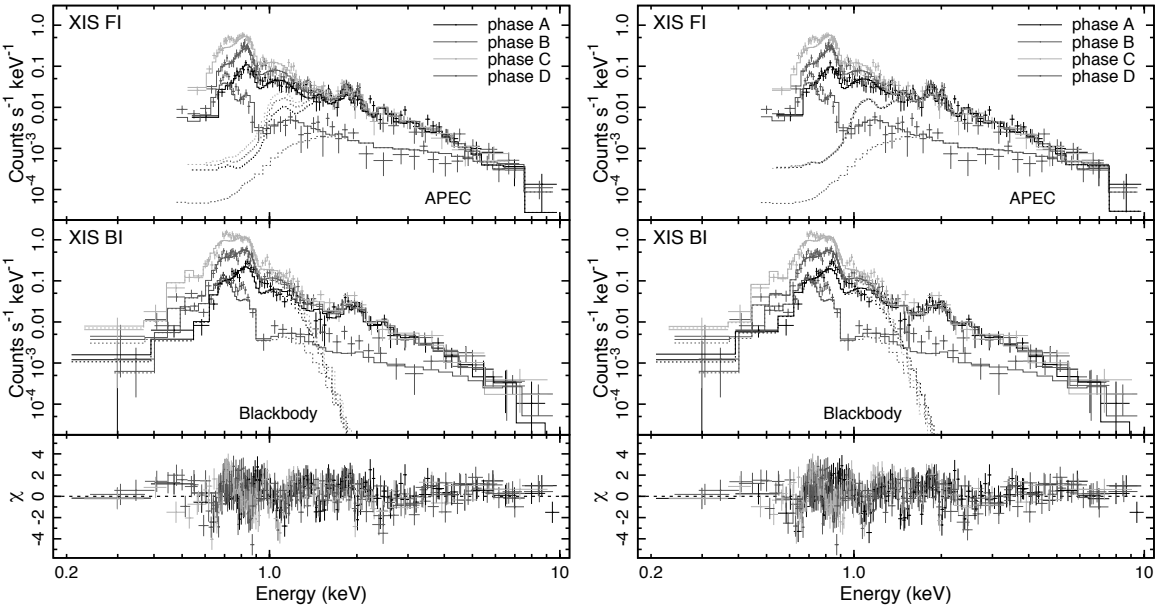

Figure 5.24: Background-subtracted X-ray spectra with the Model 1 (left) and 2 (right). The symbols follow figure 5.23. The time-sliced eight spectra with both FI and BI CCDs are simultaneously fitted. The best-fit model is shown by the solid (total) and dashed (each component) histograms. The lower panel shows the residual from the best-fit model.

Next, we study the soft excess emission below 1 keV, which is highly variable during the observations. The obtained spectra are characterized by a soft and bright continuum with a heavy attenuation below 0.6 keV and in the 0.8–1.0 keV energy bands, which cannot be explained by the APEC component applied for the hard continuum. We therefore attempted an additional component such as APEC, blackbody, or power-law for the soft spectra. In any cases, an additional local absorption component is necessary to explain the heavy attenuation in the 0.8–1.0 keV energy band. Largely improved fits were obtained by the combination of a soft blackbody emission component ($k_{\rm B}T^{\rm bb}$ for temperature) and a photoelectric absorption K edge from $\rm O_{VIII}$ ($\tau_{\rm O_{VIII}}$ for optical depth) at 0.8714 keV (Scofield, 2009).

At this stage, a clear structure still remains in the residual of the fits at $\sim$0.5 keV. The spectra are highly absorbed below $\sim$0.6 keV, while they are less absorbed in the 0.7–0.8 keV energy range. For the combination of the heavy attenuation below $\sim$0.6 keV and a shallow absorption edge at $\sim$0.55 keV, largely improved fits were obtained by introducing the photoelectric absorption model with variable abundances of O ($Z_{\rm O}$). In addition, we also see another attenuation in the $\sim$0.7–0.8 keV energy range particularly in the spectra of the slice D. Introducing an additional absorption K edge from $\rm O_{VII}$ ($\tau_{\rm O_{VIII}}$ for optical

depth) at 0.7393 keV (Scofield, 2009) can also improve the fits. The improvements are found significant at >3 σ levels in the F-test.

For the spectral development, we tried two fitting models with different constraints on the free parameters with the same components. One is the Model 1, in which an absorption column density ($N_{\rm H}$) is a free parameter to explain the spectral evolution in slices A–C. The other is the Model 2, in which the free parameters are the temperature and the luminosity of the blackbody component. As the plasma condition changed by the slice D, the column density for the photoelectric absorption, the optical depths for the absorption edges, and the temperatures and luminosities for the emission components were varied for the fitting except the abundance pattern. The fitting results do not differ so much between the two models, with a reasonably good fit for a relatively simple model and the simplifying assumption. We show the spectra for both the Model 1 and Model 2, and the residual in figure 5.24. The best-fit parameters for Model 1 and 2 are summarized in table 5.12. An X-ray flux ($F_{\rm X}^{\rm bb}$ and $F_{\rm X}^{\rm th}$) and luminosity ($L_{\rm X}^{\rm bb}$ and $L_{\rm X}^{\rm th}$) are respectively derived for the blackbody and thin-thermal plasma components, assuming a distance of 15 kpc.

Table 5.12: Best-fit parameters of V2672 Oph.

Comp.	Param.	Unit	Model 1[abcd] A	B	C	D
Absorption	$N_{\rm H}$	(10^{22} cm^{-2})	$1.82^{+0.11}_{-0.08}$	$1.52^{+0.11}_{-0.08}$	$1.28^{+0.11}_{-0.08}$	$1.04^{+0.20}_{-0.18}$
	$Z_{\rm O}$	(solar)	$0.54^{+0.04}_{-0.05}$	.....	.....	.....
Edge	Energy	(keV)	0.7393 (fixed)	.....	.....	.....
	$\tau_{\rm O\,VII}$		$0.06^{+0.16}_{-0.06}$	.....	.....	$2.14^{+0.39}_{-0.39}$
Edge	Energy	(keV)	0.8714 (fixed)	.....	.....	.....
	$\tau_{\rm O\,VIII}$		$1.66^{+0.20}_{-0.19}$	.....	.....	$3.98^{+1.18}_{-0.88}$
Blackbody	$k_{\rm B}T^{\rm bb}$	(eV)	$62.0^{+2.8}_{-2.9}$	.....	.....	$75.6^{+12.1}_{-10.7}$
	$F_{\rm X}^{\rm bb}$	(10^{-12} erg s^{-1} cm^{-2})	$0.67^{+0.96}_{-0.32}$	$1.84^{+2.65}_{-0.89}$	$4.41^{+6.37}_{-2.14}$	$0.57^{+2.85}_{-0.44}$
	$L_{\rm X}^{\rm bb}$	(10^{38} erg s^{-1})	$11.1^{+16.0}_{-5.4}$	.....	.....	$0.30^{+1.48}_{-0.23}$
APEC	$k_{\rm B}T^{\rm th}$	(keV)	$1.52^{+0.10}_{-0.10}$	.....	.....	$7.49^{+33.3}_{-3.65}$
	$F_{\rm X}^{\rm th}$	(10^{-12} erg s^{-1} cm^{-2})	$0.39^{+0.04}_{-0.04}$	$0.40^{+0.04}_{-0.04}$	$0.42^{+0.05}_{-0.04}$	$0.21^{+0.06}_{-0.03}$
	$L_{\rm X}^{\rm th}$	(10^{34} erg s^{-1})	$1.42^{+0.15}_{-0.14}$	.....	.....	$0.60^{+0.17}_{-0.09}$
	$Z_{\rm Si}$	(solar)	$2.20^{+0.51}_{-0.44}$	.....	.....	.....
χ^2/d.o.f						790.8/505

Comp.	Param.	Unit	Model 2[abcd] A	B	C	D
Absorption	$N_{\rm H}$	(10^{22} cm^{-2})	$1.47^{+0.12}_{-0.09}$	.....	.....	$1.07^{+0.21}_{-0.18}$
	$Z_{\rm O}$	(solar)	$0.56^{+0.04}_{-0.04}$	.....	.....	.....
Edge	Energy	(keV)	0.7393 (fixed)	.....	.....	.....
	$\tau_{\rm O\,VII}$		$0.07^{+0.17}_{-0.07}$	.....	.....	$2.22^{+0.39}_{-0.39}$
Edge	Energy	(keV)	0.8714 (fixed)	.....	.....	.....
	$\tau_{\rm O\,VIII}$		$1.59^{+0.21}_{-0.20}$	.....	.....	$4.03^{+1.20}_{-0.88}$
Blackbody	$k_{\rm B}T^{\rm bb}$	(eV)	$69.5^{+3.9}_{-3.8}$	$62.0^{+3.3}_{-3.3}$	$56.7^{+3.0}_{-3.0}$	$74.7^{+11.6}_{-10.4}$
	$F_{\rm X}^{\rm bb}$	(10^{-12} erg s^{-1} cm^{-2})	$0.68^{+1.03}_{-0.35}$	$1.86^{+3.11}_{-1.00}$	$4.36^{+7.88}_{-2.39}$	$0.57^{+2.98}_{-0.44}$
	$L_{\rm X}^{\rm bb}$	(10^{38} erg s^{-1})	$1.57^{+2.41}_{-0.82}$	$10.0^{+16.7}_{-5.4}$	$46.8^{+84.5}_{-25.6}$	$0.38^{+1.96}_{-0.29}$
APEC	$k_{\rm B}T^{\rm th}$	(keV)	$1.56^{+0.08}_{-0.10}$	.....	.....	$7.39^{+30.8}_{-3.59}$
	$F_{\rm X}^{\rm th}$	(10^{-12} erg s^{-1} cm^{-2})	$0.40^{+0.04}_{-0.04}$	.....	.....	$0.21^{+0.06}_{-0.03}$
	$L_{\rm X}^{\rm th}$	(10^{34} erg s^{-1})	$1.37^{+0.15}_{-0.13}$	.....	.....	$0.60^{+0.17}_{-0.09}$
	$Z_{\rm Si}$	(solar)	$2.31^{+0.52}_{-0.46}$	.....	.....	.....
χ^2/d.o.f						814.5/503

[a] The statistical uncertainties indicate the 90% confidence ranges.
[b] Dotted columns indicate the values are tied to that of the phase A for the fitting.
[c] The flux values are respectively derived in the 0.2–2.0 keV and 2.0–10.0 keV bands for the blackbody and the APEC models.
[d] A distance of 15 kpc (§ 5.4.5.1) is assumed to derive the luminosities.

5.4.5 Results

5.4.5.1 Distance and Absorption

For discussion, we first estimate the distance to be ∼15 kpc based on the empirical relation by Downes & Duerbeck (2000). The relation is known between the maximum magnitude and the rate of decline among classical novae (MMRD relation; della Valle & Livio 1995; Downes & Duerbeck 2000), in which the intrinsically brighter ones fade faster. Such a relation can provide good distance indicator by optical observations. We calculated the distance from the observed maximum V-band magnitude of 11.9 mag, the value of $t_2 \sim 3$ d, and the $B-V$ color of 1.81 mag (see §5.4.2.1), assuming that an intrinsic $B-V$ color is 0 mag.

Assuming the distance of 15 kpc to V2672 Oph, the absorption-corrected X-ray luminosity of the thin-thermal plasma component is $\sim 10^{34}$ erg s^{-1} in the 2–10 keV energy band. The value is in a typical range for classical novae (Mukai et al., 2008). In contrast, that of the blackbody component exceeds the Eddington luminosity of white dwarfs with Chandrasekhar mass in some epochs for both fitting models 1 and 2. It has to be noted that blackbody fits to the SSS spectra have the tendency to overestimate the bolometric luminosity and thus the radius (e.g., Krautter et al. 1996).

The hydrogen-equivalent column density is more than $\sim 1\times10^{22}$ cm^{-2} in all four time-slices (table 5.12). The heavy absorption is consistent with the estimated large distance (∼15 kpc). Here, the absorption integrated through our Galaxy toward V2672 Oph is estimated as $\sim 3.8\times10^{21}$ cm^{-2} from H$_{\rm I}$ intensity maps (Kalberla et al., 2005). The observed column density is much larger than the upper limit for an interstellar absorption of a Galactic source. Also, the observed $N_{\rm H}$ varies with time. These two indicate the presence of a dense circumstellar absorption by the ejecta.

5.4.5.2 Soft X-ray Evolution

We described the soft X-ray evolution on the classical nova with the simple two model assumptions; Model 1 with the free parameters of absorption column densities, and Model 2 with the free parameters of temperatures and luminosities for the blackbody component. The results provide important clues to guess the origin of the rapid flux amplification.

For Model 1, the presence of an asymmetric ejecta is suggested with the rapid decline of the absorption column density in slices A–C. The spectral evolution is characterized by the decline of the absorption column density with $\sim 3\times10^{21}$ cm^{-2} in a period of $\sim 10^4$ s, suggesting that an absorber quickly disappeared in the line of sight. When we assume that an absorber is the surrounding ejecta with a uniform density and a constant expansion velocity (v_0), the absorption column density is approximated as $N_{\rm H,CSM} \sim n(t)\delta r(t) \sim \Delta M/4\pi(v_0 t)^2$, where $n(t)$ is the density, $\delta r(t)$ is the thickness, ΔM is the mass of the ejecta, and t is the time after the outburst. As a result, the value of $N_{\rm H,CSM}$ decreases by a factor of $((t + 10^4)/t)^{-2}$ over 10^4 under a symmetric expansion of the ejecta. Assuming that the t is $\sim 10^6$ s (∼12 day), the factor is calculated to be ∼2%, indicating that the observed rapid decline of the absorption column density cannot be explained simply by the symmetric expansion of the ejecta. This encourages us to pursue spherically asymmetric situations such as the non-uniform circumstellar material density in the expanding ejecta. Indeed, the

non-uniformity in a nova ejecta shell is expected to grow (Sokoloski et al., 2008), as thin parts of the shell are possibly broken by the radiation pressure, leaving a hole in the shell. The ejecta shell may be full of holes like a swiss-cheese, through which the super-soft X-ray emission went through in the line of sight.

For Model 2, we need to introduce a rapid evolution in the temperature and luminosity of the blackbody component in slice A–C. The spectral evolution is characterized by the decline of the temperature with ∼5–8 eV and the increase of the luminosity with a factor of ∼2.5 in a period of ∼0.1 d. The temperature increases more in the later phase (slice D), and a non-monotonical time development of the blackbody temperature is required.

Finally, we argue that the scenario with the asymmetric ejecta is more favorable than that with rapid time variation of SSS emission. Both stable (slice A) and increasing (slice B–C) phases are seen in the *Suzaku* light curve, suggesting that the event occurs occasionally. We have no reason to change the condition of radiation plasma quickly. In contrast, introducing the asymmetric ejecta, the variations are easily and completely explained by the spatial distribution, which is likely to be in the classical novae.

5.4.5.3 Absorption Edges

Absorption features by ionized species in the blackbody spectra are thought to arise from absorption by the atmosphere of the white dwarf (e.g., Heise et al. 1994). These features provide valuable tools to diagnose the physical state of the atmospheric plasma. The temperature of the white dwarf atmosphere can be estimated from the observed optical depths of the O_{VII} and O_{VIII} absorption K edges. In the two fitting models, the ratio of the optical depths between O_{VII} and O_{VIII} is 0.04 (Model 1) and 0.5 (Model 2). The K edge absorption cross sections for O_{VII} and O_{VIII} are respectively 2.4×10^{-19} and 1.2×10^{-19} cm^2 (Lang, 2006). The ratio of the optical depths can be converted to that of the column density of O_{VII} to O_{VIII} as ∼0.02 and ∼0.25. The fractional density of ions at various ionization stages for several elements (C, N, O, Ne, and Fe) are calculated by Ebisawa et al. (2001) as a function of plasma temperature (0–150 eV), and two electron densities ($n_e = 10^{18}$ and 10^{19} cm^{-3}). From the ratio and figure 1 in Ebisawa et al. (2001), the atmosphere temperature is constrained to be $\gtrsim$65 and ∼58 eV assuming the electron density of 10^{19} cm^{-3}. The observed blackbody temperatures of ∼60–80 eV (table 5.12 are roughly consistent with the values.

5.4.5.4 Hard X-ray Evolutions

In the hard X-ray band, the long-term *Swift* light curve shows a decline since the time of discovery (figure 5.20), indicating that the origin of the hard emission is different from that of the soft emission. The hard X-ray evolution is also similar to those of typical novae (e.g., RS Oph; Bode et al. 2008, V2491 Cyg; Page et al. 2010), in which the origin of thin-thermal plasma emission is considered to be due to kinematic interactions of the ejecta with the surrounding medium or within the ejecta (e.g.,Mukai & Ishida 2001).

The elemental abundance of the hard emission is one of the indicators for the amount of white dwarf material. In slices A–C, intense emission lines from Si were shown in the spectra, and we found the enhanced Si abundance with thin-thermal plasma component in

both fitting models (table 5.12). If the white dwarf lost mass by the outburst, the abundance pattern of the ejecta reflects the chemical composition of its core, and the metal abundances become higher than that of the accreted material. Here, the underlying white dwarf can have two different sets of chemical composition; a CO-type and an ONe-type. The major nuclear reactions in the CO-type white dwarf do not involve elements heavier than O, while that in the ONe-type reaches up to Si and S. In the case of V2672 Oph, the enhanced Si abundance suggests that the white dwarf contains heavy elements up to Si and the core is ONe-type.

Chapter 6

Discussion

In this chapter, we first discuss the five research items listed in section 3.1 (section 6.1). We then summarize the results into a unified picture (section 6.2).

Contents

6.1 Various Aspects of Classical Novae

6.1.1 X-ray Evolution in the Outburst

The first objective of this research (see section 3.1.1) is to classify types of X-ray emission from classical novae. Various types of X-ray emission were reported and different characteristics were revealed in time-resolved spectroscopic studies in the post-outburst phase of classical novae. We here summarize the typical characteristics of the five types X-ray emission (section 6.1.1.1–6.1.1.5) and put them in a time line after an explosion. Table 6.1 summarizes the detection of the five types of emission in classical novae observed in the X-ray energy band to date.

6.1.1.1 Super-Hard Emission

The super-hard emission shows the following observational characteristics.

- Power-law emission with a flat photon index dominant above $\sim$10 keV.
- Luminosity is in the order of $\sim 10^{36}$ erg s^{-1} in the 15–70 keV energy band.
- Emission appears in the initial post-outburst phase and disappears quickly.

The super-hard emission has been found only in our *Suzaku* observation for the classical nova V2491 Cyg so far (table 6.1). Therefore, the characteristics mentioned above are all from the only case. Enrichment of the sample is necessary to better characterize the system. The origin of the super-hard emission component was described in section 5.3 and below discussion. We note that the super-hard emission is closely associated with the γ-ray emission from the symbiotic nova V407 Cyg observed by the *Fermi* satellite (Abdo et al., 2010).

6.1.1.2 Hard-Thermal Emission

The hard-thermal emission shows the following observational characteristics.

- Optically-thin thermal plasma emission dominant in the $\sim$2–10 keV energy band.
- Plasma temperature is in the order of $\sim$0.1–10 keV.
- Luminosity is in the order of $\sim 10^{33}$–10^{35} erg s^{-1} in the 2–10 keV energy band.
- Emission emerges in the early phase of the post-outburst development.
- Decay with a time scale of several weeks to months.
- Presence of emission lines from highly-ionized elements (e.g., O, Ne, Mg, and Fe).
- Deficiency of the Fe abundance is widely seen in the spectra.

The hard-thermal emission has been reported in many post-outburst X-ray observations of classical novae (table 6.1). The hard thermal bremsstrahlung continuum with emission lines from highly ionized ions is clear evidence that a classical nova explosion produces hot optically-thin thermal plasma in the early development. Overall, observational results indicate that the origin of the hard-thermal emission is shock-heated plasma, in which kinetic

energy of the expanding ejecta at a velocity of several thousand km s^{-1} is thermalized. The shock velocity (v_s) produces a hot plasma with a temperature (T) in a strong shock. T is approximately expressed as a function of v_s with the Rankine-Hugoniot relation described as

$$k_{\rm B}T = \frac{2(\gamma-1)}{(\gamma+1)^2}\mu m_{\rm H} v_s^2, \tag{6.1}$$

where $k_{\rm B}$ is the Boltzmann constant, γ is the specific heat ratio, $\mu \sim 1$ is the mean molecular weight to hydrogen mass, and $m_{\rm H}$ is the hydrogen mass. Assuming the non-relativistic monoatomic gas ($\gamma = 5/3$), the relation can be explained as

$$k_{\rm B}T = \frac{3}{16}\mu m_{\rm H} v_s^2. \tag{6.2}$$

The observed temperature of several keV implies the shock velocity of a few thousand km s^{-1}, which is consistent with the observed velocity of the ejecta. The presence of highly variable absorption column density suggests that the X-ray emitting region is inside the ejecta.

How these shocks occur for the hard X-ray production remains an open question. Two ideas have already been proposed (e.g., Balman et al. 1998): (1) One is internal shocks, which is a collision between fast wind with pre-existing slow wind from the white dwarf. This is likely the case for most classical novae with a dwarf companion, in which thick circumbinary material is not expected for the shocks with the nova wind. (2) Another is external shocks, in which the ejecta collides with the shell by the previous explosions or with the wind from a red giant companion. This is likely the case for classical novae from symbiotic system such as RS Oph and RR Tel, in which thick circumbinary material is expected for the shocks with the wind from a red giant companion.

6.1.1.3 Super-Soft Emission

The super-soft emission shows the following observational characteristics.

- Blackbody-like continuum emission dominant below ∼1 keV.
- Bolometric luminosity is $\sim 10^{36}$–10^{38} erg s^{-1}.
- Color temperature is ∼10–100 eV.
- Presence of absorption features from highly-ionized elements (e.g., C, N, and O).
- Emission starts in the middle phase of the post-outburst development.
- Decay time scale is several weeks to years.

The super-soft emission has been reported in many post-outburst X-ray observations of classical novae (table 6.1). The soft blackbody-like emission with a temperature of ∼10–100 eV is clear evidence for the presence of an optically-thick thermal plasma. This component is considered to be photospheric emission from the hot layer on the white dwarf surface. The dominant energy source is nuclear burning in the CNO cycle using the residual fuels after the explosion. Assuming the mass of a white dwarf ($M_{\rm WD} \lesssim 1.4\ M_\odot$), the bolometric

luminosity as the blackbody approximation is near (or above) the Eddington limit described as

$$L_{Edd} \;=\; \frac{4\pi c G M_{\rm WD}}{\kappa_T} \;\sim\; 1.3\times10^{38}(\frac{M_{\rm WD}}{M_\odot})\ [\rm erg\ s^{-1}], \tag{6.3}$$

where c is the light speed ($\sim$3$\times10^{10}$ cm s^{-1}), G is the gravitational constant ($\sim$6.7$\times10^{-8}$ cm^3 s^{-2} g^{-1}), and κ_T is the Thomson opacity ($\sim$0.4 cm^2 g^{-1}). In addition, the observed temperatures ($T \lesssim 10^6$ K) and bolometric luminosities are also consistent with the white dwarf radius ($R \sim 5\times10^8$ cm);

$$L_{bol} \;\sim\; 4\pi R^2 \sigma T^4, \tag{6.4}$$

where the X-ray emitting region is assumed to be spherically symmetric, and σ is the Stefan-Boltzmann constant ($\sim$5.7$\times10^{-5}$ erg s^{-1} cm^{-2} K^{-4}).

6.1.1.4 Quiescent Emission

The quiescent emission shows the following observational characteristics.

- Emission continues even after the three types of emission stated above (section 6.1.1.1–6.1.1.3) disappears after a nova.
- Optically-thin thermal plasma emission is dominant in the X-ray spectra.
- Plasma temperature is in the order of 0.1–10 keV.
- X-ray luminosity is in the order of 10^{31}–10^{34} erg s^{-1}.
- Fluorescent emission line from Fe is widely seen in the X-ray spectra.

The quiescent emission has also been reported in several X-ray observations of classical novae (table 6.1), which is in several decades after an eruption. The X-ray spectra are typically characterized by a thermal bremsstrahlung-like continuum with Kα emission lines from highly ionized as well as quasi-neutral Fe (e.g., Hernanz & Sala 2002 and Orio et al. 2009). The dominant energy source is the gravitational energy, and the X-ray emission is attributable to the boundary layer between the inner accretion disk and the white dwarf surface (non-magnetic CVs) or the shock at the base of the accretion funnel very close to a magnetic pole on the surface (magnetic CVs). The prominent fluorescent emission line from Fe indicates that the plasma emission illuminates the white dwarf surface and/or the accretion disk.

Based on the observed X-ray luminosity, we can roughly estimate the mass accretion rate ($\dot{m}$) using the relation described as

$$L_{bol} \;\sim\; \eta(G\frac{M_{\rm WD}\dot{m}}{r}), \tag{6.5}$$

where η is efficiency and r is the radius at the release of gravitational energy through accretion. Assuming that the X-ray plasma is located near the white dwarf surface (r =

5×10^8 cm), the mass accretion rate can be calculated as

$$\dot{m} \sim \frac{1}{\eta}\frac{rL_{bol}}{GM} \tag{6.6}$$

$$\lesssim \frac{1}{\eta}\,10^{-9}\ [M_\odot\ \mathrm{yr}^{-1}], \tag{6.7}$$

which is in the range typically seen in binary systems causing a classical nova explosion in the evolution ($\lesssim 10^{-7}\ M_\odot\ \mathrm{yr}^{-1}$; c.f., figure 2.13) using the typical efficiency ($\eta \sim 0.1$).

6.1.1.5 Nova-Remnant Emission

The nova-remnant emission shows the following observational characteristics.

- Diffuse X-ray emission around classical novae as a relic of an explosion.
- Optically-thin thermal plasma emission is dominant in the X-ray spectra.
- Plasma temperature is in the order of 0.1–10 keV.
- X-ray luminosity is in the order of 10^{32}–10^{34} erg s^{-1}.

The nova-remnant emission has been found in three binary systems causing classical novae several decades after its eruption (table 6.1). While a thin-thermal plasma component is dominant in the spectra, the presence of a power-law component is argued in a *Chandra* observation (Balman, 2005). The released energy and material of a classical nova explosion propagate through the circumstellar material, and the origin of X-ray emission can be considered a shock structure similar to those found in supernova remnants. In some classical novae, it is difficult to distinguish the components between the nova-remnant, the quiescent, and the hard-thermal emission with insufficient imaging capability.

Table 6.1: List of classical novae with X-ray characteristics.

Date	Name[a]	Super-Hard	Hard-Thermal	Super-Soft	Quiescent	Nova-Remnant
1848.04.27	V841 Oph				Orio et al. (2001a)	
1860.05.21	T Sco				Orio et al. (2001a)	
1895.04.08	RS Car				Cordova et al. (1981a)	
1901.02.21	GK Per				Orio et al. (2001a)	Balman & Ögelman (1999)
					Hellier & Mukai (2004)	Balman (2005)
					Eracleous et al. (1991)	
1906.02.14	AR Cir				Cordova et al. (1981a)	
1908	RR Tel				Orio et al. (2001a)	
1918.06.08	V603 Aql				Orio et al. (2001a)	
					Mukai & Orio (2005)	
					Drechsel et al. (1983)	
					Haefner et al. (1988)	
					Eracleous et al. (1991)	
1925.05.25	RR Pic				Cordova et al. (1981a)	
					Orio et al. (2001a)	
					Pekön & Balman (2008)	
1927.07.30	EL Aql				Cordova et al. (1981a)	
1931.05.09	MT Cen				Cordova et al. (1981a)	
1934.12.12	DQ Her				Orio et al. (2001a)	
1936.06.18	CP Lac				Orio et al. (2001a)	
1936.09.18	V356 Aql				Cordova et al. (1981a)	
1942.11.09	CP Pup				Cordova et al. (1981a)	
					Eracleous et al. (1991)	
					Balman et al. (1995)	
					Orio et al. (2001a)	
					Orio et al. (2009)	
1943.09.05	V500 Aql				Cordova et al. (1981a)	
1953.04.08	RR Cha				Cordova et al. (1981a)	
1960.03.07	V446 Her				Orio et al. (2001a)	
1978.03.05	LW Ser				Cordova et al. (1981a)	
1979.04.05	PU Vul				Eracleous et al. (1991)	
1983.01.18	GQ Mus			Oegelman et al. (1984)		
				Oegelman et al. (1987)		
				Oegelman et al. (1993)		
				Shanley et al. (1995)		
				Balman & Krautter (2001)		
				Orio et al. (2001a)		
				Cordova & Mason (1984)		
1984.07.27	PW Vul			Oegelman et al. (1987)		
1984.12.18	QU Vul			Oegelman et al. (1987)	Orio et al. (2001a)	
				Balman & Krautter (2001)		
1991.12.27	V351 Pup		Orio et al. (1996)?		Orio et al. (1996)?	
			Orio et al. (2001a)?		Orio et al. (2001a)?	
			Balman & Krautter (2001)?		Balman & Krautter (2001)?	
1991.03.24	V838 Her		Lloyd et al. (1992)			
			Orio et al. (2001a)			
1992.02.19	V1974 Cyg		Krautter et al. (1996)	Krautter et al. (1996)		
			Balman et al. (1998)	Balman et al. (1998)		
			Orio et al. (2001a)	Orio et al. (2001a)		
1995.08.24	V723 Cas			Ness et al. (2007a)?		
				Ness et al. (2008a)?		
1998.06.15	V2487 Oph				Hernanz & Sala (2002)	
1998.03.22	V4633 Sgr		Hernanz & Sala (2005)			
1999.12.01	V1494 Aql		Rohrbach et al. (2009)	Drake et al. (2003)		
1999.05.22	V382 Vel		Mukai & Ishida (2001)	Orio et al. (2002)		
			Orio et al. (2001a)			
			Ness et al. (2005)			
2002.09.20	V4743 Sgr		Ness et al. (2003b)	Ness (2010a)		
			Leibowitz et al. (2006)			
2004.11.20	V574 Pup		Ness et al. (2007a)	Ness et al. (2007a)		
2005.08.01	V1047 Cen		Ness et al. (2007a)			
2005.06.09	V1663 Aql		Ness et al. (2007a)			
2005.03.13	V382 Nor		Ness et al. (2007a)			
2005.03.28	V5115 Sgr		Hernanz & Sala (2010)	Hernanz & Sala (2010)		
2005.07.04	V5116 Sgr			Sala et al. (2008)		
2006.04.02	V2362 Cyg		Lynch et al. (2008b)			
2007.08.04	V458 Vul		(section 5.2)			
			Tsujimoto et al. (2009)	Ness et al. (2009c)		
			Ness et al. (2009c)			
2007.08.08	V598 Pup		Page et al. (2009)	Page et al. (2009)		
2008.04.10	V2491 Cyg	(section 5.3)	(section 5.3)	(section 5.3)	(section 5.3)	
		Takei et al. (2009)	Page et al. (2010)	Ness (2010a)	Ibarra et al. (2009)	
			Takei et al. (2009)	Takei & Ness (2010)	Page et al. (2010)	
				Page et al. (2010)		
2009.08.16	V2672 Oph		(section 5.4)	(section 5.4)		
1866.05.12	T CrB				Cordova & Mason (1984)	
1999.02.25	U Sco		Kahabka et al. (1999a)	Kahabka et al. (1999a)		
1966	T Pyx					Balman (2010)
1985.01.26	RS Oph		Mason et al. (1987)	Mason et al. (1987)	Orio (1993)?	Luna et al. (2009)
				Orio (1993)?	Orio et al. (2001a)	
2006.02.12	RS Oph		Sokoloski et al. (2006)	Ness et al. (2007b)		Luna et al. (2009)
			Ness et al. (2007b)	Nelson et al. (2008)		
			Nelson et al. (2008)	Ness et al. (2009b)		
			Drake et al. (2009)	Ness (2010a)		
			Ness et al. (2009b)			
1919.03.11	V1017 Sgr				Cordova et al. (1981a)	
					Cordova & Mason (1984)	
1917.06.15	CI Aql		Greiner & Di Stefano (2002)	Greiner & Di Stefano (2002)?		
1920.07.07	IM Nor		Orio et al. (2005)	Greiner & Di Stefano (2002)		

[a] Red sources are our data sets in this thesis.

6.1.2 Diagnosis of White Dwarf Atmosphere

The next objective of this research (see section 3.1.2) is to constrain the white dwarf mass using the temperature of its atmosphere, which is observed as the super-soft X-ray emission. We performed a CCD spectroscopic study with a high signal-to-noise ratio for the super-soft emission using the *Suzaku* satellite, and successfully detected the super-soft emission in three classical novae (section 5.1, 5.3, and 5.4). We found absorption edges from highly-ionized O in super-soft X-ray emission from two of them (section 5.1 and 5.4).

The ratio of absorption edges between two different ionization stages can be calculated using the Saha ionization equation (Rybicki & Lightman, 1985) described as

$$\frac{N_{j+1}N_e}{N_j} = \frac{2U_{j+1}(T)}{U_j(T)} \left(\frac{2\pi m_e k_{\rm B} T}{h^2}\right)^{3/2} e^{-\epsilon/k_{\rm B}T}, \tag{6.8}$$

where T is the temperature, ϵ is the ionization potential from j to $j+1$, N_j or N_{j+1} is the total number density of ions at an ionization stage of j and $j+1$, respectively, N_e is the electron density, and $U_j(T)$ or $U_{j+1}(T)$ is the corresponding partition function for the j-th and $(j+1)$-th ionization stage. Comparing the observed ratio of absorption depths and the calculated values for the white dwarf atmosphere (Ebisawa et al., 2001), we can constrain the temperature. This method is better than the spectral fitting with a simple blackbody approximation because the local absorption features are less contaminated by other emission. Absorption edges particularly from highly-ionized O are a typical signature in the super-soft emission, but the previous X-ray instruments cloud not resolve such local features except for exceptionally bright sources with grating spectroscopy. Recent X-ray CCD spectrometers with high sensitivity and sufficient energy resolution in this energy band provide a powerful tool to conduct such a diagnosis.

The effective temperature of the super-soft emission is also a function of white dwarf mass (e.g., figure 13 in Ebisawa et al. 2001), in which the temperature becomes larger as the mass increases. Using the relation, we can estimate the white dwarf mass for moderately bright targets using X-ray CCD spectrometers.

For very bright targets, extremely high resolution spectra ($\lambda/\Delta\lambda \sim 100$–$1000$) with grating observations with *XMM-Newton* and *Chandra* provide more powerful diagnostic tools for the atmosphere. For example, the absorption edge as well as line features from highly-ionized elements are found in the high resolution spectra (e.g. Ness et al. 2007b). The absorption lines were blue-shifted in all novae that have been observed with grating instruments, and an expanding atmosphere is argued in Ness (2010a). Non-local thermodynamic equilibrium atmosphere models were also applied for spectra with ionized absorption features (e.g., Rauch et al. 2010). On the other hand, several emission lines were detected in the spectra. The origin of these emission lines is considered to be a photo-ionized plasma due to the bright super-soft emission in the white dwarf.

Future studies should be performed with a spectral quality similar to those of the grating observations for individual classical novae with a moderate brightness, and the nature of the atmosphere should be studied with improved models.

6.1.3 Ejecta Chemistry

The third objective (see section 3.1.3) is to constrain the chemical composition of the white dwarf core through spectroscopy of the plasma in the ejected material. Therefore, we performed X-ray spectroscopy with sufficient energy resolution, signal-to-noise ratio, and sensitivity using the XIS onboard *Suzaku* for three recent classical novae (section 5.2, 5.3, and 5.4).

The hard-thermal emission was detected in many classical novae after the *Swift* launch. As the luminosity of the hard-thermal emission is quite small, resolving emission lines was difficult in the previous observatories with a poor energy resolution and sensitivity. The intensity ratio of emission lines is sensitive to constrain the plasma temperature and its chemical composition. The recent improvements in spectral quality made it possible to diagnose the plasma and its chemical composition of the ejecta from moderately bright targets. Actually, we successfully constrained the chemical composition of the ejecta in the hard-thermal emission, and argued the type of white dwarf core in three classical novae (section 5.2, 5.3, and 5.4). As a result, a wide variety of the chemical abundance is seen in the spectra, in which Kα emission lines from highly-ionized Ne, Mg, and Si are a common signature. We here demonstrated the ability of X-ray CCD instruments to constrain the chemical abundance of the ejecta and resultantly the type of the white dwarf core from moderately bright classical novae for the first time.

The white dwarf loses a part of the accreted material as well as the material of its own, thus the abundance pattern of the ejecta reflects the chemical composition of the white dwarf core. The underlying white dwarf can have two different sets of chemical composition; a CO-type and an ONe-type. In general, more massive white dwarf core consists with more heavy metals in abundance. Therefore, the chemical composition of the ejecta provides a unique observational tool.

For particularly bright sources, such as the recurrent nova RS Oph, extremely high energy resolution spectra with grating observations provide more powerful plasma diagnostic tools (e.g., Nelson et al. 2008). For example, (1) the grating spectra can resolve Doppler shifted components with a few hundred eV, indicating that we can diagnose the geometry of X-ray emitting region. Actually, in the case of RS Oph, the emission lines from highly-ionized N, O, Mg, and Si were blue-shifted at a velocity of $\sim$500–1300 km s^{-1}, as well as they were broadened by $\sim$2000 km s^{-1} on day 14 (Nelson et al., 2008). Based on the asymmetric line features, in which the blue-shifted components are brighter than the red-shifted components due to a large circumstellar absorption, the total of ejecta mass can be estimated (Drake et al., 2009). (2) The grating spectra can resolve He-like triplets. For thin-thermal plasma emission, He-like ions provide three intense emission lines; the resonance line (r; $1s^2\ ^1S_0$ – $1s2p\ ^1P_1$), the intercombination line (i; $1s^2\ ^1S_0$ – $1s2p\ ^3P_{1,2}$), and the forbidden line (f; $1s^2\ ^1S_0$ – $1s2s\ ^3S_1$). The dominant ionization source of the plasma can be determined using the ratio of He-like triplets, which is defined to be the G-ratio described as $G = (f+i)/r$. We can diagnose that the origin is dominated by the collisionally-ionized plasma ($G \sim 1$) or the photo-ionized ($G \gtrsim 4$) plasma using the value (Porquet et al., 2001). The plasma emission in RS Oph was also constrained to be the collisional-ionization (Nelson et al., 2008).

Future studies should be performed with a spectral quality similar to those of the grating

observations for individual classical novae with a moderate brightness, and the relationship between the chemical composition of the white dwarf core will be revealed for more number of sources.

6.1.4 Reestablishment of Accretion

The fourth objective (see section 3.1.4) is to confirm the reestablishment of an accretion process from classical novae after the explosion, which can be achieved by monitoring the development of its fluorescence emission. We performed spectroscopy at a high-cadence with sufficient energy resolution and sensitivity in the Fe K complex band using the X-ray CCD spectrometers onboard *Suzaku*, *XMM-Newton*, and *Swift* (section 5.3). We successfully confirmed a significant time-development of a Kα fluorescent emission line in the time-series X-ray spectra.

The quiescent emission in the systems causing a classical nova was detected in several archived data. The recent improvement of the sensitivity and the energy resolution in the Fe K complex band provides a powerful tool to confirm the reestablishment of accretion process using the Fe emission lines. The Fe Kα fluorescent emission line was confirmed in a total of four binary systems causing a classical nova so far (GK Per; Hellier & Mukai 2004, V2487 Oph; Hernanz & Sala 2002, CP Pup; Orio et al. 2009, and V2491 Cyg; section 5.3). The observed equivalent widths for the Fe K fluorescent line are $\gtrsim$100 eV, which is consistent with fluorescence at the white dwarf surface or at the surface of the accretion disk. The Doppler shifted red wing are also confirmed in GK Per and CP Pup with a width of $\sim$200–300 eV, which is considered to be caused by a Compton downscattering and pre-shock material falling at a near-escape velocity.

A clear development of the fluorescent lines has been confirmed from systems causing classical novae for the first time in our research (section 5.3). The time for the reestablishement of the accretion process coincides with the time when the super-soft emission starts to decline. Based on the results, we argued the following scenario. The accretion process in the binary system was likely destroyed by the blast at a nova explosion (Drake & Orlando, 2010). Immediately after the eruption, the strong radiation pressure inhibits rejuvenation of the accretion process and likely exceeds the ram pressure of the accretion flow once reestablished, thereby preventing accretion to occur. When the Hydrogen-rich fuel had been consumed on the white dwarf surface by nuclear burning and the radiation pressure started to drop, the accretion resumed.

The rekindled accretion process is a key event in the classical nova evolution. However, clear signature of rekindled accretion has been found only in four classical novae, all of which are considered to be intermediate polar systems. This might be explained by the fact that hard X-ray luminosities of intermediate polars ($\sim10^{33}$–10^{34} erg s^{-1}) are generally higher than the values from non-magnetic ($\sim10^{32}$ erg s^{-1}) or polar systems ($\sim10^{31}$ erg s^{-1}).

6.1.5 Non-Thermal Process in Explosion

6.1.5.1 Origin of the Emission

The final objective (see section 3.1.5) is to discover yet to be detected hard X-ray non-thermal emission by conducting sensitive super-hard band observations at an appropriate time after a burst in classical novae. We conducted high-sensitivity spectroscopy in the super-hard X-ray energy band using the *Suzaku* satellite, and successfully detected the super-hard emission in classical novae for the first time (section 5.3). After that, the detection of γ-ray emission from a symbiotic nova was also reported using the *Fermi* satellite (Abdo et al., 2010). Only in two cases, the power-law emission, which is likely to be produced in a non-thermal process, has been discovered in the early phase of novae. Three major ideas have been developed to explain the non-thermal emission from these novae.

(1) The presence of an accelerated population of charged particles with the non-thermal energy distribution was argued in this thesis (section 5.3) and in Takei et al. (2009). Non-thermal emission has also been speculated as the interaction between the accelerated particles with magnetic fields, photons, or protons. Here, the photon flux of the power-law emission is described as

$$I(E) \propto AE^{-\Gamma} \text{ [photons s}^{-1} \text{ cm}^{-2}\text{]}, \tag{6.9}$$

where A is a constant factor, Γ is a photon index, and E is a photon energy. This can be converted to the energy flux as

$$F(E) \propto AE^{-\alpha} \text{ [erg s}^{-1} \text{ cm}^{-2}\text{]}, \tag{6.10}$$

using the spectral index of $\alpha = (\Gamma - 1)$. For example, when we assume the synchrotron radiation due to accelerated electrons with a power-law energy distribution of index P, the spectral index (e.g., Rybicki & Lightman 1985) is described as

$$\alpha = \frac{P-1}{2}. \tag{6.11}$$

Assuming the mechanism of the first-order Fermi acceleration, the index of the electron energy distribution is larger than $\sim$2. In this method, we can compare the observed photon index of the power-law emission with the simple approximation of acceleration and radiation mechanisms. We also tested the claim for the *Suzaku* spectra with the combination of the first-order Fermi acceleration model and typical radiation mechanisms (e.g., inverse Compton, synchrotron, and bremsstrahlung emission), but the extremely flat photon index ($\Gamma = 0.1$) of the power-law radiation is ruled out for these models. To explain the extremely flat X-ray spectra, additional explanations would be necessary in this scenario; e.g., acceleration mechanisms include multiple shocks, turbulence, and magnetic reconnection (e.g., Pittard & Dougherty 2006).

(2) The flat power-law spectra might be explained by multiple scatterings in the inverse Compton process. The degree of change in the spectral shape depends on the Compton y parameter, which is a product of the fractional energy change and the scattering number. As the scattering number is also a function of an optical depth, the spectral index becomes

flat with the presence of dense circumstellar material consisting of sufficient high energy electrons. However, in this scenario, we do not know the mechanism for providing such high energy electrons in classical novae.

(3) Compton degradation of γ-ray emission lines produced by the radioactive decay of ^{22}Na is argued by Livio et al. (1992). When ^{22}Na occurs β^+-decay to a stable isotope ^{22}Ne, both positron and photons of the 1275 keV energy are produced. The positron additionally produce photons of the 511 keV energy in the annihilation with electron. The Compton down-scattering process of these two γ-ray emission lines can explain the *Suzaku* spectra and its time-scale (Suzuki & Shigeyama, 2010), in which a fast ejecta leads to the fast decline. However, a large discrepancy still remains in explaining the required amount of ^{22}Na ($\sim 3\times10^{-5}$ $M_\odot$) for the observed flux of the super-hard emission. The total mass of the ejecta in a typical classical nova is expected to be $\sim10^{-5}$ $M_\odot$, indicating that the total mass of ^{22}Na is insufficient.

(4) Compton degradation of γ-ray emission due to the π^0-decay process of proton collisions is also argued to explain the power-law γ-ray spectra with the *Fermi* satellite. The idea is consistent with the *Fermi* spectra in the early evolution. However, as the dominant emission due to the π^0-decay process is $\sim7\times10^4$ keV, a different explanation is required to explain the super-hard emission dominant in the X-ray band.

Non-thermal emission from high energy phenomena in classical novae had been studied only in theoretical contexts. Our first discovery of the super-hard X-ray emission using the *Suzaku* satellite and the subsequent detection of γ-ray emission using the *Fermi* satellite (Abdo et al., 2010) are long-awaited discoveries to understand the phenomena. As we do not reach a consistent interpretation, it should be examined by future studies both in theory and observations in high energy bands.

6.1.5.2 Contribution to the Galaxy

Our X-ray observations of classical novae with the *Suzaku* satellite eventually revealed that an explosion possibly produces high energy particles, suggesting that classical novae possibly contribute to cosmic-rays in our Galaxy. The origin of cosmic-rays still remains an open question since the discovery in 1912 (Hess, 1912). The energy spectrum of cosmic-rays (figure 6.1) shows the "knee" at the energy of 10^{15}–10^{16} eV, and the spectrum below this energy is expected to be of Galactic origins. One of the Galactic cosmic-ray source candidates is super-nova remnants at present. Assuming that the efficiency of particle acceleration in super-nova remnants is $\sim$1%, the total energy of Galactic cosmic-rays is compensated.

We therefore roughly estimate the energies of accelerated particles for classical novae with the following procedures. First, three simple assumptions are introduced: (1) The dominant emission mechanism is the synchrotron due to accelerated electrons with an energy of E_e. (2) The magnetic field strength of the emitting region (B) is similar to those of the cosmic value ($\sim10^{-6}$ gauss). (3) The emitted photon energy (K) is $\sim$100 keV. The synchrotron produces the radiation most effectively at the energy of

$$K \;=\; \gamma E_e \frac{B}{B_e}, \tag{6.12}$$

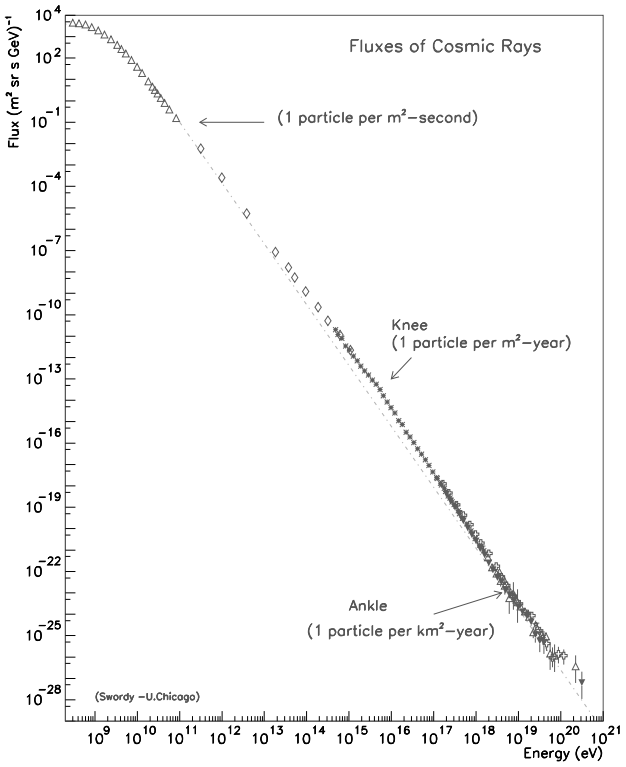

Figure 6.1: Particle spectrum of cosmic-rays (e.g., Cronin et al. 1997; Swordy 2001).

where γ is the Lorentz factor and B_e is the critical magnetic field strength of electrons ($\sim$4.4$\times$10^{13} gauss). As the Lorentz factor can be converted to

$$\gamma \;=\; \frac{E_e}{mc^2} \;\sim\; \frac{E_e}{511\ keV}, \tag{6.13}$$

the electron energy can be calculated as

$$E_e \;=\; \sqrt{100\ keV \times 511\ keV \times \frac{B_e}{B}} \;\sim\; 10^{15}\ [\mathrm{eV}]. \tag{6.14}$$

The energy of accelerated electrons in classical novae is roughly consistent with the energy at the "knee". Assuming that protons are also accelerated, classical novae possibly contribute to cosmic-rays in the Galaxy from the simple assumptions.

Finally, we estimate the contribution of classical novae to cosmic-rays in the Galaxy with the following procedures: The total flux of cosmic-rays was estimated to be $\sim$10^{-2} erg cm^{-2} s^{-1}, which can be converted to $\sim$10^{-12} erg cm^{-3} using the light speed ($\sim$3$\times$10^{10} cm s^{-1}). The volume of the Galaxy (V_G) is $\sim$10^{66}–10^{67} cm^3. Therefore, the total energy of cosmic-rays in the Galaxy is $\sim$10^{54}–10^{55} erg. In contrast, the average life of particles confined in the Galaxy (τ_{cr}) is $\sim$10^7 yr. The total energy of a classical nova outburst (E_{CNe}) is $\sim$10^{45}–10^{46} erg. The rate of classical novae (N_{CNe}) is expected to be $\sim$10–100 yr^{-1} in

the Galaxy (see section 2.2). Assuming that the input energy into particle accelerations in classical novae (P_{CNe}) is $\sim$1% of the total energy, the contribution to the Galaxy is

$$E_{cr} \;=\; \tau_{cr} E_{CNe} P_{CNe} N_{CNe} \;\sim\; 10^{51-53}\ [\mathrm{erg}], \tag{6.15}$$

indicating that classical novae possibly contribute $\sim$10% of cosmic-rays in the Galaxy. We speculate that the contribution of classical novae plays an important role in our Galaxy.

6.2 Picture of Classical Novae

6.2.1 Evolution of X-ray Phenomena

We described various aspects of X-ray emission from classical novae, including their typical behaviors and the diagnostics that they bring; i.e., the first discovery of the super-hard emission, the confirmation of reestablished accretion, the construction of ejecta chemistry, the diagnosis of the white dwarf atmosphere, and the establishment of the classification for these phenomena. We show a schematic view of a classical nova as a time development of representative X-ray phenomena in figure 6.2.

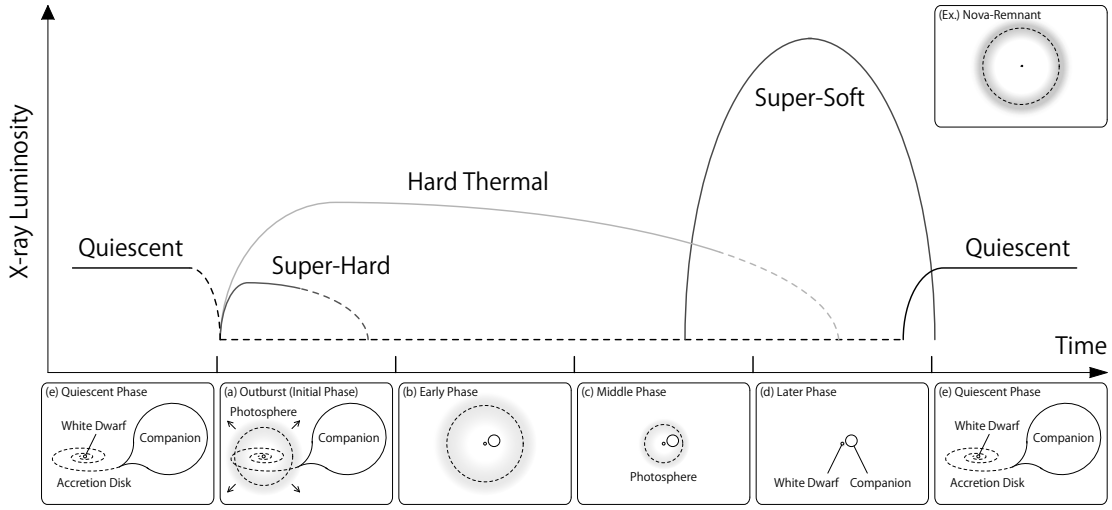

Figure 6.2: Time development of X-ray phenomena in classical novae.

A sequence of the X-ray evolution in a classical nova explosion is described as follows. During a nova eruption, the ejecta quickly expands at a velocity of several thousand km s^{-1} (figure 6.2a). At the initial stage, the energy source of the super-hard emission is immediately provided by the explosion, such as accelerated particles or electron annihilation lines. During the early phase, the ejected particles with different velocities collide to produce the shock-heated plasma, which produces the hard-thermal emission (figure 6.2b). The shock-heated plasma can also be produced when dense surrounding material is present for stellar winds from a red giant companion, a planetary nebula, or circumstellar materials ejected in previous nova explosions. After the ejecta expands and becomes less opaque, photospheric emission in the white dwarf emerges in the soft X-ray band, which is observed as the bright super-soft mission from many classical novae (figure 6.2c–d). When the surface nuclear fuel is consumed, the event of the nova outburst is terminated, then the reestablished accretion process starts to accumulate material again for the next eruption (figure 6.2d–e). The quiescent emission originates from the accretion process in particular in systems with a magnetized white dwarf. In a long-term behavior, the expanding ejecta can also produce adiabatic shocks similar to a super-nova remnant. Both thermal and non-thermal X-rays are observed as the nova-remnant emission around some binary systems.

6.2.2 Astrophysical Orientation of X-ray Phenomena

We finally show the schematic view of the X-ray emission and their diagnostic utility to reveal physical quantities in classical novae (figure 6.3). The systematic X-ray observations provide powerful tools to unveil important high energy phenomena of classical novae and eventually enhance our understanding of the mechanisms of cosmic-rays, the evolution of white dwarfs, binary systems, and the Universe.

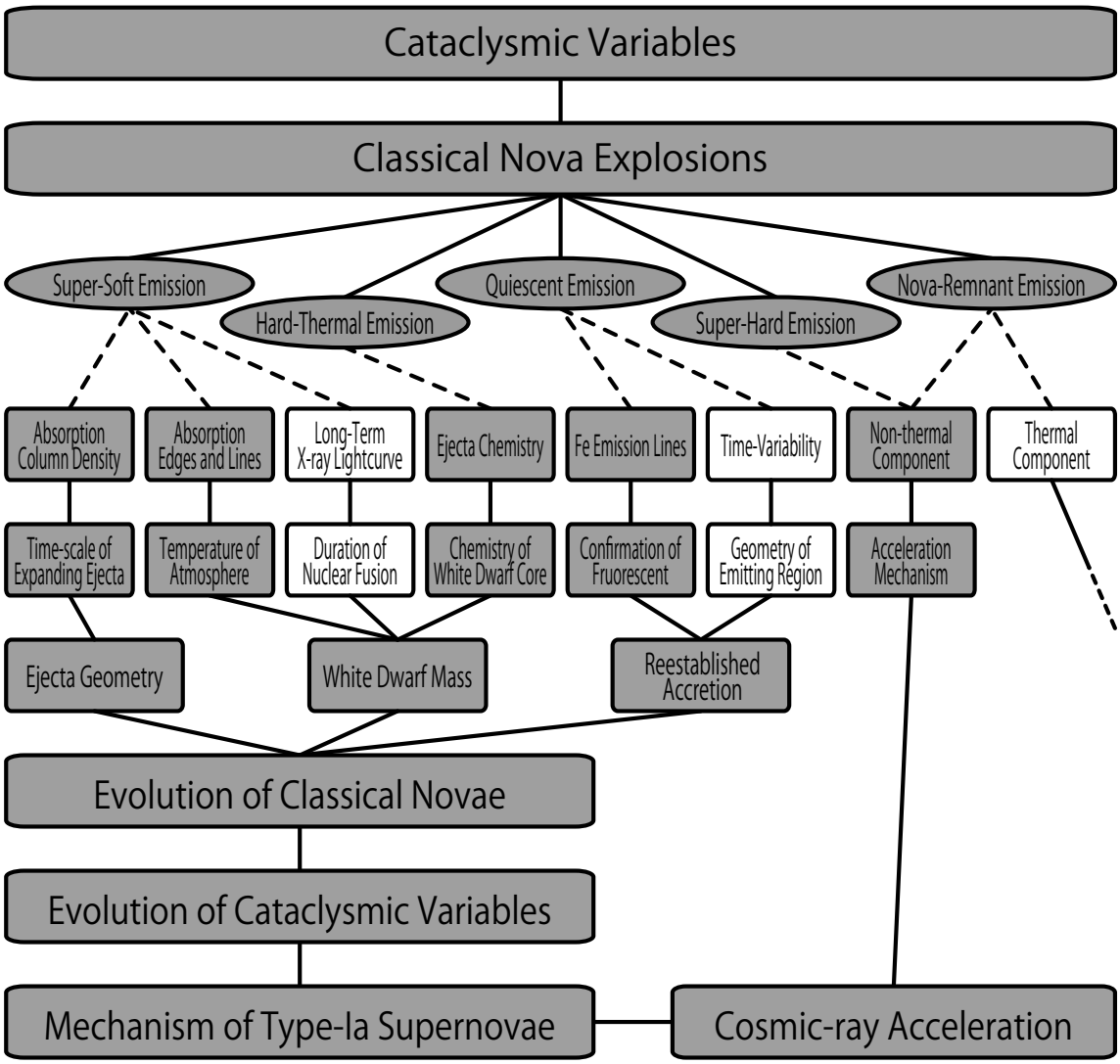

Figure 6.3: Correlation chart of X-ray phenomena and their diagnostic utility in classical novae. Filled symbols indicate our results in this thesis.

Chapter 7

Conclusions

We discussed the mechanism of classical novae taking an X-ray observational approach to understand the wide variety of high-energy phenomena including all previous studies and our latest discoveries.

1. We developed an effective observing system of classical novae using several X-ray satellites to overcome the difficulties of the faint and the transient nature of these events.

2. Deep X-ray observations of four classical novae were successfully performed using the *Suzaku*, the *XMM-Newton*, and the *Swift* satellites.

3. We discovered super-hard X-ray emission in the early evolution of classical novae for the first time during the observation of V2491 Cygni. A non-thermal origin is suggested to explain power-law emission.

4. The mechanism of the expanding ejecta was discussed using the data set of V2672 Ophiuchi, in which the flare-like flux amplification is significantly detected.

5. The chemical abundance of the plasma is presented for classical novae V458 Vulpeculae and V2491 Cygni with the spectroscopy of hard X-ray emission.

6. We newly discovered soft X-ray emission from a classical nova, which was named Suzaku J0105−72 based on the archival data. We also estimate the mass of the white dwarf from the data set.

7. The re-establishment of accretion process was confirmed in the X-ray observations of V2491 Cygni with the detection of quasi-neutral Fe emission line.

8. We discussed the nature of classical novae, and classified the X-ray emission to explain all results in the literature and those presented in this thesis.

Bibliography

Abdo, A. A., Ackermann, M., Ajello, M., et al. 2010, Science, 329, 817

Anders, E. & Grevesse, N. 1989, *Geochimica et Cosmochimica Acta*, 53, 197

Ashok, N. M., Banerjee, D. P. K., Joshi, V., et al. 2008, Central Bureau Electronic Telegrams, 1354, 1

Atwood, W. B., Abdo, A. A., Ackermann, M., et al. 2009, *Astrophysical Journal*, 697, 1071

Ayani, K. & Matsumoto, K. 2008, Central Bureau Electronic Telegrams, 1334, 1

Ayani, K., Murakami, N., Hata, K., et al. 2009a, Central Bureau Electronic Telegrams, 1911, 1

Ayani, K., Murakami, N., Hata, K., et al. 2009b, *International Astronomical Union Circular*, 9064, 2

Baklanov, A., Pavlenko, E., & Berezina, E. 2008, The Astronomer's Telegram, 1514, 1

Balman, Ş. 2005, *Astrophysical Journal*, 627, 933

Balman, Ş. 2010, *Monthly Notices of the Royal Astronomical Society*, 404, L26

Balman, Ş. & Krautter, J. 2001, *Monthly Notices of the Royal Astronomical Society*, 326, 1441

Balman, S., Krautter, J., & Oegelman, H. 1998, *Astrophysical Journal*, 499, 395

Balman, Ş. & Ögelman, H. B. 1999, *Astrophysical Journal Letters*, 518, L111

Balman, S., Orio, M., & Ogelman, H. 1995, *Astrophysical Journal*, 449, L47

Balman, S., Pekon, Y., & Kiziloglu, U. 2008, The Astronomer's Telegram, 1504, 1

Bamba, A., Fukazawa, Y., Hiraga, J. S., et al. 2008, *Publication of Astronomical Society of Japan*, 60, 153

Barthelmy, S. D., Barbier, L. M., Cummings, J. R., et al. 2005, Space Science Reviews, 120, 143

Baskill, D. S., Wheatley, P. J., & Osborne, J. P. 2005, *Monthly Notices of the Royal Astronomical Society*, 357, 626

Becker, R. H. 1981, *Astrophysical Journal*, 251, 626

Becker, R. H. & Marshall, F. E. 1981a, *Astrophysical Journal Letters*, 244, L93

Becker, R. H. & Marshall, F. E. 1981b, *Astrophysical Journal*, 244, L93

Bianciardi, G., Puig, X., & Forne, E. 2007a, Central Bureau Electronic Telegrams, 1038, 2

Bianciardi, G., Villegas, J. M., & Sanchez, A. 2007b, Central Bureau Electronic Telegrams, 1035, 2

Blandford, R. D. & Ostriker, J. P. 1980, *Astrophysical Journal*, 237, 793

Bode, M. F. 2010, Astronomische Nachrichten, 331, 160

Bode, M. F. & Evans, A. 2008, Classical Novae, ed. Bode, M. F. & Evans, A.

Bode, M. F., O'Brien, T. J., Osborne, J. P., et al. 2006, *Astrophysical Journal*, 652, 629

Bode, M. F., Osborne, J. P., Page, K. L., et al. 2008, in Astronomical Society of the Pacific Conference Series, Vol. 401, Astronomical Society of the Pacific Conference Series, ed. A. Evans, M. F. Bode, T. J. O'Brien, & M. J. Darnley, 269

Boella, G., Butler, R. C., Perola, G. C., et al. 1997, *Astronomy & Astrophysics Supplement*, 122, 299

Boldt, E. 1987, in IAU Symposium, Vol. 124, Observational Cosmology, ed. A. Hewitt, G. Burbidge, & L. Z. Fang, 611–615

Borkowski, K. J., Lyerly, W. J., & Reynolds, S. P. 2001, *Astrophysical Journal*, 548, 820

Borkowski, K. J., Sarazin, C. L., & Blondin, J. M. 1994, *Astrophysical Journal*, 429, 710

Bradt, H. V., Rothschild, R. E., & Swank, J. H. 1993, *Astronomy & Astrophysics Supplement*, 97, 355

Bradt, H. V. D., Ohashi, T., & Pounds, K. A. 1992, *Annual Review of Astronomy & Astrophysics*, 30, 391

Brahe, T. 1969, De nova et nullius aevi memoria prius visa stella iam pridem anno a nato Christo 1572 mense novembri primium conspecta, ed. Brahe, T.

Broens, E., Hornoch, K., Cloesen, P., et al. 2007, *International Astronomical Union Circular*, 8878, 2

Brown, N. J., Amorim, A., Liller, W., et al. 2008, *International Astronomical Union Circular*, 8931, 1

Buil, C. & Fujii, M. 2007, *International Astronomical Union Circular*, 8862, 2

Burrows, D. N., Hill, J. E., Nousek, J. A., et al. 2005, Space Science Reviews, 120, 165

Burrows, D. N., Hill, J. E., Nousek, J. A., et al. 2004, in Society of Photo-Optical Instrumentation Engineers (SPIE) Conference Series, Vol. 5165, Society of Photo-Optical Instrumentation Engineers (SPIE) Conference Series, ed. K. A. Flanagan & O. H. W. Siegmund, 201–216

Byckling, K., Mukai, K., Thorstensen, J. R., & Osborne, J. P. 2010, *Monthly Notices of the Royal Astronomical Society*, 408, 2298

Capaccioli, M., della Valle, M., Rosino, L., & D'Onofrio, M. 1989, *Astronomical Journal*, 97, 1622

Capalbi, M., Perri, M., Saija, B., Tamburelliu, F., & Angelini, L. 2005, The *Swift* XRT Data Reduction Guide, version 1.2

Casas, R., Fernandez-Ocana, M. A., Diepvens, A., Scarmato, T., & Lehky, M. 2007, Central Bureau Electronic Telegrams, 1035, 3

Chandrasekhar, S. 1931a, *Monthly Notices of the Royal Astronomical Society*, 91, 456

Chandrasekhar, S. 1931b, *Astrophysical Journal*, 74, 81

Chanmugam, G., Ray, A., & Singh, K. P. 1991, *Astrophysical Journal*, 375, 600

Ciardullo, R., Tamblyn, P., Jacoby, G. H., Ford, H. C., & Williams, R. E. 1990, *Astronomical Journal*, 99, 1079

Citterio, O., Campano, S., Conconi, P., et al. 1996, in Society of Photo-Optical Instrumentation Engineers (SPIE) Conference Series, Vol. 2805, Society of Photo-Optical Instrumentation Engineers (SPIE) Conference Series, ed. R. B. Hoover & A. B. Walker, 56–65

Cordova, F. A., Jensen, K. A., & Nugent, J. J. 1981a, *Monthly Notices of the Royal Astronomical Society*, 196, 1

Cordova, F. A. & Mason, K. O. 1984, *Monthly Notices of the Royal Astronomical Society*, 206, 879

Cordova, F. A., Mason, K. O., & Nelson, J. E. 1981b, *Astrophysical Journal*, 245, 609

Cronin, J. W., Gaisser, T. K., & Swordy, S. P. 1997, Scientific American, 276, 44

Cropper, M. 1990, *Space Science Reviews*, 54, 195

Cruise, A. M. 1977, *Nature*, 267, 685

Däppen, W. 2000, Allen's Astrophysical Quantities, ed. Cox, A. N., Vol. 27

Darnley, M. J., Bode, M. F., Kerins, E., et al. 2006, *Monthly Notices of the Royal Astronomical Society*, 369, 257

della Valle, M. & Livio, M. 1995, *Astrophysical Journal*, 452, 704

den Herder, J. W., Brinkman, A. C., Kahn, S. M., et al. 2001, *Astronomy & Astrophysics*, 365, L7

Dickey, J. M. & Lockman, F. J. 1990, *Annual Review of Astronomy & Astrophysics*, 28, 215

Downes, R. A. & Duerbeck, H. W. 2000, *Astronomical Journal*, 120, 2007

Downes, R. A., Webbink, R. F., Shara, M. M., et al. 2005, Journal of Astronomical Data, 11, 2

Drake, J. J., Laming, J. M., Ness, J., et al. 2009, *Astrophysical Journal*, 691, 418

Drake, J. J. & Orlando, S. 2010, *Astrophysical Journal Letters*, 720, L195

Drake, J. J., Page, K., Osborne, J., et al. 2007, The Astronomer's Telegram, 1246, 1

Drake, J. J., Page, K. L., Osborne, J. P., et al. 2008, The Astronomer's Telegram, 1721, 1

Drake, J. J., Wagner, R. M., Starrfield, S., et al. 2003, *Astrophysical Journal*, 584, 448

Drechsel, H., Rahe, J., Wargau, W., Seward, F. D., & Wang, Z. R. 1983, *Astronomy & Astrophysics*, 126, 357

Ebisawa, K., Bourban, G., Bodaghee, A., Mowlavi, N., & Courvoisier, T. 2003, *Astronomy & Astrophysics*, 411, L59

Ebisawa, K., Mukai, K., Kotani, T., et al. 2001, *Astrophysical Journal*, 550, 1007

Eracleous, M., Halpern, J., & Patterson, J. 1991, *Astrophysical Journal*, 382, 290

Evans, C. J., Howarth, I. D., Irwin, M. J., Burnley, A. W., & Harries, T. J. 2004, *Monthly Notices of the Royal Astronomical Society*, 353, 601

Ezuka, H. & Ishida, M. 1999, *Astrophysical Journal*, 120, S277

Faulkner, J. 1971, *Astrophysical Journal Letters*, 170, L99

Ferro, F., Lavagno, A., & Quarati, P. 2004, Physica A Statistical Mechanics and its Applications, 340, 477

Filipović, M. D., Bohlsen, T., Reid, W., et al. 2002, *Monthly Notices of the Royal Astronomical Society*, 335, 1085

Filipović, M. D., Haberl, F., Pietsch, W., & Morgan, D. H. 2000, *Astronomy & Astrophysics*, 353, 129

Frank, J., King, A., & Raine, D. 1992, Accretion power in astrophysics., ed. Frank, J., King, A., & Raine, D.

Frank, J., King, A., & Raine, D. J. 2002, Accretion Power in Astrophysics: Third Edition, ed. Frank, J., King, A., & Raine, D. J.

Friedjung, M. 1987, *Astronomy & Astrophysics*, 180, 155

Fujimoto, R., Mitsuda, K., Mccammon, D., et al. 2007, *Publication of Astronomical Society of Japan*, 59, 133

Fukazawa, Y., Mizuno, T., Watanabe, S., et al. 2009, *Publication of Astronomical Society of Japan*, 61, 17

Gaposchkin, C. H. P. 1957, The galactic novae., ed. Gaposchkin, C. H. P.

Garmire, G. P., Bautz, M. W., Ford, P. G., Nousek, J. A., & Ricker, Jr., G. R. 2003, in Society of Photo-Optical Instrumentation Engineers (SPIE) Conference Series, Vol. 4851, Society of Photo-Optical Instrumentation Engineers (SPIE) Conference Series, ed. J. E. Truemper & H. D. Tananbaum, 28–44

Gehrels, N., Chincarini, G., Giommi, P., et al. 2004, *Astrophysical Journal*, 611, 1005

Gehrz, R. D., Truran, J. W., Williams, R. E., & Starrfield, S. 1998, *Publication of Astronomical Society of Pacific*, 110, 3

George, I. M. & Fabian, A. C. 1991, *Monthly Notices of the Royal Astronomical Society*, 249, 352

Giacconi, R., Branduardi, G., Briel, U., et al. 1979, *Astrophysical Journal*, 230, 540

Greiner, J. 2000, *New Astronomy*, 5, 137

Greiner, J. & Di Stefano, R. 2002, *Astrophysical Journal Letters*, 578, L59

Haberl, F., Filipović, M. D., Pietsch, W., & Kahabka, P. 2000, *Astronomy & Astrophysics Supplement*, 142, 41

Hachisu, I. & Kato, M. 2001, *Astrophysical Journal*, 558, 323

Hachisu, I. & Kato, M. 2005, *Astrophysical Journal*, 631, 1094

Hachisu, I. & Kato, M. 2006, *Astrophysical Journal Supplement*, 167, 59

Hachisu, I. & Kato, M. 2009, *Astrophysical Journal Letters*, 694, L103

Hachisu, I., Kato, M., & Luna, G. J. M. 2007, *Astrophysical Journal Letters*, 659, L153

Haefner, R., Metz, K., & Pietsch, W. 1988, *Astronomy & Astrophysics*, 200, 75

Hamilton, A. J. S., Chevalier, R. A., & Sarazin, C. L. 1983, *Astrophysical Journal Supplement*, 51, 115

Hartmann, H. W. & Heise, J. 1997, *Astronomy & Astrophysics*, 322, 591

Heise, J., van Teeseling, A., & Kahabka, P. 1994, *Astronomy & Astrophysics*, 288, L45

Hellier, C. & Mukai, K. 2004, *Monthly Notices of the Royal Astronomical Society*, 352, 1037

Helton, L. A., Woodward, C. E., Vanlandingham, K., & Schwarz, G. J. 2008, Central Bureau Electronic Telegrams, 1379, 1

Henden, A. & Munari, U. 2008, Information Bulletin on Variable Stars, 5834, 1

Hernanz, M. & Sala, G. 2002, Science, 298, 393

Hernanz, M. & Sala, G. 2005, in Astronomical Society of the Pacific Conference Series, Vol. 330, The Astrophysics of Cataclysmic Variables and Related Objects, ed. J.-M. Hameury & J.-P. Lasota, 447

Hernanz, M. & Sala, G. 2007, *Astrophysical Journal*, 664, 467

Hernanz, M. & Sala, G. 2010, Astronomische Nachrichten, 331, 169

Hess, V. F. 1912, Zeitschrift fur Physik, 13, 1084

Hoffman, J. A., Lewin, W. H. G., Brecher, K., et al. 1976, *Nature*, 261, 208

Hyodo, Y. 2009, PhD thesis, Kyoto University

Hyodo, Y., Tsujimoto, M., Hamaguchi, K., et al. 2008, *Publication of Astronomical Society of Japan*, 60, S85

Ibarra, A. & Kuulkers, E. 2008, The Astronomer's Telegram, 1473, 1

Ibarra, A., Kuulkers, E., Beardmore, A., et al. 2008, The Astronomer's Telegram, 1478, 1

Ibarra, A., Kuulkers, E., Osborne, J. P., et al. 2009, *Astronomy & Astrophysics*, 497, L5

Iben, Jr., I. & Tutukov, A. V. 1989, *Astrophysical Journal*, 342, 430

Inoue, H., Koyama, K., & Tanaka, Y. 1983, in IAU Symposium, Vol. 101, Supernova Remnants and their X-ray Emission, ed. J. Danziger & P. Gorenstein, 535–540

Ishida, M., Silber, A., Bradt, H. V., et al. 1991, *Astrophysical Journal*, 367, 270

Ishisaki, Y., Maeda, Y., Fujimoto, R., et al. 2007, *Publication of Astronomical Society of Japan*, 59, 113

Jansen, F., Lumb, D., Altieri, B., et al. 2001, *Astronomy & Astrophysics*, 365, L1

Jose, J. & Hernanz, M. 1998, *Astrophysical Journal*, 494, 680

José, J. & Hernanz, M. 2007, Journal of Physics G Nuclear Physics, 34, 431

Jurdana-Sepic, R. & Munari, U. 2008, Information Bulletin on Variable Stars, 5839, 1

Kabashima, F., Corelli, P., Guido, E., & Sostero, G. 2009, *International Astronomical Union Circular*, 9089, 1

Kahabka, P. 1998, *Astronomy & Astrophysics*, 331, 328

Kahabka, P., Hartmann, H. W., Parmar, A. N., & Negueruela, I. 1999a, *Astronomy & Astrophysics*, 347, L43

Kahabka, P., Pietsch, W., Filipović , M. D., & Haberl, F. 1999b, *Astronomy & Astrophysics Supplement*, 136, 81

Kalberla, P. M. W., Burton, W. B., Hartmann, D., et al. 2005, *Astronomy & Astrophysics*, 440, 775

Kazarovets, E. 2007, *International Astronomical Union Circular*, 8850, 2

Kazarovets, E. 2009, *International Astronomical Union Circular*, 9100, 2

Kazarovets, E. 2010, *International Astronomical Union Circular*, 9140, 3

Kazarovets, E. & Samus, N. N. 2010a, *International Astronomical Union Circular*, 9120, 3

Kazarovets, E. & Samus, N. N. 2010b, *International Astronomical Union Circular*, 9119, 2

Kazarovets, E., Waagen, E. O., Kok, Y., et al. 2009, *International Astronomical Union Circular*, 9061, 2

Kazarovets, E. V. & Samus, N. 2009, *International Astronomical Union Circular*, 9043, 3

Kelley, R. L., Mitsuda, K., Allen, C. A., et al. 2007, *Publication of Astronomical Society of Japan*, 59, 77

Kimeswenger, S., Dalnodar, S., Knapp, A., et al. 2008, *Astronomy & Astrophysics*, 479, L51

Kinugasa, K., Nishiyama, K., Kabashima, F., et al. 2009, *International Astronomical Union Circular*, 9041, 1

Kiss, L. & Sarneczky, K. 2007, Central Bureau Electronic Telegrams, 1038, 1

Kiyota, S., Vollmann, W., Koberger, H., et al. 2010, *International Astronomical Union Circular*, 9112, 1

Kokubun, M., Makishima, K., Takahashi, T., et al. 2007, *Publication of Astronomical Society of Japan*, 59, 53

Koyama, K., Tsunemi, H., Dotani, T., et al. 2007, *Publication of Astronomical Society of Japan*, 59, 23

Krauss Hartman, M. I., Rupen, M. P., & Mioduszewski, A. J. 2009, The Astronomer's Telegram, 2195, 1

Krautter, J. 2008, X-ray Emission from Classical Novae in Outburst, ed. Bode, M. F. & Evans, A., 232–251

Krautter, J., Oegelman, H., Starrfield, S., Wichmann, R., & Pfeffermann, E. 1996, *Astrophysical Journal*, 456, 788

Kuulkers, E., Ibarra, A., Page, K. L., et al. 2008, The Astronomer's Telegram, 1480, 1

Labordena, C., Forne, E., & Ardanuy, A. 2007, *International Astronomical Union Circular*, 8863, 3

Lang, K. R. 2006, A Companion to Astronomy and Astrophysics, ed. Lang, K. R.

Leibowitz, E., Orio, M., Gonzalez-Riestra, R., et al. 2006, *Monthly Notices of the Royal Astronomical Society*, 371, 424

Liedahl, D. A., Osterheld, A. L., & Goldstein, W. H. 1995, *Astrophysical Journal Letters*, 438, L115

Liller, W. 2008, *International Astronomical Union Circular*, 9004, 1

Liller, W., Bolt, G., Santallo, R., et al. 2007a, *International Astronomical Union Circular*, 8850, 1

Liller, W., Heathcote, B., Schmeer, P., et al. 2007b, *International Astronomical Union Circular*, 8800, 1

Liller, W. & Jones, A. 1999, Information Bulletin on Variable Stars, 4774, 1

Liller, W. & Mayer, B. 1987, *Publication of Astronomical Society of Pacific*, 99, 606

Livio, M., Mastichiadis, A., Oegelman, H., & Truran, J. W. 1992, *Astrophysical Journal*, 394, 217

Lloyd, H. M., O'Brien, T. J., Bode, M. F., et al. 1992, *Nature*, 356, 222

Lomb, N. R. 1976, *Astrophysics and Space Science*, 39, 447

Luna, G. J. M., Montez, R., Sokoloski, J. L., Mukai, K., & Kastner, J. H. 2009, *Astrophysical Journal*, 707, 1168

Lynch, D. K., Russell, R. W., Rudy, R. J., & Woodward, C. E. 2007, *International Astronomical Union Circular*, 8883, 1

Lynch, D. K., Russell, R. W., Rudy, R. J., Woodward, C. E., & Schwarz, G. J. 2008a, *International Astronomical Union Circular*, 8935, 1

Lynch, D. K., Woodward, C. E., Gehrz, R., et al. 2008b, *Astronomical Journal*, 136, 1815

Lynch, D. K., Woodward, C. E., Gehrz, R., et al. 2008c, *Astronomical Journal*, 136, 1815

M. Hernanz & J. José, ed. 2002, American Institute of Physics Conference Series, Vol. 637, in Classical Nova Explosions, ed. M. Hernanz & J. José, 462

Mason, K. O., Breeveld, A., Much, R., et al. 2001, *Astronomy & Astrophysics*, 365, L36

Mason, K. O., Córdova, F. A., Bode, M. F., & Barr, P. 1987, in RS Ophiuchi (1985) and the Recurrent Nova Phenomenon, ed. M. F. Bode, 167

Mayer, W. F. 1975, Johns Hopkins APL Technical Digest, 14, 14

Mewe, R. 1999, in Lecture Notes in Physics, Berlin Springer Verlag, Vol. 520, X-Ray Spectroscopy in Astrophysics, ed. J. van Paradijs & J. A. M. Bleeker, 109

Meyssonnier, N. & Azzopardi, M. 1993, *Astronomy & Astrophysics Supplement*, 102, 451

Mitsuda, K., Bautz, M., Inoue, H., et al. 2007, *Publication of Astronomical Society of Japan*, 59, 1

Miyata, E., Katsuda, S., Tsunemi, H., et al. 2007, *Publication of Astronomical Society of Japan*, 59, 163

Monet, D., Canzian, B., Harris, H., et al. 1998, VizieR Online Data Catalog, 1243, 0

Monet, D. G., Levine, S. E., Casian, B., & et al. 2002, VizieR Online Data Catalog, 1284, 0

Moretti, A., Campana, S., Mineo, T., et al. 2005, in Society of Photo-Optical Instrumentation Engineers (SPIE) Conference Series, Vol. 5898, Society of Photo-Optical Instrumentation Engineers (SPIE) Conference Series, ed. O. H. W. Siegmund, 360–368

Moshir, M. & et al. 1990, in IRAS Faint Source Catalogue, version 2.0 (1990), 0

Mukai, K. & Ishida, M. 2001, *Astrophysical Journal*, 551, 1024

Mukai, K. & Orio, M. 2005, *Astrophysical Journal*, 622, 602

Mukai, K., Orio, M., & Della Valle, M. 2008, *Astrophysical Journal*, 677, 1248

Mukai, K. & Shiokawa, K. 1993, *Astrophysical Journal*, 418, 863

Mukerjee, K., Osborne, J. P., Wells, A. A., et al. 2004, in Society of Photo-Optical Instrumentation Engineers (SPIE) Conference Series, Vol. 5165, Society of Photo-Optical Instrumentation Engineers (SPIE) Conference Series, ed. K. A. Flanagan & O. H. W. Siegmund, 251–261

Munari, U., Moretti, S., & Tomaselli, S. 2007, Central Bureau Electronic Telegrams, 1029, 1

Munari, U., Saguner, T., Ochner, P., et al. 2009, Central Bureau Electronic Telegrams, 1912, 1

Naik, S., Banerjee, D. P. K., & Ashok, N. M. 2009, *Monthly Notices of the Royal Astronomical Society*, 394, 1551

Nakajima, H., Yamaguchi, H., Matsumoto, H., et al. 2008, *Publication of Astronomical Society of Japan*, 60, 1

Nakamura, Y., Yamaoka, H., Dillon, W. G., et al. 2007, Central Bureau Electronic Telegrams, 1029, 2

Nakano, S., Beize, J., Jin, Z., et al. 2008a, *International Astronomical Union Circular*, 8934, 1

Nakano, S., Beize, J., Jin, Z., et al. 2008b, *International Astronomical Union Circular*, 8934, 1

Nakano, S., Kadota, K., Waagen, E., et al. 2007a, *International Astronomical Union Circular*, 8861, 2

Nakano, S., Kadota, K., Waagen, E., et al. 2007b, *International Astronomical Union Circular*, 8861, 2

Nakano, S., Kaneda, H., & Kadota, K. 2008c, *International Astronomical Union Circular*, 8927, 2

Nakano, S., Nishimura, H., Guido, E., Sostero, G., & Kazarovets, E. V. 2009a, *International Astronomical Union Circular*, 9093, 1

Nakano, S., Nishimura, H., Itagaki, K., et al. 2010a, *International Astronomical Union Circular*, 9111, 2

Nakano, S., Nishimura, H., Kadota, K., et al. 2007c, *International Astronomical Union Circular*, 8824, 1

Nakano, S., Nishimura, H., Kiyota, S., et al. 2010b, *International Astronomical Union Circular*, 9119, 1

Nakano, S., Nishiyama, K., Kabashima, F., et al. 2008d, *International Astronomical Union Circular*, 8937, 1

Nakano, S., Nishiyama, K., Kabashima, F., et al. 2008e, *International Astronomical Union Circular*, 8950, 1

Nakano, S., Nishiyama, K., Kabashima, F., et al. 2008f, *International Astronomical Union Circular*, 8972, 1

Nakano, S., Sakurai, Y., Itagaki, K., & Koff, R. 2007d, *International Astronomical Union Circular*, 8832, 1

Nakano, S., Tago, A., Itagaki, K., et al. 2008g, *International Astronomical Union Circular*, 8907, 1

Nakano, S., Tago, A., Nishiyama, K., & Sakamoto, T. 2007e, *International Astronomical Union Circular*, 8821, 1

Nakano, S., Yamaoka, H., Itagaki, K., et al. 2009b, *International Astronomical Union Circular*, 9064, 1

Nakano, S., Yamaoka, H., Itagaki, K., et al. 2009c, *International Astronomical Union Circular*, 9064, 1

Nakano, S., Yamaoka, H., & Kadota, K. 2009d, Central Bureau Electronic Telegrams, 1910, 1

Nauenberg, M. 1972, *Astrophysical Journal*, 175, 417

Nelson, T., Orio, M., Cassinelli, J. P., et al. 2008, *Astrophysical Journal*, 673, 1067

Ness, J. 2010a, Astronomische Nachrichten, 331, 179

Ness, J., Drake, J. J., Beardmore, A. P., et al. 2009a, *Astronomical Journal*, 137, 4160

Ness, J., Drake, J. J., Starrfield, S., et al. 2009b, *Astronomical Journal*, 137, 3414

Ness, J., Schwarz, G., Starrfield, S., et al. 2008a, *Astronomical Journal*, 135, 1328

Ness, J., Schwarz, G. J., Retter, A., et al. 2007a, *Astrophysical Journal*, 663, 505

Ness, J., Starrfield, S., Beardmore, A. P., et al. 2007b, *Astrophysical Journal*, 665, 1334

Ness, J., Starrfield, S., Burwitz, V., Drake, J. J., & Krautter, J. 2003a, Astronomische Nachrichten Supplement, 324, 139

Ness, J., Starrfield, S., Burwitz, V., et al. 2003b, *Astrophysical Journal Letters*, 594, L127

Ness, J., Starrfield, S., Jordan, C., Krautter, J., & Schmitt, J. H. M. M. 2005, *Monthly Notices of the Royal Astronomical Society*, 364, 1015

Ness, J.-U. 2010b, Astronomische Nachrichten, 331, 179

Ness, J.-U., Drake, J. J., Starrfield, S., et al. 2009c, *Astronomical Journal*, 137, 3414

Ness, J.-U., Osborne, J. P., Dobrotka, A., et al. 2011, *Monthly Notices of the Royal Astronomical Society*, submitted.

Ness, J.-U., Starrfield, S., Gonzalez, R., et al. 2008b, The Astronomer's Telegram, 1561, 1

Ness, J.-U., Starrfield, S., Gonzalez, R., et al. 2008c, The Astronomer's Telegram, 1573, 1

Ngeow, C. & Kanbur, S. M. 2006, *Monthly Notices of the Royal Astronomical Society*, 369, 723

Nishimura, J., Mitsuda, K., & Itoh, M. 1986, *Publication of Astronomical Society of Japan*, 38, 819

Nishiyama, K., Kabashima, F., Corelli, P., et al. 2009a, *International Astronomical Union Circular*, 9100, 1

Nishiyama, K., Kabashima, F., Kiyota, S., et al. 2010a, *International Astronomical Union Circular*, 9120, 1

Nishiyama, K., Kabashima, F., Liller, W., Yusa, T., & Maehara, H. 2010b, *International Astronomical Union Circular*, 9140, 1

Nishiyama, K., Kabashima, F., Nakano, S., et al. 2008, *International Astronomical Union Circular*, 8947, 1

Nishiyama, K., Kabashima, F., Pojmanski, G., et al. 2009b, *International Astronomical Union Circular*, 9061, 1

Nishiyama, K., Kabashima, F., Sakurai, Y., et al. 2010c, *International Astronomical Union Circular*, 9142, 1

Nissinen, M., Hentunen, V., Kiyota, S., & Elenin, L. 2009, Central Bureau Electronic Telegrams, 1910, 2

Norton, A. J. & Watson, M. G. 1989, *Monthly Notices of the Royal Astronomical Society*, 237, 715

O'Brien, T. J., Lloyd, H. M., & Bode, M. F. 1994, *Monthly Notices of the Royal Astronomical Society*, 271, 155

Oegelman, H., Beuermann, K., & Krautter, J. 1984, *Astrophysical Journal Letters*, 287, L31

Oegelman, H., Krautter, J., & Beuermann, K. 1987, *Astronomy & Astrophysics*, 177, 110

Oegelman, H., Orio, M., Krautter, J., & Starrfield, S. 1993, *Nature*, 361, 331

Orio, M. 1993, *Astronomy & Astrophysics*, 274, L41

Orio, M., Balman, S., della Valle, M., Gallagher, J., & Oegelman, H. 1996, *Astrophysical Journal*, 466, 410

Orio, M., Covington, J., & Ögelman, H. 2001a, *Astronomy & Astrophysics*, 373, 542

Orio, M., Ebisawa, K., Heise, J., & Hartmann, J. 2004, in Revista Mexicana de Astronomia y Astrofisica Conference Series, Vol. 20, Revista Mexicana de Astronomia y Astrofisica Conference Series, ed. G. Tovmassian & E. Sion, 210–210

Orio, M., Mukai, K., Bianchini, A., de Martino, D., & Howell, S. 2009, *Astrophysical Journal*, 690, 1753

Orio, M., Parmar, A., Benjamin, R., et al. 2001b, *Monthly Notices of the Royal Astronomical Society*, 326, L13

Orio, M., Parmar, A., Benjamin, R., et al. 2001c, *Monthly Notices of the Royal Astronomical Society*, 326, L13

Orio, M., Parmar, A. N., Greiner, J., et al. 2002, *Monthly Notices of the Royal Astronomical Society*, 333, L11

Orio, M., Tepedelenlioglu, E., Starrfield, S., Woodward, C. E., & Della Valle, M. 2005, *Astrophysical Journal*, 620, 938

Osborne, J., Page, K., Beardmore, A., et al. 2006, The Astronomer's Telegram, 838, 1

Osborne, J. P., Page, K., Evans, P., et al. 2008, The Astronomer's Telegram, 1542, 1

Osborne, J. P., Page, K. L., Beardmore, A. P., et al. 2011, *Astrophysical Journal*, submitted.

Ozawa, M., Uchiyama, H., Matsumoto, H., et al. 2009, *Publication of Astronomical Society of Japan*, 61, 1

Page, K. L., Osborne, J. P., Evans, P. A., et al. 2008, The Astronomer's Telegram, 1523, 1

Page, K. L., Osborne, J. P., Evans, P. A., et al. 2010, *Monthly Notices of the Royal Astronomical Society*, 401, 121

Page, K. L., Osborne, J. P., Read, A. M., et al. 2009, *Astronomy & Astrophysics*, 507, 923

Pagnotta, A., Schaefer, B. E., Xiao, L., Collazzi, A. C., & Kroll, P. 2009, *Astronomical Journal*, 138, 1230

Patterson, J. 1994, *Publication of Astronomical Society of Pacific*, 106, 209

Patterson, J. & Raymond, J. C. 1985a, *Astrophysical Journal*, 292, 550

Patterson, J. & Raymond, J. C. 1985b, *Astrophysical Journal*, 292, 535

Payne-Gaposchkin, C. 1957, The Galactic Novae, ed. C. Payne-Gaposchkin

Pekön, Y. & Balman, Ş. 2008, *Monthly Notices of the Royal Astronomical Society*, 388, 921

Pereira, A. J. S., McGaha, J. E., Young, J., & Rhoades, H. 2007, *International Astronomical Union Circular*, 8895, 1

Pietsch, W., Haberl, F., Sala, G., et al. 2007, *Astronomy & Astrophysics*, 465, 375

Pittard, J. M. & Dougherty, S. M. 2006, *Monthly Notices of the Royal Astronomical Society*, 372, 801

Poggiani, R. 2008, *Astrophysics and Space Science*, 315, 79

Pojmanski, G., Szczygiel, D., & Pilecki, B. 2008, Central Bureau Electronic Telegrams, 1497, 1

Pojmanski, G., Szczygiel, D., Pilecki, B., et al. 2009, *International Astronomical Union Circular*, 9043, 1

Porquet, D., Mewe, R., Dubau, J., Raassen, A. J. J., & Kaastra, J. S. 2001, *Astronomy & Astrophysics*, 376, 1113

Prater, T. R., Rudy, R. J., Lynch, D. K., et al. 2007, *International Astronomical Union Circular*, 8904, 2

Predehl, P. & Schmitt, J. H. M. M. 1995, *Astronomy & Astrophysics*, 293, 889

Protassov, R., van Dyk, D. A., Connors, A., Kashyap, V. L., & Siemiginowska, A. 2002, *Astrophysical Journal*, 571, 545

Rauch, T., Orio, M., Gonzales-Riestra, R., et al. 2010, *Astrophysical Journal*, 717, 363

Raymond, J. C. & Smith, B. W. 1977, *Astrophysical Journal Supplement*, 35, 419

Read, A. M., Saxton, R. D., & Esquej, P. 2007, The Astronomer's Telegram, 1282, 1

Reinsch, K., van Teeseling, A., Beuermann, K., & Thomas, H. 1999, in Highlights in X-ray Astronomy, ed. B. Aschenbach & M. J. Freyberg, 70

Revnivtsev, M., Sazonov, S., Gilfanov, M., Churazov, E., & Sunyaev, R. 2006, *Astronomy & Astrophysics*, 452, 169

Rohrbach, J. G., Ness, J., & Starrfield, S. 2009, *Astronomical Journal*, 137, 4627

Romano, P., Campana, S., Chincarini, G., et al. 2006, *Astronomy & Astrophysics*, 456, 917

Roming, P. W. A., Kennedy, T. E., Mason, K. O., et al. 2005, Space Science Reviews, 120, 95

Rothenflug, R. & Arnaud, M. 1985, *Astronomy & Astrophysics*, 144, 431

Rothschild, R., Boldt, E., Holt, S., et al. 1979, Space Science Instrumentation, 4, 269

Rudy, R. J., Lynch, D. K., Russell, R. W., Woodward, C. E., & Covey, K. 2008, *International Astronomical Union Circular*, 8938, 2

Rupen, M. P., Mioduszewski, A. J., & Sokoloski, J. L. 2008, *Astrophysical Journal*, 688, 559

Russell, S. C. & Dopita, M. A. 1992, *Astrophysical Journal*, 384, 508

Rybicki, G. B. & Lightman, A. P. 1985, Radiative processes in astrophysics., ed. Rybicki, G. B. & Lightman, A. P.

Sala, G., Hernanz, M., Ferri, C., & Greiner, J. 2008, *Astrophysical Journal Letters*, 675, L93

Samus, N. 2009, *International Astronomical Union Circular*, 9048, 2

Samus, N. & Kazarovets, E. V. 2008, *International Astronomical Union Circular*, 9004, 3

Samus, N. & Kazarovets, E. V. 2009, *International Astronomical Union Circular*, 9089, 4

Samus, N. N. 2007a, *International Astronomical Union Circular*, 8800, 3

Samus, N. N. 2007b, *International Astronomical Union Circular*, 8803, 3

Samus, N. N. 2007c, *International Astronomical Union Circular*, 8812, 3

Samus, N. N. 2007d, *International Astronomical Union Circular*, 8821, 5

Samus, N. N. 2007e, *International Astronomical Union Circular*, 8824, 3

Samus, N. N. 2007f, *International Astronomical Union Circular*, 8863, 2

Samus, N. N. 2007g, *International Astronomical Union Circular*, 8863, 2

Samus, N. N. 2007h, *International Astronomical Union Circular*, 8832, 3

Samus, N. N. 2008a, *International Astronomical Union Circular*, 8928, 1

Samus, N. N. 2008b, *International Astronomical Union Circular*, 8934, 2

Samus, N. N. 2008c, *International Astronomical Union Circular*, 8934, 2

Samus, N. N. 2008d, *International Astronomical Union Circular*, 8949, 2

Samus, N. N. 2008e, *International Astronomical Union Circular*, 8951, 1

Samus, N. N. & Pereira, A. J. S. 2007, *International Astronomical Union Circular*, 8896, 1

Samus, N. N., Santangelo, M. M. M., Hornoch, K., Souza, W., & Fidrich, R. 2008, *International Astronomical Union Circular*, 8940, 2

Samus, N. N., Waagen, E. O., Dvorak, S., et al. 2007, *International Astronomical Union Circular*, 8898, 1

Sasaki, M., Haberl, F., & Pietsch, W. 2000, *Astronomy & Astrophysics Supplement*, 147, 75

Saxton, R. D., Read, A. M., Esquej, P., et al. 2008, VizieR Online Data Catalog, 348, 611

Scarmato, T. 2007, Central Bureau Electronic Telegrams, 1038, 3

Schaefer, B. E. 2010, *Astrophysical Journal*, 187, S275

Schaefer, B. E., Harris, B. G., Dvorak, S., Templeton, M., & Linnolt, M. 2010, *International Astronomical Union Circular*, 9111, 1

Schlegel, D. J., Finkbeiner, D. P., & Davis, M. 1998, *Astrophysical Journal*, 500, 525

Schwarz, G. J., Osborne, J. P., Page, K., et al. 2009, The Astronomer's Telegram, 2173, 1

Scofield, J. H. 2001, in X-ray Data Booklet

Scofield, J. H. 2009, in X-ray Data Booklet

Serlemitsos, P. J., Soong, Y., Chan, K., et al. 2007, *Publication of Astronomical Society of Japan*, 59, 9

Seward, F. D. & Mitchell, M. 1981, *Astrophysical Journal*, 243, 736

Shanley, L., Ogelman, H., Gallagher, J. S., Orio, M., & Krautter, J. 1995, *Astrophysical Journal Letters*, 438, L95

Shapiro, S. L. & Teukolsky, S. A. 1986, Black Holes, White Dwarfs and Neutron Stars: The Physics of Compact Objects, ed. Shapiro, S. L. & Teukolsky, S. A.

Skoda, P., Kubat, J., Votruba, V., et al. 2007, Central Bureau Electronic Telegrams, 1035, 1

Smith, J. F. & Courtier, G. M. 1976, Royal Society of London Proceedings Series A, 350, 421

Smith, R. K., Brickhouse, N. S., Liedahl, D. A., & Raymond, J. C. 2001, *Astrophysical Journal Letters*, 556, L91

Sokoloski, J. L., Luna, G. J. M., Mukai, K., & Kenyon, S. J. 2006, *Nature*, 442, 276

Sokoloski, J. L., Rupen, M. P., & Mioduszewski, A. J. 2008, *Astrophysical Journal*, 685, L137

Starrfield, J. H., Illiadis, C., & Hix, W. R. 2008, Thermonuclear Processes, ed. Bode, M. F. & Evans, A., 77–101

Strüder, L., Briel, U., Dennerl, K., et al. 2001, *Astronomy & Astrophysics*, 365, L18

Sun, G. & Gao, X. 2009, *International Astronomical Union Circular*, 9049, 1

Suzaku Help Desk Team. 2009, The *Suzaku* First Step Guide, version 4.0.3

Suzaku Science Working Group. 2009, The *Suzaku* Technical Description, Announcement of Opportunity #5

Suzuki, A. & Shigeyama, T. 2010, ArXiv e-prints

Swift Mission Participants. 2004, *Swift* Explorer News Media Kit

Swift Science Center. 2009, The *Swift* Technical Handbook, version 6.0

Swordy, S. P. 2001, *Space Science Reviews*, 99, 85

Takahashi, T., Abe, K., Endo, M., et al. 2007, *Publication of Astronomical Society of Japan*, 59, 35

Takei, D., Ness, J., Tsujimoto, M., et al. 2011, *Publication of Astronomical Society of Japan*, submitted.

Takei, D. & Ness, J.-U. 2010, Astronomische Nachrichten, 331, 183

Takei, D., Tsujimoto, M., Kitamoto, S., et al. 2008, *Publication of Astronomical Society of Japan*, 60, 231

Takei, D., Tsujimoto, M., Kitamoto, S., et al. 2009, *Astrophysical Journal*, 697, L54

Tanaka, Y., Inoue, H., & Holt, S. S. 1994, *Publication of Astronomical Society of Japan*, 46, L37

Tarasova, T. N. 2007, Information Bulletin on Variable Stars, 5807, 1

Tatischeff, V. & Hernanz, M. 2007, *Astrophysical Journal Letters*, 663, L101

Taylor, B. G., Andresen, R. D., Peacock, A., & Zobl, R. 1981, *Space Science Reviews*, 30, 479

Tomov, T., Mikolajewski, M., Brozek, T., et al. 2008a, The Astronomer's Telegram, 1485, 1

Tomov, T., Mikolajewski, M., Ragan, E., Swierczynski, E., & Wychudzki, P. 2008b, The Astronomer's Telegram, 1475, 1

Trümper, J. 1984, Physica Scripta Volume T, 7, 209

Tsujimoto, M., Feigelson, E. D., Grosso, N., et al. 2005a, *Astrophysical Journal*, 160, S503

Tsujimoto, M., Kobayashi, N., & Tsuboi, Y. 2005b, *Astronomical Journal*, 130, 2212

Tsujimoto, M., Takei, D., Drake, J. J., Ness, J., & Kitamoto, S. 2009, *Publication of Astronomical Society of Japan*, 61, 69

Turner, M. J. L., Abbey, A., Arnaud, M., et al. 2001, *Astronomy & Astrophysics*, 365, L27

Uchiyama, H., Ozawa, M., Matsumoto, H., et al. 2009, *Publication of Astronomical Society of Japan*, 61, 9

Udalski, A. 1998, *Acta Astronomica*, 48, 113

van den Heuvel, E. P. J., Bhattacharya, D., Nomoto, K., & Rappaport, S. A. 1992, *Astronomy & Astrophysics*, 262, 97

van Teesellng, A., Heise, J., & Kahabka, P. 1996, in IAU Symposium, Vol. 165, Compact Stars in Binaries, ed. J. van Paradijs, E. P. J. van den Heuvel, & E. Kuulkers, 445

Venturini, C. C., Rudy, R. J., Lynch, D. K., Mazuk, S., & Puetter, R. C. 2004, *Astronomical Journal*, 128, 405

Verbunt, F. & Zwaan, C. 1981, *Astronomy & Astrophysics*, 100, L7

Voges, W., Aschenbach, B., Boller, T., et al. 2000, VizieR Online Data Catalog, 9029, 0

Waagen, E. O., Henden, A., Maury, A., et al. 2008, *International Astronomical Union Circular*, 8999, 1

Wang, Q. & Wu, X. 1992, *Astrophysical Journal Supplement*, 78, 391

Warner, B. 2003, Cataclysmic Variable Stars, ed. Warner, B.

Warner, B. 2008, Properties of Novae: an Overview, ed. Bode, M. F. & Evans, A., 16–33

Weisskopf, M. C., Brinkman, B., Canizares, C., et al. 2002, *Publication of Astronomical Society of Pacific*, 114, 1

Wells, A. A., Castelli, C. M., Denby, M., et al. 1997, in Society of Photo-Optical Instrumentation Engineers (SPIE) Conference Series, Vol. 3114, Society of Photo-Optical Instrumentation Engineers (SPIE) Conference Series, ed. O. H. Siegmund & M. A. Gummin, 392–403

Wesson, R., Barlow, M. J., Corradi, R. L. M., et al. 2008, *Astrophysical Journal*, 688, L21

Williams, R. E. 1992, *Astronomical Journal*, 104, 725

Williams, R. E., Hamuy, M., Phillips, M. M., et al. 1991, *Astrophysical Journal*, 376, 721

Wilms, J., Allen, A., & McCray, R. 2000, *Astrophysical Journal*, 542, 914

XMM-Newton Community Support Team. 2010, The *XMM-Newton* Users Handbook, issue 2.8.1

XMM-Newton Science Operations Centre User Support Team. 2010, The *XMM-Newton* Technical Description

Yamaoka, H., Itagaki, K., Guido, E., et al. 2009, *International Astronomical Union Circular*, 9098, 1

Yamaoka, H., Itagaki, K., Korotkiy, S., & Samus, N. N. 2008a, *International Astronomical Union Circular*, 8971, 2

Yamaoka, H., Itagaki, K., Nakano, S., et al. 2008b, *International Astronomical Union Circular*, 8989, 1

Yamaoka, H., Nakamura, Y., Itagaki, K., Nakano, S., & Nishimura, H. 2007a, *International Astronomical Union Circular*, 8810, 1

Yamaoka, H., Nakamura, Y., Nakano, S., Sakurai, Y., & Kadota, K. 2007b, *International Astronomical Union Circular*, 8803, 1

Yokogawa, J., Imanishi, K., Tsujimoto, M., Koyama, K., & Nishiuchi, M. 2003, *Publication of Astronomical Society of Japan*, 55, 161

Appendix A

Acronyms

The following table lists acronyms used in this thesis.

Acronym	Definition
AAVSO	American Association of Variable Star Observers
ACIS	Advanced Charge Coupled Device Imaging Spectrometer
APEC	Astrophysical Plasma Emission Code
ARF	Ancillary Response File
ASCA	Advanced Satellite for Cosmology and Astrophysics
ASM	All-Sky Monitor
BAT	Burst Alert Telescope
Beppo-SAX	Satellite per Astronomia X, "Beppo" in honor of Giuseppe Occhialini
BGO	Bismuth Germanate
BI	Back-Illuminated
CBAT	Central Bureau for Astronomical Telegrams
CBET	Central Bureau Electronic Telegrams
CCD	Charge Coupled Device
CNe	Classical Novae
CNO	Carbon-Nitrogen-Oxygen
CO	Carbon-Oxygen
COR	Cut-Off Rigidity
CR	Count Rate
CSM	Circumstellar Matter
CTE	Charge Transfer Efficiency
CV	Cataclysmic Variable
CXB	Cosmic X-ray Background
CXOU	Chandra X-ray Observatory Unregistered Source
DARTS	Data Archives and Transmission System
DETX	Detector X (Coordinate)
DETY	Detector Y (Coordinate)
DSS	Digitalized Sky Survey
EEF	Encircled Energy Function
EM	Emission Measure
EPIC	European Photon Imaging Camera
ESA	European Space Agency
ESAC	European Space Astronomy Centre
EXOSAT	European X-ray Observatory Satellite
FI	Front-Illuminated
FPCS	Focal Plane Crystal Spectrometer
FWHM	Full Width at Half Maximum
FWZI	Full Width at Zero Intensity
GBM	Gamma-ray Large Area Space Telescope Burst Monitor
GIS	Gas Imaging Spectrometer
GLAST	Gamma-ray Large Area Space Telescope
GRB	Gamma-Ray Burst
GRXE	Galactic Ridge X-ray Emission
GSO	Gadolinium Silicate

Acronym	Definition
GSFC	Goddard Space Flight Center
HEAO	High Energy Astronomy Observatories
HEA	High Energy Astrophysics
HEASARC	High Energy Astrophysics Science Archive Research Center
HEXTE	High Energy X-ray Timing Experiment
HPD	Half-Power Diameter
HPGSPC	High Pressure Gas Scintillator Proportional Counter
HR	Hardness Ratio
HRI	High Resolution Imager
HXD	Hard X-ray Detector
IAU	International Astronomical Union
IAUC	International Astronomical Union Circular
INTEGRAL	International Gamma Ray Astrophysics Laboratory
IP	Intermediate Polar
IPAC	Infrared Processing and Analysis Center
IPC	Imaging Proportional Counter
IR	InfraRed
ISAS	Institute of Space and Astronautical Science
ISM	Interstellar Medium
JAXA	Japan Aerospace Exploration Agency
JSPS	Japan Society for the Promotion of Science
LAT	Large Area Telescope
LECS	Low Energy Concentrator Spectrometer
LED	Low Energy Detector
LR	Low Rate
LTE	Local Thermodynamic Equilibrium
MECS	Medium Energy Concentrator Spectrometer
MIDEX	Medium-sized Explorer
MJD	Modified Julian Date
MMRD	Maximum Magnitude and Rate of Decline
MOS	Metal Oxide Semiconductor
MPC	Monitor Proportional Counter
NASA	National Aeronautics and Space Administration
NED	National Aeronautics and Space Administration Extragalactic Database
NEI	Non-Equilibrium Ionization
NLTE	Non-Local Thermodynamic Equilibrium
NXB	Non X-ray Background
OBF	Optical Blocking Filter
OGS	Objective Grating Spectrometer
OM	Optical Monitor
ONe	Oxygen-Neon
PC	Photon-Counting
PCA	Proportional Counter Array
PDS	Phoswich Detection System
PIN	PIN silicon diodes
PLAIN	Planning and Information
PN	PN-type Charge Coupled Device
PP	Proton-Proton
PSF	Point Spread Function
PSPC	Position Sensitive Proportional Counter
PU	Piled-up Photodiode
RGS	Reflection Grating Spectrometer
RMF	Redistribution Matrix Function
ROSAT	Roentgen Satellite
RXP	Roentgen Satellite Position Sensitive Proportional Counter Source
RXS	Roentgen Satellite All-Sky Survey Faint Source
RXTE	Rossi X-ray Timing Explorer
SAA	South Atlantic Anomaly
SAO	Smithsonian Astrophysical Observatory
SAS	Science Analysis Software
SOC	Science Operation Center
SCI	Spaced-row Charge Injection
SIMBAD	Set of Identifications, Measurements, and Bibliography for Astronomical Data
SIS	Solid-state Imaging Spectrometer
SMC	Small Magellanic Cloud

Acronym	Definition
SNR	Super-Nova Remnant
SSS	SuperSoft X-ray Source
TRISPEC	Triple Range Imager and Spectrograph
UD	Upper Discriminator
USC	Uchinoura Space Center
USNO	United States Naval Observatory
UT	Universal Time
UV	Ultra-Violet
UVOT	Ultra-Violet and Optical Telescope
VSNET	Variable Star Network
VSOLJ	Variable Star Observers League in Japan
WD	White Dwarf
WFC	Wide Field Camera
WT	Windowed-Timing
XIS	X-ray Imaging Spectrometer
XMM-Newton	X-ray Multi-Mirror Mission - Newton
XMMSL	XMM-Newton SLew survey
XRS	X-Ray Spectrometer
XRT	X-Ray Telescope

Acknowledgments

This research was supported by wonderful and precious collaborators, and this thesis could not have been completed without their help. I am really grateful to Shunji Kitamoto who introduced me to the X-ray astronomy and has been encouraging me throughout my graduate course. I also sincerely appreciate Masahiro Tsujimoto for an immense amount of time and effort to instruct me in all research activities. I would like to express my sincere gratitude to Jan-Uwe Ness, who kindly invited me into his office, and gave me invaluable advice on astronomy. I am also grateful to Jeremy J. Drake, who introduced me to X-ray observations of classical novae.

For discussion of the topics of this thesis, I am particularly grateful to Izumi Hachisu and Mariko Kato, who instructed me in theoretical approaches of classical novae. Ken Ebisawa, Manabu Ishida, and Koji Mukai also gave me invaluable advises on the X-ray astronomy of cataclysmic variables. Akira Arai, Akira Imada, and Kenzo Kinugasa also helped me to obtain the optical data and to publish the results. I also acknowledge the members of the *Swift* Nova-CV group for their interesting discussions on X-ray emission from classical novae.

For X-ray observations and data reduction, I really appreciate Hiroshi Murakami, who helped me to perform prompt and reliable observations as a specialist of *Suzaku* operation and for invaluable advice. I am also grateful to Hiromitsu Takahashi for expert's help of the *Suzaku*/HXD data reduction, to Yoshitomo Maeda who gave me precious information of the *Suzaku* telescope modules to examine the source at the edge of field of view, to Matteo Guianazzi who gave me a technical help in reducing the *XMM-Newton*/EPIC data, to Eirc D. Miller and Mikio Morii who also helped me to improve the manuscript of a publication.

My gratitude is also for Julian P. Osborn, Kim L. Page, and Greg Schwarz, who invited me to join the *Swift* Nova-CV Group, gave me precious information of the *Swift* observations, and let me use the observational data prior to publication, and for Bradley E. Schaefer who invited me to the world-wide monitoring campaign of a recurrent nova.

I also acknowledge the members of my laboratory and University for their encouragements. In particular, Noriaki Shibazaki, Takayoshi Kohmura, and Takato Hirayama helped me to improve manuscripts in my research activities. I would also like to thank Kimiko Saito, Hiroko Shirai, and the members of the Center for Research Initiatives of Rikkyo University for their support in reducing paperwork. I really appreciate Tomohiro Harada and Kazuo Ieki for their constructive refereeing of this thesis.

Finally, I express my most sincere appreciation to my thesis advisor, Professor Shunji Kitamoto, for the continuous support of my research.

This research is based on data observed by the *Suzaku*, *XMM-Newton*, and *Swift* observatories. We thank the *Suzaku* telescope managers for allocating a part of the director's discretionary time, the *XMM-Newton* Science Operation Center (SOC) for their support in scheduling the target-of-opportunity observations, and the *Swift* Mission Operations Center for taking a lot of observations in classical novae. We also appreciate the members of *Suzaku* and *XMM-Newton* helpdesk for providing the useful comments.

For the near-infrared and optical data, we acknowledge the *Kanata* TRISPEC team in Hiroshima University for providing the K_s-band data of V2491 Cyg prior to publication. Kazuhiro Nakajima and Hitoshi Yamaoka in the Variable Star Observers League in Japan (VSOLJ) for providing optical data of V458 Vul. We also acknowledge with thanks a wealth of observational data accumulated in the AAVSO International Database and the VSOLJ Observation Database contributed by observers worldwide and used in this research. We also thank the members in the Variable Star Network (VSNET) for providing an enormous amount of information about classical novae.

This research made use of data obtained from the Data ARchives and Transmission System (DARTS) provided by the PLAIN center at JAXA/ISAS, the NASA/IPAC Extragalactic Database (NED) which is operated by the Jet Propulsion Laboratory, California Institute of Technology, under contract with the NASA, and of the SIMBAD database, operated at CDS, Strasbourg, France. The *Einstein*, *ROSAT*, *ASCA*, *Beppo-SAX*, *Chandra*, and *XMM-Newton* data were obtained through the High Energy Astrophysics Science Archive Research Center Online Service provided by the NASA/Goddard Space Flight Center.

I acknowledge financial support by the Japan Society for the Promotion of Science (JSPS). I expresses gratitude for the European Space Astronomy Centre (ESAC) faculty members and the hospitality at the center during the course of this work.